PHYSICS OF RF HEATING SYSTEMS ON PROTO-MPEX

BY

PAWEL A. PIOTROWICZ

DISSERTATION

Submitted in partial fulfillment of the requirements
for the degree of Doctor of Philosophy in Nuclear, Plasma, and Radiological Engineering
in the Graduate College of the
University of Illinois at Urbana-Champaign, 2019

Urbana, Illinois

Doctoral Committee:

Professor David N. Ruzic, Chair
Professor Daniel Andruczyk
Dr. John B. O. Caughman, Oak Ridge National Laboratory
Professor Davide Curreli
Professor Jianming Jin

Abstract

Realizing controlled fusion as a commercial energy source is faced with many challenges. One of the main challenges being the development of Plasma Facing Components (PFC) that can survive the extreme environment encountered in a fusion reactor. To expedite the testing and development of PFCs Oak Ridge National Laboratory (ORNL) is building the Materials Plasma Exposure eXperiment (MPEX), which is a linear device purposed specifically for studying Plasma Material Interactions (PMI). Current linear devices cannot produce plasmas with fusion divertor relevant electron and ion temperatures and instead rely on electrostatic biasing of the target to simulate the relevant ion energies. This methodology inhibits studying the interaction of the eroded material and recycled neutral gas with a fusion relevant divertor plasma and does not properly simulate the angular energy distribution of the ion fluxes, therefore, PMI studies on these linear devices omit a vast amount of rich physics important to PFC development. MPEX will enable the study of fusion relevant PMI by producing fusion divertor relevant plasma conditions in front of a target station using RF technology. Proto-MPEX is the device that is currently operating at ORNL, where the viability of this RF technology is being demonstrated. The electron density, electron temperature, and ion temperature of the target plasma will be controlled independently with separate RF heating systems. This thesis focuses on the electron density production system and the ion heating systems on Proto-MPEX and their viability for MPEX.

The electron density production on Proto-MPEX is accomplished by a helicon plasma source. Helicon plasma sources have been shown to efficiently produce high-density plasmas for a relatively low amount of RF power. Efficient electron density production of helicon plasma sources in light ions is hypothesized to be enabled by strong core power deposition when the plasma conditions allow for the formation of helicon normal modes. Experimental evidence supporting this hypothesis is presented in the form of B-dot probe and IR camera measurements, showing the increase of on-axis RF magnetic field strength and the formation of eigenmode structure concurrently with an increase in core power deposition at the expense of power deposition in the periphery of the plasma column. An RF full-wave model of the helicon region is made, which predicts the formation of cavity-like structures of the RF magnetic field when core power deposition is increased. Next, the problem that Proto-MPEX's helicon source has been shown to not operate efficiently at higher magnetic field strengths is addressed. The hypothesis that the power balance does not allow enough density production for the helicon antenna to sustain a mode of operation that enhances core power deposition is tested by coupling a 2D axisymmetric full-wave simulation of the helicon antenna to a volume integrated 0D power/particle balance. This model is compared to experimental measurements of electron density and shows that there is a decrease in electron density production due to a decrease in core power coupling in the region where electron density decreases on Proto-MPEX. The model shows that if the Proto-MPEX helicon plasma source is operated at even higher magnetic fields strengths than efficient electron density production is recovered. Finally, the performance of Proto-MPEX is compared with other experimental devices by calculating the ionization cost of the plasma source, which shows that improvements to efficiency can practically be achieved to match the ionization cost of other plasma sources. Experimental improvements to the helicon source region are suggested and quantified with the couple RF and particle/power balance model.

The ion heating on Proto-MPEX is accomplished by ion cyclotron heating via the beach heating technique. This technique is expected to increase ion temperatures on Proto-MPEX to values of $T_i = 20$ eV or more. The beach heating technique has been successfully demonstrated on previous devices, however, these devices were operating at much lower electron densities than Proto-MPEX. A theoretical route to core ion heating is first explored. At magnetic field strengths near the ion cyclotron resonance, the higher electron density in Proto-MPEX brings the existence of the Alfvén resonance into the Proto-MPEX plasma. This layer acts to cut-off the cold plasma slow wave, called the inertial Alfvén wave for the high-density core plasma. On the high-density side of the Alfvén resonance, the kinetic Alfvén wave can propagate when the electron temperature allows. In Proto-MPEX this wave is thought to be responsible for the core heating of ions in the device. A simplified kinetic plasma tensor is implemented in COMSOL to simulate the propagation of this wave and to show that at Proto-MPEX relevant conditions this wave is responsible for core heating of the ions. Next, experimental evidence for core ion heating is presented in the form of ion temperature and target heat flux measurements. However, the core heating is shown to transiently cool, which is proposed to be due to the charge exchange with neutral gas born from plasma recombination at the target. When the target material is changed from carbon to stainless steel, the heat flux at the target reaches an increased steady state and higher ion temperatures are measured throughout the plasma column. The axial peak of the ion temperature is also located closer to the target for the case of the stainless steel target. These phenomena are hypothesized to be due to the increased reflection coefficient of the target material, and a model for quantifying this hypothesis shows that the flux of energetic neutral particles born from the reflection of sheath accelerated ions could explain these observations. Finally, experimental optimization of the magnetic field in the ICH region is shown with COMSOL simulations showing good agreement with these experimental results. The numerical simulations are then used to explore the parameter space of driving frequency, antenna length, and distance of the antenna to the ion cyclotron resonance on the predictions of heating in the ion cyclotron region.

Table of Contents

List of Tables

List of Figures

Chapter 1

Introduction

This chapter will not serve to review and motivate the entirety of the science of thermonuclear fusion, many authors have done this already and the following references should enlighten interested readers to learn more about the science of thermonuclear fusion [6, 7, 8, 9]. Here, we simply aim to point out that designing plasma facing components is one of the most significant engineering challenges facing the realization of fusion as a commercial energy source. Plasma-material interactions (PMI) and their effect on the boundary plasma is an active area of research in the fusion community. The physics involved spans many areas of expertise, including plasma physics, materials science, gas phase chemistry, transport of neutral gas. These processes also span several orders of magnitude in relevant temporal and spatial scales which makes predictive simulation work of this incredibly challenging. The community, therefore, looks to experimental devices to empirically study plasma-material interactions. To expedite the development of plasma facing components several linear plasma devices built to specifically study plasma-material interactions exist around the world including Magnum-PSI [10] and PISCES [11]. However, these devices are unable to independently control electron density, electron temperature, and ion temperature and instead rely on electrostatic biasing of the target to simulate the relevant ion energies. Relying on electrostatic biasing does not allow studying the interaction of the eroded material and recycled neutral gas with a fusion relevant divertor plasma and does not properly simulate the angular energy distribution of the ion fluxes, therefore, PMI studies on these linear devices omit a vast amount of rich physics important to PFC development. Oak Ridge National Laboratory (ORNL) is building a new user facility called the Materials Plasma Exposure eXperiment (MPEX) which will be a linear device that uses RF technology to independently control the electron density, electron temperature, and ion temperature of the plasma in front of a material target. This capability will then allow MPEX to study plasma-material interactions that cannot be studied on other linear devices and that are relevant to developing PFCs.

1.1 Material Compatibility for Fusion Reactors

Realizing controlled thermonuclear fusion as an energy source is envisioned to have a dramatically beneficial effect on our society as it would provide a nearly limitless supply of clean energy. In fact, this achievement has been recognized by the National Academy of Engineering as one of the 14 Grand Challenges for the 21st century [12]. The challenges involved with Plasma Materials Interactions (PMI) and Plasma Facing Components (PFC) have been highlighted as major knowledge gaps that should be prioritized research areas if fusion advances beyond ITER are to be realized [13, 14]. Recently the Fusion Energy Sciences (FES) program management launched a technical workshop to review the current understanding and to identify the challenges facing PMI and to discuss options to address those challenges [15]. Some of the identified major challenges that need to be addressed on the road to commercial fusion reactors include Power exhaust, PFC lifetime, and Tritium retention. The present technology is able to handle 10 MWm^{-2} heat fluxes. ITER is designed to maintain the heat flux of < 10 MWm^{-2}. This corresponds to parallel plasma heat flux of about 80 MWm^{-2}, that will strike the divertor, in addition to the heating from radiation and neutral particles. In addition to these high heat fluxes PFCs are exposed to large ion fluxes ($\Gamma > 10^{24} m^{-2} s^{-1}$) which will lead to material erosion and re-deposition of material as well as surface modification of the surface. The conditions of the plasma interaction with the materials surface can vary from a dense and cold plasma (T_e 1 eV, $n_e > 2 \times 10^{21}$ m^{-3}) to a hot lower density plasma ($5 < T_e < 20$ eV, $10^{19} < n_e < 10^{21}$ m^{-3}). These plasma conditions will dictate regions of erosion and deposition on the PFC surface and need to be studied. Tritium retention of a material is another issue that needs to be addressed is that currently, experiments are limited to fluence levels of $10^{27} - 10^{28}$ D/m^2. To address the issue of tritium retention experiments are needed that are capable of attaining fluences beyond the 10^{28} D/m^2 [16, 17, 18]

1.2 Materials Plasma Exposure eXperiment

Many expert panel reports have concluded that the knowledge gaps associated with PMI need to be urgently addressed [14, 19]. The 2012 FESAC report [20] stated that the current facilities in the US are no longer unique or world leading and cannot answer outstanding scientific questions associated with PMI. The report continues to state that, moderate investments in medium scale facilities can lead to high-impact fusion research. Oak Ridge National Laboratory (ORNL) is developing the source technology for the new Material-Plasma Exposure eXperiment (MPEX) facility that would address the outstanding questions associated with PMI.

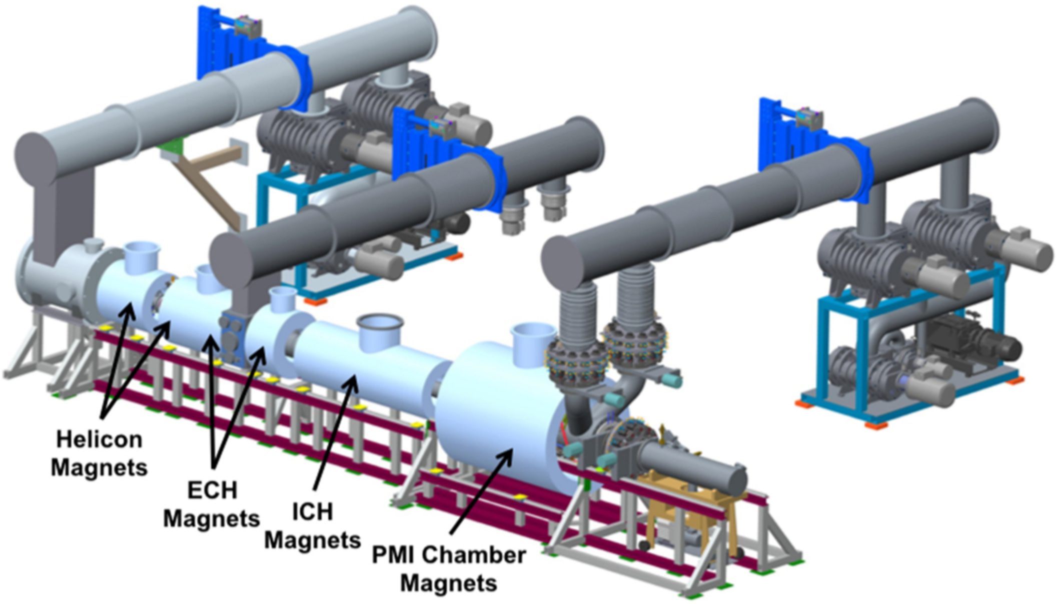

Figure 1.1: Schematic of the conceptual design for the Material Plasma Exposure eXperiment (MPEX).

Figure 1.1 shows the conceptual design of the MPEX facility. MPEX will be a steady-state device that is enabled by superconducting magnet technology, Niobium-titanium (NbTi) magnets are planned for MPEX, and RF source technology. The total planned RF power on MPEX will be 800 kW of power, 200 kW helicon, 200 kW electron heating, and 400 kW of ion heating. The target station will be remotely controlled, thus enabling irradiated sample handling on MPEX. Some of the specifications for the MPEX facility will fulfill are power fluxes of $10\ MWm^{-2}$, inclined target ($B_0 > 1\ T$), steady state up to $10^6 sec$, including exposure of liquid metal targets, neutron-irradiated samples with significant dpa, and independent control of T_e and T_i. Some linear devices address part of these requirements but not all of them. Table 1.1 summarizes the capabilities of MPEX versus the PISCES and MAGNUM facilities [21, 10, 11].

Table 1.1: Comparison table of the current linear PMI experiments vs MPEX proposed parameters.

Parameter / Capability	MPEX	PISCES	Magnum
Steady-state heat flux (90°) $[MWm^{-2}]$	≥ 10	≈ 10	≥ 10
Steady-state heat flux (5°) $[MWm^{-2}]$	3	N/A	N/A
Target T_e $[eV]$	1-15	N/A	≤ 5
Target T_i $[eV]$	1-20	N/A	≤ 5
Plasma Diameter [cm]	up to 10	2-5	5
Ion flux $[m^{-2}s^{-1}]$	$10^{21} - 10^{19}$	$\leq 10^{19}$	$10^{22} - 10^{19}$
Annual Fluence	10^{31}	10^{29}	10^{31}
Surface morphology changes	Y	N	Y
Neutron irradiated samples	Y	N	N
Divertor component mockups	Y	N	Y

The plasma source currently planned for MPEX is a helicon source chosen for its high ionization efficiency. The plasma is then heated with auxiliary heating to heat the electrons and ions independently. The electron heating is planned to be carried out by Electron-Bernstein Wave (EBW) heating [22, 23, 24, 25]. While the ion heating will be achieved by the "beach-heating" method [17, 16, 18, 26]. This thesis will focus on demonstrating the viability of the helicon source and ion heating on Proto-MPEX.

1.3 Light Ion Helicon Sources

Ever since Boswell published on the ionization efficiency of inductively coupling RF waves to the natural oscillations in a plasma column [27, 28], helicon plasma sources have gained interest in many applications. Some areas of research that have found application for helicon sources are semiconductor processing [29, 30], and space propulsion [31, 32]. A recent application of helicon sources has been as plasma sources for fusion-relevant PMI investigation [18, 16, 33, 34, 35, 17, 36]. However, in order for helicon sources to be relevant to PMI investigation, they must be able to produce high-density plasmas with light ion fuels (H_2, D_2, He). This work will show that the conditions in Proto-MPEX necessitate significant contribution from the fast wave in power deposition to attain high electron density with the helicon source.

Most authors attribute the efficient ionization of helicon sources in heavy ion discharges to the collisional damping of the Trivelpiece Goulde mode (TG) [37, 38, 39, 40, 41]. The TG mode, slow-wave, is typically excited through non-resonant mode conversion of the helicon mode, fast-wave, that occurs at the periphery of the plasma [42], therefore power deposition is typically edge dominated in helicon sources using heavy ions. Chen and Curreli [41, 40] have shown that regardless of where the ionization occurs, the centrally peaked profile in heavy ion helicon discharges can be explained by the short circuit effect. The short circuit effect is restricted to short discharges with unmagnetized ions. In discharges using light ions, this effect is then typically not applicable and hollow density profiles are observed when significant core power deposition is not observed [43].

There are two main aspects that make light-ion helicon sources different from heavy-ion sources: ion magnetization and the effect of the lower hybrid resonance. At high densities, the lower hybrid resonance has the effect of restricting the slow-wave to a very thin layer in the plasma periphery and creates an evanescent layer between the fast-wave in the high plasma density region (core) and the slow-wave in the low plasma density region (edge) of the discharge [44]. Ion magnetization precludes transport effects that cause centrally peaked electron density profiles in heavy-ion discharges [40, 41]. Therefore in discharges with strongly magnetized ions and electrons, production of centrally peaked density profiles necessitates the deposition of power directly at the core. This mechanism is only accessible via the fast-wave.

Light ion helicon sources have proven more difficult to achieve high-density plasmas with [44, 45] than heavy ion helicon sources. Sakawa [44] showed that for a helicon source fueled with D_2 and H_2 gas, electron density would reach a maximum at $B_0 \approx 0.02$ T then sharply fall off. This is not the case using Ar gas to fuel the discharge, which would show a linear increase in electron density past $B_0 = 0.15$ T. That work then showed that the reduced ion mass moves the high-density limit of the lower hybrid resonance (HDLH), which reduces to the root of the product of the electron and ion cyclotron frequencies as $\omega_{HDLH} = \sqrt{\omega_{ce}\omega_{ci}}$, to lower magnetic field values. Operating in magnetic field values above the HDLH, $B_0 0.02$ T for D_2, restricts the slow-wave to the low electron density region of the plasma column and the helicon wave to the high-density region, thus creating a region in the plasma that is evanescent to both waves. Light and Chen [45] later showed that low-frequency instabilities that have characteristics of the resistive drift wave instability and the Kelvin-Helmholtz instability were more prevalent in plasmas with light ion mass operating above the HDLH. Another difficulty associated with working with Deuterium gas is that it naturally exists as a molecular gas. Molecular gas presence in a plasma opens more avenues of power loss in the form of rotational and vibrational excitation cross sections.

Several devices have been able to achieve high electron densities in light ion plasmas [3, 46, 34, 17, 43] operating in magnetic fields above the HDLH. These devices all used a converging magnetic field geometry. However, the effect of this magnetic geometry on the success of these devices is not understood. Mori [3] measured fast-wave radial normal modes on the mini-RFTF devices and attributed their excitation to the variation of electron density with the magnetic field. On the Proto-MPEX device, the "helicon-mode" is attributed to exciting radial normal modes of the fast-wave in the plasma column [17, 43, 47, 48].

1.4 Ion Heating via Beach-Heating Technique

Direct ion heating is expected to increase ion temperatures on the Prototype Material Plasma Exposure eXperiment (Proto-MPEX) to values of 20 eV or more [49] at the target. In this regime, Proto-MPEX can simulate the plasma material interactions in a fusion relevant divertor, in which ion temperature is expected to play an important role in the plasma-material interaction physics [50]. Ion heating on Proto-MPEX will be accomplished by launching a left-hand polarized wave from a region of high magnetic field to a region of decreasing magnetic field strength, where the wave encounters the ion cyclotron resonance. At the cyclotron resonance, the rotating electric field of the wave accelerates ions that are in phase with it and therefore leads to an increase in the perpendicular energy of the ions and damping of the wave [51, 52]. Figure 1.2 depicts a conceptual drawing of the wave propagation in this heating scenario. This ion heating technique is well known and is referred to as "beach heating". Beach heating has been demonstrated to heat ions efficiently on several devices including the B-66 stellarator in the 1960s [53], later on, tandem mirrors such as Phaedrus [54] and Tara [55], and more recently on VASIMR VX-50[56]. The high electron density of Proto-MPEX makes this a novel environment for beach heating. The electron density is an order of magnitude higher on Proto-MPEX than the devices this technique was previously demonstrated. This work aims to show that a theoretical route to efficient core ion heating exists [26] at such high electron density, and has been demonstrated on Proto-MPEX [57, 58].

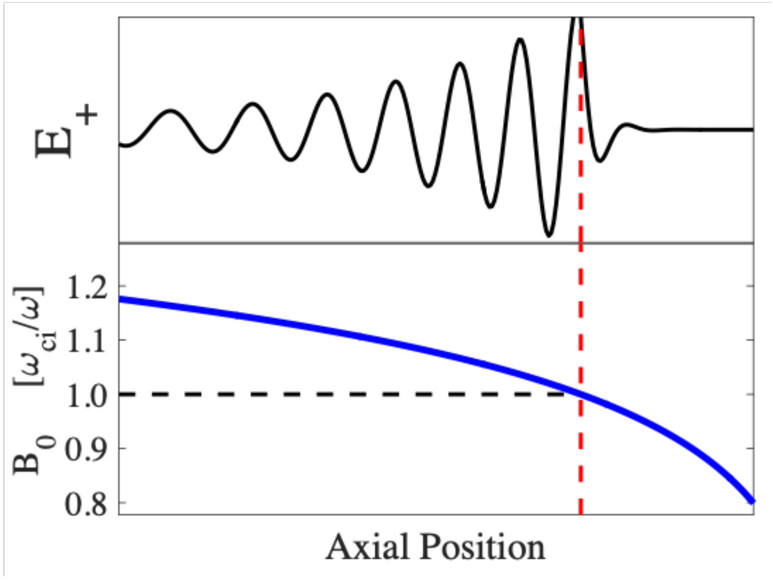

Figure 1.2: Conceptual drawing of the wave propagation in a beach heating scenario.

Wave propagation in this regime has been studied across several areas of plasma science including the Earth's magnetosphere, fusion devices, and the solar corona. This regime has been studied in-depth on the LAPD device [59, 60, 61, 62]. The wave of interest to the ICH region on Proto-MPEX is the shear Alfvén wave. This wave propagates on the slow wave branch of the dispersion relation and is classified in the literature into two limits of propagation corresponding to either cold or hot electrons and is typically sorted by comparing the Alfvén velocity to the thermal velocity of the electrons. With cold electrons ($v_{th_e} \ll v_A$) the wave propagates in the inertial regime and a cold plasma tensor can capture the propagation of this wave. However, when this wave propagates in a plasma with hotter electrons ($v_{th_e} \gg v_A$) the wave is said to propagate in the kinetic regime and a kinetic plasma tensor is required to describe the wave propagation. McVey [63] classifies the propagation of these waves by different means. The shear Alfvén wave in the inertial limit propagates on the low electron density side of the Alfvén resonance, or when the parallel index of refraction of the wave is greater than the S component of the Stix tensor ($n_{\|}^2 \geq S$), and the parallel phase velocity of the wave is greater than the electron thermal velocity of the wave ($v_{p_{\|}} \gg v_{th_e}$). McVey then describes the shear Alfvén wave in the kinetic regime to propagate on the high electron density side of the Alfvén resonance ($n_{\|}^2 \leq S$) and the parallel phase velocity of the wave is less than the electron thermal velocity of the wave ($v_{p_{\|}} \ll v_{th_e}$). Here we will refer to the shear Alfvén wave in the inertial regime as the inertial Alfén wave (IAW) and in the kinetic regime as the kinetic Alfvén wave (KAW).

Proto-MPEX can operate in a regime where both the IAW and the KAW propagate for magnetic field configurations where the driving frequency is near the ion cyclotron frequency ($\omega/\omega_{ci} > 0.7$). Proto-MPEX typically operates with an electron temperature between $T_e = 1$ and 6 eV such that the electron thermal velocity is approximately equivalent to the expected parallel phase velocity of the wave $v_{th_e} \approx \omega/k_{\|}$. Fig. **??** shows the Fourier spectrum from the ICH antenna on Proto-MPEX. The electron density gradient across the plasma column is such that the IAW wave propagates at the periphery of the plasma ($n_{\|}^2 \geq S$) and the KAW propagates in the core plasma ($n_{\|}^2 \leq S$). Therefore, for a constant magnetic field strength, the $n_{\|}^2 = S$ contour lies across the plasma's electron density gradient and separates the regions where the IAW and the KAW can propagate. This contour is known as the Alfvén resonance, and its presence has noteworthy consequences on the heating and wave propagation characteristics of the ion cyclotron heating (ICH) region. The Alfvén resonance location restricts the propagation of the KAW inside the plasma core and significant electron heating can take place along this contour [64, 65]. Previous authors have described the heating of electrons in this layer due to mode conversion of the shear Alfvén wave (slow wave branch) to lower hybrid oscillations (fast wave branch) [66, 67].

1.5 Thesis Overview

This thesis will be covering the physics and operation of both the helicon plasma source and the ion cyclotron heating antenna on Proto-MPEX. Chapter 2 is an overview of the Proto-MPEX experiment and diagnostics installed on the device that are pertinent to the results and discussions in this thesis. This chapter first introduces the device and naming conventions used throughout the results section. Next, the diagnostics used in the results section are described. The following chapter, Chapter 3 serves to introduce some of the theoretical background that will be relevant to the discussions of the thesis, as well as introduces some aspects of the modeling such as the dielectric tensor used to describe the plasma response, the analytical model used to describe the antenna's of the ICH and the helicon, and the description of the electron density profile throughout the device. Chapter 4 describes the results from the helicon plasma source on Proto-

MPEX. Throughout this chapter, we show that core power deposition by the fast-wave plays a vital role in the efficient electron density production in Proto-MPEX, with both experimental evidence and full-wave simulations coupled to a 0D particle/power balance. The performance of Proto-MPEX is tracked and compared with other experimental devices by calculating the ionization cost of the plasma source, and experimental improvements to the helicon source region are suggested and quantified with the particle/power balance. Chapter 5 moves into the ion cyclotron heating on the Proto-MPEX device. First, a theoretical route to core ion heating is presented in this chapter, something that has not been achieved in a device with the high electron density of Proto-MPEX. Next, the role of neutral gas is introduced and quantified; experimental evidence of neutral gas build-up from plasma recombination at the target plate leading to diminishing the heat observed by the ICH is presented. The results of changing the target material from a carbon target to a stainless steel target are presented and show that the stainless steel target supports higher ion temperatures and the steady state increased heat flux to the target. The reflection coefficient of the two materials is proposed as the reason for this dramatic change in behavior and the effect of this on the ion power balance is quantified. Finally, experimental optimization of the magnetic field in the ICH region is shown with COMSOL simulations showing good agreement with these experimental results. The numerical simulations are then used to explore the parameter space of driving frequency, antenna length, and distance of the antenna to the ion cyclotron resonance on the predictions of heating in the ion cyclotron region. Finally, Chapter 6 gives a summary and conclusion of the work presented here as well as future work.

Chapter 2

Experimental Apparatus and Diagnostics

2.1 Proto-MPEX configuration

This section is written to fill in the readers understanding of the experimental configuration of Proto-MPEX. The main focuses of this chapter will be: 1) the general layout and naming conventions used in the experiment, 2) the neutral gas fueling and pumping arrangement in the device 3) the axial magnetic magnetic field configurations throughout the device for both the original configuration of the device and the new configuration installed during the 2018 experimental campaign, and 4) the design of the Helicon and ICH antennas. These experimental configurations have been published in several journal articles and are summarized here [17, 43, 68, 69].

2.1.1 General Experimental Layout

In this section, an overview of the Proto-MPEX device will be given to give a general understanding of the experimental configuration and naming conventions used in the device.

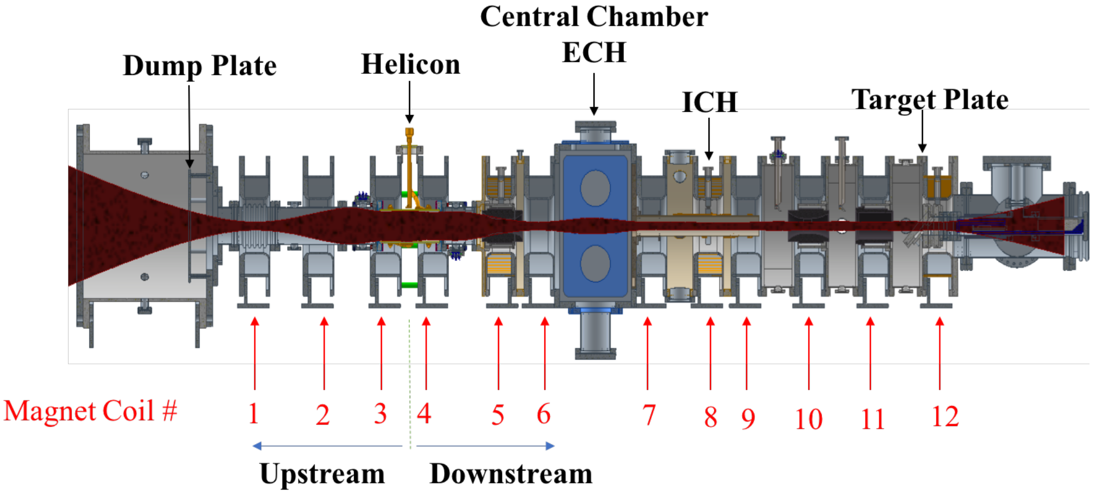

Figure 2.1: Schematic of the original Proto-MPEX configuration showing the location of the helicon antenna, ECH launcher, and ICH antenna, dump plate, target plate, and magnetic coil configuration.

Figure 2.1 shows the schematic of Proto-MPEX. The device consists of a vacuum chamber with 12 solenoid magnets. The magnets have an inner diameter of 21.7 cm and are made of 40 turns of a water-cooled copper conductor. They were originally constructed for the Elmo Bumpy Torus experiment [70] and are designed to operate continuously at 9000 A. In our experiments, most of the coils typically operate at up to 6500 A, which produces a peak axial magnetic field of approximately $B_0 = 1.5$ T. The two magnets around the helicon antenna operate at currents of between 200 and 400 A, with magnetic fields up to $B_0 = 0.1$ T. The magnet coil geometry is shown and labeled here and will be referenced throughout this work to give the location of diagnostics and heating schemes. For example, a Langmuir probe's location that is installed on the spool piece between magnet coils 9 and 10 will be referred to as "spool 9.5". The direction label of "upstream" will be given to the $-\hat{z}$ direction and "downstream" will be given to the $+\hat{z}$ direction. The plasma is terminated at both the ends by solid material plates. The upstream plate located in the dump tank is 1.5 mm thick stainless steel with a diameter of 40 cm. The plate is large enough to capture the expanding magnetic field lines from the plasma. On the furthest downstream side of the device, the plasma is terminated by a target plate. The distance between the dump-plate and the target-plate is ≈ 3.8 m. The location of the Helicon and ICH antennas, as well as the ECH launcher, is shown in this schematic as well.

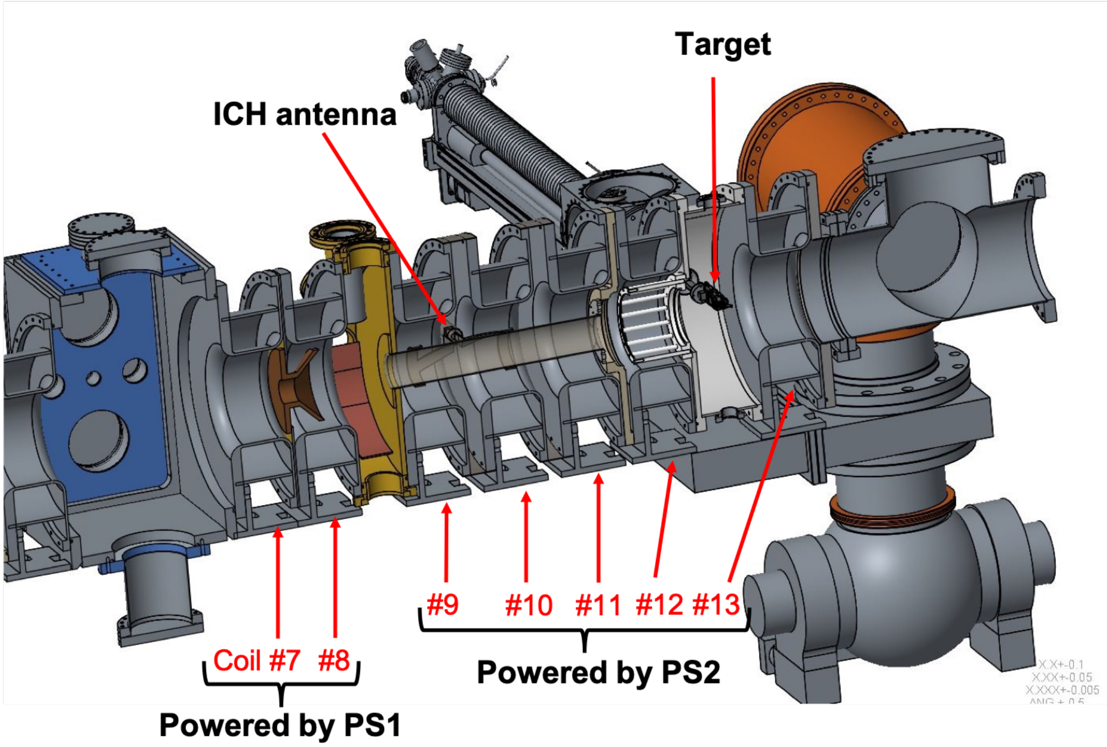

Figure 2.2: Schematic of the section downstream of the central chamber in the new configuration used in the 2018 experimental campaign.

A magnetic field reconfiguration in the early 2018 experimental campaign was motivated by 1) reducing the magnetic field ripple to improve particle transport along the axis of the device, 2) allowing second harmonic electron cyclotron heating at 105 GHz, 3) improve magnetic field shape for ICH coupling and support external antenna operation, and 4) improve pumping at target and allow new target station to be installed. This upgrade in Proto-MPEX took place during the early part of 2018 and the majority of the 2018 experimental campaign results were taken with this device configuration. The upgrade consisted of changing the magnetic field coil configuration downstream of the central chamber. The central chamber and the magnetic field configuration upstream of it was not affected by this upgrade. Figure 2.2 shows the schematic of the Proto-MPEX downstream of the central chamber after the device upgrade. This upgrade included adding an additional magnetic field coil and, with the total number of field coils on Proto-MPEX now being 13 instead of 12. The coil spacing was also shortened between coils 7 and 8 to reduce the field ripple and allow achieving magnetic fields of $B_0 \approx 2.0$ T at that location. The gap between coils 9 through 12 was also reduced as compared to the previous assembly of coils, allowing for magnetic field profile with reduced ripples in the ICH section, and a longer distance from the antenna to the ion cyclotron resonance location. Spool 8.5 was replaced with a custom spool for injection of microwave heating (both 28 GHz and 105 GHz), Spool 12.5, the new location of the target plate, was also replaced with a new spool with additional ports for diagnostic access. However, the locations between Spool 9 through 11 have become inaccessible by diagnostics, and Spool 11.5 only had mini-conflat flanges which did not allow previously proposed experimental measurements in locations other than the target for locations downstream of the ICH.

2.1.2 Neutral Gas Fueling and Pumping

The vacuum chamber and the pumping system are composed of a variety of components. Starting from the left-hand side of Fig. 2.1, a large dump tank is located upstream of the helicon antenna and consists of a 66 cm long, 61 cm diameter stainless steel tank. A small 150 l/s turbopump is located there as well. The section between the dump tank and the fifth magnet consists of 15.2 cm diameter stainless steel vacuum components. Downstream from that point, the vacuum chamber is formed by the aluminum housing of the magnets and stainless steel spool pieces ($\approx$ 49 cm inner diameter) that connect them. The "central chamber" shown in the figure is an aluminum box which is 41 cm wide, 66 cm high, and 69 cm deep. A 2800 l/s and 1000 l/s turbo pump are located there. A skimmer plate with a 5.8cm diameter hole is located between the helicon antenna region and the central chamber to provide differential pumping between the source region and the central chamber. An additional skimmer plate with an 8.6 cm diameter hole is located on the downstream of the central chamber. Beyond the target plate, is a large-volume ballast tank (6.3 m^3) that provides effective pumping for pulsed gas operations and includes a 2500 l/s turbopump. The base pressure of the chamber is 10^{-6} Torr. In the new configuration, the large ballast tank was removed and the 2500 l/s turbo pump attached to it was moved directly behind coil 13. This was done to improve conductance to the turbopump, and therefore improve pumping at the target.

Schematic of the Proto-MPEX is shown in Fig. 2.3. The vacuum chamber is divided into three parts hereafter referred to as the (1) "Source", (2) "Heating", and (3) "Target" sections. The conductance-limiting elements (skimmers) described above support differential pumping between the "Source", "Heating", and "Target" sections. There are three neutral gas injection points G1, G2 and G3 as illustrated in Fig. 2.3. Gas injection at locations G1 and G2 are controlled with a mass flow controller (MKS model 246) and at location G3 with a piezo-electric valve (Veeco instruments model PV-10). Both gas injectors are controlled with a voltage pulse whose amplitude and duration determine the flow rate and the length of time the neutral gas is "puffed" into the vacuum chamber. The MKS mass flow controller provides a calibrated analog output voltage which is proportional to the delivered gas flow. This signal is digitized to determine the deuterium gas flow rate. The time response of the MKS mass flow controller takes approximately 200 ms to fully open the valve. The piezo-electric valve does not produce an analog output voltage to determine gas flow; therefore, it has been absolutely calibrated by injecting gas pulses of 100 to 1000 ms duration into a known volume and measuring the pressure rise as a function of the input voltage. This information is used to produce a table of the flow rate versus input voltage for use during experiments.

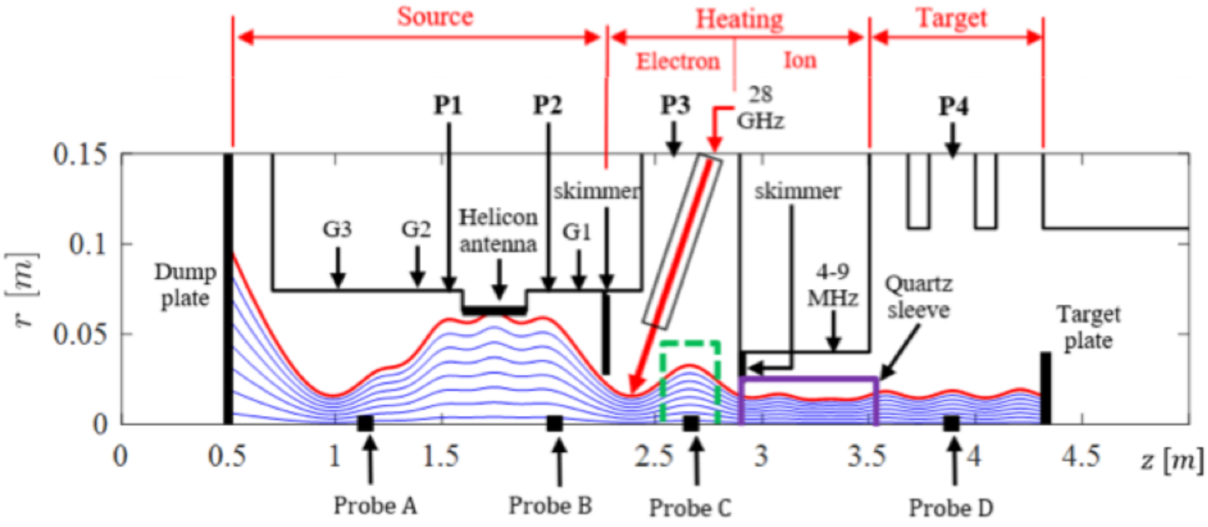

Figure 2.3: Schematic of Proto-MPEX showing the location of the two skimmers, ICH quartz sleeve, helicon antenna, gas injection locations (G1 to G3), magnetic flux lines, location of four pressure gauges (P1-P4) and four double Langmuir probes (Probe AB). The green rectangle indicates the region where a fast camera collects D_α emission from the plasma. The vertical lines (light blue) in the electron "Heating" section represent 2nd harmonic electron cyclotron resonance surfaces (at 28 GHz) near the waveguide.

The plasma is radially limited under the helicon antenna window as illustrated by the red magnetic flux line in Fig 2.3. The plasma is axially bounded at the "Dump" and "Target" plate located at z = 0.5 m and at z = 4.3 m respectively. Four fast pressure gauges (P1 to P4) are located along with the device as illustrated in Fig 2.3. A fast camera collects line-integrated D_α emission from the plasma region enclosed by the green rectangle in Fig. 2.3. More information on the behavior of the gas pressure during Proto-MPEX, as well as optimization of the fueling, can be found in [68].

2.1.3 Magnetic Field Profiles

This subsection is meant to give the reader an appreciation of the Proto-MPEX magnetic field profile before and after the magnetic field reconfiguration. The coils can be configured to operate at currents up to 6500

A, and up to 8500 amps for the new magnetic field configuration coils 7 and 8. However, this section will present a magnetic field configuration that is typically used for experiments in Proto-MPEX. The results presented in this thesis from the new magnetic field configuration are presented in Section 5.4.

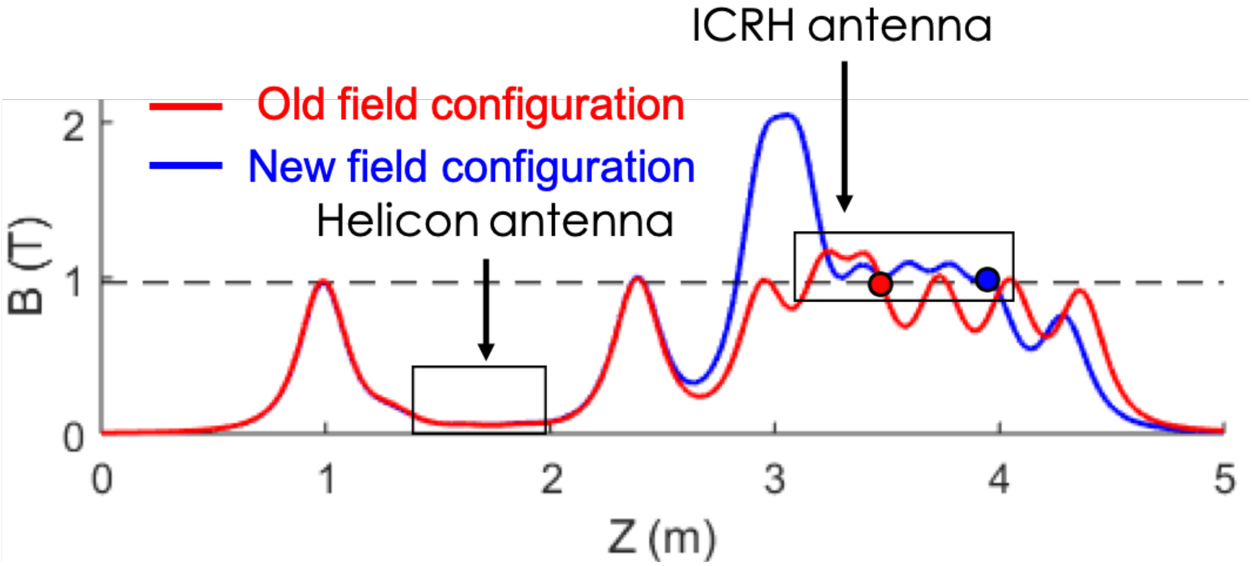

Figure 2.4: On-axis magnetic field strength in Proto-MPEX for the old and new magnetic field configurations. The ion cyclotron resonance, at a frequency of $f = 7.5$ MHz, location is shown for the old configuration (red dot) and the new configuration (blue dot).

On-axis magnetic field strength is provided in Fig. 2.4 for a typical Proto-MPEX configuration before and after the magnetic field reconfiguration. The lowest magnetic field strength in the device is in the helicon source region, which is typically operated with magnetic field strengths between $B_H = 0.02 - 0.07$ T. The helicon source regions has two magnetic mirror regions upstream and downstream of the antenna produced by coils 1 and 5 respectively. The next lowest magnetic field in the device is in the central chamber, where a large gap exists between coils 6 and 7 producing a magnetic field minimum in the center of the central chamber. Downstream of the central chamber the magnetic field is kept around $B_0 \approx 1.0$ T in the peaks of the profile. The old magnetic field configuration of Proto-MPEX contained many magnetic field ripples which were removed in the new magnetic field configuration by reducing the spacing of the magnetic field coils. The locations of the Helicon and ICH antennas are labeled here. The ion cyclotron resonance locations for the old and new configurations are labeled here by the appropriately colored dots. The ion cyclotron resonance in the new magnetic field configuration was therefore moved further away from the ICH antenna. The target plate is typically located several cms from the center of Spool 11.5 for the old configuration and

Spool 12.5 for the new configuration.

2.1.4 Helicon Antenna

The Proto-MPEX produces plasma utilizing a helicon plasma source, the antenna of the helicon system is described in this section. The helicon antenna is quarter turn helical antenna, which is located in the air, and the power is coupled through an aluminum nitride cylinder forming the vacuum boundary in this region. This boundary is referred to as the “helicon window”. The antenna is located outside the vacuum due to the fact that high neutral pressures in the range 0.1 3 Pa are required in the helicon section in order to produce the required plasma densities, and at this pressure and power level antenna sputtering would otherwise be likely to occur that could contaminate material samples being tested. However, a drawback is that up to 20% of the power launched by the antenna is deposited on the inner surface of the window due to RF-plasma sheath interactions and the production of energetic neutrals from charge exchange reactions in the helicon region. The window thus must be adequately cooled so that thermal stresses do not become excessive and break the ceramic window. In order to reduce stresses, aluminum nitride (AlN), (Ceradyne CeralloyVR 1370 DP) 30 cm long with an inner diameter of 13.8 cm, has been chosen for the window material due to its very high thermal conductivity. A water-cooled version of this window is being tested at the Controlled Shear Decorrelation Experiment (CSDX) located at the University of California San Diego for the MPEX design.

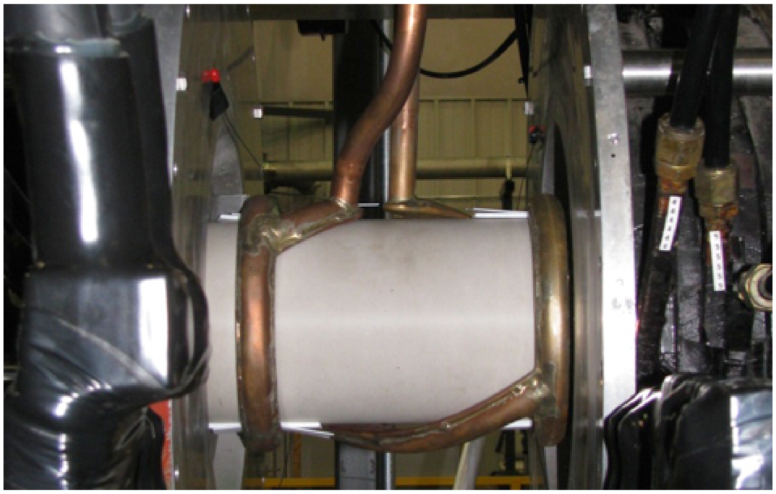

Figure 2.5: Picture of the Proto-MPEX helicon antenna installed.

Figure 2.6 shows the helicon antenna installed on Proto-MPEX. The helicon antenna is a 25 cm helical right-handed quarter-turn antenna and is currently powered by ≥100 kW of RF power at 13.56 MHz frequency, the power of the helicon antenna has been recently increased to ≥200 kW, however this power level has not been tested and reported in regards to the discussions in this thesis. The helicon antenna is called a right-handed antenna which confusingly has a left-hand twist which primarily couples to the right-handed fast-wave. Currently, the limiting factor in running the helicon antenna in steady-state is the heat load imposed on the vacuum window. The RF power is generated by either a 100 kW Sairem RF generator operating at 13.56 MHz frequency, or using a Continental Electronics model FRT-86 RF transmitter that amplifies 13.56 MHz signal to 100 kW. The power is then efficiently coupled to the plasma through an L-type matching network that is located in close proximity to the helicon antenna. The forward and reflected power of the helicon antenna is digitized by a pair of calibrated directional couplers located close to the matching network.

2.1.5 ICH antenna

The antenna utilized for ion cyclotron heating is described in this section. Two different ICH antennas were utilized on Proto-MPEX. Before the upgrade for the 2018 experimental campaign the ICH antenna consisted of an antenna that was 25 cm long with a right-handed helical half-turn, this antenna is referred to as a left-handed helical antenna because it is designed to couple power primarily to a left-hand polarized wave. This antenna is operated in a vacuum but is separated from the plasma by an 85 mm outer diameter, 80 mm inner diameter, and 61cm long quartz tube. The antenna was operated at a forward power level up to $P_{ICH} \approx 30$ kW using a Continental Electronics model FRT-85 transmitter, the driving frequency was changed from $f = 6.5 - 8.5$ MHz.

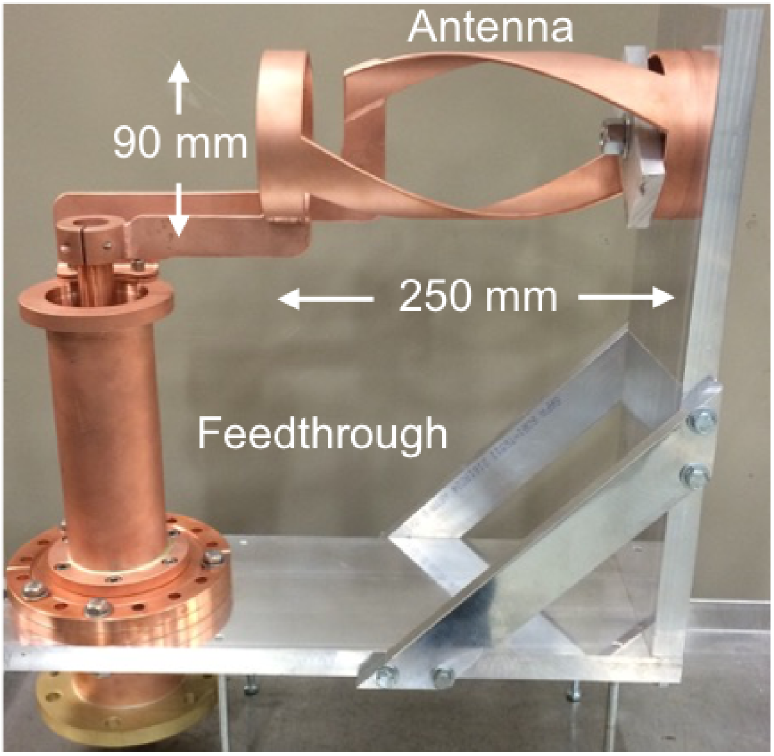

Figure 2.6: Picture of the Proto-MPEX ICH antenna for the 2016 through early 2018 campaign.

Figure 2.6 shows the ICH antenna that was used on Proto-MPEX prior to the 2018 experimental campaign upgrade to the device. After the 2018 experimental upgrade the antenna length was changed to a 30 cm antenna, otherwise the geometry of the antenna was still that of a left-handed helical antenna, since this antenna design efficiently couples to the $m = -1$ azimuthal mode in the plasma, which is predominantly left-hand circularly polarized and shown to heat ions efficiently[71]. The ICH antenna during the 2018 campaign was operated with a driving frequency set to $f = 6.5$ MHz. In order to prevent any chance of sputtering in the region of the ion cyclotron antenna, and in order to prevent RF arcing along magnetic field lines, the antenna utilized was changed to an external antenna with power coupled through the wall of a cylindrical alumina vacuum window, very similar to the helicon section. It was originally proposed to minimize the distance between the antenna and plasma by putting this antenna in a vacuum, but the total distance between the inner surface of the antenna and the inner surface of the window, including utilizing coaxial water cooling as is done with the helicon window, can be ≤ 10 mm. In this case, the gap between the antenna inner surface and the plasma outer surface will not be affected. In addition, the window, which is a smaller diameter than the surrounding vacuum chamber, serves to limit the flow of gas from the target back into the ion and electron heating sections. Because B_0 is higher at the location of the ICH antenna than at the helicon antenna, the diameter of the plasma is smaller in the ICH section and the ICH window's ID is 9 cm. The matching network for the ICH system will use a two-capacitor L-type matching network. The matching capacitors are adjusted automatically during operation based on signals obtained from the directional couplers located on both sides of the matchboxes.

2.2 Diagnostics

The main diagnostics used throughout this work are IR thermography, B-dot probes, retarding-field energy analyzer (RFEA), Ar II Doppler broadening spectroscopy, and Double Langmuir probes. First, the design of the B-dot probes and the measuring circuitry is shown. Next, Doppler Broadening spectroscopy of Ar II was an important technique used in measuring the ion temperature and therefore demonstrating that the ICH is heating ions in Proto-MPEX. The description of this measurement will be presented with a review of the error analysis and Abel inversion analysis done to show that the contribution of the edge temperature does not dramatically affect the core temperature measurement. Then, an overview of the IR thermography is presented and a discussion of the data analysis to retrieve heat flux information is presented. Finally, a brief description of the Double Langmuir Probes used in measuring electron temperature and density is given.

2.2.1 B-dot Probes

B-dot Probes were used to measure the phase and amplitude of the RF wave fields in Proto-MPEX. B-dot probes are a simple diagnostic that consists of a conducting coil used to measure time-varying magnetic flux by exploiting Faraday's law of induction. When immersed in a time-harmonic magnetic field a B-dot probe with a coil that with area A_e generates a voltage.

$$V = \omega B_1 A \tag{2.1}$$

Thus knowing the effective area of the coil and the operating frequency (ω) we can calculate the time-harmonic magnetic field (B_1). Since the magnetic flux is a vector quantity the probe only picks up the vector component of the magnetic field that is pointing in the direction normal to the face of the coil. The B-dot probe constructed for Proto-MPEX consists of 2 coils orthogonal to each other, one directed radially and one that can be rotated to either measure the azimuthal or axial direction of $\vec{B_1}$.

Probe Design

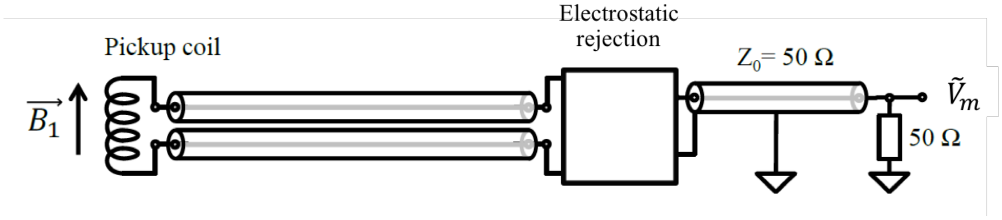

Figure 2.7: Schematic of the B-dot Probe used

The B-dot probe design is based on [72], and a schematic of the design is shown in Fig. 2.7. The signal wires are shielded by a custom coax that was constructed of hypodermic tubing and small diameter ceramic tubing. The electrical signals are brought outside of vacuum via 4 pins to BNC CF flange. Electrostatic rejection is achieved by connecting the signal wires to a 180° power splitter/combiner (ZMSCJ-2-1), the final signal should be a purely electromagnetic signal. This signal is then processed through measuring circuitry that digitizes only the amplitude and phase information of the reference signal, greatly reducing the amount of data that needs to be stored during the helicon pulse. The measuring circuitry is described in more detail below.

Measuring Circuitry

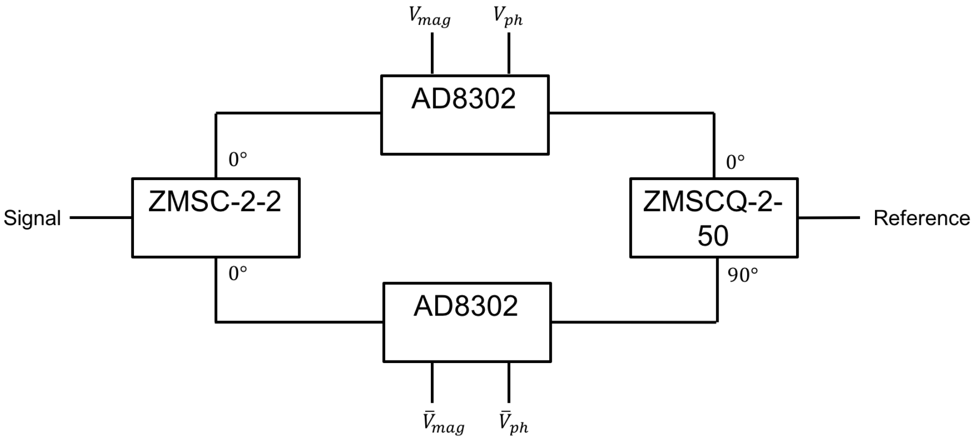

Figure 2.8: Schematic of the amplitude and phase detector used to process the B-dot probe signals

After the electrostatic rejection the electric signal is processed by the amplitude and phase detector circuit shown in Fig. 2.8. The amplitude and phase detector circuit uses two AD8302 chips to resolve sign ambiguity of the phase and improve accuracy of the phase detector. There are 4 outputs from this phase and amplitude

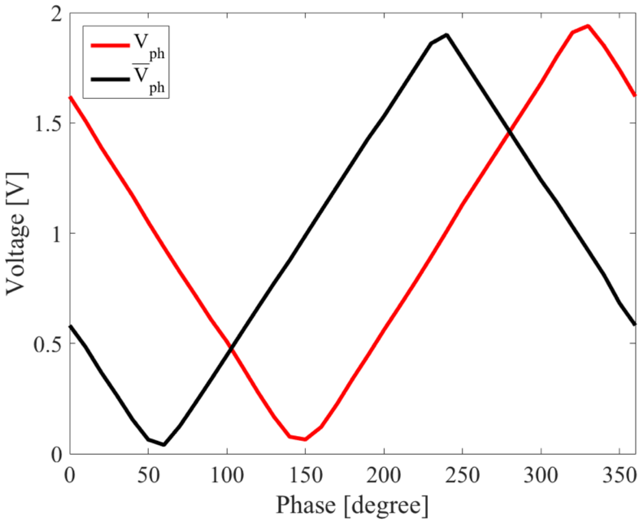

Figure 2.9: The voltage vs phase difference between the reference and signal.

detector ($V_{ph}, \bar{V}_{ph}, V_{mag}, \bar{V}_{mag}$), however only 3 need to be digitized ($V_{ph}, \bar{V}_{ph}, V_{mag}$) since both magnitude voltages ($V_{mag}, \bar{V}_{mag}$) are the same value.

Figure 2.9 shows the response of $V_{ph}, \bar{V}_{ph}$ when feeding the reference with a constant RF signal and varying the phase of the input signal. With only one AD8302 chip we would not be able to resolve the phase fully from 0 to 360 degrees. However with one of the AD8302 chips being fed with an input signal that is phase shifted by 90 degrees we can resolve the full quadrant of the phase.

2.2.2 Retarding Field Energy Analyzer

A retarding field energy analyzer (RFEA) is installed on Proto-MPEX at spool 10.5. The grids in this analyzer are spaced 130 μm apart to reduce space charge effects in the energy analyzer. All the grids are nickel grids spot welded to stainless steel plates. They are insulated from each other and spaced by alumina spacers. The entrance aperture currently has entrance holes that are 100 μm in diameter which is much larger than the Debye length of the plasma $\approx$ 10 μm. This larger front grid was installed to allow the energy analyzer to survive the high heat flux. With the larger grid installed, however, concerns of plasma leaching into the analyzer and the sheath electric field not being uniform and thus distorting the ion energy distribution function arose. This is because the aperture size was now larger than the Debye length which has been shown to cause inaccurate interpretation of the measured data [73, 74].

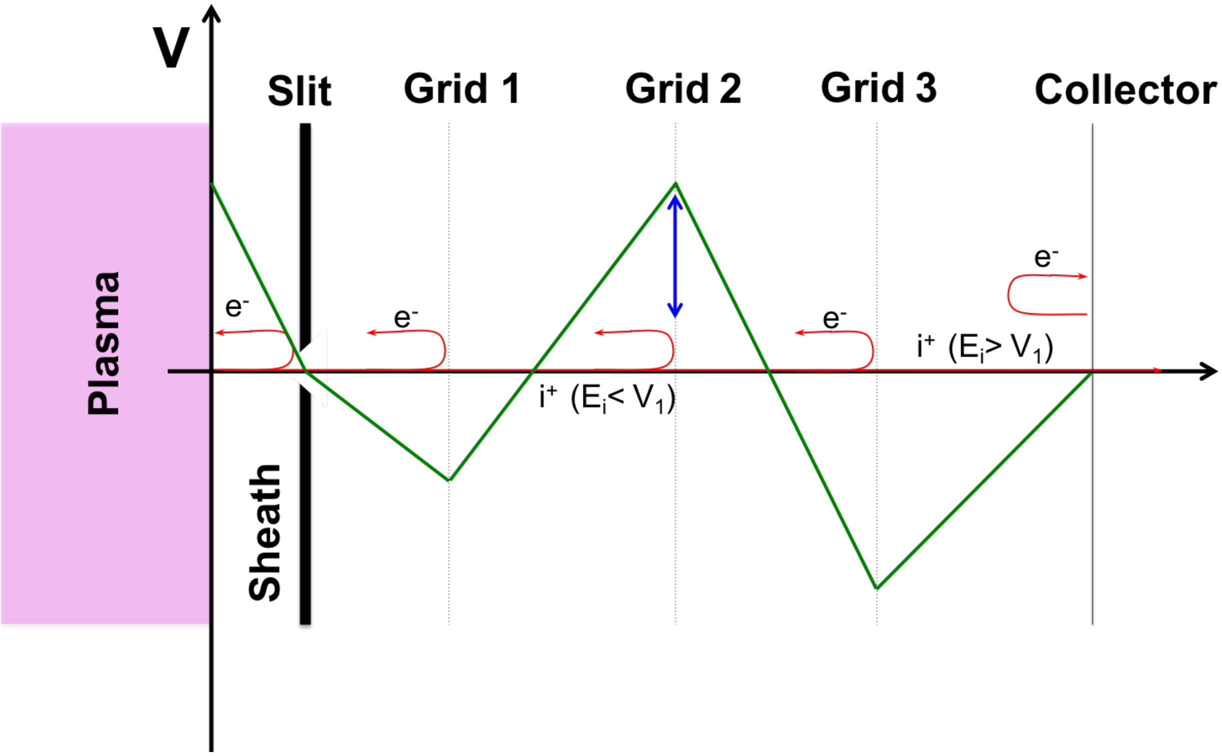

Figure 2.10: A schematic of a typical RFEA.

Figure 2.10 shows a schematic of how an RFEA works and describes the function of each grid. The entrance aperture is exposed to the plasma and creates a sheath which rejects low energy electrons because of the potential barrier formed and attracts ions. Once the plasma passes through the entrance slit it encounters grid 1 which is negatively biased to -150 V to reject the high energy electrons that have passed through the entrance slit. The next grid the ion beam encounters is the ion discrimination grid (grid 2). Grid 2 is swept from -30 V to 80 V, at a 50 Hz frequency, to discriminate the ion energy that is collected. A 3rd grid is installed in front of the collector to reduce false currents associated with secondary electrons emitted by the collector, this grid is biased to -150 V.

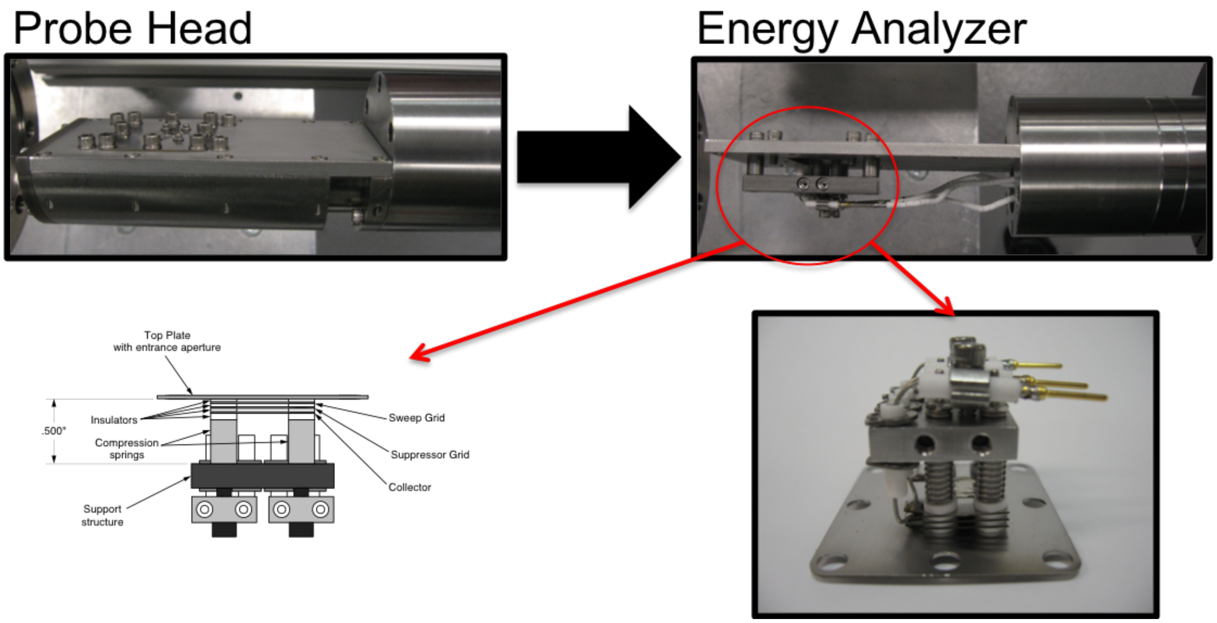

Figure 2.11: Picture of the RFEA that is installed on Proto-MPEX. Top left is a picture of the assembled probe head. The picture on the top right is of the energy analyzer mounted to the probe head assembly. The bottom right picture is a stand-alone picture of the energy analyzer. The bottom left picture is a schematic of the energy analyzer.

Figure 2.11 shows a picture of the RFEA designed for Proto-MPEX. The RFEA head is made out of Stainless Steel and designed to fit through a 4.5" port on Proto-MPEX. The front of the RFEA has a molybdenum heat shield to protect the entrance grid from the heat flux of the plasma. Vent holes exist on the front head of the RFEA to allow the incoming flux of particles that neutralize inside the RFEA to escape the head and not build up pressure in the device.

Data Analysis

The data collected by the RFEA is taken by collecting the current (I_c) on the collector as a function of the applied voltage on the discriminator grid (V_d). This is called the I-V characteristic. From the I-V characteristic, the plasma potential (V_p) can be determined along with the ion temperature with the following definition [75].

$$I_c = \begin{cases} I_0 & V_d < V_p \\ I_0 e^{-}(V_d - V_p)/T_i & V_d \geq V_p \end{cases} \tag{2.2}$$

For the case of a plasma in the presence of RF that sees an induced voltage V_{RF}, the collector current can be described as follows:

$$I_c = \begin{cases} I_0 & V_d \leq V_p - V_{RF} \\ \frac{I_0}{2}(e^{-(V_d-(V_p-V_{RF}))/T_i} + 1) & V_d < (V_p + V_{RF}) \\ I_0 e^{-(V_d-V_p)/T_i} \cosh \frac{V_{RF}}{T_i} & V_d \geq V_p + V_{RF} \end{cases} \tag{2.3}$$

In addition to the ion temperature and the plasma potential being determine from the I-V characteristic, the ion energy distribution function can be determined from this measurement. The ion energy distribution function is determined by differentiating the current with respect to the voltage $f(E) \propto \frac{dI}{dV}$. The data collected by the RFEA is typically very noisy which makes differentiating the data directly troublesome. Instead, the data is first smoothed by taking a moving average and then the smoothed data is differentiated and reported as the IED.

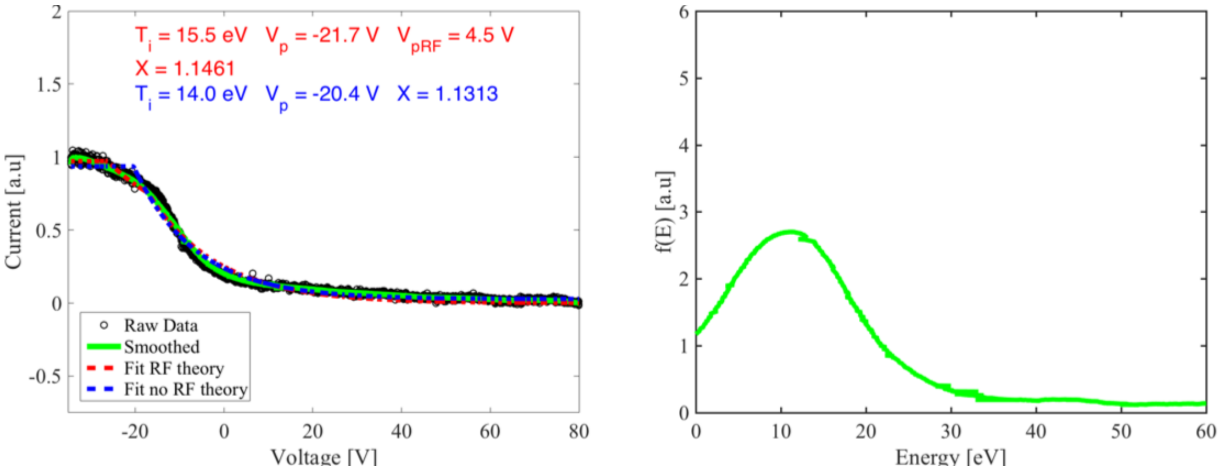

Figure 2.12: A plot of I-V characteristic of an RFEA measurement taken on Proto-MPEX, with smooth data, and plots fitting the theoretical curves from the data analysis routine (Left). Ion energy distribution function measured by the RFEA by differentiating the I-V characteristic (Right).

Figure 2.12 shows an example of a measured I-V characteristic taken by the RFEA. The smoothed data used to calculate the IED is also plotted on top of the raw data. The fit from Eq. 2.2 is shown as well as the ion temperature predicted by this fit, the fit from Eq. 2.3 is shown with the ion temperature predicted from this theory being higher than for the fit without the effect of an RF induced voltage V_{RF}. The IED function is also shown by differentiating the smoothed data.

Measurements

The data reported here show some of the measurements taken by the RFEA that reinforce the proof of core ion heating observed by Ar II Doppler Broadening Spectroscopy and IR camera measurements. These measurements are not reported in the chapter however because there are concerns over the interpretation of this data as the larger front grid that was installed to allow the energy analyzer to survive the high heat flux, also raised the question of plasma leaching into the analyzer and the sheath electric field being distorted. This is because the aperture size of the thicker grid was now larger than the Debye length which has been shown to cause inaccurate interpretation of the measured data [73, 74]. Therefore, this data is only reported in this section as tangential evidence supporting ion heating during ICH in Proto-MPEX.

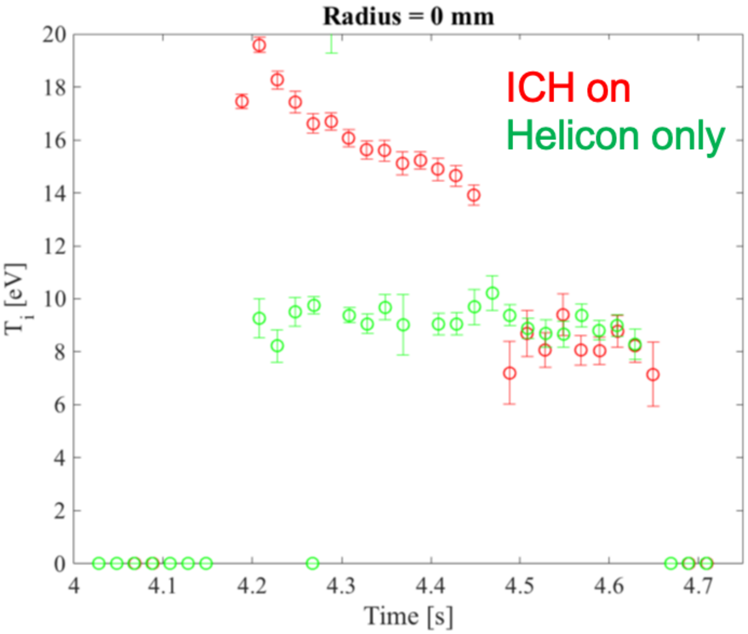

Figure 2.13: Ion temperature as a function of time extracted from RFEA measurements for a case where in increase in ion temperature was measured. ICH power was on from the time $t = 4.15 - 4.45$ s.

Figure 2.13 shows the ion temperature measurements for a plasma where the helicon power was reduced to $P_{helicon} = 80$ kW to lower the core electron density to $n_e = 4 \times 10^{19}$ m^{-3}, the RFEA opening slot was positioned at the center of the plasma column. From this figure we see that the ion temperature is increased during ICH operation, the RFEA predicts an ion temperature that is approximately double what is measured by the Ar II Doppler Broadening spectroscopy. However, due to the issues with interpreting the data mentioned above, this will not be dwelt on too long and instead, the focus here will be on interpreting the relative data. Qualitatively this data does indicate that the IED is broadened during the application of ICH heating. It's important to note here that when the helicon power is raised to full power such that $P_{helicon} = 100$ kW, increases of ion temperature in the core plasma were not observed on the RFEA even though they were observed with both Ar II spectroscopy and IR camera heat flux measurements to the target.

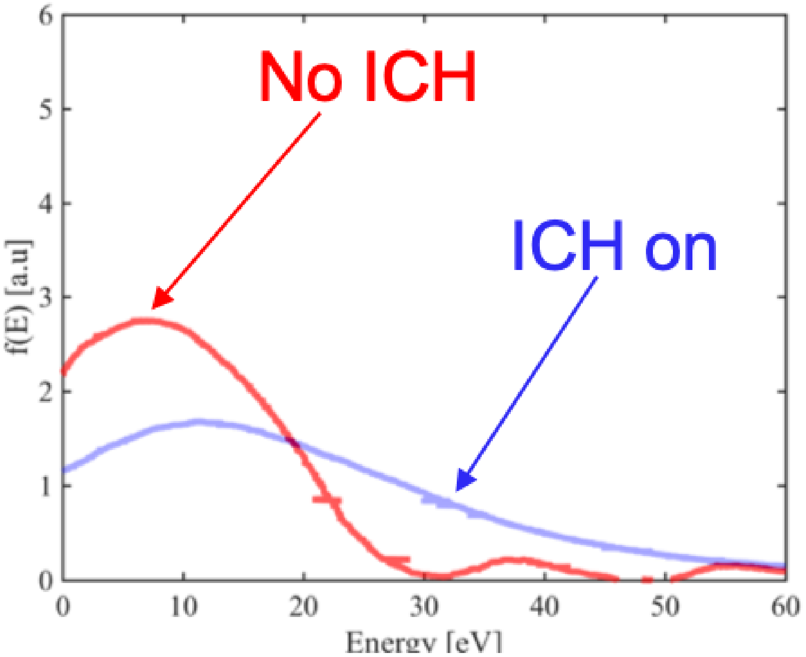

Figure 2.14: Ion energy distribution function measured by the RFEA by differentiating the I-V characteristic for a case of ICH on and Helicon only plasma conditions. The x-axis here is defined as $V_d - V_p$. Measured in the core plasma column.

Figure 2.14 shows the differentiated I-V characteristic measured by the RFEA for a plasma pulse with ICH on and for a helicon only shot. This data shows that the RFEA does indeed indicate a broadening of the IED when ICH is applied to the Proto-MPEX plasma column.

2.2.3 Ar II Doppler Broadening

A full description of the Ar II Doppler broadening measurement can be found in [69]. This chapter will summarize the technique and discuss the Monte Carlo method used to determine the error. Deuterium is the primary working gas, but during the experiments to measure Doppler broadening of Ar II, the plasma was seeded with 10% Argon. The argon ion temperature measurement is assumed to be a good indication of the deuterium ion temperature as the energy equilibration time between the two ions is on the order of ≈ 1 ms. Proto-MPEX has over one hundred lines of sight for optical viewing but only five spectral profiles at a time are simultaneously measured with a McPherson 2051 Czerny-Turner 1-m spectrometer using a set of optical fibers. An 1800 grooves/mm grating and a slit width of 30 μm are employed for all measurements. The spectra are recorded by a Princeton Instruments PhotonMAX 512b EMCCD camera. The CCD camera has 512 x 512 pixels that are binned into five groups. Each bin of pixels corresponds to a 38.4 $\mathring{A}$ wide viewing range or a resolution of 0.075 $\mathring{A}$. Spectra can be acquired throughout the time of the helicon pulse every 25 ms, with a 25 ms integration time. In addition to the Doppler width, the measured line shape is broadened by the instrument profile with a broadening that has been calibrated by an argon pen lamp which emits a very narrowly broadened transition and therefore the broadening of this emission can be assumed to be completely due to the instrument function. The instrument function varies slightly between the channels of the McPherson spectrometer, on average the full-width at half-maximum of the instrument function was determined to be $FWHM = 2\sqrt{2ln(2)}\sigma = 25\ \mathring{A}$ which corresponds to an argon ion temperature of $T_i \approx 3$ eV. Thus, measured temperatures, which are of the order of a few eV, often contribute only a small fraction to the total line profile and uncertainties can be up to 1.0 eV (standard deviation of measured temperatures) depending upon the number of counts observed in the spectra. This error is quantified in below with a Monte Carlo approach. Figure 2.15 shows an example of a measured spectrum in Proto-MPEX and shows the full spectrum and the instrument function broadened spectrum.

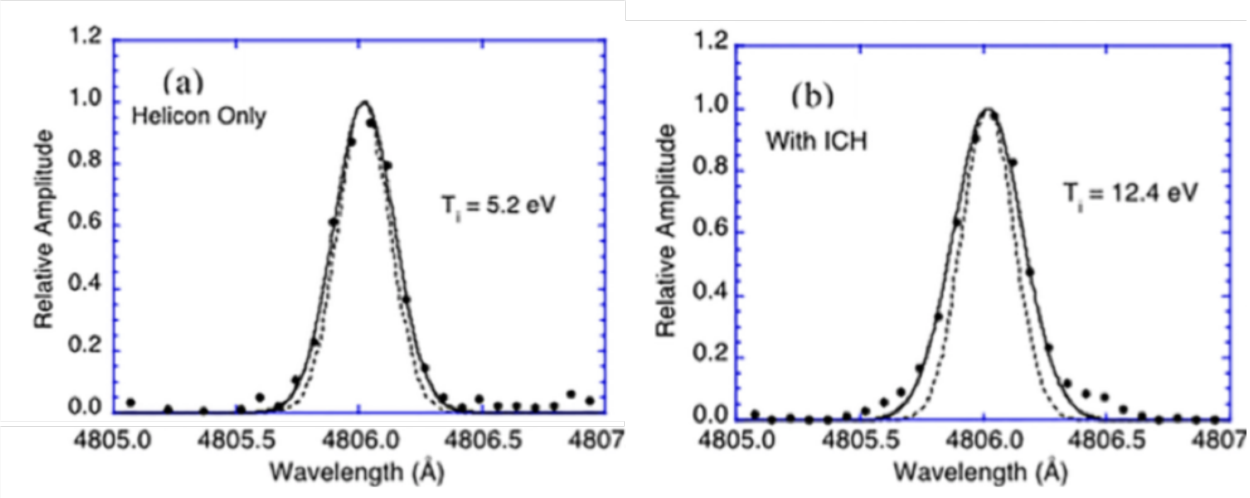

Figure 2.15: Profiles for the spectroscopic measurement of ion temperature observed at Spool 9.5 top viewing location using the line fitting technique are shown in for helicon only shot (a) and a shot with applied ICH power (b). The solid circles are the experimental data with the background subtracted, the solid curves are the best fits, and the dotted lines are the instrument profiles.

The 4806 $\mathring{A}$ $^4P^{\circ}_{5/2}$ to $^4P_{5/2}$ Ar II line is used for spectral analysis. In addition to the Doppler width, the measured line shape is broadened by the instrument profile (which was calibrated and mentioned above) and the Zeeman splitting in the magnetic field. Simple Zeeman pattern with the central pi-component polarized parallel to the magnetic field and two sigma-components polarized perpendicular to the field on either side of the pi- component. The sigma components were removed from the profile by using appropriate polarizers, and therefore the Zeeman splitting is not taken into account when analyzing the spectroscopic data. The measured spectra is then fit with:

$$I(\lambda) = Ae^{\frac{-(\lambda_0-\lambda)^2}{2\sigma_T}} \tag{2.4}$$

$$\sigma_T^2 = \sigma_{IF}^2 + \sigma_{DB}^2 \tag{2.5}$$

$$\sigma_{IF} = \frac{FWHM}{\sqrt{8ln(2)}} \tag{2.6}$$

$$\sigma_{DB} = \sqrt{\frac{kT_i}{m_i c^2}} \tag{2.7}$$

Where $I(\lambda)$ is the Doppler-broadened intensity profile as a function of the wavelength of the light emission λ, the central wavelength λ_0, the total Gaussian broadening σ_T of the spectrum is then determined by convoluting the known broadening from the instrument function with the Doppler broadening. For the convolution of two Gaussians, this is simply just written as an addition of the square of the two broadening terms in each Gaussian. The Gaussian broadening term that represents the instrument broadening, σ_{IF}, is a known calibrated quantity. The broadening term that represents Doppler Broadening is σ_{DB} and is dependant on the ion temperature. The amplitude A is normalized for the data since it doesn't contain terms that help determine the ion temperature of the system. Eq. 2.4 is then fit to the measured spectra with an efficient nonlinear regression fitting function in Matlab "fminsplea" [76]. Besides the electron temperature, other fitting parameters in this model are: λ_0 which can change from 480.6 $\AA$ when flows in the plasma introduce Doppler shifting. Pixelation of the spectrum is taken into account by integrating a high-resolution spectrum onto a "pixelated" spectrum which has the same wavelength resolution as the experimental data. This represents the experimental measurement more closely and it's been observed that not taking this into account artificial gives higher electron temperatures when the resolution of the spectrometer is low, from the measurement. Pixelation to each pixel of the spectrometer can be written as:

$$I_i = \int_{\lambda_i-(d\lambda-\Lambda)}^{\lambda_i+\Lambda} I(\lambda)d\lambda \tag{2.8}$$

Where I_i is the intensity of the spectrum at the pixel location i, λ_i is the center wavelength associated with I_i, $d\lambda$ is the spectral resolution of the spectrometer which is stated above as $d\lambda = 0.075$ $\mathring{A}$, and Λ is the centralization of the integration bounds on pixel i, *Lambda* is then a fitting parameter as well as this has experimental uncertainty. This method of obtaining ion temperature from the measurement has been compared to fitting done by Explicit Zeeman Stark Spectral Simulation (EZSSS) code [77] and Isler et al. method of performing this [78] analysis with no significant error between the techniques.

Error Analysis

The error analysis for determining the error associated with the Ar II measurement was determined with a Monte Carlo error analysis that is described in this section. The error analysis is vital in determining the accuracy of the measured data. The idea for this error analysis is that random error is added into simulated Doppler Broadened profiles of a known T_i^0. The noisy data is then fit again with the Matlab routine used for determining the experimentally measured ion temperature described above. The T_i^N from fitting the noisy data is then typically not the same as the T_i used to create the original set of data. This procedure is done for 100 Monte Carlo runs to gather statistics and the standard deviation of $(T_i^0 - T_i^N)$ is found and reported as the error. This procedure is done for values of ion temperature between $T_i = 0.1 - 40$ eV and signal to noise ratios between 1 to 100; the results of this study are tabulated as a function of these variables in a look-up table. Whenever the data is analyzed the signal to noise ratio and ion temperature determined by the analysis routine is used to interpolate an error in ion temperature.

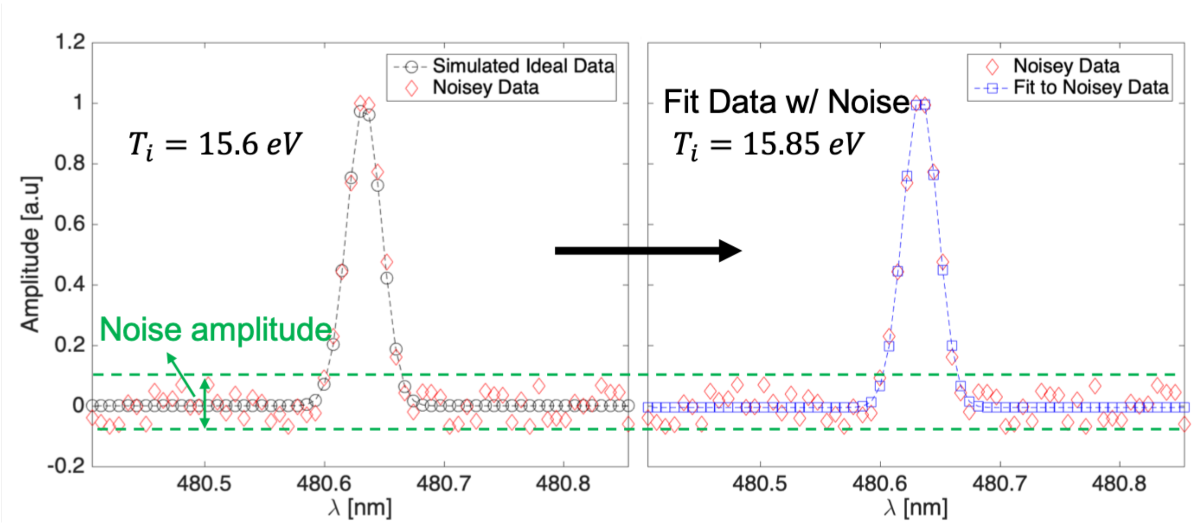

Figure 2.16: Figures showing process of the Monte Carlo Error Analysis. “Simulated Ideal Data” plotted along with random noise added (Left). “Noisy Data” with new fit to data showing different ion temperature than used for original data (Right).

Figure 2.16 shows an example of the error analysis done for one Monte Carlo run at an ion temperature of $T_i^N = 15.6$ eV. The signal to noise amplitude is experimentally determined by first determining the noise amplitude. This is determined by taking the absolute value of the difference between the minimum and maximum points in the baseline that is centered around 0 (away from any peaks), this is then called the noise amplitude (NA). The maximum intensity of the Ar II is then normalized by the noise amplitude and this is number is called the signal to noise ratio. The Monte Carlo simulations signal to noise ratio is then defined in this manner as a noise vector is added to the clean signal. The noise vector is defined as $N_i = NA(2R_i - 1)$, where R_i is a uniformly generated random number between 0 and 1 with Matlab's “rand” function [79]. The vector N_i is added to the data that is simulated with an “ideal” Gaussian broadened spectrum defined exactly from Eq. 2.4. This simulated noisy data is then fit with the same fitting routine used to determine experimental ion temperatures and T_i^N is determined; statistics are collected for 100 Monte Carlo for each condition and the standard deviation of $(T_i^0 - T_i^N)$ is then called the error. This procedure is repeated for $T_i^0 = 0.1 - 40$ eV, and the signal to noise varying from 1 to 100. The error in ion temperature is then tabulated and this is used as a look-up table to interpolate the error from when measuring T_i in the experiment.

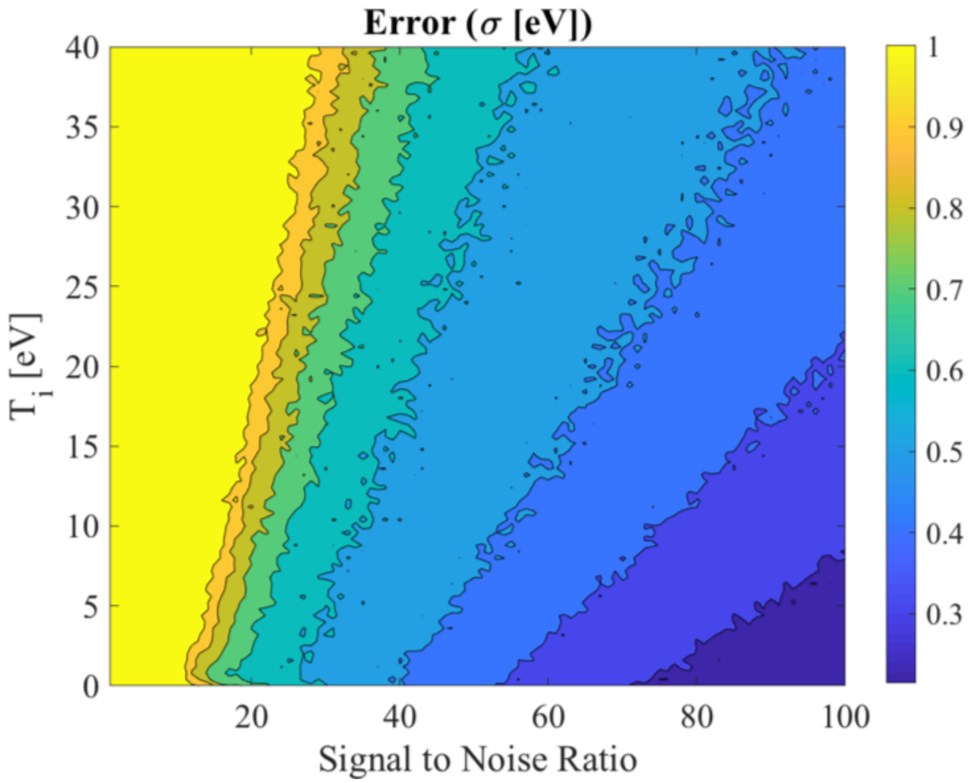

Figure 2.17: Contours of Standard Deviation of ion temperature from Monte Carlo error analysis as a function of electron temperature and signal to noise ratio.

Figure 2.17 shows the tabulated error in ion temperature as a function of ion temperature and signal to noise ratio. This table is used to look up the error from experimental measurements. We notice that as the ion temperature is increased the error increases; however. the percentage error is actually decreased as a function of electron temperature. The expected trend occurs with an increasing signal to noise ratio, as the error decreases significantly. For our regime of interest, a signal to noise ratio is required for ion temperature measurements within an error of $\delta T_i = \pm 1$ eV.

Abel Inversion

Another important consideration for the analysis of the ion temperature from the Ar II spectroscopy discussed in this subsection is determining the contribution of the edge of the plasma on the measurement of T_i in the central view chords. Since the spectroscopic measurement is a line integrated measurement it is important to analyze the effect of the line integration on this measurement. To accomplish this an inversion method was used to reconstruct the radial profile of the ion temperature similar to that used by Bell [80, 81].

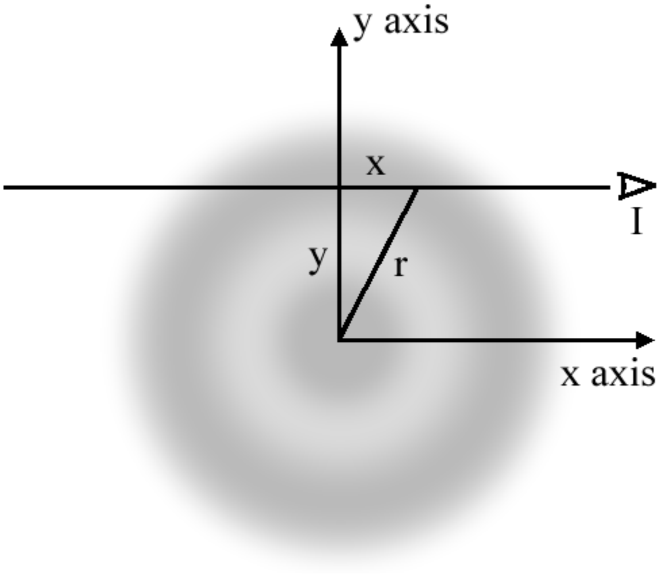

Figure 2.18: Schematic of the measurement geometry.

Figure 2.18 shows a schematic of the assumed measurement geometry of the Ar II Doppler Broadening spectroscopy measurements. This measurements geometry assumes an azimuthally symmetric density of light emitter with a radially varying intensity and ion temperature profile profile $f(r, \lambda)$. The observation points, or in this case the fiber optic locations, are located along the y plane, at several y locations, a distance d away from the object. The light emission observed by spectrometer fibers can then be written as:

$$F(y, \lambda) = \int_0^d \frac{f(r, \lambda)}{\sqrt{r^2 - y^2}} r dr \tag{2.9}$$

$$f(r, \lambda) = I(r) e^{\frac{-(\lambda_0 - \lambda)^2}{\sigma(r)}} \tag{2.10}$$

$$\sigma(r) = \sqrt{\frac{kT_i(r)}{m_i c^2}} \tag{2.11}$$

From Eq. 2.9 we see that we assumed that the light emission profile experimentally observed $F(y, \lambda)$ is defined as an integration of the physical space light emission profile $f(r, \lambda)$. The physical space light emission profile is then dependant on a radial dependent light intensity amplitude $I(r)$ and ion temperature profile $T_i(r)$. The quantity that is of interest to measure is the radial dependant ion temperature profile $T_i(r)$ that is convoluted inside of $F(y, \lambda)$. Finding $T_i(r)$ is then an inverse problem that is attempted to be solved in this section.

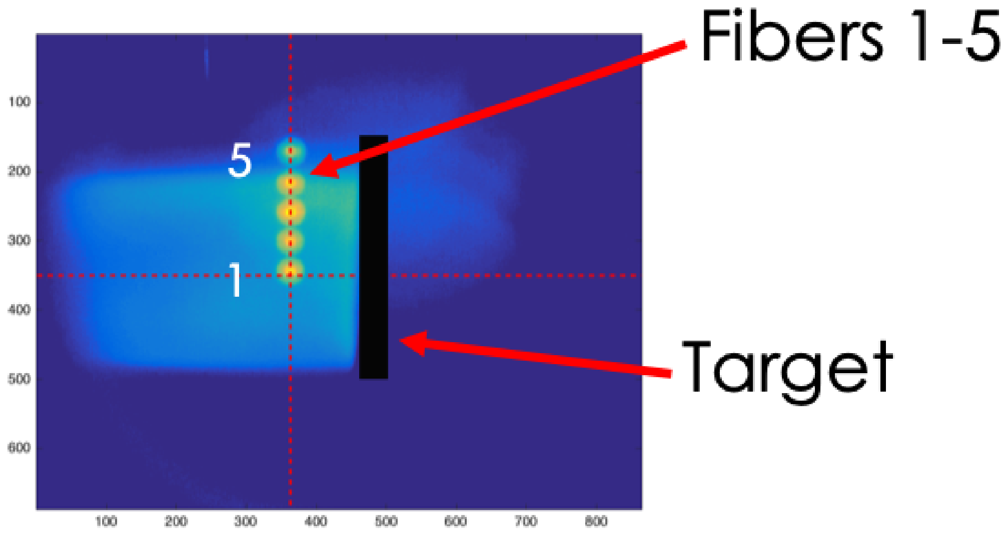

Figure 2.19: Alignment image of the fiber views near the target with respect to the plasma column. The fibers are shown in the yellow dots and labeled 1 through 5 with 1 being the centermost fiber and 5 being the outer most fiber. The target plate is depicted by the solid black line and labeled in this figure.

The alignment of the fibers with the plasma for the Abel inversion was accomplished with a setup where a beam splitter split the light emission, from Spool 12.5, and diverted the light to a fast frame camera as well as an array of fiber optics which were connected to a spectrometer. Figure 2.19 shows an image taken by aligning the fiber views to the plasma column. This image consists of 2 images taken separately, one of these images, was an image of the backlit fibers through a beam splitter that aligned the fast frame camera view with the views of the fibers. The second image was an image taken with the beam splitter setup mounted on Proto-MPEX and aligned with a view close target plate. The image in Fig. 2.19 thus shows the alignment of the fibers to the fast frame camera image which shows an image of the plasma column taken during a Proto-MPEX pulse.

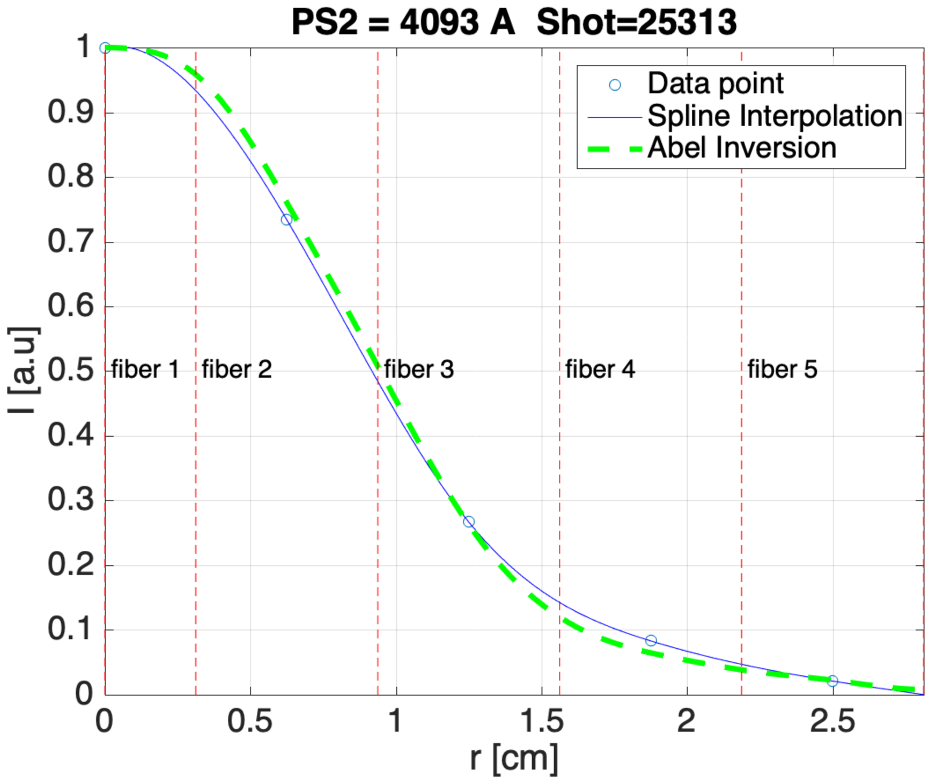

Figure 2.20: Amplitude measured by each fiber in the array (black circles) for a typical shot with ICH, fit with a spline interpolation (blue curve), Abel inversion of the spline interpolated amplitude (dashed green curve), reverse Abel Inversion compared to original interpolation (black dotted line). The radial extent of each fibers measurement shown by dashed red lines and labeled by each fiber number.

The first problem in attempting to solve for $T_i(r)$ is to reconstruct $I(r)$ from the intensity profile measured $I_i(y)$. The method we consider here to reconstruct $I(r)$ is an Abel transformation, where $I(r)$ is assumed to be azimuthally symmetric. The inverse Abel transform is defined by $I(r) = -\frac{1}{\pi}\int_r^{\infty} \frac{dF}{dy}\frac{dy}{\sqrt{y^2-r^2}}$ and is performed by Abel Inversion Algorithm in Matlab [82]. Figure 2.20 shows the measured intensity profile along with a spline fit of the measured data, and an inverse Abel transformation of the spline fit data. The radial extent of each fiber measurement is shown by the dashed red lines and the fiber is labeled. Now that $I(r)$ has been retrieved, what is left to do is to reconstruct $T_i(r)$.

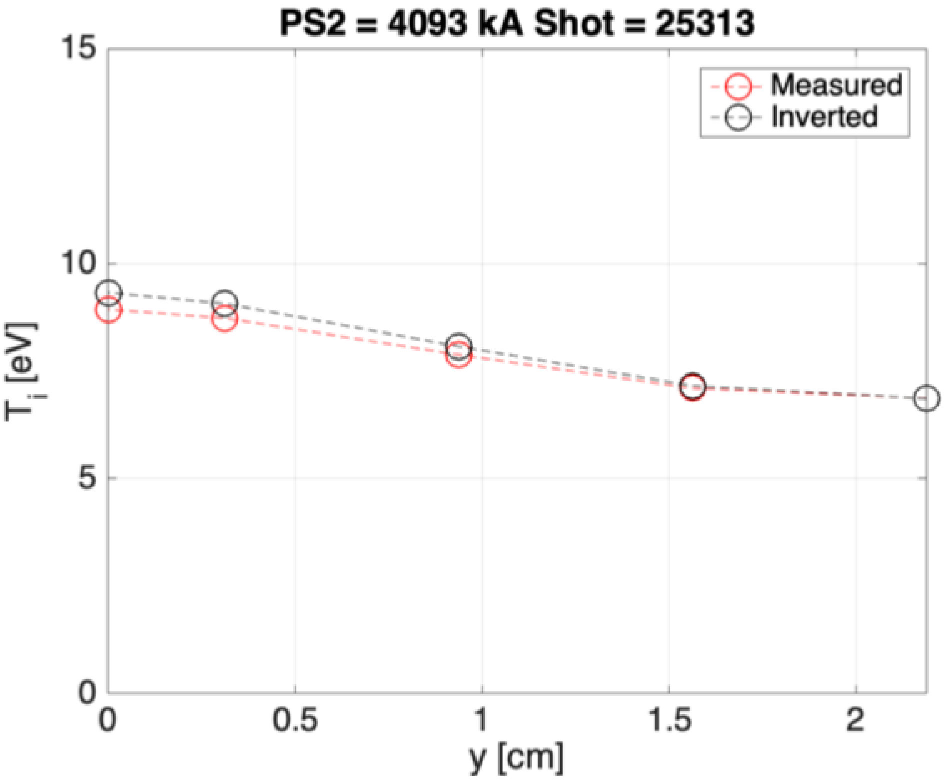

Figure 2.21: Measurement across the radius of the plasma showing ion temperatures from fitting the line integrated spectrum (Measured) and a comparison to the ion temperatures reconstructed from the onion peeling model(Inverted).

The value of ion temperature that is reported experimentally is $T_i(y)$ from fitting $F(y,\lambda)$, most of the measurements did not have the luxury of having 5 aligned views to invert the temperature, therefore, this exercise was to show that the measurement reported by fitting $F(y,\lambda)$ was a good approximation of $T_i(r)$. From Fig. 2.21 which shows the $T_i(y)$ compared to the reconstructed profile $T_i(r)$ it is observed that for a typical measurements that the inverted $T_i(r)$ is very close to the reported $T_i(y)$. The reconstruction of T_i was done with an "onion peeling" method similar to that used by Bell [80, 81]. However, here we instead started with the outside temperature and used a Newton-Raphson iteration to converge on the reconstructed ion temperature at the next inward measurement location. The derivative used in the Newton-Raphson scheme was determined numerically from the previous guess of the reconstructed electron temperature, with the initial derivative being determined by guessing a small offset from the measured temperature. The Newton-Raphson converged with a convergence criterion of $T_e = 0.1$ eV, which is typically within the range of error for the measurement of $T_i(y)$.

2.2.4 IR Thermography

Details about the IR thermography measurement can be found in [83], and this section will summarize the technique used to measure heat flux in Proto-MPEX. The heat flux deposition profile at the target plate has been measured by viewing both the front-side (the side where plasma strikes the target) and back-side (the side where plasma does not strike) of the target using a FLIR A655sc IR camera. The A655sc cameras detector is an uncooled bolometer. It has a spectral range of $7.5 - 14\ \mu m$, a detector pitch of $17\ \mu m$, and a resolution of 640×480 pixels. The camera has a full window frame-rate of 50 Hz and a maximum frame-rate of 200 Hz (for a minimum window of 640×120). The camera has two temperature range settings: $40^\circ - 150^\circ$ C and $100^\circ - 650^\circ$ C, with an accuracy of $\pm 2^\circ$ C or $\pm 2\%$ of the reading. The camera is connected to the computer through a gigabit Ethernet cable. The camera is further set up to receive an external trigger to begin recording. The camera begins recording 0.5 s prior to the plasma shot and records for 4 s total.

The 2016 experimental campaign focused on back-side imaging of the target, the only relevant data to this thesis where IR camera data was taken in this manner is the data reported in Fig. 4.7 reported in Chapter 4. All the other data relevant to this thesis is presented for front-side viewing of the target plate. The target image is seen through a 4.6 cm diameter ZnSe window on a 2 3/4” CF flange. The front-side imaging is achieved with a periscope that reflects the image of the target from a polished stainless steel mirror to the camera. Fiducial markings on the target plate are placed to convert the image from pixel space to physical space, these fiducial markings typically consist of either etched markings on the viewing side of the target, or small holes placed in the target. After the reconfiguration of Proto-MPEX for the 2018-2019 experimental campaign, the viewing angle of the target was very sharp ($\approx 20^\circ$), and therefore homography had to be performed on the IR image because the image was stretched. Homography was performed utilizing Matlab to reconstruct the homography matrix according to [84], and the fiducial markings were for reference points.

Emissivity

Different materials have been used for imaging, here we are concerned with carbon and stainless-steel. The carbon target was dark and not reflective and therefore no surface treatment of the carbon target was done for the imaging. The 304 stainless-steel target is bead-blasted to raise the surface emissivity, and reduce the reflectivity of the surface to aid in image analysis. Accurately measuring changes in temperature on the back-side of the target plate require accurate emissivity values. The IR camera is calibrated for emissivity both in-situ and ex-situ. The ex-situ calibrations are performed via bench testing. The IR camera is set up on a lab bench top approximately 1 m away from a target plate. A heat gun is located behind the target plate to act as the heat source. A type-K thermocouple is embedded at the side of the target plate. The thermocouple connects to a portable meter, which reads the temperature. When the heat gun begins heating the target plate, the thermocouple readings are compared to the IR camera readings. The emissivity value is adjusted until it reasonably matches the thermocouple readings. The in-situ calibrations are performed during plasma operations, the IR camera measurements of target plate temperatures are compared against embedded thermocouple temperature measurements.

Heat Flux Calculation

The heat flux calculation is then dependant on if the temperature imaging is done on the front face of the target or on the back face. If the imaging is done on the back face of the target then the following analysis is applicable and gives a reasonable estimate for the heat flux if the target plate is thin enough. The time scale on which this measurement is taken as well as the heat diffusion constant of the SS target allows ignoring radial and azimuthal heat diffusion within the target plate by satisfying $\frac{\partial T}{\partial t} \gg D(\nabla_{\perp}^{2} T)$ Therefore, the time-differentiated thermal images give a two-dimensional (2D) profile of the plasma heat flux as determined by Eq. (2.12).

$$\frac{\partial T}{\partial t} = \frac{q_v}{\rho c_p} \tag{2.12}$$

where T is the temperature measured by the IR camera, c_p and ρ is the specific heat and density of SS, t is the time, q_v is the volumetric heat source which in the case of a plasma heat flux on the surface is written as $q_v(r, \phi, z) = q_s(r, \phi)\delta(z - z_0)$ where z_0 is the location of the target. This analysis, however, is not applicable to imaging the front side of the IR target. Instead, in the case of front side imaging, the 2D time-dependent temperature measured by the IR camera is used as a boundary condition for a 3D finite element simulation of the heat diffusion problem. The other boundary condition for this analysis is set to radiative cooling boundaries. COMSOL's heat transfer module [85] is used to solve the heat diffusion problem numerically, and the heat flux can then be calculated as a post process.

2.2.5 Double Langmuir Probe

Double Langmuir Probes (DLPs) are utilized in Proto-MPEX to measure electron density (n_e) and temperature (T_e) frequently. Previous work [4, 86] has shown that DLP measurements of density and electron temperature are weakly affected by RF rectification provided sheath effects are small $\frac{r_p}{\lambda_d} \gg 1$, where r_p represents the probe radius and λ_d the Debye length. This condition is readily satisfied for the conditions typically encountered in Proto-MPEX, as we chose an appropriate probe tip diameter so that for conditions typical of Proto-MPEX such the Debye length is much smaller than the probe radius and therefore we avoid RF induced sheath expansion effects. Therefore, a DLP has been chosen over a single Langmuir probe because they provide intrinsic RF compensation [4], and therefore there is no need to provide additional RF compensation for the probe.

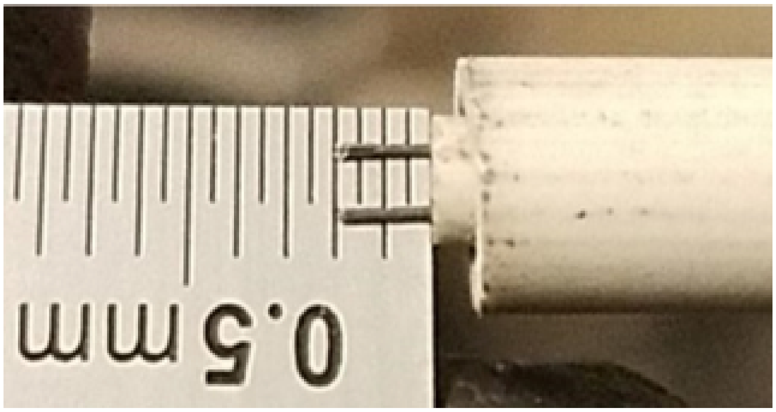

Figure 2.22: The following is an image of the DLP and the current collecting tips.

An image of a DLP probe head is shown in Fig. 2.22, where a two-bore Al_2O_3 ceramic is used to electrically isolate the inner tungsten conductors. An electrostatic shield, consisting of a stainless steel tube, is placed close to the probe tips. The electrostatic shield is then enclosed in a larger diameter Al_2O_3 tube to protect this from the plasma heat load. The electrostatic shield is grounded using a custom-made standoff, which is in contact with the conical flange of the the probe drives. The DLPs used in this study were swept at 200 Hz using a 1:1 magnetically coupled power supply providing triangular waveform of -60 to 60 V. The current collecting tips are made from Tungsten wire 0.25 mm in diameter and 2 mm in length.

2.2.6 Electron temperature and density calculation

As per the experimental setup in Stampa 1978 [86], a symmetric Double Langmuir Probe (DLP) and a 1:1: transformer to galvanically decouple the DLP from the ground. Therefore, the DLP was electrically floating relative to the plasma. The probe voltages then are in reference to each other, and no net current is drawn by the probe. Therefore, the conditions that must be satisfied by a symmetric DLP are written as follows:

$$i_1 + i_2 = 0 \tag{2.13}$$

$$V = V_1 - V_2 \tag{2.14}$$

The probe I-V characteristics to each probe tip is given by Eq. 2.15 and Eq. 2.16.

$$i_1 = i_0(e^{e(V_1-V_f)/kT_e} - 1) \tag{2.15}$$

$$i_2 = i_0(e^{e(V_2-V_f)/kT_e} - 1) \tag{2.16}$$

In Eq. 2.15 and Eq. 2.16, V_f is the floating potentialof the plasma, T_e is the electron temperature, $V_{1,2}$ is the voltage on probe tips 1 and 2 respectively, and $i_{1,2}$ is the current drawn by probe tips 1 and 2 respectively. Because only the relative voltage is measured between the probes, the plasma potential cannot be determined from this measurement. An equation in terms of this relative voltage V must then be derived. Solving for V_1 and substituting for i_1 we get a hyperbolic tangent equation, given by Eq. 2.17,

$$i_1 = i_0 \tanh\left(eV/\left(2kT_e\right)\right) \tag{2.17}$$

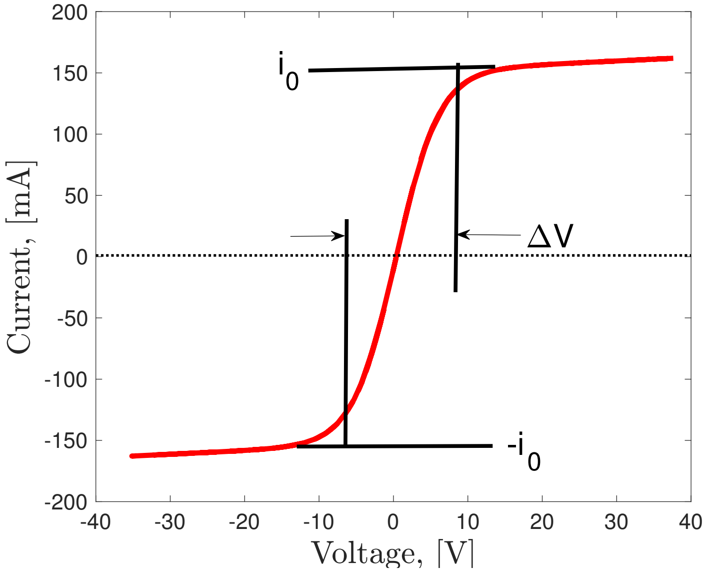

Figure 2.23: IV characteristics from a symmetric DLP where i_0 is the maximum current collected by probe tip during the voltage sweep.

Once electron temperature (T_e) is obtained from fitting Eq. 2.17 to the collected data, the electron density (n_e) can be evaluated using the equation for a thin sheath probe given by Eq. 2.18.

$$n_e = \frac{i_0}{qA\sqrt{Z_i k T_e / m_i}} \tag{2.18}$$

where Z_i is the charge state of the ion, A is the area of the probe tip, and q is the fundamental charge.

Chapter 3

Modeling and Theoretical Background

3.1 Cold Plasma Response to EM Fields

One way to understand wave propagation in plasma is to derive dielectric properties of the plasma based on its characteristic properties such as the electron density (n_e), the background magnetic field strength (B_0), electron (m_e) and ion (m_i) mass. From these properties, it is possible to solve for a plasma current based on the particle velocity, its charge, and density. To solve for the particle velocity one can take many approaches, the most straightforward to formulate is to ignore electron and ion temperature effects, which essentially reduces the plasma equations to the equation of motion of a single particle. This approach is able to adequately describe wave propagation in a "cold plasma", in which finite temperature effects can be neglected. The following section outlines the derivation of the STIX tensor which contains the dielectric properties of a cold plasma [87]. Then a general dispersion relation will be obtained from the STIX tensor which can be reduced to a quadratic formula for the square of the index of refraction (n^2). The quadratic form of the dispersion relation signifies that there exists two wave solutions for a set of plasma properties. These waves will have different characteristic length scales and propagation characteristics. The phase velocity of the wave will be presented and the meaning and uses of it will be discussed. The group velocity (v_g) of the wave can also be derived from the dispersion relation. The angle of the group velocity from the magnetic field dictates the direction the electromagnetic energy of the wave will propagate in the plasma.

3.1.1 Cold Plasma Dielectric Tensor Derivation

To start the derivation of the STIX tensor we must write an equation that will allow us to solve for velocity of the electron and ion particles. The cold plasma approximation allows us to write the equation of motion for a single charged particle.

$$m_j \frac{dv_j}{dt} = q_j(\vec{E} + \vec{v} \times \vec{B}) \tag{3.1}$$

In Eq. 3.1 the properties of particle j are the mass (m_j), velocity (v_j), and charge q_j. The forces present on the charge are the electric charge from the electric field $(\vec{E})$, and the magnetic field $(\vec{B})$. Next we write Maxwell's equations.

$$\nabla \times \vec{E} = -\frac{\partial \vec{B}}{\partial t} \tag{3.2}$$

$$\nabla \times \vec{B} = \mu_0(\vec{J} + \frac{\partial \vec{D}}{\partial t}) \tag{3.3}$$

Where if we set $D = \epsilon_0 \vec{E}$ then Eq. 3.2 and 3.3 describe the propagation of electromagnetic waves in vacuum with a current source $(\vec{J})$ given by the charged particles present in the plasma. We then write the current as a function of the charged particle's density, charge, and velocity; then sum over the particle species present in the plasma.

$$\vec{J} = \sum_j (n_j q_j \vec{v}_j) \tag{3.4}$$

Next Fourier transform Eq. 3.1, 3.2, and 3.3 which amounts to approximating the spatial variation of the components as plane waves with the wavevector given by $\vec{k}$, and temporal variation of the wave components with a frequency given by ω.

$$\vec{E} = \vec{E_1} e^{i(\vec{k}\cdot\vec{r}-\omega t)} \tag{3.5}$$

$$\vec{B} = B_0 \hat{z} + \vec{B_1} e^{i(\vec{k}\cdot\vec{r}-\omega t)} \tag{3.6}$$

$$\vec{v} = \vec{v_1} e^{i(\vec{k}\cdot\vec{r}-\omega t)} \tag{3.7}$$

From Eq. 3.6 we see that we expanded the magnetic field into a DC component given by B_0 that is oriented in the $\hat{z}$ direction and an RF component with plane wave variation. In the equation of motion we have also ignored the RF magnetic field approximating that it is much weaker than the DC component. We have simplified terms that contain the ion cyclotron frequency $\omega_{cj} = \frac{q_j B_0}{m_j}$. Next we use the definitions given by Eq. 3.5 through 3.7 in Eq. 3.1 and solve for the particle velocity.

$$v_{xj} = \frac{i q_j}{m_j(\omega^2 - \omega_{cj}^2)}(\omega E_x + i\omega_{cj} E_y) \tag{3.8}$$

$$v_{yj} = \frac{i q_j}{m_j(\omega^2 - \omega_{cj}^2)}(-i\omega_{cj} E_x + \omega E_y) \tag{3.9}$$

$$v_{zj} = \frac{i q_j}{m_j \omega} E_z \tag{3.10}$$

To simplify Eq. 3.8 and 3.9 we can introduce the rotating coordinate system such that $v_\pm = v_x \pm iv_y$ and $E_\pm = E_x \pm iE_y$.

$$v_\pm = \frac{iq_j}{m_j(\omega \mp \omega_{cj})} E_\pm \tag{3.11}$$

We can then write the plasma current in the rotating coordinate system as.

$$J_\pm = i\epsilon_0 \sum \frac{iq_j}{m_j(\omega \mp \omega_{cj})} E_\pm \tag{3.12}$$

$$J_z = i\epsilon_0 \sum \frac{\omega_{pj}^2}{\omega} E_z \tag{3.13}$$

Here we introduce the plasma frequency given by $\omega_{pj}^2 = \frac{n_j q_j}{\epsilon_0 m_j}$. Now we can define the displacement current caused by the presence of the plasma as follows.

$$\vec{J} - i\omega\epsilon_0 \vec{E} \equiv -i\omega\epsilon_0 (\overleftrightarrow{K} \cdot \vec{E}) \tag{3.14}$$

From Eq. 3.14 we can solve for the terms of the dielectric tensor $\overleftrightarrow{K}$, and organize the tensor with STIX notation given as follows.

$$\overleftrightarrow{K} = \begin{bmatrix} S & -iD & 0 \\ iD & S & 0 \\ 0 & 0 & P \end{bmatrix} \tag{3.15}$$

The terms given in Eq. 3.107 are defined as follows.

$$S = \frac{1}{2}(R + L) \tag{3.16}$$

$$D = \frac{1}{2}(R - L) \tag{3.17}$$

$$P = 1 - \sum_j \frac{\omega_{pj}^2}{\omega^2} \tag{3.18}$$

$$R = 1 - \sum_j \frac{\omega_{pj}^2}{\omega(\omega + \omega_{cj})} \tag{3.19}$$

$$L = 1 - \sum_j \frac{\omega_{pj}^2}{\omega(\omega - \omega_{cj})} \tag{3.20}$$

With the STIX tensor now defined we can use this tensor to describe the dielectric properties of the plasma of interest and solve Mawell's equations in the presence of a cold plasma.

3.1.2 Dispersion Analysis

With the STIX tensor defined and the displacement current in place of the the plasma current. We can now rewrite Maxwell's equations as follows:

$$i\vec{k} \times \vec{E} = -i\omega\vec{B} \tag{3.21}$$

$$i\vec{k} \times \vec{B} = -i\omega\epsilon_0\mu_0\overleftrightarrow{K} \cdot \vec{E} \tag{3.22}$$

We can now reorganize Eq. 3.21 and 3.22 into the Helmholtz equation given by

$$\vec{n} \times (\vec{n} \times \vec{E}) + \overleftrightarrow{K} \cdot \vec{E} = 0 \tag{3.23}$$

$$\vec{n} = \frac{\vec{k}c}{\omega} \tag{3.24}$$

Assuming now that θ is the angle between $\vec{k}$ and B_0 we can expand Eq. 3.23 to the following matrix equation.

$$\begin{pmatrix} S - n^2cos^2\theta & -iD & n^2cos\theta sin\theta \\ iD & S - n^2 & 0 \\ n^2cos\theta sin\theta & 0 & P - n^2sin^2\theta \end{pmatrix} \begin{pmatrix} E_x \\ E_y \\ E_z \end{pmatrix} = 0 \tag{3.25}$$

Here we see that any non-trivial solution to the wave equation requires the determinant of the coefficient matrix to vanish. This condition can be summarized as follows.

$$An^4 - Bn^2 + C = 0 \tag{3.26}$$

$$A = Ssin^2\theta + Pcos^2\theta \tag{3.27}$$

$$B = RLsin^2\theta + PS(1 + cos^2\theta) \tag{3.28}$$

$$C = PRL \tag{3.29}$$

Eq. 3.26 is called the cold plasma dispersion relation. This relation gives 2 solutions of n^2 which determines the wave characteristics that can propagate in a cold plasma. Conditions that lead to the solution of Eq. 3.26 to $n^2 \rightarrow \infty$ are called resonance conditions, where conditions leading to $n = 0$ are called cutoff conditions. Since this equation's solutions behave differently at various propagation angles, which are typically unknown to experimentalists, a more useful formulation is required. Rewriting Eq. 3.26 in terms of the perpendicular refractive index given as $n_\perp^2 = n^2sin^2\theta$ allows formulating the problem in terms of parameters that are typically known to experimentalists like the axial wave-number which is primarily driven by the antenna geometry.

$$A_1 n_\perp^4 - B_1 n_\perp^2 + C_1 = 0 \tag{3.30}$$

$$A_1 = S \tag{3.31}$$

$$B_1 = RL + PS - n_z^2(P+S) \tag{3.32}$$

$$C_1 = P(n_z^2 - R)(n_z^2 - L) \tag{3.33}$$

With Eq. 3.30 we can now understand the perpendicular propagation characteristics of the wave that has an axial wave-number driven by the antenna geometry we've designed. The perpendicular wave-number solved for by Eq. 3.30 is typically complex, the real part of this gives the perpendicular wavelength of the propagating wave while the imaginary part gives the damping length of the propagating wave. However, as discussed in further in this section, to estimate power coupling with the cold plasma approximation one must employ an effective mass term.

The solutions to Eq. 3.30 can be further approximated by making assumptions on the phase velocity of the wave. The fast-wave given by Eq. 5.1 is given the name due to the relative perpendicular phase velocity of the wave being larger than the wave given by Eq. 5.2, which is then called the slow wave. The dispersion relation for the slow and fast wave are written here as:

$$k_{\perp_{FW}}^2 = \frac{(k_0^2 R - k_\parallel^2)(k_0^2 L - k_\parallel^2)}{k_0^2 S - k_\parallel^2}, \tag{3.34}$$

and

$$k_{\perp_{SW}}^2 = \frac{P}{S}(k_0^2 S - k_\parallel^2). \tag{3.35}$$

The perpendicular wave number of the wave solved for by Eqs. 5.1 and 5.2 is a complex quantity. The real part gives the perpendicular wave number while the imaginary part gives the inverse of the damping length. With the dispersion relation, the propagation characteristics of the slow and fast waves can be mapped out to help interpret results from the full-wave simulation.

Phase Velocity

An important concept in plasma wave physics that can be understood from the propagation characteristics determined by the dispersion relationship is the phase velocity of the wave. A description and derivation of the phase velocity can be found in [87] and the equation describing it is presented below.

$$\vec{v}_p = \omega \frac{\vec{k}}{|k|^2} \tag{3.36}$$

The magnitude of the phase velocity characterizes the speed at which points of constant phase on the wave. These points of constant phase travel in the direction of the wave-vector. This phase velocity relevant for understanding kinetic damping such as Landau and cyclotron damping, but also is a useful concept in understanding wave patterns from wave-field measurements and simulations.

Group Velocity

The phase velocity, however, does not give us an understanding of the propagation of power in the plasma. The group velocity is the quantity that predicts the direction of the Poynting vector in the plasma or the direction of energy propagation. Unlike for the vacuum case, the direction of the phase velocity and the group velocity in plasma is not the same. A derivation of the group velocity is found in [87] and the result of that derivation is shown here.

$$\vec{v}_g = \nabla_k \omega(k) \tag{3.37}$$

The direction of the group velocity is useful to understand if one wants to know how the energy from the antenna then propagates into the plasma. Defining the wave-vector in terms of its magnitude and direction from the magnetic field $\vec{k} = k(sin\theta\hat{\perp} + cos\theta\hat{z})$ we derive an expression for the angle of the group velocity with respect to the magnetic field (α) and write the expression below.

$$tan\alpha = -\frac{1}{k}\frac{\partial k}{\partial \theta} \tag{3.38}$$

From α we can now understand the direction the energy propagates with respect to the DC magnetic field. With an understanding of this direction and a damping length, we can estimate how much wave power can reach the core of the plasma from an antenna.

The cold plasma dielectric tensor does not predict a power deposition mechanism on its own. In fact, there are no absorption mechanisms present in the form given by Eq. 3.107. To calculate a power absorption mechanism one can modify the derivation of the STIX tensor to include power deposition mechanisms. In the conditions of the Proto-MPEX plasma, we will only consider collisional absorption of the waves since the plasma conditions are very collisional which reduces the mean free path such that kinetic effects in the plasma are unlikely to occur.

3.1.3 Collisional Power Absorption by Plasma

The cold plasma dielectric tensor does not predict a power deposition mechanism on its own. In fact, there are no absorption mechanisms present in the form given by Eq. 3.107. To calculate a power absorption mechanism one can modify the derivation of the STIX tensor to include power deposition mechanisms. In the conditions of the Proto-MPEX plasma, we will only consider collisional absorption of the waves since the plasma conditions are very collisional which reduces the mean free path such that kinetic effects in the plasma are unlikely to occur.

Collisional absorption in a cold plasma derivation can be accounted for by the Krook model which is considered by modifying the collision term, $\left(\frac{\partial f}{\partial t}\right)_{coll}$, in the Boltzman equation describing the evolution of the distribution function, $f(\vec{r},\vec{v},t)$, for charged particles as:

$$\frac{\partial f}{\partial t} + \vec{v}\cdot\nabla f + \frac{q}{m}(\vec{E}+\vec{v}\times\vec{B})\cdot\nabla_v f = \left(\frac{\partial f}{\partial t}\right)_{coll} \tag{3.39}$$

The Krook model then assumes that the form of the collision term is given as:

$$\left(\frac{\partial f}{\partial t}\right)_{coll} = -\nu f_1 = -\nu(f - f_0) \tag{3.40}$$

$$f_0(\vec{r},\vec{v}) = Ae^{-E/kT} \tag{3.41}$$

In Eq. 3.41 the equilibrium distribution function is given by a Maxwellian distribution. E is the sum of the potential and kinetic energy of the particle, A is a normalization constant, k is the Boltzmann constant, T is the thermodynamic temperature, ν is the collision frequency, and f_1 is the perturbed distribution function. Taking the first moment of the distribution function by averaging Eq. 3.39 in velocity to revive the momentum equation then yields.

$$\rho_j\left(\frac{\partial \vec{v}_j}{\partial t} + \vec{v}_j\cdot\nabla\vec{v}_j\right) = -qn_e(\vec{E}+\vec{v_j}\times\vec{B}) - \nabla p_j - \rho_j\vec{v}_j\nu \tag{3.42}$$

Fourier transforming Eq. 3.42 and rearranging terms gives.

$$(\nu + i\omega)(\rho\vec{v}_j) = -qn_r(\vec{E} + \vec{v}_e \times \vec{B}) - \nabla p_e \tag{3.43}$$

This result shows that the collisions interrupt the particle momentum. This momentum interruption can be accounted for in the cold plasma theory by replacing all the ω terms that came from the equations of motion in the STIX tensor by $\omega \rightarrow (\omega + i\nu)$. This is more easily accomplished by replacing the mass terms in Eq. 3.107 with $m_{j_{effective}} \equiv m_j(1 + i\frac{\nu}{\omega})$.

3.2 Kinetic Plasma Response to EM Fields

A more rigorous approach to studying plasma wave phenomena is to increase the level of description of the plasma response to include collective effects, and effects of finite temperature. The approach taken in this thesis is to use the dielectric tensor derived assuming that all species of particles in the plasma have a Maxwellian distribution. This level of description of the plasma response to an electromagnetic wave includes thermal effects that will be needed for describing the plasma wave physics in the ICH section of Proto-MPEX.

3.2.1 Simplified Maxwellian Plasma Tensor

The derivation of the Maxwellian plasma tensor can be found in [88]. The derivation of this tensor is tedious but essentially follows the same route as the derivation of the cold plasma tensor shown in Section 3.1. Instead of deriving the plasma response from the the equation of motion of a single particle, this tensor derives the plasma responses with the linearized collisionless Vlasov equation:

$$\frac{\partial f_1}{\partial t} + \vec{v}\frac{\partial f_1}{\partial \vec{r}} + (\vec{v} \times \vec{\omega}_{c0}) \cdot \frac{\partial f_1}{\partial \vec{v}} = -\frac{q}{m}(\vec{E} + \vec{v} \times \vec{B}_1 \cdot \frac{\partial f_0}{\partial \vec{v}}) \tag{3.44}$$

The derivation assumes a uniform background magnetic field in the $+\hat{z}$ direction. The derivation then assumes all species in the plasma have a Maxwellian velocity distribution defined as:

$$f_\alpha(\vec{v}) = (\pi^{3/2} v_{th_\alpha}^3)^{-1} e^{\frac{-v^2}{v_{th_\alpha}^2}} \tag{3.45}$$

where, the thermal velocity f the species α is defined as $v_{th_\alpha} = \sqrt{\frac{2kT_\alpha}{m_\alpha}}$ which defines the "most probable" velocity in the distribution function. The rest of the derivation can be found in [88] and the result of the derivation is instead summarized here and then reduced to the tensor used in the RF model in COMSOL [85]. The dielectric tensor of a Maxwellian plasma takes on the form:

$$\overleftrightarrow{K} = \begin{bmatrix} \epsilon_{xx} & \epsilon_{xy} & \epsilon_{xz} \\ \epsilon_{yx} & \epsilon_{yy} & \epsilon_{yz} \\ \epsilon_{zx} & \epsilon_{zy} & \epsilon_{zz} \end{bmatrix} \tag{3.46}$$

and the terms in Eq. 3.46 are written as follows:

$$\epsilon_{xx} = 1 - \sum_\alpha \frac{\omega_{p_\alpha}^2}{\omega^2} \sum_{n=-\infty}^{n=+\infty} \frac{n^2}{\lambda_\alpha} I_n(\lambda_\alpha) e^{-\lambda_\alpha}(-\xi_{0\alpha} Z(\xi_{n\alpha})) \tag{3.47}$$

$$\epsilon_{xy} = -\epsilon_{yx} = -i \sum_\alpha \frac{\omega_{p_\alpha}^2}{\omega^2} \sum_{n=-\infty}^{n=+\infty} n[I_n'(\lambda_\alpha) - I_n(\lambda_\alpha)] e^{-\lambda_\alpha}(-\xi_{0\alpha} Z(\xi_{n\alpha})) \tag{3.48}$$

$$\epsilon_{xz} = \epsilon_{zx} = -\frac{1}{2} n_\perp n_\parallel \sum_\alpha \frac{\omega_{p_\alpha}^2 v_{th\alpha}^2}{\omega \omega_{c\alpha} c^2} \sum_{n=-\infty}^{n=+\infty} \frac{n}{\lambda_\alpha} I_n(\lambda_\alpha) e^{-\lambda_\alpha}(\xi_{0\alpha}^2 Z'(\xi_{n\alpha})) \tag{3.49}$$

$$\epsilon_{yy} = 1 - \sum_\alpha \frac{\omega_{p_\alpha}^2}{\omega^2} \sum_{n=-\infty}^{n=+\infty} \left(\frac{n^2}{\lambda_\alpha} I_n(\lambda_\alpha) - 2\lambda_\alpha [I_n'(\lambda_\alpha) - I_n(\lambda_\alpha)] \right) e^{-\lambda_\alpha}(-\xi_{0\alpha} Z(\xi_{n\alpha})) \tag{3.50}$$

$$\epsilon_{yz} = -\epsilon_{zy} = -\frac{i}{2} n_\perp n_\parallel \sum_\alpha \frac{\omega_{p_\alpha}^2 v_{th\alpha}^2}{\omega \omega_{c\alpha} c^2} \sum_{n=-\infty}^{n=+\infty} [I_n'(\lambda_\alpha) - I_n(\lambda_\alpha)] e^{-\lambda_\alpha}(\xi_{0\alpha}^2 Z'(\xi_{n\alpha})) \tag{3.51}$$

$$\epsilon_{zz} = 1 - \sum_\alpha \frac{\omega_{p_\alpha}^2}{\omega^2} \sum_{n=-\infty}^{n=+\infty} I_n(\lambda_\alpha) e^{-\lambda_\alpha}(\xi_{0\alpha} \xi_{n\alpha} Z'(\xi_{n\alpha})) \tag{3.52}$$

where,

$$\lambda_\alpha = \frac{\mu_\alpha^2}{2} = \frac{k_\perp^2 v_{th\alpha}^2}{2\omega_{c\alpha}^2} \tag{3.53}$$

$$\xi = \frac{\omega - n\omega_{c\alpha}}{k_\parallel v_{th\alpha}} \tag{3.54}$$

Here, $Z(\xi)$ is the plasma dispersion function, where the real argument behaves like a damped resonant factor center at $\xi = 0$, with a width of $\delta x \approx 1$. This gives rise to the perpendicular damping of the waves that models the wave absorption by the n^{th} harmonic of the cyclotron frequency, and has a width of $\delta\omega \approx k_\parallel v_{th}$

which is on the order of a thermal Doppler frequency shift. The summation which includes terms with the Modified Bessel function of the first kind ($I_n(\lambda)$) and its derivative ($I'_n(\lambda)$) are rapidly converging functions when the thermal Larmor radius is smaller than the perpendicular wavelength. In Proto-MPEX this is indeed true and the tensor components above will be simplified by $\lambda_\alpha << 1$ and only terms of order $n = 0$ and $n = 1$ will be retained in this tensor. Fundamental cyclotron resonance is retained for the $n = 1$ term, harmonic cyclotron heating is can be included by retaining terms of $n > 1$, however these terms are not relevant to the Proto-MPEX conditions and therefore are ignored in our simplification. Now we apply the Taylor expansion for $\lambda_\alpha << 1$ and assume $\lambda_\alpha \to 0$ while only retaining terms up to $n = 1$. With these assumptions the following terms simplify as follows, $e^{-\lambda_\alpha} = 1$, $I_0(\lambda_\alpha) = 1$, $I'_0(\lambda_\alpha) = 0$, $I_{\pm 1}(\lambda_\alpha) = 0$, and finally $I'_{\pm 1}(\lambda_\alpha) = \frac{1}{2}$. The dielectric tensor can now be simplified to look like the form of the STIX tensor derived for the cold plasma in Eq. 3.107. Except with the components taking the form:

$$R = 1 + \sum_\alpha \frac{\omega_{p\alpha}^2}{\omega k_\parallel v_t h\alpha} Z(\xi_1) \tag{3.55}$$

$$L = 1 + \sum_\alpha \frac{\omega_{p\alpha}^2}{\omega k_\parallel v_t h\alpha} Z(\xi_{-1}) \tag{3.56}$$

$$P = 1 - \sum_\alpha \frac{\omega_{p\alpha}^2}{(k_\parallel v_t h\alpha)^2} Z'(\xi_0) \tag{3.57}$$

$$\xi_n = \frac{\omega + n\omega_{c\alpha}}{k_\parallel v_t h\alpha} \tag{3.58}$$

The components in Eq. 3.55 through 3.58 are the same components found in [63]. These components can be further simplified to the cold plasma tensor with the assumption that thermal effects are negligible, or more formally written as $v_{th\alpha} \to 0$. With this assumption the Taylor expansion for the plasma dispersion function simplifies to $Z(\xi) = -\xi^{-1}$ and its derivative simplifies to $Z'(\xi) = \xi^{-2}$, which reduces the tensor back to the cold plasma tensor. Eq. 3.55 through 3.58 assumes a collisionless plasma. Collisions are an important process in our plasma and the modifications to the kinetic tensor again come through the Krook model. The new terms associated with the collisional kinetic plasma tensor have been derived in [63] and are written here as:

$$\xi_n = \frac{\omega + n\omega_{c\alpha} + i\nu_\alpha}{k_\parallel v_t h\alpha} \tag{3.59}$$

$$P = 1 - \sum_\alpha \frac{\omega_{p\alpha}^2}{(k_\parallel v_t h\alpha)^2} Z'(\xi_0) \left(1 + \frac{i\nu_\alpha}{k_\parallel \nu_\alpha} Z(\xi_0)\right)^{-1} \tag{3.60}$$

Eq. 3.59 through 3.60 can now describe a Maxwellian plasma with collisions. In these equations the kinetic behavior of the plasma is captured by plasma dispersion function $Z(\epsilon_n)$ and it's derivative, this function and it's implementation will be described in the next section. The terms in the above equations are the following:

$v_{th\alpha}$ = thermal velocity of particle α
ν_α = collision frequency of particle α
$\omega_{p\alpha}$ = plasma frequency of particle α
$\omega_{c\alpha}$ = cyclotron frequency of particle α
ω = driving frequency
$k_\parallel$ = axial wavenumber
$k_\perp$ = perpendicular wavenumber

Eq. 3.59 through 3.60 contain a dependence on $k_\parallel$ throughout the dispersion function. This is not known before solving Maxwell's equations in 2D. However, an approximation can be made that $k_\parallel = constant$ and equal to the peak value from the antenna spectrum. This wavenumber is expected to dominate the plasma spectrum, especially in a half-helix antenna. This approximation can be removed by using a spectral approach such as the AORSA code[89].

3.2.2 Dispersion Analysis

Because the form of the dielectric tensor of the simplified Maxwellian plasma, is the same as the cold plasma dielectric tensor the analysis to solve for the perpendicular wavenumber is exactly the same as described in Section 3.1 and the same dispersion relations are used as given by Eq. 3.30 and Eq. 5.1 - 5.2 except that the cold plasma terms are substituted with the terms given by Eq. 3.55 through 3.58. Solving for the parallel wavenumber, however, is non-trivial as the Maxwellian plasma tensor contains terms that depend on the parallel wavenumber. Therefore, an iterative solver can be used to solve the dispersion relation for the parallel wavenumber.

3.2.3 Power Absorption by Plasma

The plasma tensor described by the components given in Eq. 3.55, 3.56, 3.60, and 3.59 now describe all the relevant power absorption processes in the Proto-MPEX plasma. These power absorption processes are Landau damping, fundamental cyclotron resonance absorption, and collisional damping. For the case of collisional damping, the collision frequency is calculated from Coulomb collisions for both electrons and ions, and electron-neutral collisions with deuterium molecules. Non-collisional electron heating (Landau damping) is also important in the ICH region because the ICH antenna operates such that $v_{p_\parallel} \approx v_{th_e}$. The ions are expected to be heated primarily by the resonant absorption of the wave at the fundamental ion cyclotron resonance. This power absorption term is captured by the plasma dispersion function, where the real argument behaves like a damped resonant factor center at $\xi = 0$, with a width of $\delta x \approx 1$. The argument of the plasma dispersion function (Eq. 3.59) tends to zero when the driving frequency is equal to the fundamental cyclotron frequency, thus giving rise to the damping in the tensor.

Power Deposition to Independent Species

The power deposited to electrons and ions can be found by separately calculating the electron and ion currents from the expected conductivity due to each species. The conductivity due to each species is calculated from the Stix tensor, while only including the species of interest in the summation. Then using Ohm's law, the power absorbed by the electrons and ions independently is,

$$P_{e,i} = \mathbf{J}_{e,i} \cdot \mathbf{E}, \tag{3.61}$$

where

$$\begin{aligned} \mathbf{J}_{e,i} &= \boldsymbol{\sigma}_{e,i} \cdot \mathbf{E}, & (3.62) \\ \boldsymbol{\sigma}_{e,i} &= i\omega\epsilon_0 \left(\mathsf{I} - \mathsf{K}_{e,i} \right). & (3.63) \end{aligned}$$

$\mathbf{J}_{e,i}$ is the induced current and $\boldsymbol{\sigma}_{e,i}$ is the conductivity tensor associated with either electrons or ions. $\mathsf{K}_{e,i}$ is the plasma tensor given by Eq. 3.107 but retaining only the terms in the summations that represent the species of interest.

3.2.4 Implementation of the Plasma Dispersion Function

The plasma dispersion function, or Z function, is a critical component of the Maxwellian dielectric plasma tensor; therefore, this subsection is taken to describe its numerical implementation. The definition of the plasma dispersion functions is:

$$Z(\xi) = 2ie^{-\xi^2} \int_{-\infty}^{i\xi} e^{-t^2} dt \tag{3.64}$$

The Z function for a complex argument is calculated in the following manner. The argument of the plasma dispersion function, ξ, is split into the real and imaginary part $\xi = \xi_r + i\xi_c$. The real part of of the argument of the Z function is, ξ_r, is then used to calculate:

$$Z_r(\xi_r) = -2e^{-\xi_r^2} \int_0^{\xi_r} e^{t^2} dt + i\sqrt{\pi} e^{-\xi_r^2} \tag{3.65}$$

and the derivative of the Z function can be defined as:

$$Z_r'(\xi_r) = -2\left(1 + \xi_r Z(\xi_r)\right) \tag{3.66}$$

The integral in Eq. 3.65, $e^{-\xi_r^2} \int_0^{\xi_r} e^{t^2} dt$, is called the Dawson integral and is evaluated using Matlab's symbolic Math Toolbox function "dawson"[90]. The Z function and its derivative are defined by Eq. 3.65 and Eq. 3.66 respectively, for the case of $Im(\xi) = 0$; for a collisionless plasma this description of the Z function is sufficient. However, as is discussed later in this chapter, collisions play a major role in the Proto-MPEX plasma since the collision frequency is on the order of driving frequency of the ICH antenna. Therefore, to take into account the collisions the Z function as defined by the ξ_r must be modified. This is achieved in the following manner:

$$Z_c(\xi) = 1 - i\xi_c Z_r(\xi_r) \tag{3.67}$$

$$Z(\xi) = \frac{Z_r(\xi_r)}{Z_c(\xi)} \tag{3.68}$$

$$Z'(\xi) = \frac{Z_r'(\xi_r)}{Z_c(\xi) Z_c i(\xi)} \tag{3.69}$$

Eq. 3.68 and Eq. 3.69 now capture the Z function with a complex argument in the entire complex plane. To implement the Z function in COMSOL Eq. 3.65 and Eq. 3.66 were tabulated from $|\xi_r| \geq 10^5$ and interpolated linearly from this table in the COMSOL software. For values of $|\xi_r| > 10^5$ the asymptotic approximation of the Z function and it's derivative is used instead, $Z(\xi_r) \approx -\frac{1}{\xi_r}$ and $Z(\xi_r) \approx \frac{1}{\xi_r^2}$. Eq. 3.67 was defined in the software and Eq. 3.68 and Eq. 3.69 are defined in the software.

3.2.5 Benchmarking of the Plasma Tensor

The Maxwellian plasma tensor defined in this section is now benchmarked in COMSOL [85]. The benchmarking consists of simulating the propagation of a plasma wave in a geometry that is representative of an infinite homogeneous plasma and comparing the wavelength that is predicted by dispersion calculations to the wavelength that is established in the simulation. This benchmark is done for the case of perpendicular and parallel propagation (wave vector direction with respect to the background magnetic field) for O-mode, X-mode, R-mode, and L-mode polarizations. Benchmarking in this way allowed locating which component of the plasma tensor had the errors in them as each wave polarization of the wave interacts with a specific component of the plasma tensor. The dispersion relation is solved using both the cold plasma tensor as well as the Maxwellian plasma tensor in a regime where the cold plasma tensor approximation is valid such that the Maxwellian plasma tensor can be benchmarked to the cold plasma tensor.

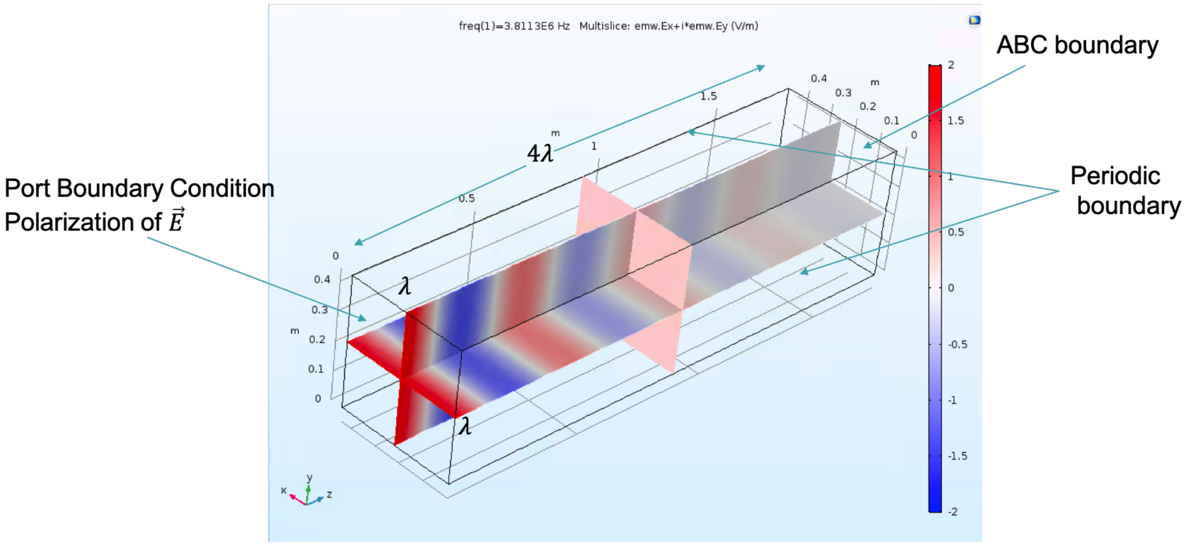

Figure 3.1: Geometry used to benchmark the Maxwellian plasma tensor.

Figure 3.1 is the geometry used for benchmarking the Maxwellian plasma tensor used in COMSOL. The domain is a rectangular domain that is about 1 wavelength long in the width and height of the domain, the length of the domain is set to be approximately 4 wavelengths long. A periodic boundary condition is set along the length of the geometry on all 4 sides. One end of the simulation domain has a second order ABC boundary condition which theoretically should allow the wave to “pass through” without being reflected, and the other end of the simulation domain has a port boundary condition and species an electric field with the appropriate polarization for the wave being excited. This simulation domain closely represents a wave propagating into an infinite homogeneous medium and therefore is perfect for benchmarking the COMSOL simulations to the results of the dispersion relation.

Perpendicular Propagation

This benchmark is done for the case of perpendicular propagation ($\vec{k} \perp \vec{B_0}$) where the wave is either polarized in the O-mode ($\vec{E} \parallel \vec{B_0}$) or X-mode ($\vec{E} \perp \vec{B_0}$). The wave is launched in a background magnetic field of $B_0 = 0.5T$ oriented in the $+\hat{z}$, and a driving frequency of $\omega = (2\pi)28$ GHz, with an ion mass equal to deuterium, and an electron and ion temperature of $T_e = T_i = 10^{-3}$ eV so that temperature effects can be neglected and the cold plasma dispersion relation is valid to benchmark the Maxwellian plasma tensor. These conditions where chosen such that the driving frequency is higher than the electron cyclotron frequency so that the wave is launched such that it can interact with the $P = 0$, $R = 0$, $S = 0$, and $L = 0$ contours so that the behavior can be benchmarked across both cutoffs and resonances. The electron density is then scanned from $n_e = 1 \times 10^{18} - 2 \times 10^{19}$ m^{-3} to observed all the contours mentioned previously.

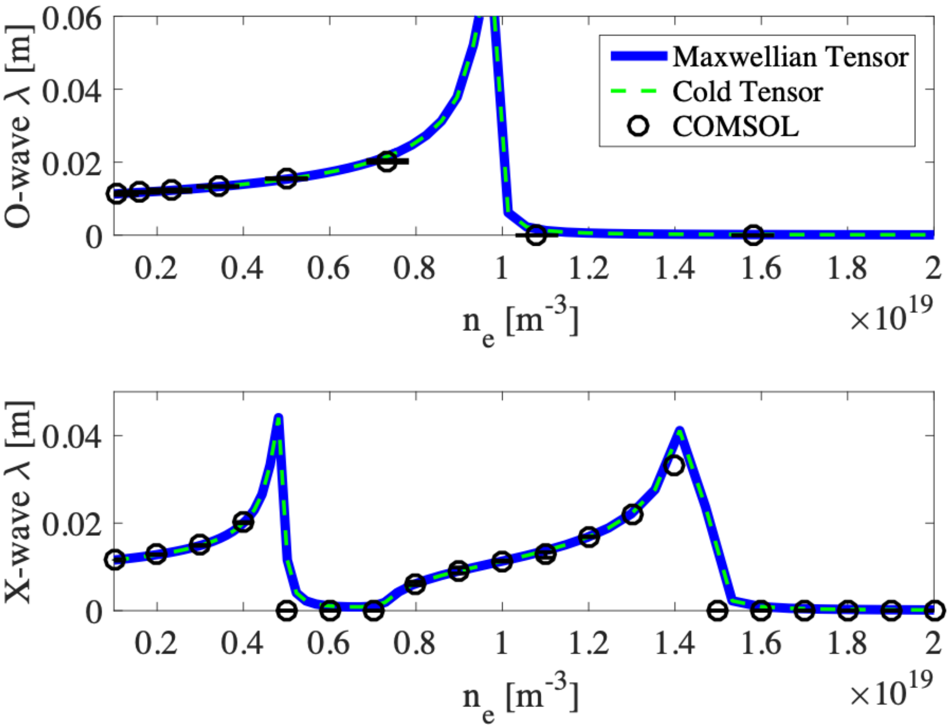

Figure 3.2: Benchmarking results of the COMSOL simulation (black circles) against the predictions of the dispersion relation for the Maxwellian (blue solid line) and Cold plasma (green dashed line) tensors, for O-mode (top) and X-mode (bottom) propagation.

Figure 3.2 shows the results of Benchmarking the simulated wavelength of the O-mode and X-mode waves in the COMSOL model against the predicted wavelength from the dispersion relations for these waves. This benchmark shows that each polarization behaves the expected way. The O-mode wave is cutoff around $n_e \approx 1 \times 10^{19}$ m^{-3} ($P = 0$) and only an evanescent wave is observed on the other side of the cutoff. The simulated wavelength of the O-mode also matches the predicted wavelength from the dispersion relation quite well. The X-mode wave is cutoff around $n_e \approx 4.5 \times 10^{18}$ m^{-3} ($R = 0$) and only an evanescent wave is observed on the other side of the cutoff until the electron density reaches the upper hybrid resonance at an electron density of $n_e \approx 7 \times 10^{18}$ m^{-3} ($S = 0$). The X-mode wave continues to propagate from the upper hybrid resonance to the next cutoff which occurs at $n_e \approx 1.4 \times 10^{19}$ m^{-3} ($L = 0$), at electron densities past the L=0 cutoff the wave is no longer observed to propagate. The simulated wavelength of the X-mode matches the predicted wavelength from the dispersion relation quite well and therefore this polarization is also well captured by the plasma tensor.

Parallel Propagation

This benchmark is next done for the case of parallel propagation ($\vec{k} \parallel \vec{B_0}$) where the wave is either polarized such that the constant phase fronts rotate in right-handed sense (R-mode) or in the left-handed sense (L-mode). The wave is launched in an electron density $n_e = 3{\times}10^{19}$ m^{-3}, and a driving frequency of $\omega = (2\pi)3.8$ MHz, with an ion mass equal to deuterium, and an electron and ion temperature of $T_e = T_i = 10$ eV so that temperature effects can be neglected but the Maxwellian plasma tensor is calculated in the regime where the Z function is interpolated. The background magnetic field is oriented in the $+\hat{z}$ and the field strength is then scanned $B_0 = 0.1-0.9$ T. These conditions where chosen such that the tensor can be benchmarked across the ion cyclotron resonance ($L \to \infty$) which allows the Z function to be tested as it's argument approaches zero which is important for the fundamental cyclotron damping that will be the relevant ion heating mechanism in Proto-MPEX.

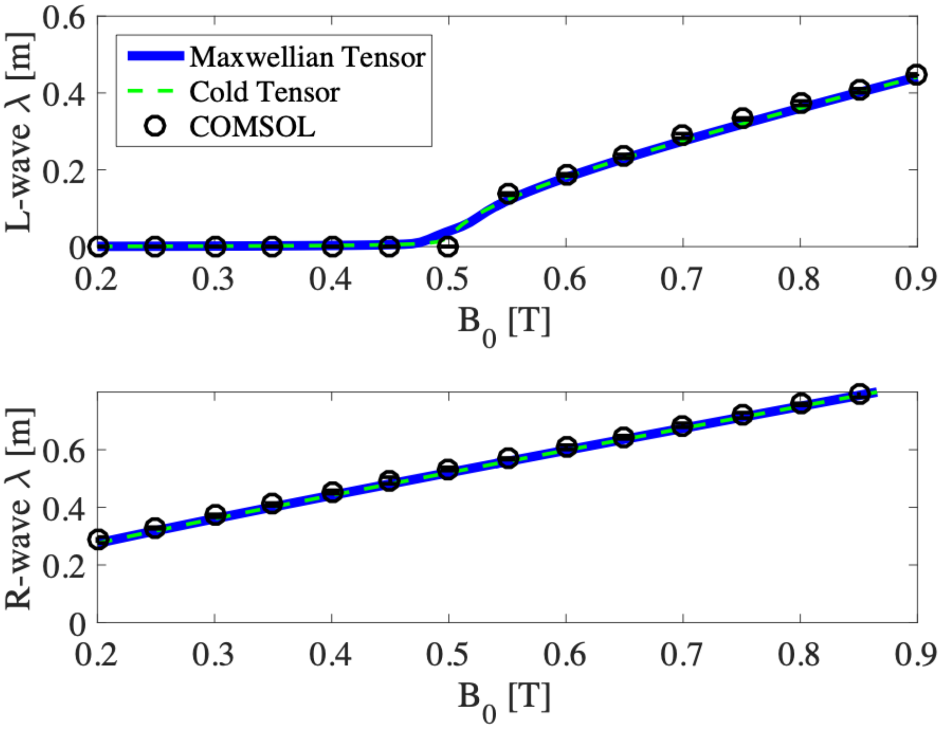

Figure 3.3: Benchmarking results of the COMSOL simulation (black circles) against the predictions of the dispersion relation for the Maxwellian (blue solid line) and Cold plasma (green dashed line) tensors, for L-mode (top) and R-mode (bottom) propagation.

Figure 3.3 shows the results of Benchmarking the simulated wavelength of the R-mode and L-mode waves in the COMSOL model against the predicted wavelength from the dispersion relations for these waves. This benchmark shows that each polarization behaves the expected way. The simulated wavelength of the R-mode matches the predicted wavelength from the dispersion relation quite well. The L-mode wave is resonant at a magnetic field strength of $B_0 \approx 0.5$ T ($\rightarrow \infty$), which is the fundamental ion cyclotron resonance. Only an evanescent wave is observed on the low magnetic field side of the resonance. The simulated wavelength of the L-mode matches the predicted wavelength from the dispersion relation quite well and therefore this polarization is also well captured by the plasma tensor.

3.3 Transport Considerations for the Proto-MPEX Plasma

3.3.1 Collisions

The collisional processes in plasma are important and govern many aspects of the plasma behavior. Collisions in the plasma will appear in the continuity, momentum balance, and power balance. In the parameter space of cold, high-density plasmas the collisions will govern the macroscopic behavior of the plasma and dictate how particles are created and how power is conserved in the plasma. As described in Section 3.1 collisions will also govern RF power deposition in a cold plasma. It is therefore important to understand the dominant collisional processes in the plasma under investigation. The neutral gas density in this region can be approximated by baratron measurements on either side of the helicon antenna. However, it is important to understand that the baratron measurement is the only representative of the edge density in Proto-MPEX, the core plasma is estimated to be close to 100% ionized [68]. A more detailed account on collisional processes in plasmas can be found in many plasma physics textbooks [91, 92, 7].

Quantifying Collisions

Collisions of both ions and electrons with neutrals will, in many typical plasmas, govern the particle and power balance that govern how plasma is ignited and sustained. Collisions of plasma particles with neutral gas particles can lead to elastic scattering, ionization, recombination, dissociation of molecules, excitation of the electrons in an atom to higher energy orbitals, charge exchange of an ion with a neutral gas particle. The quantification of collisional events in a plasma starts with the concept of the collisional cross section $\sigma(v_r)$, where v_r is the relative velocity between the particles. The collisional cross section is defined by the following situation, imagine a flux of particles defined by $\Gamma = nv$, having a fixed number density n, and velocity v. This flux of particles is incident on a "target" of stationary particles, so that $v = v_r$, that have a number density n_g and a differential thickness dx. The number of particles from Γ that is removed by the target is dn and can be written as:

$$dn = -\sigma n n_g dx \tag{3.70}$$

Where the constant of proportionality σ is the definition of the scattering cross section and it takes on units of area. The collision rate of the particles can then be determined by integrating the collision cross section by the velocity distribution of the colliding particles (relative velocities if the "target" is non-stationary) as:

$$K =< \sigma_{en} v_e >= \int \sigma_{en}(v) f(v) dv \tag{3.71}$$

The collision frequency ν, which is the inverse of the mean time between collisions, can be determined by then multiplying the collision rate by the density of "target" particles as:

$$\nu = n_g < \sigma_{en} v_e > \tag{3.72}$$

The mean free path λ,or the typical distance a particle travels between "collision", 90° scattering events for the case of Coulomb collision, can be define as:

$$\lambda = \frac{v}{\nu} \tag{3.73}$$

These definitions allow us to quantify the effect of collisions on the plasma. The energy-dependent cross section for many collisional processes can be found on LxCat database online [93]. Rate coefficients for atoms can also be found in Atomic Data and Analysis Structure (ADAS) [94].

Elastic and Non-Elastic Collisions

The total momentum and energy of the colliding particles are conserved during collisional events in plasmas. Neutral gas atoms and molecules, as well as ions that are only partially ionized (still have electrons left in their atomic orbitals) have internal energy levels. These particles with internal energy levels can be excited, de-excited, or ionized. These processes then change the potential energy of the particle, typically at the expense (or benefit) of the kinetic energy of the particles in the collision. Collisions that do not result in changes in the kinetic energy of the particles involved are said to be elastic collisions. On the contrary, if this is not true and there is a net change in the kinetic energy of the particles involved, these are called inelastic collisions. Inelastic collisions are often either ionization or excitation collisions. These come at the expense of the kinetic energy of the colliding particles and therefore are important in the energy balance considerations. The kinetic energy used for ionization is usually "paid back" during recombination events, however recombination collisions in plasmas are very unlikely except at very low temperatures $T_e < 1$ eV; therefore, creating electron-ion pairs in the plasma acts as an energy sink on the plasma particles. Excitation collisions act in much of the same way, the kinetic energy used to excite an atom is typically lost from the plasma, as the potential energy gained by the atom is then typically released by the emission of light. The plasma is usually transparent to the light and this energy is deposited at the wall of the vacuum vessel containing the plasma[92].

Charge Exchange Collisions

Ions in plasma can collide with a neutral gas atom so that it captures its valence electron which results in a transfer of an electron from the neutral atom to the ion. In general the kinetic energy of the colliding particles is not conserved in this type of collision; however, if the atom and ion have the same nucleus (both are Argon for example), then the transfer can occur such that their kinetic energy is conserved and the interaction is called resonant charge exchange. So the process then can typically be summarized as:

$$Ar^{+}(fast) + Ar(slow) \rightarrow Ar(fast) + Ar^{+}(slow) \tag{3.74}$$

For the purposes of this thesis and the discussions here, only resonant charge exchange is considered and the kinetic energy of the initial particles is assumed to be completely conserved. More about charge exchange collisions can be found in plasma physics textbooks[92].

Coulomb Collisions

The lengthy derivation of Coulomb collisions can be found in [92]. The analytical treatment to obtain the Coulomb collision frequency requires to calculate the cross section for a 90-degree deflection of a particle trajectory by integrating over many single small-angle collisions. Throughout this subsection, the equations used for calculating the Coulomb collision frequencies will be presented. Writing the equations of a reduced mass for a particle is written:

$$m_{rij} = \frac{m_i m_j}{m_i + m_j} \tag{3.75}$$

For the case of the derivation $i, j = e, i$ representing either electron or ion mass. Next, we write the definitions for the Coulomb logarithm's used.

$$ln(A_{ei}) = log\left(\frac{\lambda_D}{q^2/(4\pi\epsilon_0 m_{rei} v_{the}^2)}\right) \tag{3.76}$$

$$ln(A_{ee}) = log\left(\frac{\lambda_D}{q^2/(4\pi\epsilon_0 m_{ree} v_{the}^2)}\right) \tag{3.77}$$

$$ln(A_{ii}) = log\left(\frac{\lambda_D}{q^2/(4\pi\epsilon_0 m_{rii} v_{thi}^2)}\right) \tag{3.78}$$

In Eq. 3.76 through 3.78, v_{the} is the electron thermal speed, v_{thi} is the ion thermal speed, and λ_D is the plasma Debye length. The equations for the Coulomb collision frequencies can now be written as:

$$\nu_{ei} = \frac{2}{3\sqrt{2\pi}} \frac{n_e Z^2 q^4}{(4\pi\epsilon_0)^2} \frac{4\pi}{\sqrt{m_e T_e^3}} ln(A_{ei}) \tag{3.79}$$

$$\nu_{ee} = \frac{1}{3\sqrt{\pi}} \frac{n_e q^4}{(4\pi\epsilon_0)^2} \frac{4\pi}{\sqrt{m_e T_e^3}} ln(A_{ee}) \tag{3.80}$$

$$\nu_{ie} = \frac{m_e}{m_i} \nu_{ei} \tag{3.81}$$

$$\nu_{ii} = \frac{1}{3\sqrt{\pi}} \frac{n_e q^4}{(4\pi\epsilon_0)^2} \frac{4\pi}{\sqrt{m_i T_i^3}} ln(A_{ii}) \tag{3.82}$$

Where Eq. 3.79 through 3.82 give the expressions for the collision frequency for electron-ion, electron-electron, ion-electron, and ion-ion collisions.

3.3.2 Cyclotron Damping

Collisionless damping mechanisms in plasmas, such as Landau damping, have been theoretically discovered and experimentally verified. Derivations of Landau damping, as well as experimental evidence for it, is presented in Ref. [7, 91]. The process relies on the motion of charged particles to be in phase with the applied electric field. In other words Landau damping effects the particles in the distribution function that have a velocity component close to the phase velocity of the electromagnetic wave, these are referred to as “resonant” particles. Resonant particles will then experience a constant electric field and an increase in kinetic energy due to the acceleration from this electric field. Landau damping is typically in reference to a mechanism that affects the parallel velocity distribution of the particles, this type of damping can lead to non-linear effects because the increase in parallel kinetic energy of the particles tends to remove the resonant particles from the velocity distribution function.

A collisionless damping mechanism that acts on the perpendicular component of the velocity distribution of the particles is referred to as cyclotron damping, this is the damping mechanism that will be exploited on Proto-MPEX to heat the ions. Cyclotron damping differs from parallel Landau damping in that the increase of perpendicular kinetic energy does not remove the particles from resonance, this can be easily seen by inspecting the term for the cyclotron frequency $\omega_c = \frac{qB_0}{m}$ and realizing this term does not include a velocity. The increase in perpendicular energy of the particles instead increases the gyroradius of the particle $r_c = \frac{mv_\perp}{|q|B_0}$. The increase in gyroradius of the particles acts favorably for the cyclotron damping mechanism because it allows the particles with higher energy to travel a longer distance in the resonance region, and therefore more work is done by the electric field on the higher energy particles compared to particles with lower perpendicular energy. This is the reason why cyclotron damping allows for a net gain in the kinetic energy of the particles since particles that are not in phase with the electric field will lose energy instead of gaining it.

3.3.3 Conservation of the Magnetic Moment

Proto-MPEX consists of sections of varying magnetic field strength throughout the device. The ion cyclotron heating on Proto-MPEX only acts to heat the perpendicular component of the velocity distribution of the ions in the device. However, the target plate and the measurement locations in Proto-MPEX are located at different magnetic field strengths then where the cyclotron heating occurs. Some of the discussions in this thesis will then rely on the concept known as the adiabatic constancy of the magnetic moment. This section serves to introduce the concept in a most basic argument as summarized from [92], more rigorous treatments of this concept can be found in [91].

$$\mu_{mag} = \frac{W_\perp}{B_z} \tag{3.83}$$

Where μ_{mag} is the magnetic moment of the particle, $W_\perp$ is the kinetic energy of the particle that is perpendicular to the magnetic field, this is defined as $W_\perp = \frac{1}{2}mv_\perp^2$. As particles move through a gradient in magnetic field strength the total kinetic energy of the particle is conserved, $W_\perp + W_z = const$, where $W_z = \frac{1}{2}mv_z$ is the kinetic energy of the particle that is parallel to the magnetic field. This expression can be differentiated to give:

$$dW_z = -dW_\perp \tag{3.84}$$

If there is a gradient in the magnetic field than the change in the parallel kinetic energy can be written as:

$$dW_z = F_z dz \tag{3.85}$$

Where the mirror force is given by:

$$F_z = -\frac{W_\perp}{Bz}\frac{\partial B_z}{\partial z} \tag{3.86}$$

Hence the differential expression for parallel kinetic energy can be written as:

$$dW_z = -\frac{W_\perp}{B_z} dB_z \tag{3.87}$$

Which can be combine with Eq. 3.84 to then give:

$$\frac{dW_\perp}{W_\perp} = \frac{dB_z}{B_z} \tag{3.88}$$

Which can be integrated to show:

$$\frac{W_\perp}{B_z} \equiv \mu_{mag} = constant \tag{3.89}$$

The implication of Eq. 3.89 is most often considered for the study of magnetic mirrors; however, this property has also been exploited for plasma acceleration for use in plasma thrusters, especially that in VASIMR [95, 96, 31], which used ICH heating to heat the perpendicular component of the ion energy distribution in a region with a strongly diverging magnetic field. This energy was converted into parallel particle motion along the diverging field and thus converted into thrust. This concept is also relevant in Proto-MPEX due to the magnetic geometry in the device where the ICH heating is localized. The ICH heating is located in a region of strong magnetic field gradient which then can undergo a significant conversion of perpendicular energy to parallel energy, therefore, this effect is important for the discussions on Proto-MPEX. It is important to mention here that this property primarily concerns nearly collisionless plasmas. The fluid equations that are derived assuming isotropic velocity distribution, do not contain a mirror force expression unless an anisotropy of the velocity distribution function exists [97]. Collisional processes in plasma tend to drive an anisotropic distribution back to an isotropic one; in other words, when the perpendicular component of the velocity distribution is heated, like in the case of fundamental cyclotron heating, that energy will be spread to the parallel component of the distribution due to collisions. This process is different from the process described by converting parallel energy to perpendicular energy in a magnetic field gradient, in that collisions tend to create an isotropic velocity distribution where conservation of the magnetic moment just shifts the velocity distribution from perpendicular to parallel. Since Proto-MPEX is considered to be a moderately collisional plasma, important time scales to keep in mind are the parallel streaming velocity which can be estimated to be the ion sound speed, $C_{si} = \sqrt{\frac{kT_i + kT_e}{m_i}}$, compared to the collision frequency of the particle, which for the case of ions in Proto-MPEX is dominated by ion-ion Coulomb collisions. Estimating the mean free path of the ion distribution function becoming isotropic after the ICH heats the perpendicular energy distribution function can then evaluate as $\lambda_{isotropic} = \frac{C_{si}}{\nu_i i}$, where $\nu_i i$ is the ion-ion Coulomb collision frequency. For a plasma with: $n_e = 5 \times 10^{19}\ m^{-3}$, $T_e = 5$ eV, $T_i = 10$ eV, and deuterium ions we estimate this length to be $\lambda_{isotropic} \approx 7$ cm. This is such that the particle distribution function can experience a mirror force when it is first heated, but isotropic distribution function is expected at the target.

3.3.4 Relevant Sheath Physics

A fundamental concept in plasma physics is the existence of a plasma sheath at a material surface that is immersed in the plasma. In this section, the basic principles of a plasma sheath will be outlined and the consequences of the plasma sheath as pertains to the discussions in this thesis will be elaborated. The basic picture of a plasma sheath is the following. In the presence of a solid object in a plasma, the plasma tends to charge positive compared to the electrical potential of the wall. This creates a potential barrier for the electrons, reflecting them from the material wall, and accelerates the ions towards the wall. Where the bulk plasma is considered to be a region of quasi-neutrality which states that $n_e \approx n_i$, the sheath is a region where quasi-neutrality does not hold and charge separation occurs. Figure 3.4 shows a schematic of the plasma sheath, showing the electron and ion density as well as the electric potential behavior across the plasma sheath.

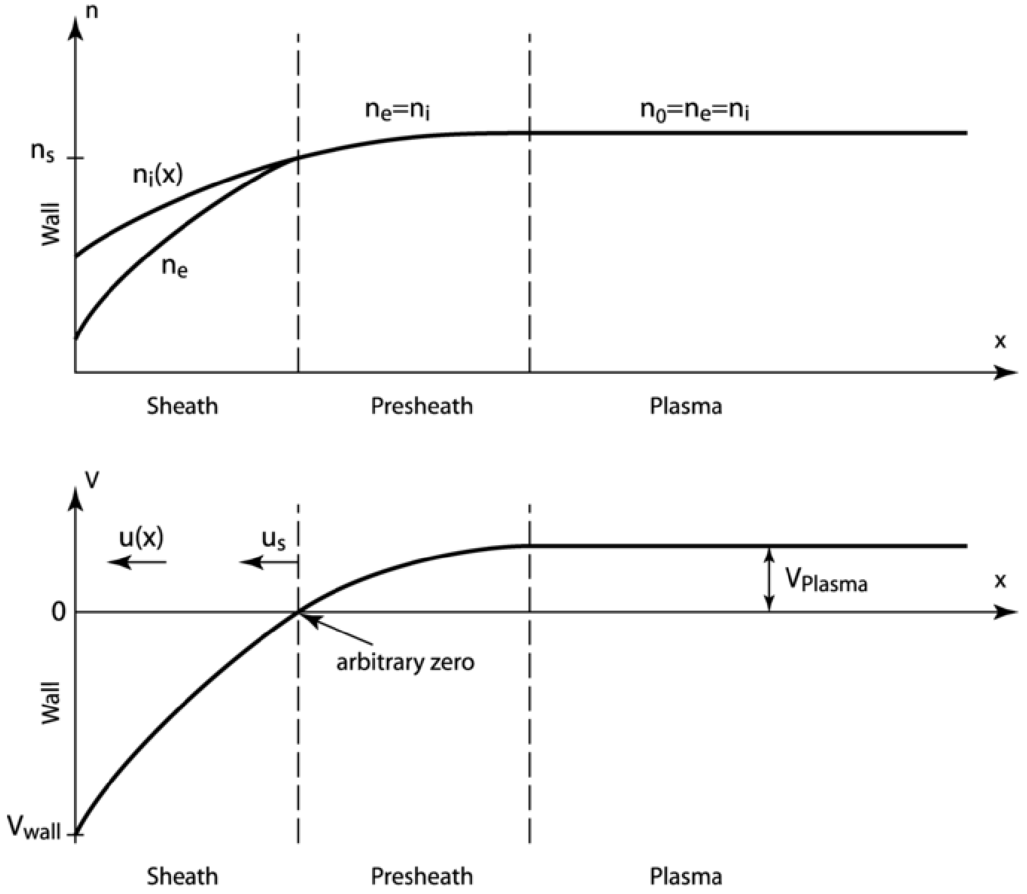

Figure 3.4: Schematic of the plasma sheath. Showing the electron and ion density throughout the bulk plasma, presheath, and sheath (top). The electric potential throughout these regions (bottom).

Bohm found that by analyzing the sheath side of the plasma-sheath interface [98] that the plasma fluid velocity exceeds the ion sound speed, therefore, at the edge of the sheath the fluid velocity of the plasma is:

$$v_{se} = \sqrt{\frac{k(T_e + T_i)}{m_i}} \tag{3.90}$$

This is known as the Bohm sheath criterion. From the perspective of this thesis, quantifying the heat and particle flux that is removed from the plasma due to the presence of a solid object in contact with the plasma is important [99]. That is to say that relating the outgoing flux of particles through the sheath edge to the bulk plasma parameters will be required. The outgoing particle flux can be written as:

$$\Gamma_{se} = n_{se} v_{se} \approx \frac{1}{2} n_0 \sqrt{\frac{k(T_e + T_i)}{m_i}} \tag{3.91}$$

Eq. 3.91 tells us the outgoing flux of particles from the bulk plasma; however, an expression for the outgoing heat flux will also be necessary to consider the energy balance of the plasma. The net electron power flow at the sheath edge can be characterized by:

$$q^e_{se} = (2kT_e + |eV_{sf}|)\Gamma_{se} \tag{3.92}$$

Where q^e_{se} represents the electron cooling power due to the sheath, $|eV_{sf}|$ represents the term that captures the high energy electrons that will be lost to the surface, and $2kT_e$ represents the thermal flux of electrons. It is important to note here that q_{se} does not represent the electron heat flux that the solid wall receives and that these terms are not equivalent. The extra electron energy leaving the plasma that does not arrive at the material wall is transferred to accelerating the ions through the sheath. The electrons energy is used in the formation of the electrostatic field that accelerates the ions. It is convenient to write Eq. 3.92 as:

$$q^e_{se} = \gamma_e k T_e \Gamma_{se} \tag{3.93}$$

Where we introduce the electron sheath heat transmission coefficient γ_e which is defined as:

$$\gamma_e = 2 + \frac{eV_{sf}}{kT_e} + \frac{eV_{pre-sheath}}{kT_e} \approx 5.5 \tag{3.94}$$

Next, we write the ion, this case is not trivial but if the ions are assumed to be a drifting Maxwellian at the sheath edge than one can write:

$$q^i_{se} = \frac{7}{2} k T_i \Gamma_{se} \tag{3.95}$$

Eq. 3.95 assumes that $T_e = T_i$, which then the ion sheath heat transmission coefficient can be defined as $\gamma_i = \frac{7}{2} = 3.5$. The final important consideration and consequence of the sheath that is required for the discussions in this thesis is the impact energy of the ions on the surface of the solid material. This is an important parameter when quantifying the effect of reflected neutral gas particles on the power balance of the ions. Without the presence of the sheath, the ion impact energy would, on average, be $\bar{E}_{impact} \approx 2kT_i$, however, with the acceleration of the ions through the sheath potential the ions gain kinetic energy from the electrons and the impact energy of the ions is then:

$$\bar{E}_{impact} \approx (2kT_i + 3kT_e) \tag{3.96}$$

Therefore, the ions are accelerated because of the presence of the sheath and their impact energy is increased.

3.3.5 Transport Equations in a Plasma

Understanding how plasma is created, maintained, and transported important to understand when developing a plasma source. This section aims to introduce rudimentary concepts in plasma transport physics summarized from [91]. The kinetic equation with a collision operator to represent interactions with neutral particles (binary collision operator) and Coulomb collisions (Landau collision operator) and a Lorentz force operator completely describe the evolution of a plasma (when coupled to Maxwell's equations). The kinetic equation for species α is written as:

$$\frac{\partial f_\alpha}{\partial t} + \vec{v} \cdot \nabla f_\alpha + \vec{a} \cdot \nabla_v f_\alpha = C_\alpha(f) \tag{3.97}$$

Where the Lorentz force is responsible for advection of the distribution function in velocity space and is written as:

$$\vec{a}_\alpha = \frac{q_\alpha}{m_\alpha}(\vec{E} + \vec{v} \times \vec{B}) \tag{3.98}$$

Where $\nabla \equiv \frac{\partial}{\partial \vec{r}}$ and $\nabla_v \equiv \frac{\partial}{\partial \vec{v}}$. Eq. 3.97 describes the evolution of the particle distribution function $f_\alpha(\vec{r}, \vec{v})$ in 6 dimensional phase space, 3 spatial dimensions, and 3 velocity dimensions. Unfortunately Eq. 3.97 is not an easily tractable equation for even reasonably sized problems, as it contains information of all the particles in the plasma. This is why moments of the kinetic equation are taken to derive velocity space averaged quantities, this is how fluid equations to describe a plasma are obtained. The zeroth moment of the kinetic of the kinetic equation, integrating Eq. 3.97 by $\int d^3\vec{v}$, yields the continuity equation for species α written as:

$$\frac{\partial n_\alpha}{\partial t} + \nabla \cdot (n_\alpha \vec{V}) = S_\alpha \tag{3.99}$$

The first moment of the kinetic equation, integrating Eq. 3.97 by $\int \vec{v} d^3\vec{v}$, gives the momentum conservation equation for species α:

$$m_\alpha n_\alpha \frac{\partial \vec{V_\alpha}}{\partial t} + \nabla p_\alpha - q_\alpha n_\alpha (\vec{E} + \vec{V_\alpha} \times \vec{B}) = \vec{F_\alpha} \tag{3.100}$$

The second moment of the kinetic equation, and the last we are considering, taken by integrating Eq. 3.97 by $\int m_\alpha \vec{v} \cdot \vec{v} d^3\vec{v}$ gives the energy conservation equation for species α:

$$\frac{3}{2}\frac{dp_\alpha}{dt} + \frac{5}{2} p_\alpha \nabla \cdot \vec{V_\alpha} + \nabla \cdot \vec{q_\alpha} = W_\alpha \tag{3.101}$$

Where:

$$\frac{d}{dt} \equiv \frac{\partial}{\partial t} + \vec{V_\alpha} \cdot \nabla \tag{3.102}$$

Where p_α is the isotropic pressure, the heat flux density is $\vec{q_\alpha}$, $\vec{V_\alpha}$ is the fluid velocity of the plasma, $\vec{F_\alpha}$ is the frictional force due to collisions with other species, W_α is the energy exchange with other species due to collisions as well as the heating due to external electric fields. Here, the terms associated with the viscosity tensor were ignored to reduce the pressure tensor to an isotropic pressure (or energy density). Eq. 3.99 - 3.102 can describe the transport of plasma, however, there is a problem in describing the system with just these equation. The quantities that are being solved for are in terms of unknown quantities such as the viscosity tensor (ignored here), heat flux density, and moments of the collision operator. The issue is that these lower order moments rely on higher order moments of the kinetic equation, for example, the continuity equation relies on the fluid velocity, and the fluid velocity relies on knowledge of the energy density, the energy density relies on knowledge of the heat flux, and so on and so forth. So rather than continuously deriving infinitely higher order moments we instead make approximations to the higher order moments from known quantities. The processes of relating and approximating these quantities are known as a closure. Throughout the discussions relevant to this thesis Braginskii style closure of the fluid equations is considered (classical transport) [100]. Braginskii closure for parallel transport quantities have been shown to describe parallel transport processes well, cross-field transport properties are not described well by classical transport however discussion of these are typically neglected in this thesis.

3.4 Simulation Inputs and Antenna Modeling

This section outlines the electromagnetic full-wave models, implemented in COMSOL Multiphysics, that are used to simulate the operations of the helicon antenna and the ICH antenna. In these models, Maxwell's equations are solved in the frequency domain using the finite element analysis software COMSOL Multiphysics [85]. The frequency domain wave equation solved is given by Eq. 3.103.

$$\nabla \times \left(\nabla \times \vec{E}\right) - k_0^2 \overleftrightarrow{\epsilon}_r \vec{E} = 0 \tag{3.103}$$

Both 2D axisymmetric and 3D geometry models of the ICH and helicon antennas have been made. The 3D models are used for: benchmarking of the 2D axisymmetric antenna model, and performing engineering calculations of the antenna, such as plasma loading estimates. The 2D axisymmetric model is used mostly for parameter space exploration, for both the understanding of wave physics and experimental optimization of the plasma source and ICH heating. First, this section will cover the electron density model used throughout the simulation. Next, it goes over the plasma tensor rotation that is important to simulate the helicon plasma source region due to the strong magnetic field gradients in that region. Finally, the models for ICH and helicon antennas are presented. The 3D antenna models are first described, next the 2D axisymmetric antenna implementation is described and the Fourier spectrum of the 2D antenna model is compared to that of the 3D model.

3.4.1 Plasma Density Profile as a Function of Magnetic Flux

The magnetic field in the simulations is calculated by solving Ampere's law from the geometry and current configuration of the magnetic field coils. The density is then implemented as a function of the radial coordinate and the azimuthal component of the magnetic vector potential ($A_\phi r$) whose contours correspond to the magnetic field lines in the geometry. The limiting flux line ($A_{\phi_{LF}} R$) is defined by the smallest value of the magnetic flux that intersects the chamber wall near the helicon region. The electron density is then defined as a function of χ.

$$n_e = \begin{cases} n_{e_{peak}} \left(1 - \chi^a\right)^b + n_{e_{edge}} & \chi \leq 1 \\ n_{e_{edge}} & \chi > 1 \end{cases} \tag{3.104}$$

$$\chi = \frac{A_\phi r}{A_{\phi_{LF}} R} \tag{3.105}$$

The peak electron density ($n_{e_{peak}}$) is typically scanned in the simulations to explore this physical parameter space. For the helicon simulations, the edge density is set to $n_{e_{edge}} = 10^{16}\ m^{-3}$, for the ICH simulations the edge density is scanned to understand the effect of this on power coupling to the core. The constants controlling the density profile in Eq. (3.104) are set to $a = 2$ and $b = 1.75$. Figure 3.5 shows Eq. (3.104) plotted against experimentally measured radial scans of electron density profiles measured at location A, B, and C. The experimental radial scans are converted to the χ coordinate based on calculated A_ϕ. The electron density is normalized to a peak density value in each measurement set. Axial variation of ($n_{e_{peak}}$) is not imposed since it is not clear, nor is it diagnosed, how this varies in the experiment under the helicon antenna.

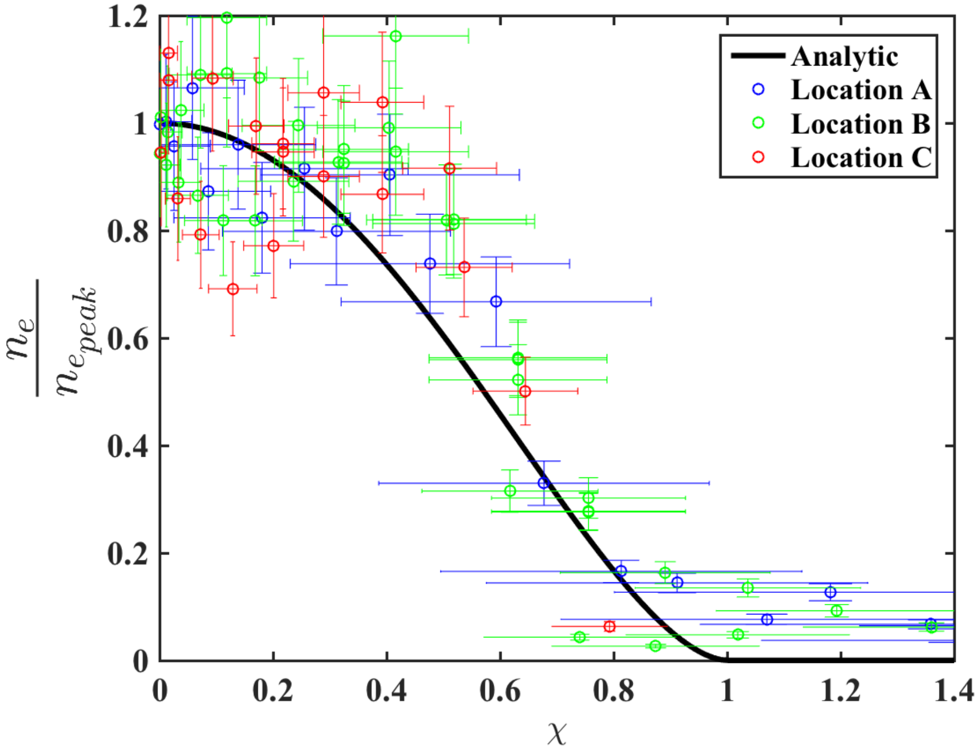

Figure 3.5: Normalized experimentally measured radial scans of electron density at location A, B, and C (which correspond to Spool 9.5, Spool 6.5, and Spool 4.5 respectively) vs the electron density profile given by Eq. (3.104) with $a = 2$, $b = 1.75$, and $n_{e_{peak}} = 1$. The radius of the experimentally measured radial scans is converted to $\chi = A_\phi r (A_{\phi_{LF}} R)^{-1}$

Figure 3.5 compares normalized experimentally measured electron density profiles (the radial variation is normalized to the flux coordinate χ) with the function given by Eq. 3.104. These density profiles were measured at axial positions where the background magnetic field is different. When plotted in magnetic flux coordinates, the radial profiles are self-similar. We note that the solid line representing our density model is not a fit to this data, but merely a representative function used to capture the flux expansion of the electron density profile.

3.4.2 Tensor Rotation

The plasma is represented as a dielectric tensor ($\overleftrightarrow{\epsilon_r}$) derived from cold plasma theory [87] assuming $\vec{B_0} = B_0\hat{z}$. The assumption that the magnetic field is strictly in $\hat{z}$ direction is not valid in the Proto-MPEX device, especially in the helicon region where strong gradients in the magnetic field result in significant curvature of the field lines. This is accounted for by rotating the dielectric tensor to the orientation of the magnetic field lines using the rotation matrix ($\overleftrightarrow{Q}$) to rotate the STIX tensor ($\overleftrightarrow{K}$) by the angle (Ψ) between the magnetic field and the axial coordinate $\hat{z}$.

$$\overleftrightarrow{\epsilon_r} = \overleftrightarrow{Q}_\phi \overleftrightarrow{K} \overleftrightarrow{Q}_\phi^T \tag{3.106}$$

$$\overleftrightarrow{K} = \begin{bmatrix} S & -iD & 0 \\ iD & S & 0 \\ 0 & 0 & P \end{bmatrix} \tag{3.107}$$

$$\overleftrightarrow{Q}_\phi = \begin{bmatrix} cos(\Psi) & 0 & sin(\Psi) \\ 0 & 1 & 0 \\ -sin(\Psi) & 0 & cos(\Psi) \end{bmatrix} \tag{3.108}$$

$$\Psi = tan^{-1}\left(\frac{B_r}{B_z}\right) \tag{3.109}$$

3.4.3 3D ICH antenna

Figure 3.6 shows a schematic of the 3D ICH simulation geometry. The coaxial feed where the port boundary condition is applied, the antenna feed, the antenna ground, and the walls of the vacuum chamber are labeled. The antenna feed is electrically connected to the center conductor of the feed coax while the antenna ground is electrically connected to the vacuum chamber. The ICH antenna geometry is replicated in COMSOL and is used for both full-wave simulations of the ICH heating region in Proto-MPEX [26] and vacuum simulations to benchmark the 2D model described in the subsection below.

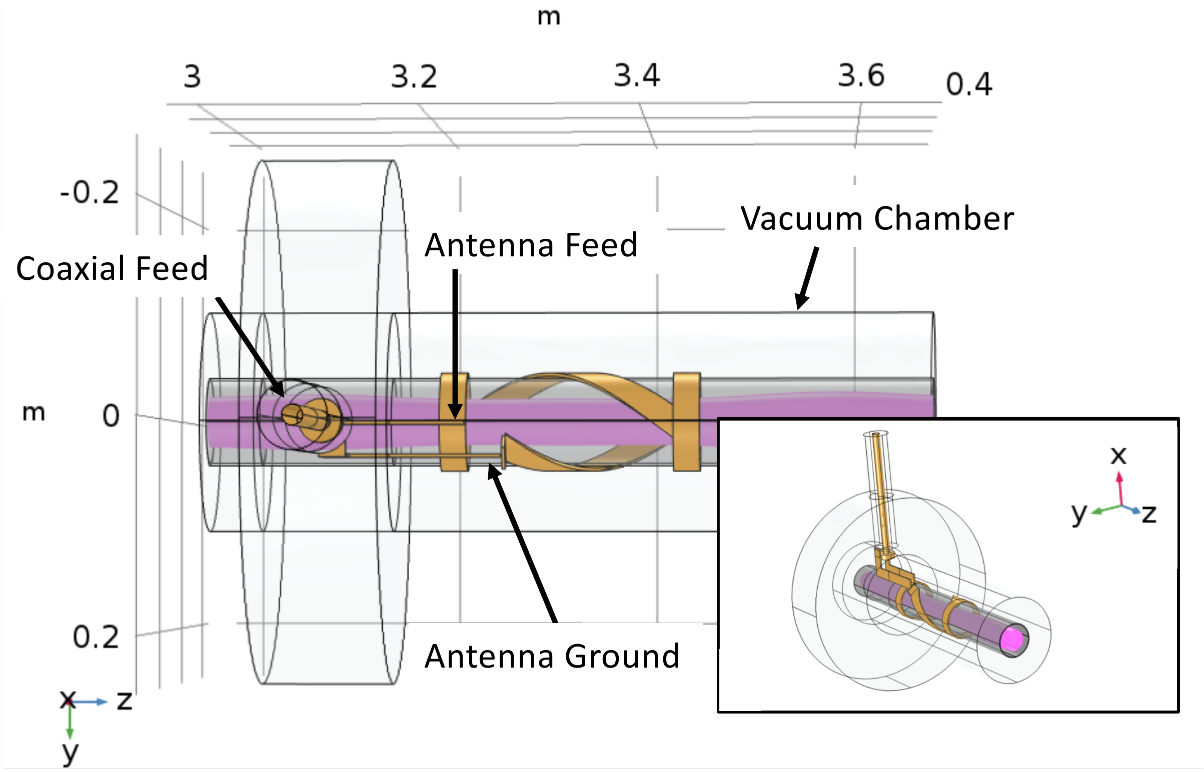

Figure 3.6: Schematic of the ICH geometry used in COMSOL for the simulation. The YZ plane is shown and the ICH antenna, coaxial feed, antenna ground, and antenna feed are labeled. The antenna structure, feed strap, and the ground strap are depicted as a golden color. The alumina window is shown in a dark grey region. Inside of the alumina window is the plasma volume where the bulk plasma is visualized by the pink contour. A 3D rendering of this geometry is shown in the lower right-hand side of the figure for clear visualization of the 3D geometry.

The simulation is excited with a port boundary condition at the coaxial feed labeled in Fig. 3.6, which launches a coaxial TEM mode. The ICH antenna and coaxial feed structures are modeled as a perfect electrical conducting boundary since we are not interested in the losses at the metal boundaries which are expected to be small compared to plasma loading. The currents along the ICH antenna are thus solved for self-consistently in the simulation. The simulation domain is divided into 3 regions with different material properties. The domain in which the antenna and coaxial structures are located has vacuum dielectric properties and is surrounded by the vacuum chamber which is also modeled as a perfect electrical conducting boundary. The region inside the vacuum region is the ceramic window, which separates the antenna from the plasma column. This region has dielectric properties of alumina with a relative permittivity of $\epsilon_r = 10.2$, and a conductivity of $\sigma = 1 \times 10^{-12}$ S/m. Finally, inside the ceramic window region is the plasma region which has dielectric properties of a Maxwellian two-species (ions and electrons) plasma, for the case of simulating a plasma or simply vacuum properties when benchmarking the 2D ICH antenna model. The dielectric properties of the plasma are described in Section 3.2. The axial ends of the simulation are terminated with second-order absorbing boundary conditions.

3.4.4 3D Helicon Antenna Model

This subsection will describe the 3D helicon antenna model. This model can also be used with the cold plasma tensor to investigate helicon physics and optimize engineering designs. However, the 3D model is more computationally intensive than the 2D axisymmetric model and presented difficulty resolving the slow-wave in a geometry large enough to study the Proto-MPEX configuration. Therefore, this model was mainly used to benchmark the analytical description of the 2D axisymmetric antenna. The current on the antenna is self consistently solved for in COMSOL after implementing a port boundary condition on the coaxial power input labeled in Fig 3.7.

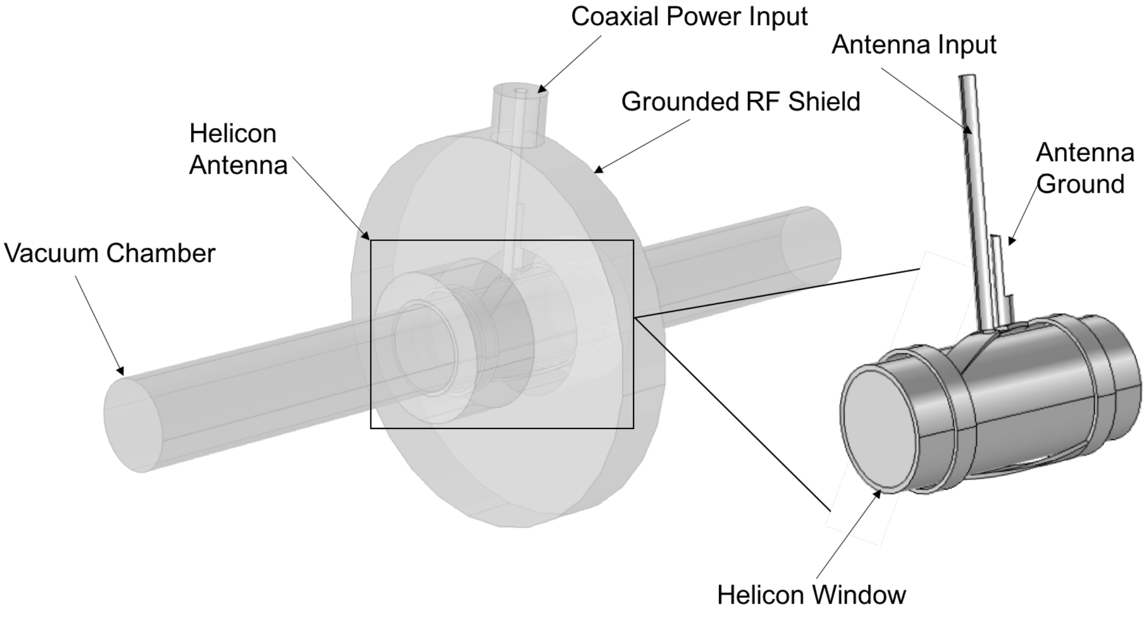

Figure 3.7: Schematic of the 3D helicon antenna model built in COMSOL Multiphysics. RF power is input in the form of a port boundary condition imposed on the Coaxial Power Input labeled and the antenna current on the helicon antenna is solved self consistently.

This geometry has essentially the same features as the 3D ICH model. The simulation is excited with a port boundary condition at the coaxial feed labeled in Fig. 3.7, which launches a coaxial TEM mode. The helicon antenna and coaxial feed structures are modeled as a perfect electrical conducting boundary. The currents along the helicon antenna are thus solved for self-consistently in the simulation. The simulation domain is divided into 3 regions with different material properties. The domain in which the antenna and coaxial structures are located has vacuum dielectric properties and is surrounded by the vacuum chamber which is also modeled as a perfect electrical conducting boundary. The region inside the vacuum region is the ceramic window, which separates the antenna from the plasma column. This region has dielectric properties of alumina with a relative permittivity of $\epsilon_r = 10.2$, and a conductivity of $\sigma = 1 \times 10^{-12}$ S/m. Finally, inside the ceramic window region is the plasma region which can have dielectric properties of plasma or dielectric properties of vacuum when benchmarking the 2D antenna model.

2D Antenna Description

The helicon and ICH antennas are described by a current imposed on a boundary at the radial location of the antenna. The current in physical space is described as a combination of the transverse current straps and the helical strap of the antenna[101]. The component of the transverse current strap is given by Eq. 3.110.

$$J_\phi^T = \frac{I_0}{2}\left(R_1(u_{\phi 1} + u_{\phi 2}) + R_2(u_{\phi 3} + u_{\phi 4})\right) \tag{3.110}$$

The first term in Eq. 3.110 describes the current ring closer to the target, and the second term describes the current ring further from the target. The current rings are described as boxcar functions in the azimuthal coordinate ϕ and in the axial coordinate z_a whose origin is at the geometric center of the antenna.

$$R_1(z_a) = H\left(\frac{L_a}{2}, \frac{L_a}{2} - R_w\right) \tag{3.111}$$

$$R_2(z_a) = H\left(\frac{-L_a}{2} + R_w, -\frac{L_a}{2}\right) \tag{3.112}$$

$$u_{\phi 1} = +H(\theta, \theta + \pi) \tag{3.113}$$

$$u_{\phi 2} = -H(\theta - \pi, \theta) \tag{3.114}$$

$$u_{\phi 3} = +H(-\theta - \pi, -\theta) \tag{3.115}$$

$$u_{\phi 4} = -H(-\theta, -\theta + \pi) \tag{3.116}$$

In equations 3.110 through 3.116 I_0 is the antenna current, L_a is the antenna length, R_w is the width of the transverse current strap, and θ is proportional to the number of helical turns (l) on the helical straps of the antenna ($\theta = \pi l$). The sign of this term also controls the directionality of the antenna; for example a helical antenna with a right handed helicity (the helicon antenna) is modeled with θ being positive, a helical antenna with a left handed helicity (the ICH antenna) is modeled with θ being negative. The helicity of the helical antenna is such that it is a quarter turn antenna this is modeled by $\theta = +\frac{\pi}{4}$, while the ICH antenna is a half turn antenna and is modeled by $\theta = -\frac{\pi}{2}$. The square function used above ($H(x)$) has properties such that:

$$H(a,b) = \begin{matrix} 1 & a < x < b \\ 0 & otherwise \end{matrix} \tag{3.117}$$

The azimuthal component of the current (J_ϕ) on the helical strap is described as:

$$J_\phi^H = I_0 \left(\delta \left(z_a + \frac{L_a}{2\theta} \phi \right) + \delta \left(z_a + \frac{L_a}{2\theta} (\phi - \pi) \right) \right) \tag{3.118}$$

The azimuthal Fourier transform of the transverse and helical current straps is then given by:

$$\bar{J}_\phi^T = \frac{I_0}{2} \frac{4i}{m\sqrt{2\pi}} \left(-R_1 e^{-im\theta} + R_2 e^{im\theta} \right) \tag{3.119}$$

$$\bar{J}_\phi^H = 2\theta \frac{I_0}{L_a} \sqrt{\frac{2}{\pi}} e^{\frac{2im\theta z_a}{L_a}} \tag{3.120}$$

The total azimuthal current of the antenna is then given by the contribution from the helical strap and the two transverse straps. To define the axial current of the helical strap we can use the divergence-free condition ($\nabla \cdot \vec{J} = 0$) which results in the following definition for the axial current.

$$\bar{J}_z = -\frac{im}{R} \int \bar{J}_\phi^H dz \tag{3.121}$$

This integration then yields:

$$\bar{J}_z = -\frac{I_0}{R} \sqrt{\frac{2}{\pi}} e^{\frac{2im\theta z_a}{L_a}} \tag{3.122}$$

Eqs. (3.119),(3.120) and (3.122) are then used in the 2D axisymmetric simulation to describe the Helicon and ICH antennas. For the 2D axisymmetric simulations, the RF Electric field is solved for assuming $m = +1$ symmetry for the Helicon and $m = -1$ symmetry for the ICH antenna. The fields are assumed to vary as $\vec{E}(r, \phi, z) = \bar{\vec{E}}(r, z)e^{-im\phi}$ for the case of the 2D simulations. The $m = +1$ mode is the dominant azimuthal mode excited by a right-handed helical antennas [102, 103] with a magnetic field oriented in $+\hat{z}$, therefore the helicon simulations only focus on the $m = +1$ azimuthal mode for the analysis of the plasma wave physics. The ICH antenna on Proto-MPEX can couple efficiently to both the $m = \pm 1$ azimuthal modes [104]. However, the $m = -1$ mode describes the left-hand polarized wave that interacts with the ion cyclotron resonance [54], it's been shown that right hand polarized waves do not interact with the ion cyclotron resonance [105] and therefore only the $m = -1$ mode is used for parameter exploration of efficient heating regimes. However, for quantitative power absorption calculations of the ICH antenna, either the 3D model or summing over both azimuthal modes should be used.

Helicon Antenna Benchmark

Benchmarking of the 2D axisymmetric helicon antenna description was an essential step in developing a 2D axisymmetric model. The 2D antenna description must adequately capture the excited k_z spectrum. When first developing the 2D simulations of the helicon antenna, higher k_z modes in the antenna near field spectrum would contribute to the excitation of slow-waves in the edge of the plasma and overestimate the amount of power deposition in the edge relative to the core. The fast-wave is expected to significantly contribute to the density production in the Proto-MPEX helicon source when operating in the “helicon-mode”, which is reliant on exciting normal-modes that are dependant on the geometry and the antenna spectrum. Thus a proper description of the antenna current was an essential step for a model that represented the Proto-MPEX helicon source.

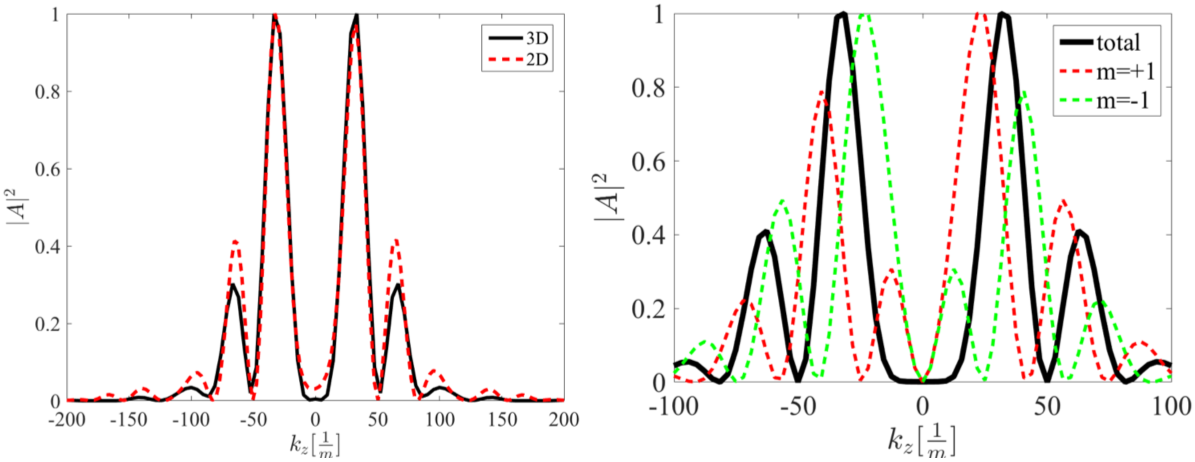

Figure 3.8: Fourier components of the vacuum B_z from the 2D axisymmetric simulation (Right) for the helicon antenna with $L_a = 25$ cm and $\theta = +\frac{\pi}{4}$. Comparison of the Fourier components of the vacuum B_z from the 2D axisymmetric simulation using the summed $m = +1$ and $m = -1$ modes of the antenna spectrum with a 3D self-consistent simulation of the helicon antenna (Left).

The vacuum spectrum of the helicon antenna from the 2D simulation with both $m = \pm 1$ modes was compared to a COMSOL 3D simulation with real antenna geometry and a self-consistent antenna current. Figure 3.8 shows the comparison of the vacuum spectra from the 2D and 3D simulations. In the 2D simulation, a damping term was added in the region where the antenna current was defined for numerical stability of the solution. Because of this damping term, the power deposition from the 2D simulation will be reported as normalized. However, this should not affect the results reported herein as the field amplitude will scale linearly with increasing power and the field profiles are not affected.

ICH Antenna Benchmark

Benchmarking of the 2D axisymmetric ICH antenna description was an essential step in developing a 2D axisymmetric model. The 2D antenna description must adequately capture the excited k_z spectrum for the ICH region. The contours of where the Alfvén resonance are located are dependant on the k_z spectrum of the antenna. The location of these contours in the plasma is critical to understanding the plasma wave physics in Proto-MPEX.

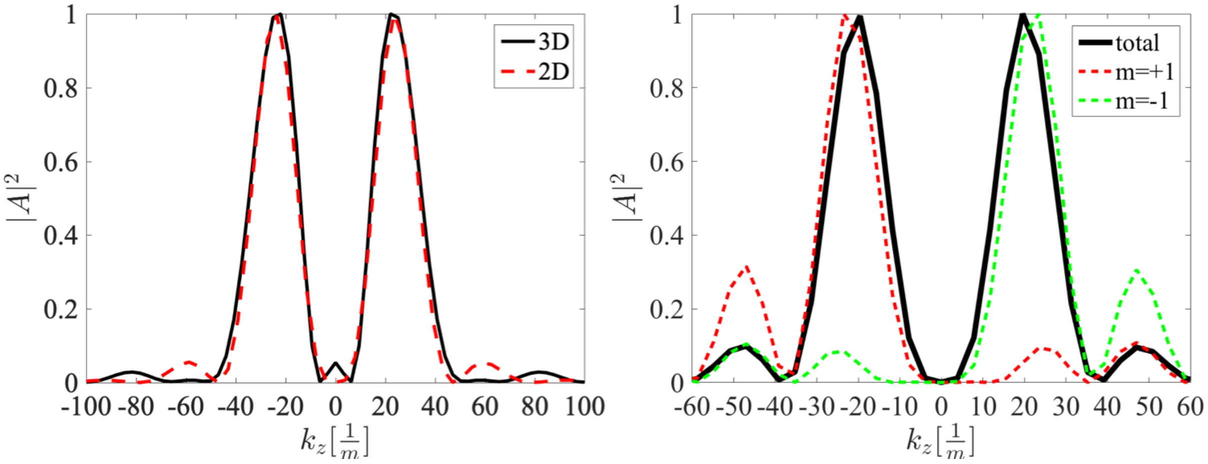

Figure 3.9: Fourier components of the vacuum B_z from the 2D axisymmetric simulation (Right) for the ICH antenna with $L_a = 25$ cm and $\theta = -\frac{\pi}{2}$. Comparison of the Fourier components of the vacuum B_z from the 2D axisymmetric simulation using the summed $m = +1$ and $m = -1$ modes of the antenna spectrum with a 3D self-consistent simulation of the helicon antenna (Left).

The vacuum spectrum of the ICH antenna from the 2D simulation with both $m = \pm 1$ modes was compared to a COMSOL 3D simulation with real antenna geometry and a self-consistent antenna current. Figure 3.9 shows the comparison of the vacuum spectra from the 2D and 3D simulations. In the 2D simulation, a damping term was added in the region where the antenna current was defined for numerical stability of the solution. Because of this damping term, the power deposition from the 2D simulation will be reported as normalized. However, this should not affect the results reported herein as the field amplitude will scale linearly with increasing power and the field profiles are not affected.

Chapter 4

Density Production by the Helicon Plasma Source

4.1 Magnetic Field Dependence

This section goes over the dependence of the helicon plasma source on the magnetic field strength. First, the motivation for operating the helicon plasma source at the higher magnetic field will be presented. The motivation can be summarized two-fold: 1) the magnetic field strength at the helicon region determines the radius of the plasma column at the target and therefore to achieve a large plasma radius the helicon will have to be operated at a higher magnetic field strength, 2) helicon plasma sources exhibit increasing ionization efficiency with magnetic field strength which will be leveraged here. Next, a discussion of the experimental evidence and numerical simulations suggesting that efficient modes of operation of the helicon plasma source are due to a reduction of mode conversion of the fast-wave to the slow-wave in the periphery of the plasma column, which allows for increased core power deposition and much larger ionization efficiency. Finally, this section will present a volume-averaged 0D model that is coupled to RF simulations of the helicon plasma source to predict electron density production in the helicon region. This coupled model predicts the trend of electron density with magnetic field strength under the helicon antenna for lower magnetic field strength; however, the second region of efficient plasma production is predicted that has not been observed experimentally. This coupled model is then used to make experimental suggestions to improve the helicon source efficiency; these suggestions include decreasing the plasma source volume by moving the dump-plate closer to the helicon antenna, floating the dump-plate to reduce power and particle losses to the target, and increasing the helicon power while operating at higher magnetic field strength to decrease the ionization cost.

4.1.1 Target Plasma Size Dependence

This subsection discusses the dependence of the target plasma size on the magnetic field strength under the helicon. The helicon window is where the magnetic flux limits in Proto-MPEX in the magnetic field configurations that are used experimentally. The consequences of this are that the magnetic field profile under the helicon antenna dictates the diameter of the plasma column at the target plate. The target plate on MPEX requires a diameter of ≈ 10 cm so that the mean free path of hydrogen and tungsten interactions with the plasma column scale in the same way as they do in the ITER divertor, and therefore these plasma-material interactions like ionization of impurities and recycling of neutral gas particles can be studied on MPEX.

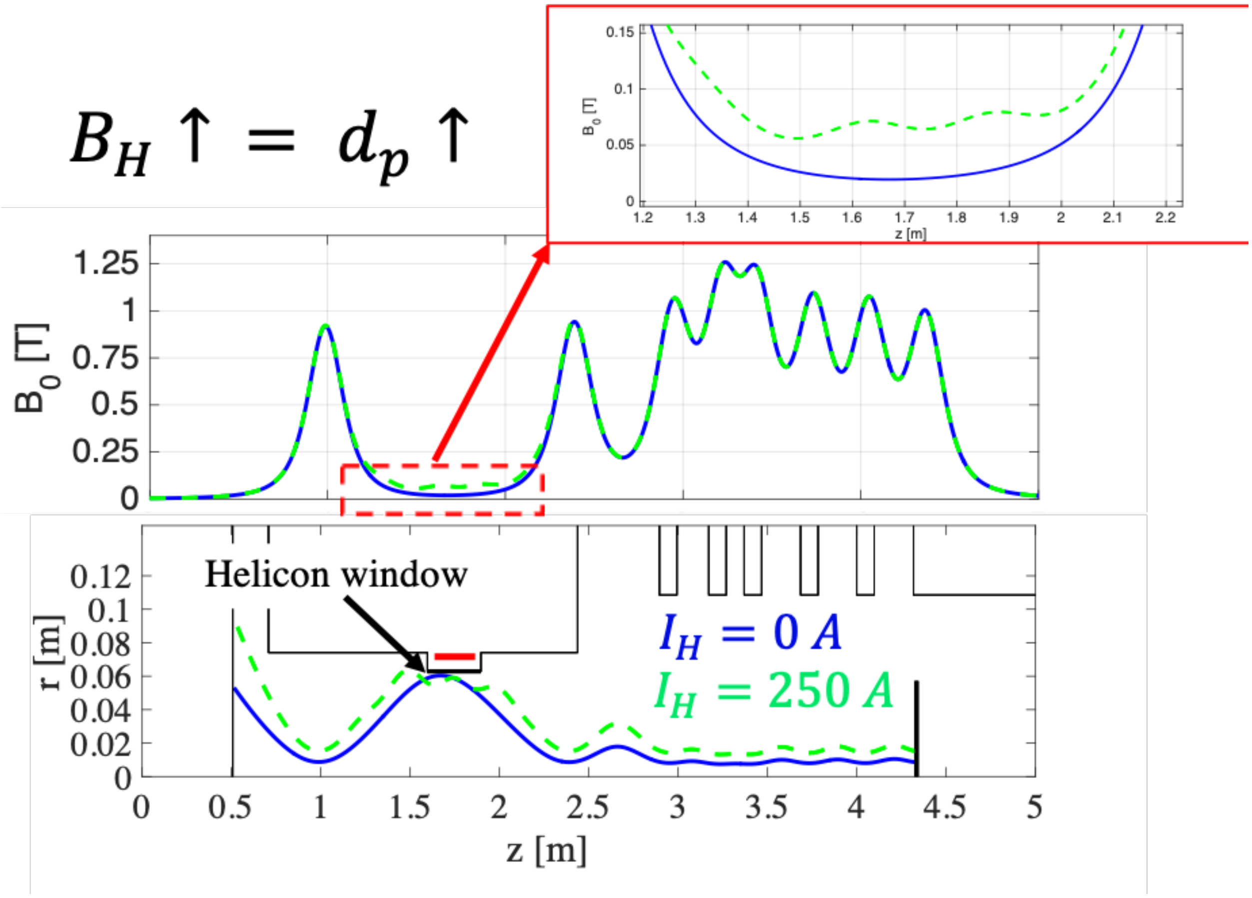

Figure 4.1: On axis magnetic field strength (top) and the limiting magnetic flux line (bottom) calculated for Proto-MPEX for 2 different currents on coil 3 and coil 4 called I_H.

Figure 4.1 shows the on-axis magnetic field strength and the limiting magnetic flux line throughout Proto-MPEX. We see that as the current for the coils in the helicon regions is increased, only the magnetic field strength under the helicon antenna is affected, but the radius of the limiting magnetic flux line downstream in the device is now at a larger radius. For MPEX to achieve the 10 cm diameter at the target in Proto-MPEX magnetic field configuration, Proto-MPEX should be able to operate at $B_H \approx 0.2$ T, while efficiently producing plasma.

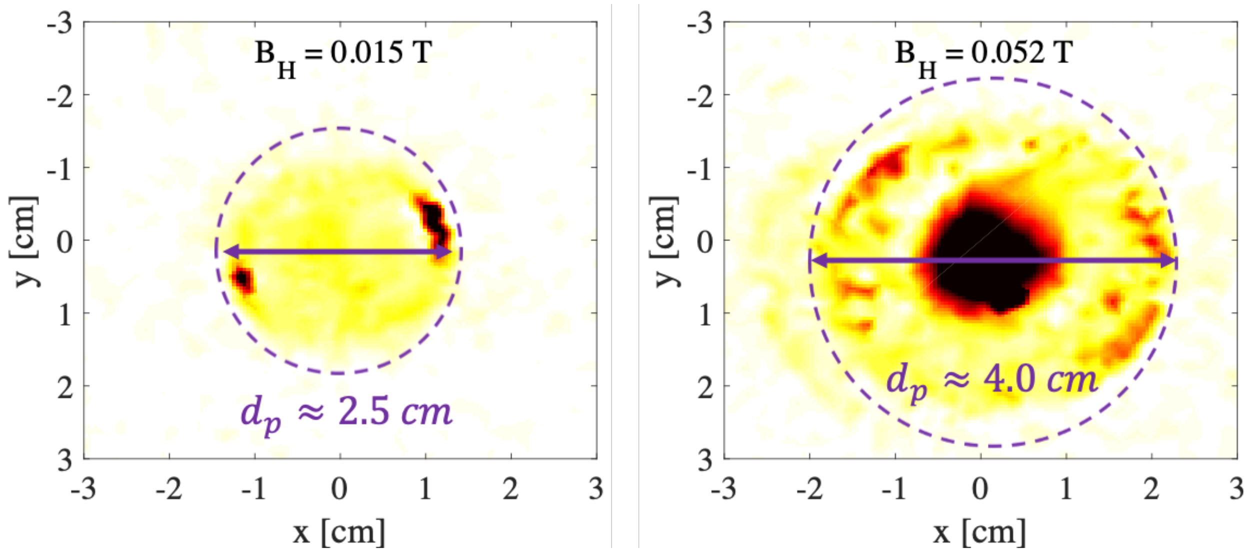

Figure 4.2: Heat flux on target when operating the helicon source at low magnetic field ($B_H = 0.015$ T) vs when operating source at a higher magnetic field ($B_H = 0.052$ T).

Figure 4.2 shows experimental evidence that the limiting magnetic flux line at the helicon window does dictate the diameter of the plasma column at the target plate. When increasing the coil currents in the magnetic field coils near the helicon antenna to increase the average magnetic field strength from $B_H = 0.015$ T to $B_H = 0.052$ T, the diameter of the plasma column, defined as where the heat flux falls $\approx 10\%$ of the value in the core, increases from $d_p \approx 2.5$ cm to $d_p \approx 4.0$ cm. Therefore, we see that operating Proto-MPEX in a higher magnetic field will be critical to achieving the plasma diameter required for MPEX.

4.1.2 Increasing Ionization Efficiency

This section will describe the observation of increasing ionization efficiency of a helicon plasma source with magnetic field strength. This trend has been observed experimentally on multiple helicon devices including Proto-MPEX when the device is operated in the ”helicon-mode”. This observation of efficient operation at high magnetic field strength is an additional motivation for operating the helicon device at higher magnetic field strengths.

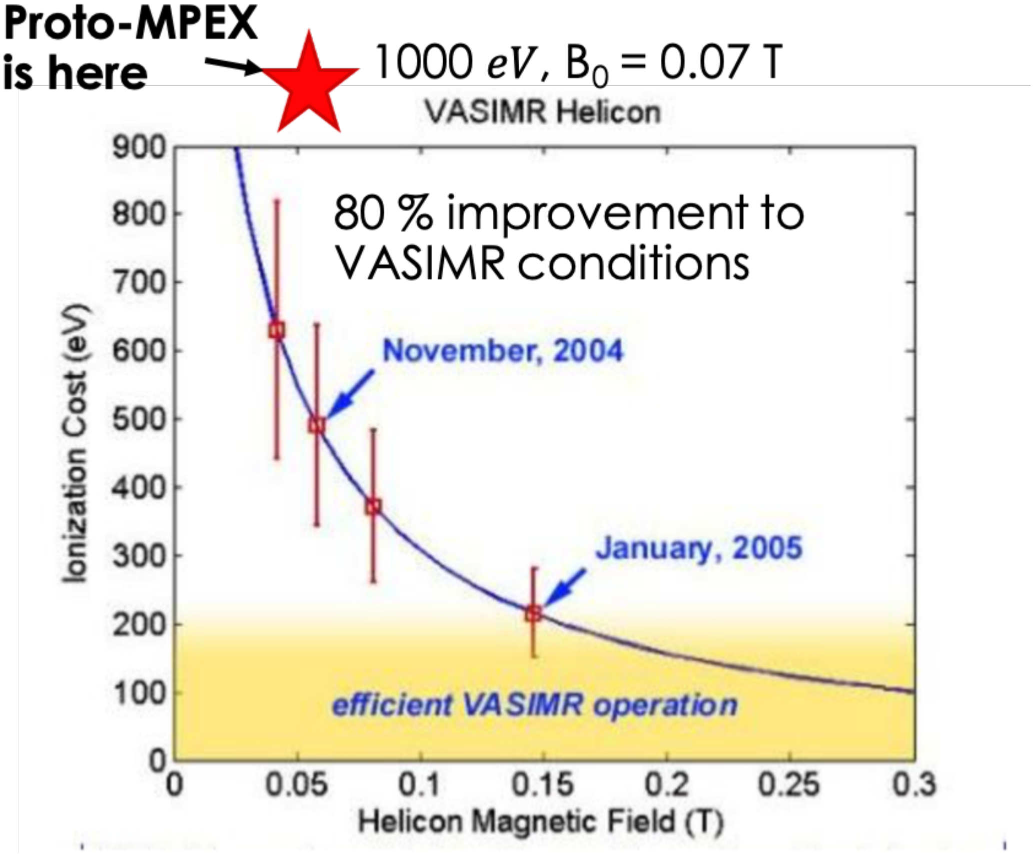

Figure 4.3: Experimentally measured ionization cost as a function of magnetic field strength under the helicon antenna from the VASIMR helicon source, the figure was published in Bering and Brukardt [1].

A device that has many similarities and inspired design choices on Proto-MPEX is the Variable Specific Impulse Magnetoplasma Rocket (VASIMR) [106, 56]. This device used a helicon to produce a high-density plasma and further heated the plasma's ions with "beach-heating" for a plasma thruster concept that is used for a space exploration concept. The VASIMR experiment's campaign focused on the optimization of the helicon for ionization cost. Ionization cost (E_{IZ}) in the sense that it is used here is the input helicon RF power divided by the integrated plasma flux away from the helicon plasma source:

$$E_{IZ} = \frac{P_{RF}}{\int_A \Gamma_i dA} \tag{4.1}$$

This definition of ionization cost gives an experimental metric to understand the energy used to create an electron-ion pair and accelerate it to the target region, or in VASIMR's case the exhaust of the plasma thruster. The measured ionization efficiency in VASIMR's helicon source is shown in Fig. 4.3 as a function of magnetic field strength under the helicon antenna. From this figure, we see that VASIMR has achieved dramatic improvements in the efficiency of their helicon source that was observed when operating the helicon plasma source at higher magnetic field strengths.

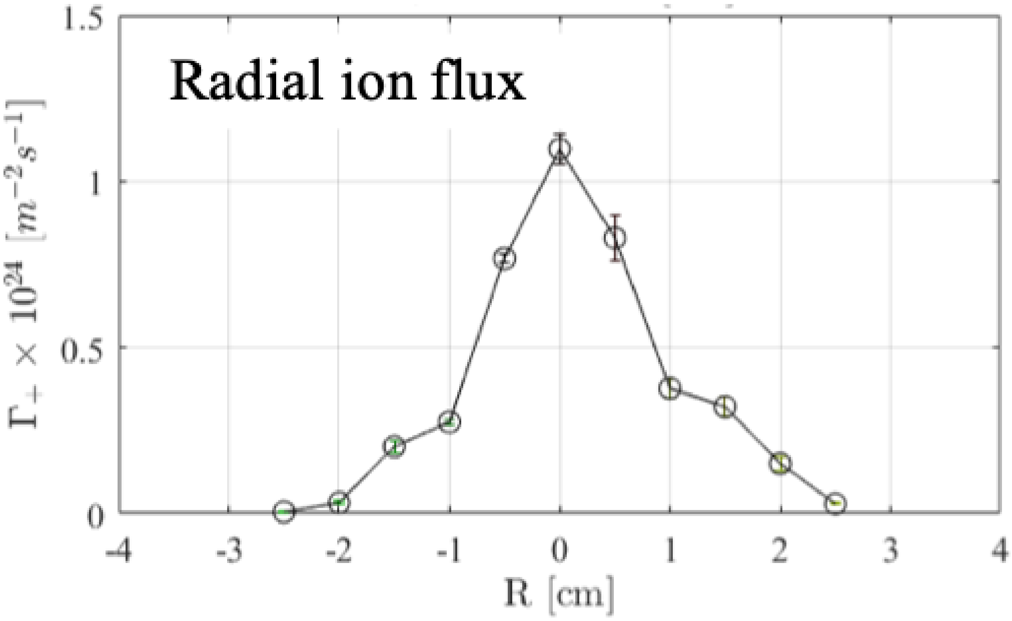

Figure 4.4: Ion flux measured with a flux probe across the radius of the plasma column in Proto-MPEX.

A radial scan of the measurements of plasma flux on Proto-MPEX is shown in Fig. 4.4. These measurements indicate that Proto-MPEX operates with a plasma flux that peaks at $\Gamma_i \approx 1 \times 10^{24}\ m^{-3}$ and has the same radial profile as the electron density. Assuming an azimuthally symmetric plasma and integrating this plasma flux to calculate the total amount of ions per second moving from the source to the target as:

$$S_i = \int_0^R (2\pi r)\Gamma_i dr \tag{4.2}$$

With a total forward power of $P_{helicon} = 85$ kW for these flux measurements, the ionization cost of the Proto-MPEX helicon source is $E_{IZ} \approx 1000\ \frac{eV}{ion}$, when operated at a magnetic field strength of $B_0 = 0.06$ T. The region of operation where Proto-MPEX is currently operating, compared to VASIMR is shown by the red star in Fig. 4.3. From this figure, we see that improvements in source efficiency can be made to

Proto-MPEX, and have been achieved practically on VASIMR.

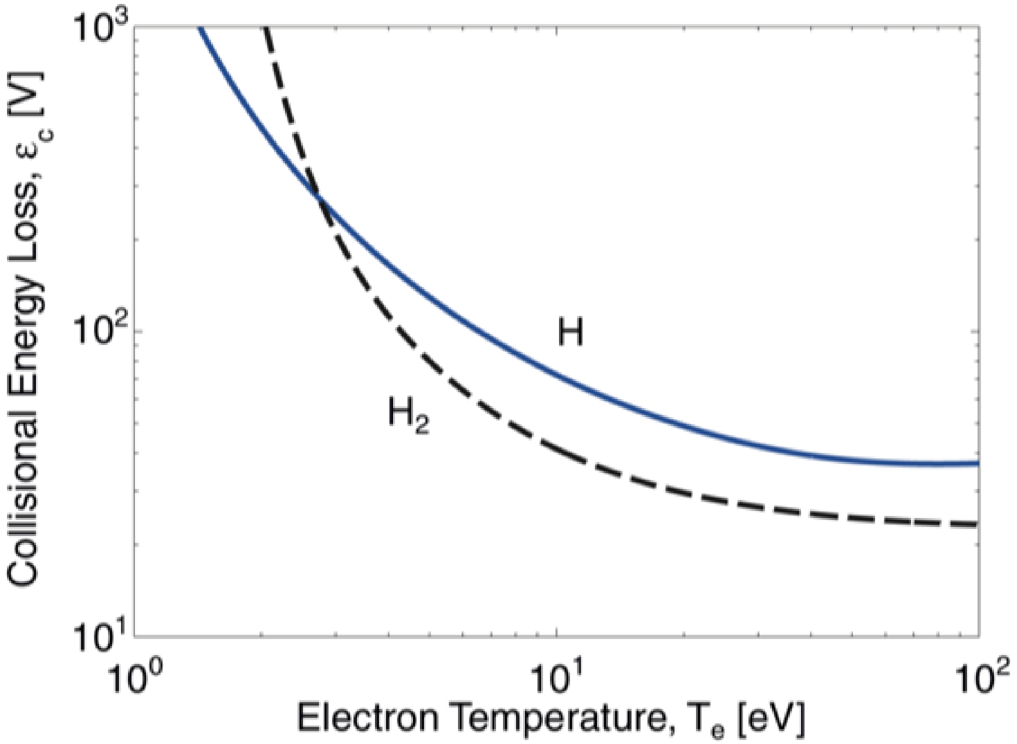

Figure 4.5: Collisional energy loss per ionization event as a function of electron temperature. Figure is taken from Samuell et. al. [2].

Figure 4.5 shows a figure of the energy lost per electron-ion pair generated (ϵ_C). This is calculated and reported in Samuell et. al. [2] by considering the energy to ionize a neutral particle, and all the avenues by which energy is dissipated, and can be calculated as:

$$\epsilon_C^{(\chi)} = \epsilon_{IZ}^{(\chi)} + \epsilon_{el}^{(\chi)} \frac{k_{el}^{(\chi)}}{k_{iz}^{(\chi)}} \frac{3m_e}{m^{(\chi)}} kT_e + \sum_i \epsilon_{ex,i}^{(\chi)} \frac{k_{ex,i}^{(\chi)}}{k_{iz}^{(\chi)}} \tag{4.3}$$

where $\epsilon_C^{(\chi)}$ is the ionization energy of species χ, and $\epsilon_{ex,i}^{(\chi)}$ and $k_{ex,i}^{(\chi)}$ are the excitation threshold energy and rate coefficient for the i^{th} excitation process of species χ respectively, $k_{el}^{(\chi)}$ is the elastic rate coefficient of species χ. This calculation then shows us the theoretical minimum ionization cost of hydrogen. Which we see for hydrogen gas at a high electron temperature ($T_e > 40$ eV) the ionization cost of hydrogen is $\epsilon_C < 40$ eV. With the electron temperatures achieved experimentally in Proto-MPEX $T_e = 2 - 5$ eV, the ionization is $\epsilon_C = 100 - 600$ eV. Therefore, if we do not lose ions to any other process this is the minimum ionization cost per ion created in Proto-MPEX.

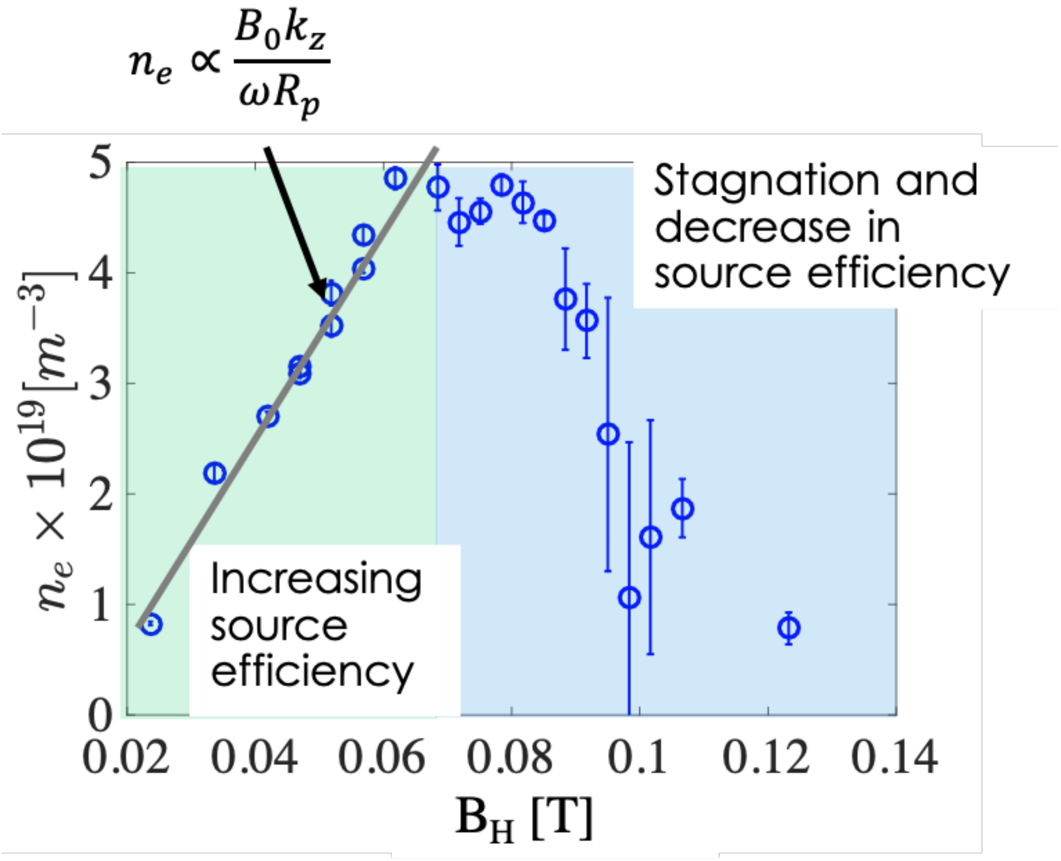

$$n_e \propto \frac{B_0 k_z}{\omega R_p}$$

Stagnation and decrease in source efficiency

Increasing source efficiency

Figure 4.6: Electron density produced by the helicon plasma source as a function of magnetic field strength under the helicon antenna.

Figure 4.6 shows the measured electron density in Proto-MPEX as a function of magnetic field strength. This figure shows that for the case of low magnetic field strength, $B_0 < 0.07$ T, there is an observed linear scaling of electron density with magnetic field strength. The ion flux was not measured as a function of magnetic field strength for this set of experiments, however, the increasing electron density does indicate that the ionization cost is decreasing in Proto-MPEX as a function of magnetic field strength in the case of the lower magnetic field strength. At the higher magnetic field strengths, $B_0 > 0.07$ T, in Proto-MPEX we see that the helicon source begins to stagnate and electron density does not increase as a function of magnetic field strength. Ultimately, the electron density production begins to degrade as a function of magnetic field strength and a decrease in peak electron density is observed.

4.1.3 Discussion

This section outlined the motivation for operating the helicon plasma source at higher magnetic field strength. This motivation is two-fold. Firstly, MPEX requires a plasma diameter of $d_p \approx 10$ cm so that the mean free path to characteristic device size of different plasma-material interactions, such as the ionization of deuterium neutralized at the target, and tungsten sputtered from the target is similar to that of an ITER relevant divertor plasma. Therefore, the size of the plasma column on MPEX is critical to the ability to study fusion-relevant plasma-material interactions on the device. Establishing the importance of the plasma diameter for MPEX, we then show that the magnetic field strength under the helicon antenna dictates the diameter of the plasma column at the target. This is because the magnetic flux lines limit at the helicon window, for typical operating conditions, and thus a higher magnetic field strength under the helicon window allows for a larger plasma diameter at the higher magnetic field strengths at the target. So operating the helicon plasma source at magnetic field strengths of $B_0 \approx 0.2$ T are required to achieve a plasma diameter of $d_p \approx 10$ cm on Proto-MPEX. The second motivation for operating the helicon plasma source at higher magnetic field strength on Proto-MPEX is to achieve more efficient plasma production. This section described the increase of electron density production of helicon plasma sources that were observed with helicon magnetic field strength for both the VASIMR and Proto-MPEX helicon sources. The concept of ionization cost was introduced in this section and thus sets a metric for normalizing source performance and comparing the helicon plasma source on Proto-MPEX to other plasma sources. The ionization cost of Proto-MPEX is estimated, by azimuthally integrating a radial scan of measured ion flux as measured by a flux probe, to be $E_{IZ} \approx 1000 \ \frac{eV}{ion}$. This ionization cost is compared with VASIMR's helicon source performance, which indicates that there is room for practical improvements to the Proto-MPEX helicon plasma source.

4.2 The Role of Core Power Deposition

This section describes the evidence, both experimental and numerical, that core power deposition by the fast-wave is the reason for the experimental observations of increases in helicon performance. This will be a critical assumption to assess helicon performance and perform the coupling of the RF simulations to a 0D model in the following section. First, experimental evidence of target heat flux measurements showing a transition from edge to core power coupling is shown in concurrence with B-dot probe measurements showing an increase in RF magnetic field energy in the core plasma and a decrease in the edge plasma. Because the fast-wave is the only wave that allows energy to access the core plasma, we conclude from this evidence that increasing the coupling of the helicon antenna to the fast-wave is responsible for the transition of edge to core power. Next, we show RF simulations of numerical evidence of operational regions of increased power deposition that depend on electron density and magnetic field strength under the helicon antenna. Inspecting the RF signature of the simulations with increased core power deposition vs those with less core power deposition, a trend is observed where simulations that indicate higher core power deposition shows a magnetic field signature that is interpreted as a fast-wave reflection from the magnetic mirror and formation of cavity-like structures in the helicon region. The simulations that indicate lower core power deposition show minimal reflection from the mirror region and only significant magnetic energy is shown in front of the antenna. The power deposition profiles of these two simulation cases show that the simulations with more core power deposition show that there is power deposition throughout the volume under the helicon antenna, while the simulation with minimum core power deposition shows that there is only core power deposition in front of the antenna. Comparing the edge power deposition in both simulation cases we see that the case of strong power deposition lacks edge power deposition away from the antenna, in the downstream magnetic mirror region, while the case of low power deposition shows significant power deposition in that region. We conclude that the increased core power deposition is likely due to excitation of fast-wave normal modes in the plasma column which are enabled due to the suppression of mode-conversion of the fast-wave to the slow-wave in the mirror regions of the plasma column. Instead of the mode-conversion of the fast-wave to the slow-wave, a reflection of the fast-wave off of the magnetic mirror is achieved leading increased core power deposition.

4.2.1 Experimental Evidence for Strong Power Deposition

The experimental observations described in this section show that a transition of power coupling from edge to the core is simultaneously accompanied by the formation of a fast-wave radial eigenmode. These observations are reminiscent of theoretical predictions made by Ref. [37], which predicts anti-resonance regimes of the fast and slow waves in the analytic treatment of a homogeneous plasma column bounded by a dielectric gap and outer conductor. In this condition, the RF fields of the wave in anti-resonance are reduced and less power is absorbed by the plasma from that wave. Therefore, a slow-wave anti-resonance result in a reduction in edge power deposition which allows for more energy available to the fast-wave, which would cause increased core power deposition. In a more complicated picture of a plasma column with a density gradient the slow-wave anti-resonance can be understood as a reduction of non-resonant mode conversion to the slow-wave by the reduction of the fast-wave amplitude at the edge of the plasma column, this process is explained in Ref. [42].

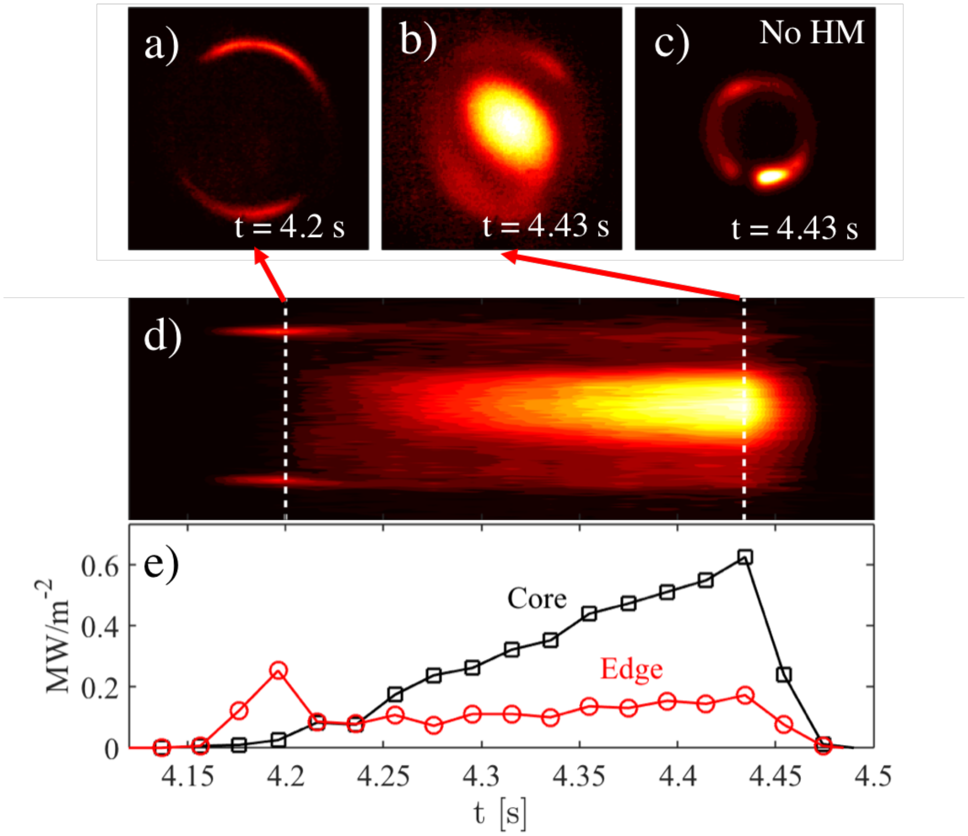

Figure 4.7: Heat flux to the target inferred from IR thermography (a) at the start of the RF pulse ($t = 4.2$ s) and (b) at the end of the RF pulse ($t = 4.43$ s). The length scale of the y-axis and x-axis is 4 cm across the image. Parts (a), (b), and (d) are the same discharge. Part (c) shows the end of the RF pulse ($t = 4.43$ s) in a condition where the discharge did not transition to core power deposition. Part (d) shows the time evolution of the heat flux to the target. Part (e) shows the time evolution of the heat flux to the target at the core (center of image) and an edge (location of the largest heat flux at $t = 4.2$ s).

The heat flux to the target plate is shown in Fig. 4.7. The two-dimensional distribution of the heat fluxes at the start and end of the RF pulse are shown in panels (a) and (b) respectively. At the start (end) of the RF pulse, the heat flux is dominated by power deposition at the edge (core) of the plasma column. As is evident in panel (d), a transition is observed at approximately $t = 4.25$ s where the edge power deposition is suppressed and the core deposition begins to dominate. At the end of the pulse, the core power deposition is clearly dominant and delivers up to 0.6 MWm^{-2} to the target plate. Extensive experimentation using 100 kW of helicon power has shown that this edge-to-core transition can be reliably produced on demand provided that (a) the neutral gas is puffed at the location of the antenna about 300 ms before the RF pulse, (b) the neutral pressure before breakdown is $2 - 3$ Pa and (c) the discharge is at least 100 ms in duration.

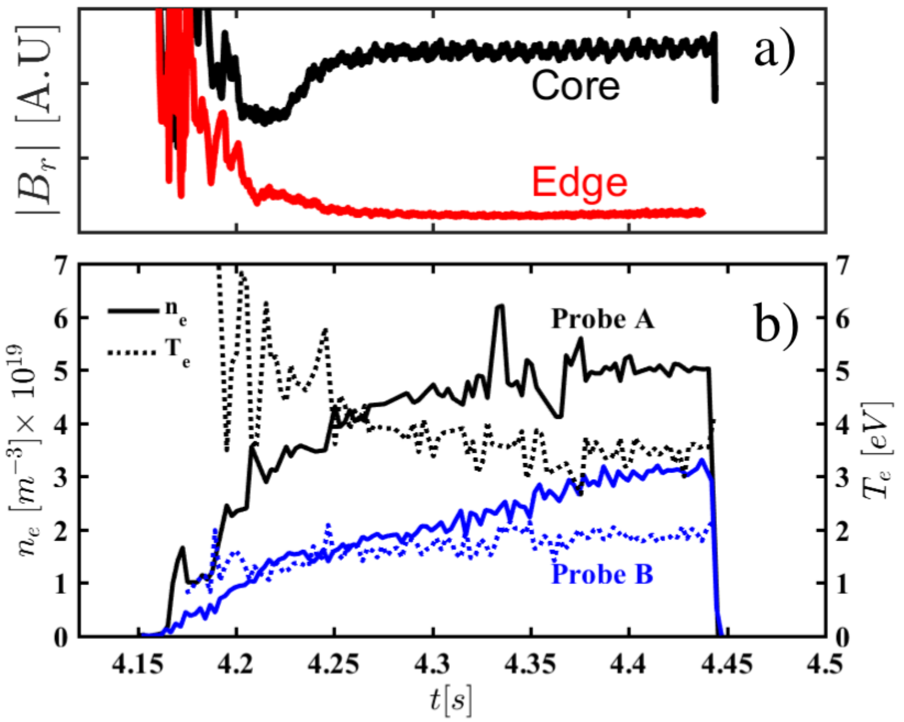

Figure 4.8: (a) B_r component of the fast-wave measured near the helicon antenna (location A) on-axis (black) and at the edge (red) of the plasma column. (b) On-axis electron density (solid line) and temperature (dotted line) measured at Spool 9.5 (black), and Spool 4.5 (blue).

At the time of the increased core power coupling, measurements performed near the helicon antenna (location A) with RF magnetic (B-dot) probes indicate: (1) an increase in fast-wave energy density in the core plasma and (2) the formation of a fast-wave radial eigenmode. Presented in Fig. 4.8 a) is the magnitude of the B_r wavefield component on axis and at the edge of the discharge. Conditions are identical to those associated with Fig. 4.7. At the same time as the transition from edge-to-core power deposition as seen in Fig. 4.7, the on-axis RF magnetic energy $|B_r|^2$ increases while the edge magnetic energy decreases. Figure 4.8 b) shows on-axis electron density and temperature measurements at Spool 9.5 and Spool 4.5. From this, we can see that once the core heating is established, there is a correspondingly high plasma density at the source and the target location.

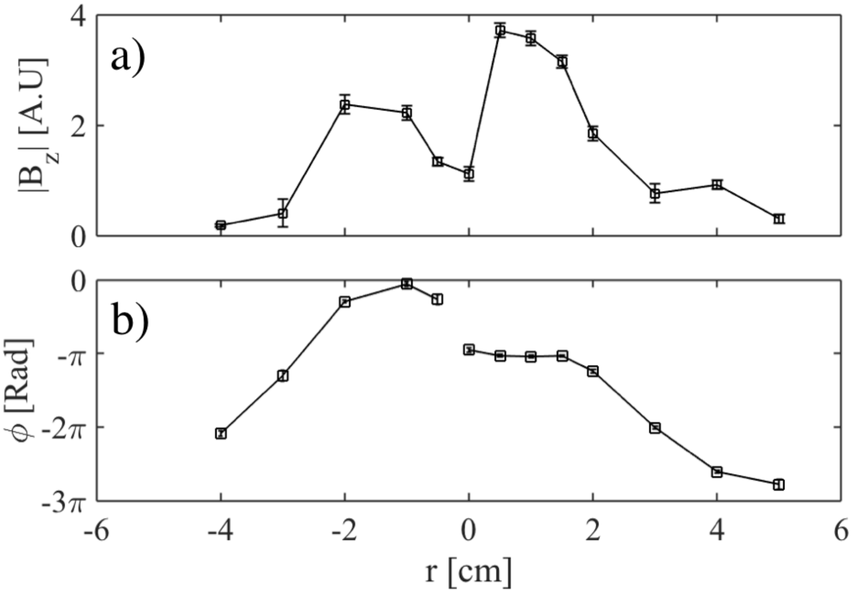

Figure 4.9: Radial variation of B_z measured with RF (B-dot) probe at location A at the end of a 150 ms RF pulse, (a) magnitude and (b) phase. The DC magnetic field at the source and target are 0.05 T and 0.6 T respectively, D_2 gas is injected at Spool 4.5.

Figure 4.9 presents a radial scan of the B_z component of the fast-wave measured near the helicon antenna (location A) during a core-heated discharge. Experimental conditions are similar to those associated with Figure 4.7. The measurements in Fig. 4.9 indicate the presence of a radial eigenmode: (a) the radial variation of the magnitude displays the characteristic bimodal shape of the B_z (m = +1) component of the helicon mode and (b) the radial phase variation has the characteristic 180 degrees phase shift on-axis. It is worth noting that before the edge-to-core transition or when this transition does not occur, both the amplitude and phase of the RF wave fields are strongly fluctuating and no clear indication of a radial eigenmode is observed.

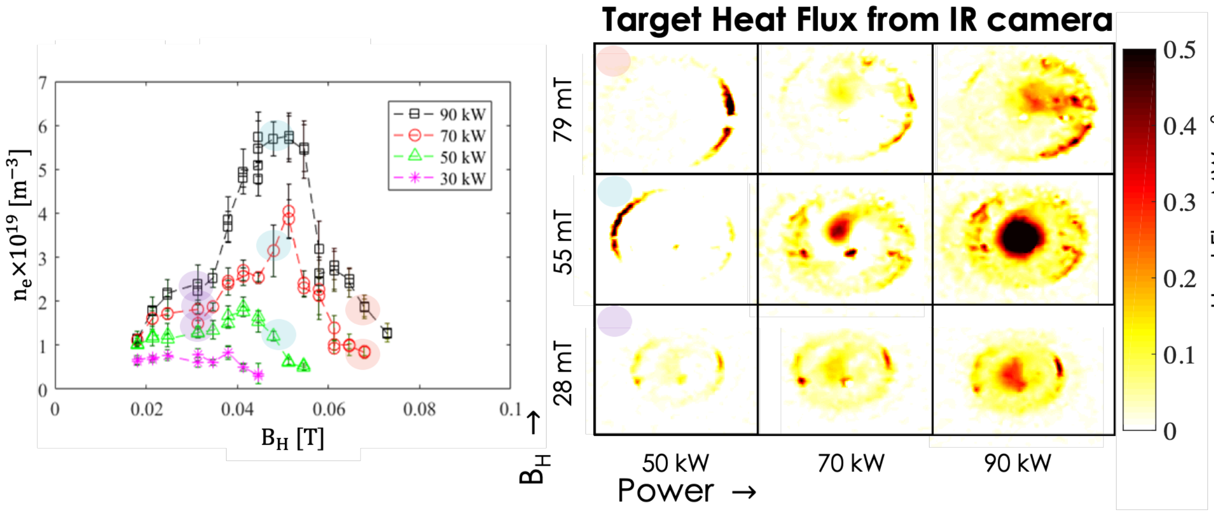

Figure 4.10: Peak electron density measured in Proto-MPEX as a function of magnetic field strength for several power levels (left), corresponding points of steady-state heat flux at different magnetic field strengths and power levels (right).

Finally, the evidence is shown in Fig. 4.10 that the core power deposition in Proto-MPEX has a dependence on magnetic field strength as well as RF power applied. This figure presents electron density measured at several power levels and an array of steady-state 2D images of heat flux to the target for several points at different magnetic field strengths and power levels. This figure shows that core power deposition has a dependence on magnetic field strength and applied RF power. In the previous figures, we showed that strong core power deposition is accompanied by increases in RF energy in the core plasma and decreases of RF energy in the edge, as well as eigenmode formations in the RF magnetic field profile across the radius of the plasma column. This was used as evidence that the excitation of helicon normal modes, which we will show in the next section correspond to conditions that suppress mode conversion of the fast-wave to the slow wave in the periphery of the plasma column, is responsible for the increased core power deposition. Helicon normal mode dependence on magnetic field and power can be explained by inspecting analytic form of the eigenmode condition which satisfies the bounded dispersion condition given by Eq. 4.4.

$$J'_m(k_\perp R_p) + \frac{m}{k_z R_p} J_m(k_\perp R_p) = 0 \tag{4.4}$$

$$k_\perp = \frac{\omega_{pe}^2}{\omega \omega_{ce}} \frac{k_0^2}{k_z} \tag{4.5}$$

The plasma frequency is ω_{pe}, k_0 is the vacuum wavenumber, m is the azimuthal mode, and k_z is the axial wavenumber of the eigenmode, J_m is the m^{th} order Bessel function, and $J_m(x)'$ is the derivative of $J_m(x)$. Eq. 4.5 can then be rearranged as:

$$n_e = \frac{c^2\epsilon_0}{q}\left(\frac{B_0 k_z}{\omega R_p}\right)\left(p_{mi} - \frac{k_z R_p}{m}\right) \tag{4.6}$$

This rearranged dispersion relation shows the dependency $n_e \propto \frac{B_0 k_z}{\omega R_p}$. This dependency says that to excite helicon normal modes, electron density must increase proportionally to magnetic field strength under the helicon antenna. However, the production of electron density under the helicon antenna is also dependant on particle and power balance in the source volume, therefore if there isn't sufficient power to produce the electron density required to sustain the $n_e \propto \frac{B_0 k_z}{\omega R_p}$ proportionality, then the helicon plasma source falls off from regions where core power deposition is optimal. The edge power deposition is increased, and the power deposition at the periphery of the plasma column typically is subject to stronger losses to the walls and flux limiting surfaces.

4.2.2 Numerical Simulations of the Source Region

Throughout this section, the results of an electromagnetic 2D axisymmetric simulation of the helicon antenna on Proto-MPEX are described and discussed. The 2D analytic antenna description represents the realistic antenna geometry as shown by comparison with a self-consistent vacuum simulation of the real geometry of the 3D antenna. The electron density profile used varies axially as a function of the magnetic flux. With this model, contours of maximum core power deposition in the parameter space of peak electron density and magnetic field strength are identified and shown to take on a linear trend. The linear trend of these contours is proposed to be due to normal modes in this parameter space and is predicted by Eq. 4.6. The normal mode solutions responsible for these contours in the experimentally relevant parameter space are analyzed. The RF field and power deposition profiles of a normal mode solution are compared to a TG mode solution (point of minimum core power deposition).

Dispersion Analysis

Dispersion analysis is critical to understanding the behavior of plasma waves in simulation and experiment. Interpretation of the wave physics in these in-homogeneous materials requires a good understanding of the conditions where waves experience cut-offs and resonance and their regions of propagation. The plasma dispersion relation in the cold plasma approximation takes the form of a bi-quadratic and therefore, predicts the propagation of two separate wave branches. In the helicon region of Proto-MPEX, these wave branches are separated in the electron density they can propagate in, the slow-wave or as commonly referred to for helicon plasma sources the Trivel-Piece Gould mode propagates at low densities that are in the periphery of the plasma. This wave also has a narrow group velocity, and therefore it's energy is confined to the periphery of the plasma. The fast-wave, also called the helicon wave in helicon plasma sources, propagates in the higher electron density region, which is typically in the plasma core. The cold plasma dispersion relation can be written for the perpendicular wavenumber as a function of the parallel wavenumber, electron density, magnetic field strength, and the driving frequency [87]. The expected parallel wavenumber propagating in the plasma can be estimated by the vacuum spectrum of the antenna [107], and is assumed here to be $k_{\parallel} = 20\ m^{-1}$, which is the peak of the antenna spectrum.

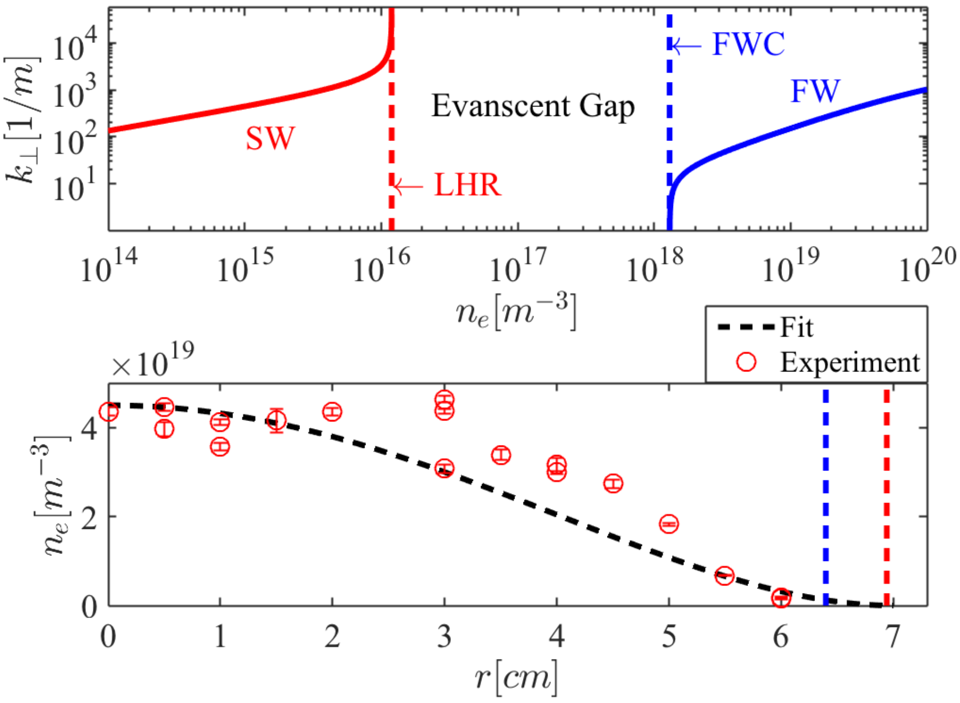

Figure 4.11: (Top) Transverse wavelength of the slow-wave (SW) and the fast-wave (FW) calculated from the cold plasma dispersion relation assuming $k_z = 20\ m^{-1}$, $B_0 = 0.05$ T, and atomic deuterium ions. (Bottom) Electron density radial profile measured at Spool 4.5. The radial locations of the lower hybrid resonance (LHR) and the fast-wave cutoff (FWC) are shown assuming a density profile fit of $n_e(r) = n_e^{max}\left(1-(r/R_p)^2\right)^2 + n_e^{edge}$ where $n_e^{max} = 4.5 \times 10^{19}\ m^{-3}$, $n_e^{edge} = 1 \times 10^{16}\ m^{-3}$, and $R_p = 7$ cm.

Figure 4.11 displays (a) the cold plasma dispersion relation relevant to Proto-MPEX's helicon experimental conditions. The real part of $k_\perp$ is plotted as a function of electron density and (b) a typical radial electron density profile associated with Fig. 4.11 measured at the helicon source (location A). Since the lower hybrid resonance (LHR) restricts the propagation of the slow-wave to the edge region where the electron density is less than $n_e < 10^{16}\ m^{-3}$, any power deposition and/or RF wave fields in the plasma core must be attributed to the fast-wave. Since the discharge equilibrium after the transition satisfies Eq. 4.4 for RF B_z component and the dispersion relation only allows the propagation of the fast wave inside of the core plasma we believe that the plasma production is fast-wave dominated and call this a "helicon-mode" discharge.

Figure 4.12 shows contours of where the perpendicular wavelength of the slow-wave (red) and the fast-wave (blue) is real. These are solved assuming a parallel wavelength of $k_z = 20\ m^{-1}$, a driving frequency of $\omega = 13.56$ MHz, an electron density profile defined by Eq. 3.104 using $n_{e_{peak}} = 2.7 \times 10^{19}\ m^{-3}$, and the magnetic field is calculated from Ampere's law from the experimental magnetic coil geometry with $I_H = 260$ A.

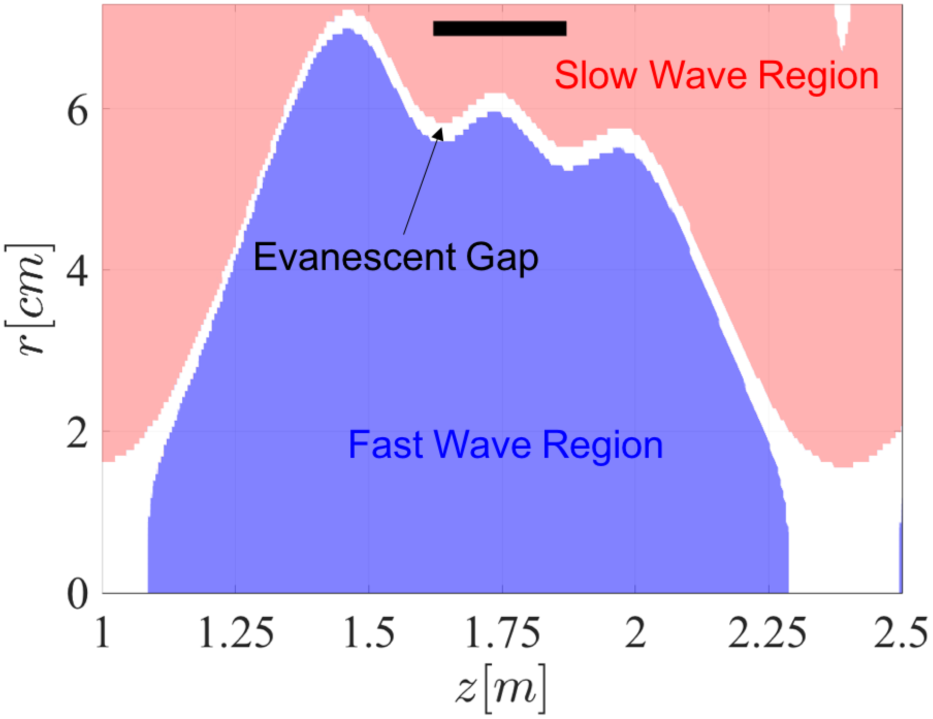

Figure 4.12: Contours of perpendicular wavelength ($k_\perp$) solved for from the cold plasma dispersion relation assuming $k_z = 20\ m^{-1}$ and electron density defined by Eq. 3.104 using $n_{e_{peak}} = 2.7 \times 10^{19}\ m^{-3}$. The magnetic field is solved for with $I_H = 260$ A. The blue contour represents where $k_\perp$ for the fast-wave solution is non-zero. The red contour represents where $k_\perp$ for the slow-wave solution is non-zero. The evanescent region, $k_\perp = 0$ for both waves, is represented by the white contour. The location of the helicon antenna is represented by the thick black line.

From Fig. 4.12 it is clear that the fast-wave does not propagate past the magnetic mirror region and is contained to the high electron density region $n_e > 1e18\ m^{-3}$. The slow-wave is contained to the low electron density region $(n_e < 1e16)\ m^{-3}$ of the plasma column. The slow-wave encounters the lower hybrid resonance along the electron density gradient and therefore does not propagate inside the plasma column. The fast-wave encounters a cut-off where $k_\perp = 0$ along the electron density gradient and along the magnetic field gradient. This cut-off along the magnetic field gradient restricts the fast-wave to the region between the magnetic mirrors and effectively creates a cavity for the fast-wave.

Collisions

An important consideration in Proto-MPEX is the high collision frequency due to Coulomb collisions and is thought to be primarily responsible for wave damping and smearing of the resonant behavior of the waves which will be discussed next. The damping mechanism of the fast-wave in helicon sources has been a point of discussion in literature [108, 109, 110]. However, with the high electron density and relatively low electron temperature produced in Proto-MPEX, it is a good candidate to be the dominant mechanism of power coupling to the electrons. Collisional damping and isotropic heating of electrons by the fast-wave is typically not considered an efficient mechanism to heat electrons.

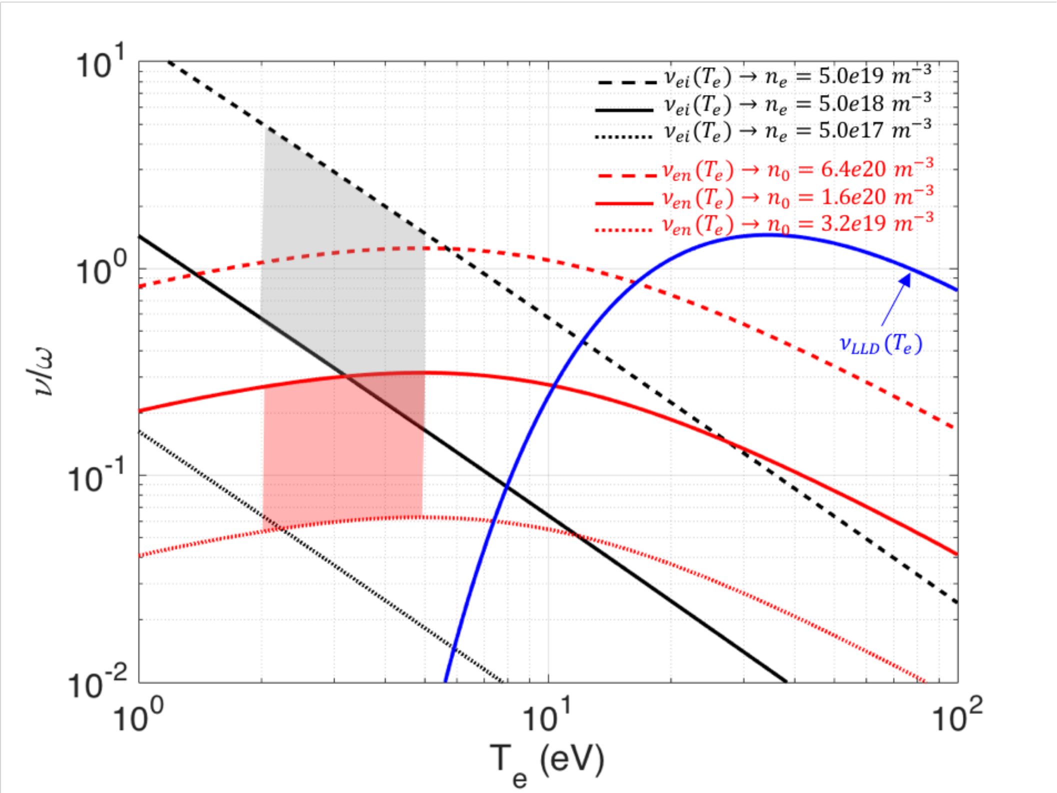

Figure 4.13: Normalized collision frequency as a function of electron temperature (T_e) for electron-ion Coulomb (black) and electron-neutral (red) collisions. The effective collision frequency for linear electron Landau damping is given by the blue curve. The highlighted regions show the relevant regions for Proto-MPEX conditions.

Figure 4.13 shows the normalized collision frequencies calculated, for electron-ion Coulomb and electron D_2 neutral collisions, as a function of electron temperature. The effective collision frequency for linear electron Landau damping [111] is also shown in this figure. From this figure, we see that for the conditions present in Proto-MPEX ($n_e \approx 5\times10^{19}\ m^{-3}$, $T_e < 10$ eV) Coulomb collisions are the dominant linear damping mechanism for coupling power from the fast-wave to the electrons. Several authors were able to explain the damping of the fast-wave in high-density light-ion plasmas with calculated collisional damping given by electron neutral and Coulomb collisions [112, 34, 107]. In this work, we follow these authors approach and only consider linear damping of the wave by collisional damping. However, since diagnostic access limits accessing the region directly under the helicon antenna, measurements of the gradients of electron density and temperature in this region are absent. This leaves the possibility of electron temperature increasing to values where collisional damping is no longer an effective damping mechanism of the fast-wave. Non-linear heating mechanisms, such as the parametric decay of the fast-wave into electron plasma and ion-sound waves [113, 110], have also been proposed to heat electrons in helicon sources. Ref. [113] estimates that the damping of the fast-wave due to excitation of ion-sound turbulence and subsequent turbulent electron heating is more effective at transferring fast-wave power to the electrons than Coulomb collisions for the experimental conditions reported in Ref. [114]. Such mechanisms have not yet been explored in light-ion helicon sources. The ion mass dependence of these parametric instabilities seems to increase its effective collision frequency, so they might be an important damping mechanism for light-ion helicon sources.

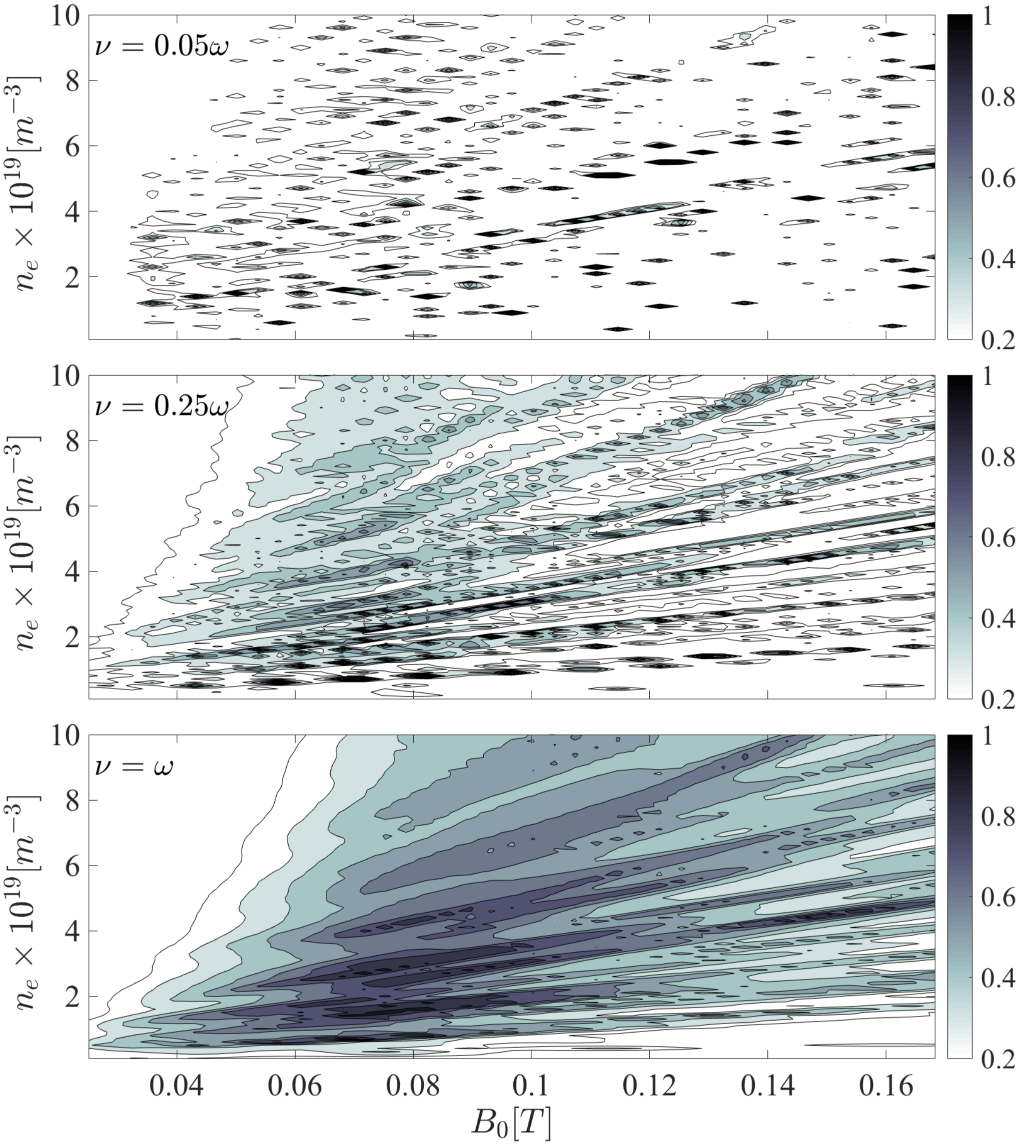

Figure 4.14: The effect of increasing collision frequency on the contours of core power deposition. Top $\nu = 0.05\omega$, middle $\nu = 0.25\omega$, bottom $\nu = \omega$. The contours show the normalized power deposited in the core.

Throughout this section, the normalized core power deposition is used as the figure of merit for identifying solutions that are normal modes of the plasma column. The core is defined as the region where $\chi < 0.5$. Fig. 4.14 shows how increasing the collision frequency (ν) reduces the sharpness of the power deposition peaks until they are destroyed. The collision frequency broadens the power deposition peaks because normal mode behavior in the discharge relies on the waves excited from the antenna to interfere constructively on-axis. If the collision frequency is high enough the wave excited by the antenna damps before it can interfere constructively on-axis. To identify the experimentally relevant normal modes the collision frequency will be held at a constant value of $\nu = \omega$, where ω is the driving frequency of the antenna, for the remainder of the analysis. At this value of ν, the higher order k_z modes from the antenna spectrum are damped such that they do not contribute to the core power deposition but the main spectral features can still form normal modes, and structure in the core power deposition plots is still observed in Fig. 4.14.

Identifying Normal Mode Solutions

Understanding how the antenna couples power to the steady-state plasma is important for predicting the density limitations of the helicon source. Light ion helicon authors have attributed successful high electron density production to excitation of helicon normal modes in the plasma column [3, 43]. In Ref. [42] it is described that in a more complicated geometry resonant behavior of the fast-wave does not exist. However, the bounded dispersion relation derived by this approach predicts anti-resonance regimes of the slow-wave. In anti-resonance, the non-resonant mode conversion of the fast-wave to the slow-wave is suppressed. This condition allows the fast-wave to couple increased power into the core plasma.

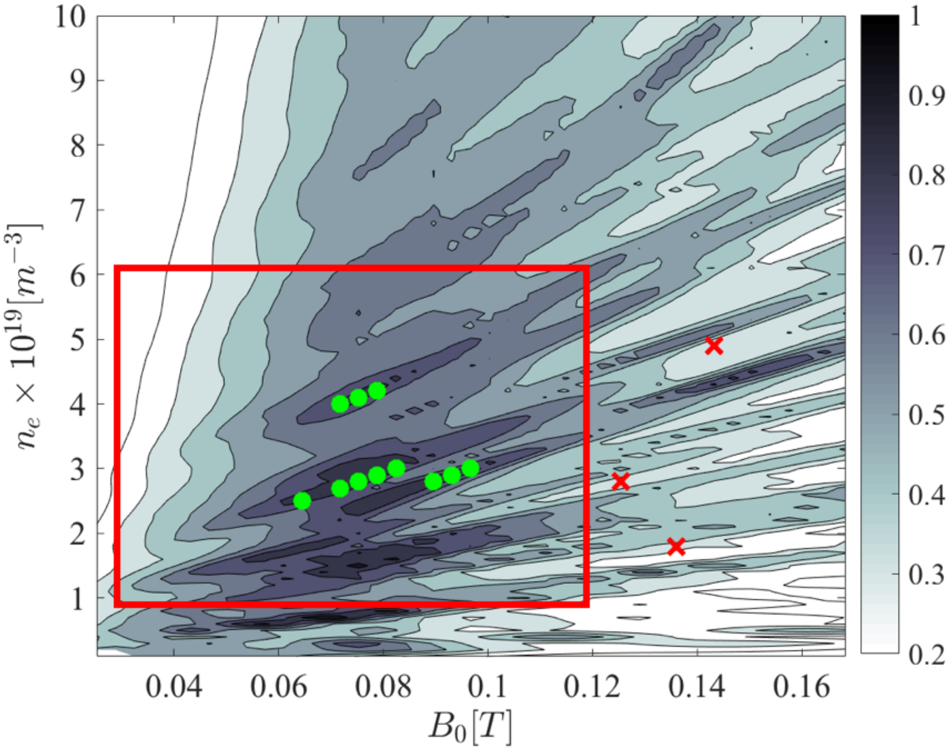

Figure 4.15: Contours of normalized core power deposition using a constant collision frequency of $\nu = \omega$. The area inside the red square marks the experimentally relevant parameters which will be the focus of the paper. The green circles mark peaks of core power deposition inside of the experimentally relevant parameter space. The red crosses mark areas of minimum core power deposition.

In Fig. 4.15 contours of normalized core power deposition are plotted as predicted by the simulation described above. The experimentally relevant parameter space is outlined by the red box. Inside the experimentally relevant parameter space points of the maximum core, power deposition is identified. These points form 3 distinct lines in $n_e(B_0)$. Since linear behavior in the peak core power deposition is predicted by the bounded dispersion relation given by Eq. 4.6, these solutions are referred to as normal mode solutions. The normal mode solutions have the following similar characteristics: A) Significant RF amplitude is present behind the antenna, and B) Reduction of edge power deposition that is not due to inductive coupling. Discussion and an interpretation of these characteristics will be presented in the following sections. Contours of RF field amplitudes and contours of core power deposition will be compared for a typical normal mode solution, $n_{e_{peak}} = 2.7 \times 10^{19}\ m^{-3}$ and $I_H = 260$ A, to a simulation with parameters corresponding to a minimum in power deposition, $n_{e_{peak}} = 2.8 \times 10^{19}\ m^{-3}$ and $I_H = 560$ A. The latter solution is referred to as a TG mode solution because the slow-wave power deposition is more prevalent in these solutions.

RF Fields

The RF field (k_z spectrum and $|B_z(r,z)|^2$ variation) of a normal mode solution will be compared to the RF fields of a TG-mode solution. Figure 4.16 shows contours of $|B_z(r,z)|^2$ in real space and radial variation of $\bar{B}_z(r,k_z)$ for the normal mode solution and Fig. 4.17 show this data for the TG mode solution. Points along a constant line that are identified as normal modes have similar RF fields as other points along that line. This behavior is expected since the normal mode solutions must satisfy Eq. 4.6 which predicts linear behavior $n_e(B_0)$ if k_z, p_{mi}, R_p, and m are held constant.

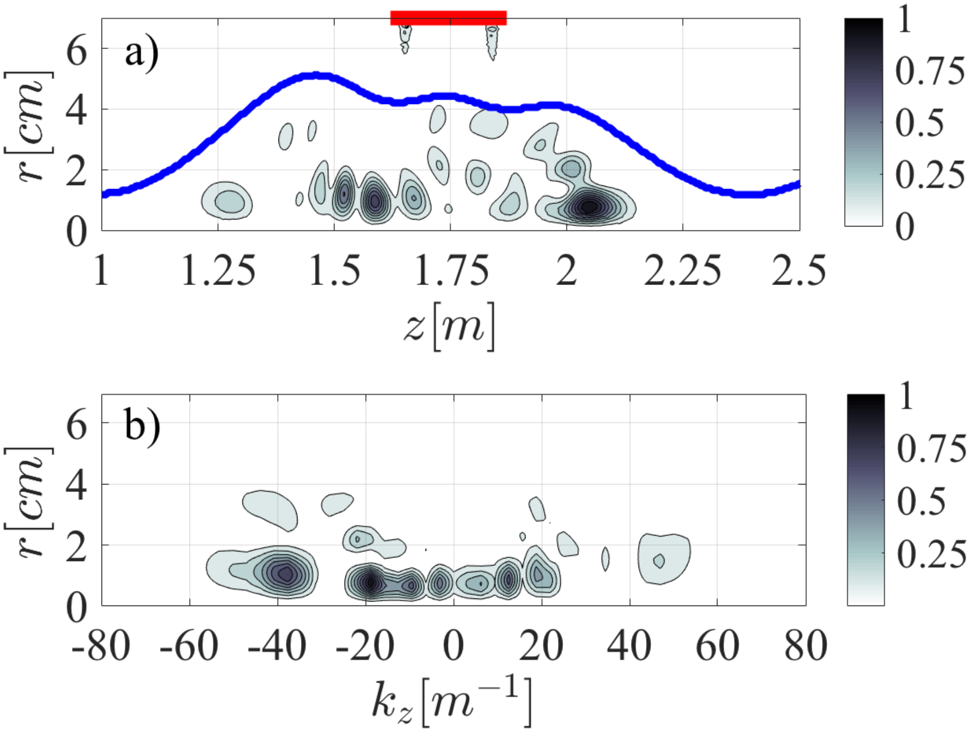

Figure 4.16: RF field of the normal mode solution. a) Normalized squared magnitude of the axial component of the RF magnetic field, $|B_z(r,z)|^2$. The blue contour line shows the location of $\chi = 0.5$. The red line shows the location of the helicon antenna. b) Discrete Fourier transform of the axial component of the RF magnetic field, $\bar{B}_z(r,k_z)$.

The wave solution in real space, Fig. 4.16 a), shows that the fast-wave is constrained to the region between the magnetic mirrors, this is due to the fast-wave cut off a present at the large magnetic fields in the magnetic mirror. The presence of these magnetic mirrors creates a cavity for the fast-wave, thus the fast-wave excited by the antenna can be reflected by the mirrors and interfere on-axis if it does not damp or loses energy to slow-wave mode conversion. Figure 4.16 shows that the plasma spectrum contains waves with negative k_z indicating the fast-wave excited has components traveling in $-\hat{z}$ as well as significant $|B_z|^2$ behind the antenna. Since the $m = +1$ mode of a helical turn antenna primarily excites waves with a positive k_z we can speculate that the waves excited for the normal mode simulations are reflected from the mirror and are allowed to interfere constructively on-axis.

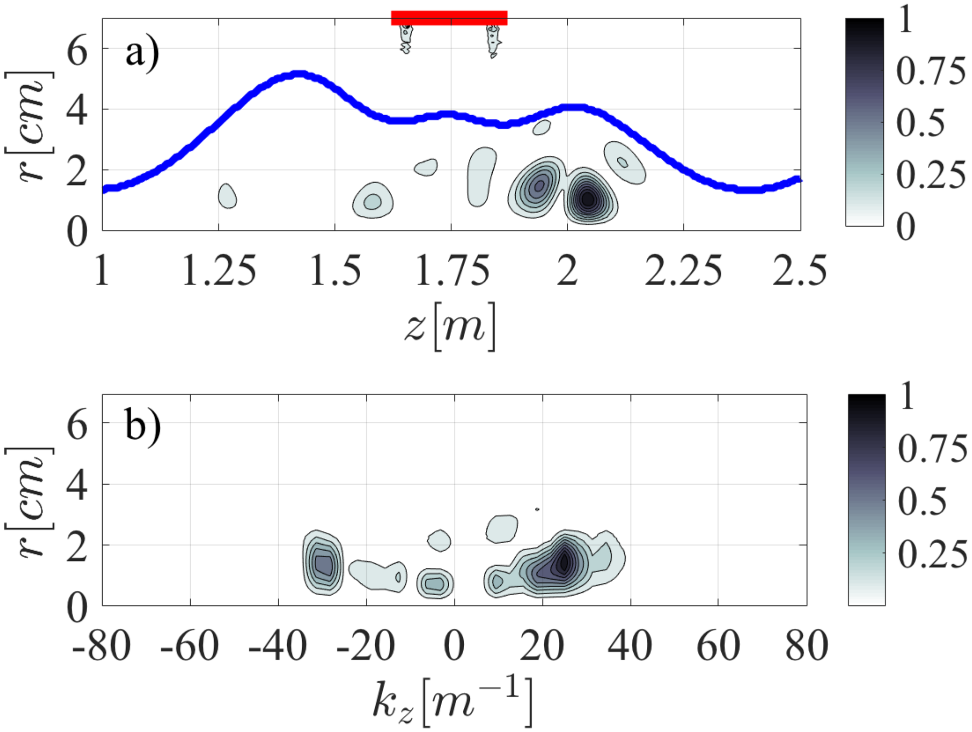

Figure 4.17: RF field of the TG mode solution. a) Normalized squared magnitude of the axial component of the RF magnetic field, $|B_z(r,z)|^2$. The blue contour line shows the location of $\chi = 0.5$. The red line shows the location of the helicon antenna. b) Discrete Fourier transform of the axial component of the RF magnetic field, $\bar{B}_z(r, k_z)$.

The plasma spectrum of the TG mode solution, shown in Fig. 4.17, is dominated by waves with $k_z \approx +20m^{-1}$ which is the dominant k_z feature of the $m = +1$ mode from the antenna vacuum spectrum. Also, there is no significant $|B_z|^2$ present behind the antenna. This indicates the fast-wave excited by the antenna is not effectively reflected by the magnetic mirror and does not constructively interfere on-axis. In the following section, we show evidence that this is due to the fast-wave mode converting to the slow-wave in the mirror region producing significant edge heating of the plasma.

Power Deposition

Figure 4.18 shows 2D contours of power loss density from the TG mode solution in Part a) and the normal mode solution in Part b). For $k_z = +20\ m^{-1}$ the dispersion relation allows only the fast-wave to propagate in the core ($\chi < 0.5$) and the slow-wave is constrained to the edge ($\chi 1.0$). Thus, the core power deposition is attributed solely to collisional damping of the fast-wave and edge power deposition is attributed to collisional damping of the slow-wave as well as inductive and capacitive heating. The inductive and capacitive heating is contained in the region directly under the antenna. Slow-wave heating that is excited by the antenna's near fields is also present under the antenna. However, edge heating that is not located directly under the antenna is attributed to slow-wave excitation through non-resonant mode conversion of the fast-wave[42].

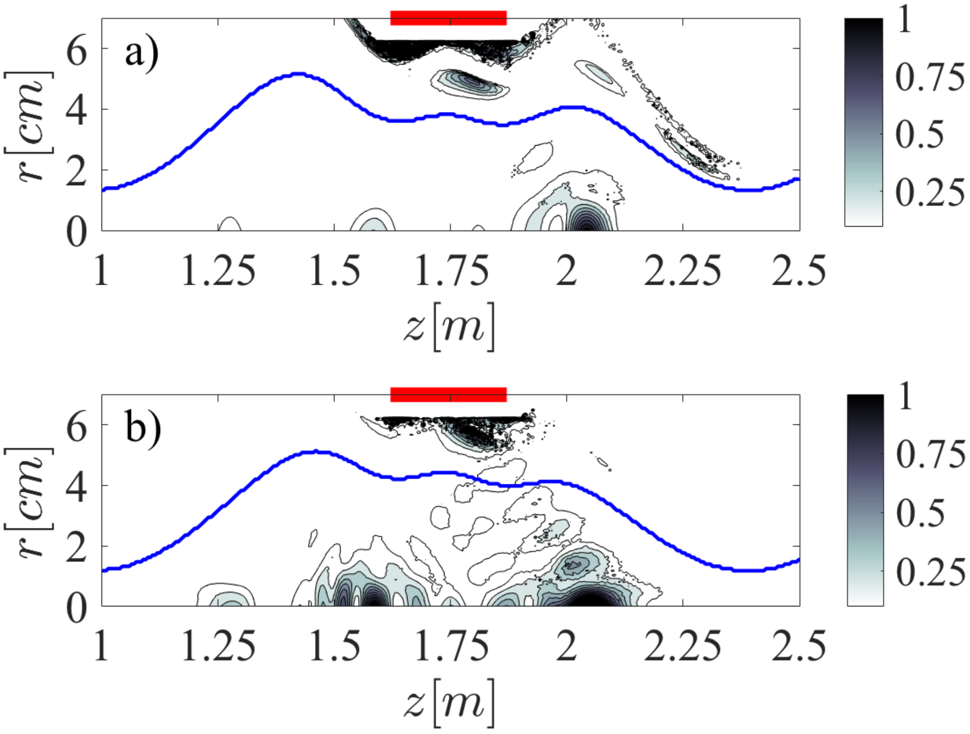

Figure 4.18: Normalized 2D power loss density for the a) TG mode solution and b) normal mode solution. The blue contour line shows the location of $\chi = 0.5$. The red line shows the location of the helicon antenna.

Figure 4.18 shows that the normal mode solution contains significantly more power deposition in the core, while the TG mode solution contains more power deposition in the edge due to non-resonant mode conversion of the fast-wave. There is significant mode conversion that occurs in the mirror region, which is apparent by the power deposition present there for $\chi > 0.5$. This is consistent with the conclusion from the analysis of the RF field of the TG solution. The fast-wave is not reflected effectively by the mirror since it losses its energy to the slow-wave in this region. This conclusion is also consistent with experimental observations that when there is a jump into the "helicon-mode" a shift from edge to core dominated power deposition is observed [17, 43]. The integrated core power deposition for the normal mode solution is 43% of the total power deposited in the plasma, while for the TG solution that fraction of power deposition is reduced to 8%. Thus, operating the helicon antenna in a mode where it can effectively excite normal modes significantly increases the amount of core heating that the antenna provides.

4.2.3 Discussion

The experimental observations described in this section show that a transition of power coupling from the edge to the core is simultaneously accompanied by the formation of a fast-wave radial eigenmode. These observations are related to theoretical predictions made by Ref. [37], which predicts anti-resonance regimes of the fast-wave and slow-wave in the analytic treatment of a homogeneous plasma column bounded by a dielectric gap and outer conductor. In this condition, the RF fields of the wave in anti-resonance are reduced and less power is absorbed by the plasma from that wave. Therefore, slow-wave anti-resonance results in a reduction in edge power deposition which allows for more energy available to the fast-wave, which would cause increased core power deposition. In a more complicated picture of a plasma column with a density gradient the slow-wave anti-resonance can be understood as a reduction of non-resonant mode conversion to the slow-wave by the reduction of the fast-wave amplitude at the edge of the plasma column, this process is explained in Ref. [42]. The analytic form of a slow-wave anti-resonance satisfies the bounded dispersion condition given by Eq. 4.4. Therefore, it is believed that the "helicon-mode" of operation in Proto-MPEX which is characterized by: (1) an increase in on-axis electron density up to $4 \times 10^{19}\ m^{-3}$ at the source location, (2) significant core power coupling, (3) suppression of edge power coupling and (4) an increase in the fast-wave energy density in the core plasma due to the (5) formation of a fast-wave radial eigenmode. The self-consistent mechanism that drives the edge-to-core transition in Proto-MPEX is not yet understood. Evidence to support this hypothesis is based on the IR thermography data as well as RF magnetic (B-dot) probe data. The IR thermography shows that the increase in core power deposition follows the suppression of the edge contribution. The B-dot probe data shows that concurrent with this power transition is an increase in on-axis magnetic energy and the formation of radial eigenmodes. These results show that in light-ion helicon sources significant power can be coupled to the core via the fast-wave. Moreover, it is shown that helicon sources have the potential to be used as plasma sources for applications requiring high electron density ($n_e > 4 \times 10^{19}\ m^{-3}$) in light gases.

Next, numerical evidence is provided to reassert that the power coupling is due to the fast-wave allowing cavity like RF magnetic field structures under the helicon antenna. A 2D axisymmetric model was used to gather these numerical evidence. The normal mode solution seems to have significant negative k_z present in its plasma spectrum, as well as significant fast-wave amplitude in the region behind the antenna $z < 1.75$ m. Since the $m = +1$ azimuthal primarily drives positive k_z fast-waves we conclude that the magnetic mirror reflects the fast-wave propagating towards it which allows the constructive interference of the fast-wave in the plasma core. Therefore the magnetic mirrors act to form a cavity for the fast-wave. In the example of the TG solution, no evidence of significant wave reflection is present. From the contours of power deposition of the TG solution, it is observed that there is significant edge heating present in the mirror region. This edge heating is not present in the mirror region for the case of the normal mode solution. These observations in the power deposition lead to the conclusion that for the case of the TG solution the fast-wave mode converts to the slow-wave in the mirror region, which leads to edge dominated power deposition in these solutions. The normal mode solution couples 43% of the total power into the core, whereas the TG solution only couples 8%. This mechanism could explain why light ion helicon plasmas have only been able to be operated successfully in the presence of a magnetic mirror [3, 46, 34, 17, 43].

This model alone cannot predict the mechanisms responsible for the transition into the “helicon-mode”. Coupling this RF model to a neutral gas and plasma transport simulation is required to shed light on the transition into the “helicon-mode”. The neutral gas fueling dependence in achieving a “helicon-mode” plasma is an open question that coupling these simulations would help answer. However, this RF model can be used to optimize the equilibrium state of the “helicon-mode” plasma in Proto-MPEX. This is done by configuring the magnetic field such that the fast-wave does not mode convert to the slow-wave at the periphery of the plasma so more power is available for density production in the core. One of the remaining questions and motivations in Proto-MPEX that remains is how to operate the helicon source at higher magnetic fields. The idea that the power-balance coupled to the plasma-wave physics dictating the operational regime of the helicon plasma source is explored in the following section with a 0D power/particle balance coupled to the RF simulations presented in this section, with the exception that Coulomb collisions are calculated as a function of electron density rather than kept constant. This following section will then address improving the helicon plasma source efficiency to compare with other experiments such as VASIMR shown in Fig. 4.3.

4.3 Power and Particle Balance

Throughout this section, a volume-averaged 0D model of the helicon plasma source is detailed. This model was made with the intention to translate the predictions of RF power deposition by the helicon antenna from the RF simulations to quantities that are diagnosed in the Proto-MPEX device such as electron density and temperature. Also, because the motivation for modeling the helicon plasma source is to explore the stagnation of the electron density at higher magnetic field strength, and ultimately to suggest experimental improvements to realize “helicon-mode” operation at higher magnetic field strengths. The hypothesis, for the stagnation of electron density production at higher magnetic field strengths observed, proposed in the previous section is that the “helicon-mode” of operation of the helicon plasma source is only realized when conditions of strong core power deposition are realized. Conditions of strong power deposition are realized when helicon-normal modes can be excited in the plasma column and mode conversion to the slow-wave at the periphery of the plasma column is suppressed. The analytical expression for this condition has been derived and the proportionality that comes out of this expression is $n_e \propto \frac{B_0 k_z}{\omega R_p}$ [42]. This expression predicts that to excite helicon normal modes in the plasma column, the electron density must scale with linear with magnetic field strength. This scaling has been observed experimentally and also has been shown to depend on applied RF power. The hypothesis for why the stagnation of the electron density depends on applied RF power is the following: since the power and particle balance dictates the electron density that can be sustained in the plasma column. When there is not enough power available, the plasma column can no longer sustain a normal-mode and core power deposition begins to deteriorate. Eventually, the plasma goes back into a mode where the power is deposited predominantly in the periphery of the plasma column, where particle and power losses at flux limiting surfaces increase the losses on the plasma column and therefore the plasma column does not sustain high electron density production.

To test this hypothesis a volume-averaged 0D model of the helicon plasma source is created and coupled to the RF simulation of the helicon plasma source. The coupling is achieved by tabulating the normalized integrated core power deposition predicted by the RF model, scaling this to the applied RF power in the experiment, and then interpolating this power deposition as a function of electron density and helicon magnetic field strength in the 0D model. This coupled 0D model is compared to experimental measurements of peak electron density as a function of magnetic field strength. From this comparison we observe that stagnation and decrease in electron density production observed at magnetic field strength $B_0 > 0.7$ T can be explained by a decrease in core power coupling predicted numerically in the region of magnetic field space between 0.07 T $< B_0 <$ 0.1 T. However, the coupled model predicts another region of increasing power deposition at magnetic field values $B_0 > 0.1$ T. This region of high magnetic field operation has not been observed experimentally; however, experimental exploration of this helicon operational regime have been limited. Finally, improvements to the helicon source region are suggested and 0D simulations used to quantify the expected increase in performance.

4.3.1 Volume Averaged Model

This subsection describes the volume averaged 0D model used in conjunction with integrated core power deposition predicted by the 2D asymmetric RF model to predict the electron density production of the helicon plasma source as a function of magnetic field strength under the helicon antenna. The power and particle balance considered here consists of continuity equations for the neutral gas and electrons. Quasineutrality is assumed between the ions and electrons and therefore a separate continuity equation for the ions is not explicitly written here. Energy conservation for the electrons and ions is written here as well.

$$\begin{aligned}
\frac{\partial n_0}{\partial t} + \nabla \cdot \mathbf{\Gamma_0} &= S_0 && (4.7)\\
\frac{\partial n_e}{\partial t} + \nabla \cdot \mathbf{\Gamma_e} &= S_e && (4.8)\\
\frac{3}{2}\frac{\partial p_e}{\partial t} + \nabla \cdot \left(\mathbf{q}_e + \frac{5}{2} p_e \mathbf{v}_e\right) &= P_{RF} + Q_e && (4.9)\\
\frac{3}{2}\frac{\partial p_i}{\partial t} + \nabla \cdot \left(\mathbf{q}_i + \frac{5}{2} p_i \mathbf{v}_i\right) &= Q_i && (4.10)
\end{aligned}$$

The terms in Eq. 4.7 - 4.10 are: $n_{0,e}$ is the neutral gas and electron density respectively, $\Gamma_{0,e}$ is the neutral gas and electron flux, $S_{0,e}$ is the volumetric source terms for the neutrals and electrons. The terms in the energy conservation equations are: $p_{e,i}$ are the electron and ion pressure defined as $p_{e,i} = n_{e,i} kT_{e,i}$, $\mathbf{q}_{e,i}$ is the conductive heat flux of electrons and ions, $\mathbf{v}_{e,i}$ is the fluid velocity of the electrons and ions, $Q_{e,i}$ are the volumetric heat sources and sinks for the electrons and ions, and P_{RF} is the core power deposition predicted by the RF simulation. The source terms in these equation are expanded as:

$$S_0 = \dot{G} - k_{iz} n_e n_0 + k_{rec} n_e n_e \tag{4.11}$$

$$S_e = k_{iz} n_e n_0 - k_{rec} n_e n_e \tag{4.12}$$

$$\begin{aligned} Q_e = \epsilon_{iz}(k_{rec} n_e - k_{iz} n_0) n_e - \\ \epsilon_{rad} k_{rad} n_e n_0 - 3\frac{m_e}{m_D} n_e \nu_{ei}(kT_e - kT_i) \end{aligned} \tag{4.13}$$

$$Q_i = 3\frac{m_e}{m_D} n_e \nu_{ei}(kT_e - kT_i) - kT_i n_0 n_e k_{cx} \tag{4.14}$$

The terms in Eq. 4.11 - 4.10 are as follows: $\dot{G}$ is the volumetric rate of neutral gas injection: which physically represents the neutral gas fueling minus the pumping due to the vacuum pumps. The ionization rate of the neutral gas is $k_{iz}n_en_0$, where k_{iz} is the effective ionization rate coefficient of atomic hydrogen. The recombination rate of the electrons and ions is $k_{rec}n_en_e$, where k_{rec} is the effective recombination rate of atomic hydrogen. The power lost from the electrons due to ionization is given by $\epsilon_{iz}n_e(k_{rec}n_e - k_{iz}n_0)$, where ϵ_{iz} is the ionization potential of atomic hydrogen. The power lost by the electrons through inelastic collisions with neutrals is represented by $\epsilon_{rad}k_{rad}n_en_0$, where $\epsilon_{rad}k_{rad}$ is the effective energy loss rate due to inelastic collisions. Elastic collisions in the Proto-MPEX plasma are dominated by Coulomb collisions and therefore only the elastic energy exchange between electrons and ions is considered here, $3\frac{m_e}{m_D}n_e\nu_{e,i}(kT_e - k_T - i)$ is the elastic energy exchanged between electrons and ions in the plasma, $\nu_{e,i}$ is the electron-ion collision frequency. Finally, charge exchange losses in the plasma volume are represented $kT_in_0n_ek_{cx}$, k_{cx} is the effective charge exchange reaction rate of atomic hydrogen. In this volume averaged model reaction rates are taken from the Atomic Data and Analysis Structure (ADAS)[94]. The reaction rates represent the average reaction rate of particles with a Maxwellian Energy distribution and are tabulated in ADAS as a function of temperature and number density of the particles species of interest (electron or ion). Because ADAS only has complete reaction rates for atomic hydrogen, this is used as a chemical proxy for deuterium; however, the two atoms have reaction rates that are very similar and therefore we believe this is a reasonable assumption. A major assumption on the neutral gas content in the plasma is that the neutral gas is assumed to be entirely comprised of atomic deuterium. This assumption, which is likely not entirely valid, greatly simplifies the problem as this eliminates the need for solving for several species in the neutral gas continuity equation. However, for the purposes of this model, these assumptions are thought to adequately represent the major processes in the Proto-MPEX source region.

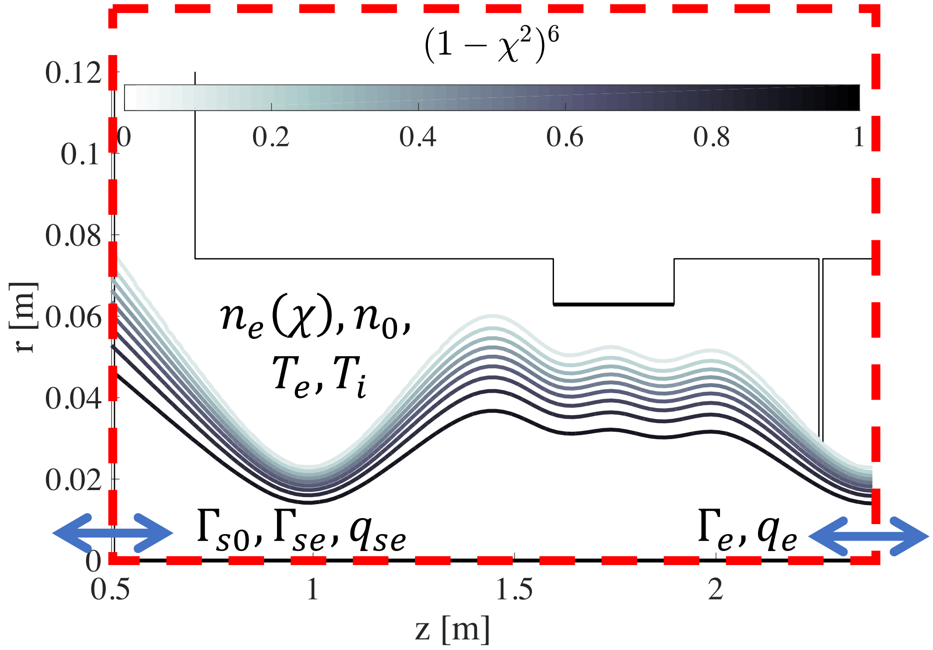

Figure 4.19: Schematic of the Proto-MPEX source region. Contours of $(1-\chi^2)^6$ are shown, volumetric and surface quantities are labeled.

Now that fundamental equations that dictate the particle and power balance have been identified a procedure to simplify these equations to an easily tractable 0D model must be made. Volume averaging Eq. 4.7 - 4.10 gives a way to simplify these equations to be very easily tractable. Firstly, a volume region must be chosen. Choosing the entire volume of Proto-MPEX overestimates the volumetric loss processes in the device because the majority of the neutral gas content in the device is contained in the source region[68] and differential pressures of up to an order magnitude can be sustained between the source region and the electron heating region. Instead the volume chosen to define the helicon plasma source region extends from the dump plate (location be referred to as z_1) to the magnetic mirror throat (location referred to as z_2), which is present directly under coil 6. The chosen source volume is shown in Fig. 4.19 and contours of the flux coordinate used to model the electron density in this region is shown for a typical Proto-MPEX magnetic field configuration. The model now ignores radial losses, which can be justified with magnetization arguments showing that the particle and heat transport along field lines is much greater than across field lines for deuterium ions and electrons in the relevant magnetic field strengths for Proto-MPEX. The model assumes azimuthal symmetry and ignores all variation in this direction. Therefore, only volumetric processes and axial losses are considered. Now, it is assumed that $n_e(\chi) = n_e(1-\chi^2)^6$, and that n_0, T_e, and T_i are constant across the volume. Integrating. Eq. 4.7 - 4.10 across the volume we can now reduce these equations to a volume averaged 0D equations and write them as follows:

$$\frac{\partial n_0}{\partial t} = \frac{1}{V}\int_V S_0 \; dV + \lambda_{rec}\Gamma_{se}\frac{S_1}{V} \tag{4.15}$$

$$\frac{\partial n_e}{\partial t} = \frac{1}{V_2}\int_V S_e \; dV - \Gamma_{se}\frac{S_1}{V_2} - \Gamma_{s2}\frac{S_1}{V_2} \tag{4.16}$$

$$\frac{3}{2}\frac{\partial p_e}{\partial t} = \frac{P_{RF}}{V_2} + \frac{1}{V_2}\int_V Q_e \; dV - \frac{5}{2}\frac{kT_e}{V_2}\left(\lambda_{se}\Gamma_{se}S_1 + \Gamma_{s2}S_2\right) + k_{\parallel}\nabla_{\parallel}T_e\frac{S_2}{V_2} \tag{4.17}$$

$$\begin{aligned}\frac{3}{2}\frac{\partial p_i}{\partial t} &= \frac{1}{V_2}\int_V Q_i \; dV + \frac{5}{2}R_N\Gamma_{se}\frac{S_1}{V_2}\left(R_E(2kT_i + 3kT_e) - \frac{3}{2}kT_i\right)\\ &\quad -\frac{5}{2}\frac{1}{V_2}\left(\Gamma_{se}\lambda_{si}kT_iS_1 + \Gamma_{s2}(kT_i + \frac{1}{2}m_Dc_s^2)S_2\right)\end{aligned} \tag{4.18}$$

$$S_1 = \int_0^{R<\chi=0.6}(2\pi r)(1-\chi^2)^6 dr|_{z=z_1} \tag{4.19}$$

$$S_2 = \int_0^{R<\chi=0.6}(2\pi r)(1-\chi^2)^6 dr|_{z=z_2} \tag{4.20}$$

$$V = \int_{z_1}^{z_2}\int_0^{R<\chi=0.6}(2\pi r)drdz \tag{4.21}$$

$$V_2 = \int_{z_1}^{z_2}\int_0^{R<\chi=0.6}(2\pi r)(1-\chi^2)^6 drdz \tag{4.22}$$

Eq. 4.15 - 4.22 shows the final form of the volume averaged power and particle balance equations used to model the helicon plasma source. In the neutral gas particle conservation, besides the volumetric sources of neutral gas described above, $\lambda_{rec}\Gamma_{se}\frac{S_1}{V}$ represents a flux of recycled neutrals from the dump plate; in this term λ_{rec} is the recycling coefficient which is set to $\lambda_{rec} = 1$ in this case, and Γ_{se} is the flux of ions striking the material target which is estimated here to be $\Gamma_{se} = \frac{1}{4}n_eC_{si}$ where $C_{si} = \sqrt{\frac{kT_e}{M_i}}$ is the ion sounds speed. Moving to the electron particle balance, this contains the volumetric terms described above as well as particle losses to the to the dump plate $\Gamma_{se}\frac{S_1}{V_2}$ and particle losses from the flux of particles moving towards the target $\Gamma_{s2}\frac{S_1}{V_2}$. The flux of particles moving towards the target is defined here as $\Gamma_{s2} = Mach\ C_{si}n_e$ where $Mach$ is the Mach number that is constrained experimentally to be between $0.2 - 0.6$ in this region, for the calculations presented bellow $Mach = 0.2$ is used. The terms in Eq. 4.17 besides the volumetric terms described above are as follows: $\frac{5}{2}\frac{kT_e}{V_2}\left(\lambda_{se}\Gamma_{se}S_1 + \Gamma_{s2}S_2\right)$ is the energy lost due to convection of electrons. The energy lost through the plasma sheath is $\lambda_{se}\Gamma_{se}S_1$, where λ_{se} is the heat transmission coefficient which is assumed to be constant here λ_{se} [99], and $\Gamma_{S2}S_2$ is the losses due to convection through the magnetic mirror region. The conduction losses through the magnetic mirror are given by $k_{\parallel}\nabla_{\parallel}T_e\frac{S_2}{V_2}$ where the parallel gradient is estimated by assuming that the electron 1 meter away from the region is constrained to $T_e = 2$

eV, which is the typical electron temperature measured in the central chamber that is 1 m away from the source region. The ion energy balance given by Eq. 4.18 contains the following terms besides the volumetric terms: $\frac{5}{2}R_N\Gamma_{se}\frac{S_1}{V_2}\left(R_E(2kT_i + 3kT_e) - \frac{3}{2}kT_i\right)$ gives a term for the flux of energetic neutrals born at the dump plate and charge exchanging in the bulk plasma where R_N and R_E are the particle and energy reflection coefficients for Stainless Steel which are taken to be constants $R_N = 0.6$ and $R_E = 0.4$ which represent these coefficients if the ion impact energy to the material is ≈ 10 eV [115]. The ion power lost to the sheath is captured by the $\Gamma_{se}\lambda_{si}kT_iS_1$ term where λ_{si} is the ion heat sheath transmission coefficient that is held constant at $\lambda_{si} = 3.5$ [99]. Finally the ion power losses towards the target are given by $\Gamma_{s2}(kT_i + \frac{1}{2}m_Dc_s^2)S_2$.

Eq. 4.15 - 4.18 are numerically integrated, using Matlab's ordinary different equation solver function "ode45" [79], until a steady state solution is reached ($t = 10$ ms). Constants that are dependant on electron temperature or density are redefined at every time step, either by interpolating from gathered data (ADAS rate coefficients) or calculated from the defining equation (ion sounds speed). The steady solution is the solution that is reported in the following sections. The initial conditions that are assigned to the solver are the following conditions: Initial neutral gas pressure of $P_0 = 2.0$ mTorr which is translated to a gas density by assuming room temperature ideal gas. The solution is fairly sensitive to neutral gas pressure and since this quantity is only measured in the periphery of the plasma and large experimental uncertainty in Proto-MPEX, it is thus adjusted such that reasonable T_e and n_e are achieved. To give an idea of the sensitivity of the model to this parameter when initial neutral gas pressure is dropped to $n_0 = 0.1$ mTorr then the steady-state electron density at $B_H = 0.07$ T is $n_e = 2 \times 10^{19}\ m^{-3}$ and electron temperature in the region reaches $T_e = 11$ eV, at initial neutral gas pressures of $n_0 = 10$ mTorr, the electron density and temperature both drop to $n_e = 3 \times 10^{19}\ m^{-3}$ and $T_e = 1.6$ eV. The initial condition for the peak electron density is set to $n_e = 1 \times 10^{18}\ m^{-3}$, electron temperature of $T_e = 6$ eV, and ion temperature of $T_i = 0.1$ eV. Initially, the system of equations as defined in Eq. 4.15 - 4.22 was not able to reach a steady state solution because the neutral particle balance did not reach steady state and as a result, the solution blew up after several ≈ 1 ms. Therefore, the gas fueling rate is adjusted from a constant to one that keeps the total number of particles in the system constant after, $t > 5\ \mu s$, this ensures a steady state solution and roughly captures the addition of a neutral gas pumping term that stabilizes the pressure in the region.

4.3.2 Comparison to Experiment

The model defined in the section above is now used with contours of integrated core power deposition predicted by the RF simulation of the helicon plasma source. Where, the section above used a constant electron collision frequency, defined by $\nu_e = \omega$, to numerically examine the behavior of the helicon antenna;

here, to replicate experiment as closely as possible, a collision frequency is calculated as a function of electron density and an assumed electron and ion temperature of $T_e = T_i = 4$ eV is used to calculate the Coulomb Collision frequency for the electron and ions. An additional electron collision frequency is calculated for elastic scattering with deuterium with a number density defined by a pressure of $P = 1$ mTorr at room temperature. This is then used in the RF simulation of the helicon plasma source and peak electron density is scanned from $n_e = 1 - 10 \times 10^{19}$ m^{-3} and the current through coil 3 and coil 4 is scanned from $I_H = 100 - 1500$ A and the magnetic field reported is the average strength of the magnetic field on axis under the helicon antenna.

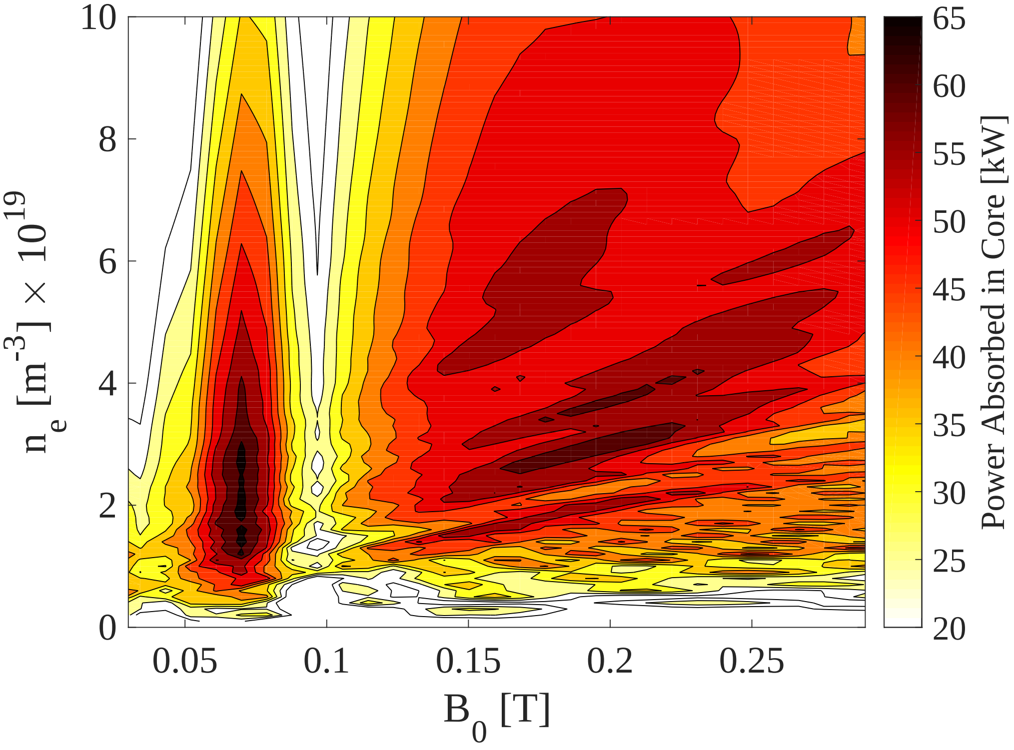

Figure 4.20: Contours of integrated core power deposition normalized to the total power deposited in the plasma volume and then multiplied by $P_{helicon} = 100$ kW, plotted as a function of peak electron density and average magnetic field strength under the helicon antenna (B_H).

Figure 4.20 shows the contours of core power deposition predicted by the RF simulation of the helicon plasma source. These contours are calculated by integrating the power deposited in the plasma core $\chi < 0.6$, then normalizing this by the total power deposited in the plasma volume and multiplying by the typical value of forwarding power used experimentally. From this figure we see that there is a region of increasing core power coupling from the lower magnetic field values until $B_H < 0.07$ T, then this core power coupling begins to deteriorate in the region of helicon magnetic field strength 0.07 T $< B_H <$ 0.11 T, this is the region of magnetic field strength where the electron density production is observed to decrease experimentally. However, in the region of higher magnetic field strength, $B_H >$ 0.11 T, the core heating efficiency of the helicon plasma source starts to recover and increases and efficient modes are available for much higher magnetic field strengths than Proto-MPEX currently operates at.

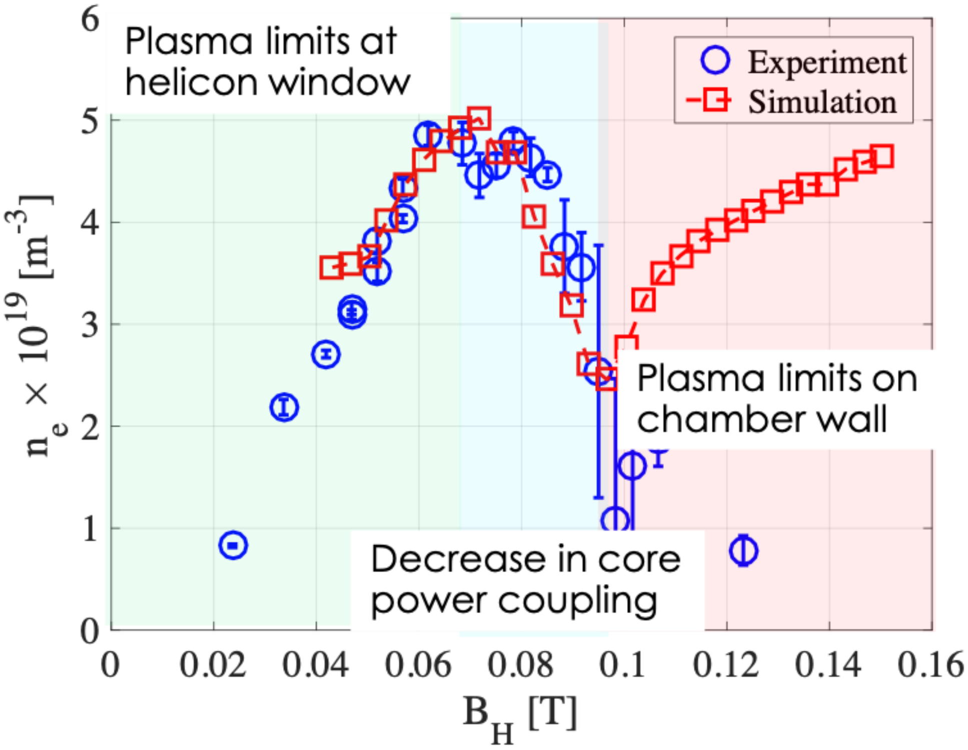

Figure 4.21: Experimentally measured electron density produced by the Proto-MPEX helicon plasma source as a function of magnetic field strength under the helicon antenna compared to predictions of peak electron density at steady predicted by the 0D power balance coupled to the RF simulation of the helicon plasma source.

Figure 4.21 shows the comparison of the results of the coupled model to the experimentally measured electron density in Proto-MPEX. The comparison appears quantitatively quite good; however, the electron density is measured at the target, and the helicon source region is known to have $\approx 30-40\%$ higher electron density than the target region, this model, therefore, quantitatively under predicts electron density production by the helicon source. The other parameters predicted from the model are also under predicted when compared to experimentally measured parameters. The electron temperature at steady state is relatively constant as a function of B_H varies between $T_e = 2.2 - 2.7$ eV, the electron temperature measured in this region is closer to $T_e = 3 - 4$ eV at Spool 2.5 and Spool 4.5, so again the electron temperature is underpredicted by $50\% - 80\%$ from the measured values. The neutral gas pressure in the region reaches steady-state around 1.5 mTorr which is approximately the steady state pressure measured by the baratrons at Spool 2.5 and Spool 4.5 (the helicon source region) [68]. The adjusted neutral gas fuelling rate is $\dot{G} \approx 1.2e20\ \frac{atoms}{s}$ particles which is also lower than the experimentally determined value of $\dot{G} \approx 5e20\ m^{-3}$. The ionization cost predicted from this model is also overpredicted by $\approx 60\%$ and the ionization cost predicted numerically is from this model is $\approx 1600\ \frac{eV}{ion}$. Overall, this simplified 0D model is not being used for exact quantitative agreement with experimental measurements.

The qualitative comparison of the experimental measurements is quite good for the magnetic field regime $0.04\ \text{T} < B_H < 0.11\ \text{T}$, where it shows linear increase in plasma production up until $B_H \approx 0.07$ T and then a subsequent decrease in electron density production until $B_H \approx 0.11$ T. At the higher range of magnetic field strengths $B_H > 0.11$ T, a region of increasing electron density production is observed numerically but not experimentally on Proto-MPEX. However, Mini-RFTF which was a helicon device operating at ORNL did observe a similar behavior to the model predictions, where electron density production deteriorated at a helicon magnetic field strength of $B_H \approx 0.02$ T and then recovered at $B_H \approx 0.05$ T. This behavior is shown in Fig. 4.22 for easy reference and was taken from Ref. [3].

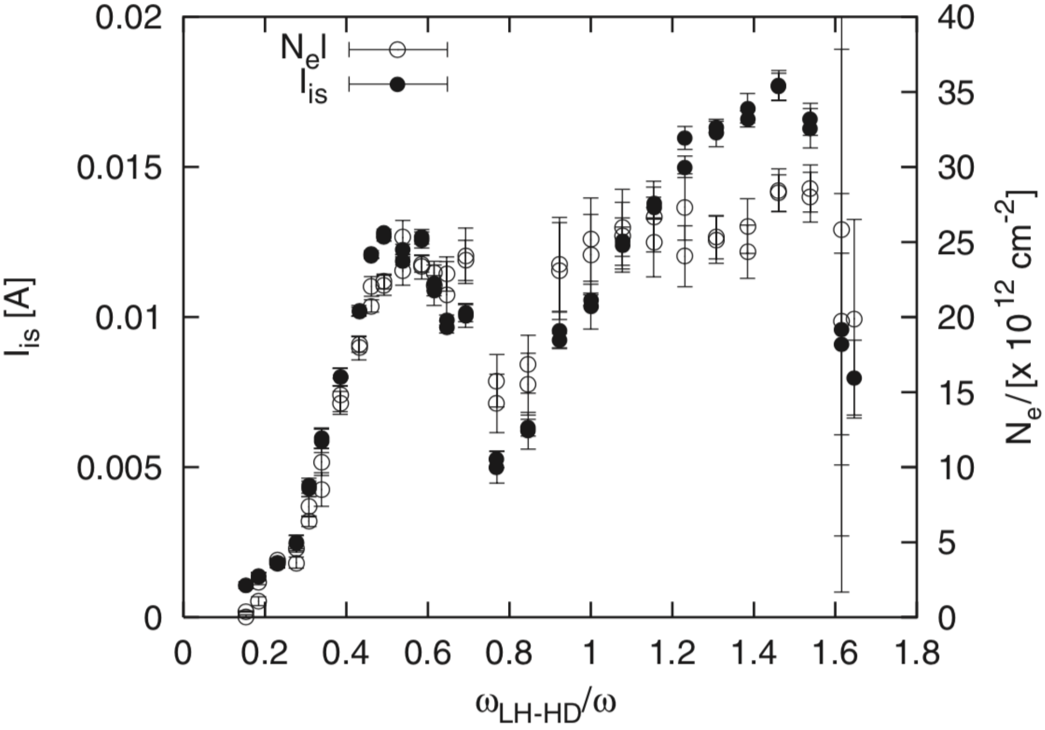

Figure 4.22: Experimentally measured electron density produced by the Mini-RFTF helicon plasma source as a function of helicon magnetic field strength. The helicon magnetic field strength is reported as a the high density limit of the lower hybrid resonance, defined as $\omega_{LH-HD} = \sqrt{\omega_{ce}\omega_{ci}}$, normalized to the driving frequency of the antenna, which is $\omega = (2\pi)21$ MHz[3].

The recovered electron density production behavior at the higher range of magnetic field strengths $B_H >$ 0.11 T, that is predicted by the model and reminiscent of the behavior observed in Mini-RFTF helicon plasma source shown in Fig. 4.22, was not observed experimentally on Proto-MPEX. This may be due to one of the following reasons: 1) The high helicon magnetic field operating conditions have not been explored experimentally very thoroughly and a stable plasma operating conditions (gas fueling timing and recipe, matching network settings) typically take experimental optimization to uncover. 2) The magnetic field configuration where this data was taken is such that the magnetic flux begins to limit not only at the helicon window but at the chamber wall for coil currents that produce the helicon fields of $B_H > 0.11$ T. This may lead to an increasing parallel loss mechanism that is not taken into account in this model. The limiting flux surface has since been removed by powering coil 2 with 600 A.

Although this model captures the electron density dependence on the helicon magnetic field strength in the region between 0.04 T $< B_H <$ 0.11 T, where the helicon plasma source is diagnosed most thoroughly, it quantitatively under-predicts experimental observable in the helicon source region by $\approx 30-50\%$. This model was not intended for an exact quantitative agreement with the helicon plasma source. Instead, it is used as a means to help quantify expected helicon plasma source performance from suggested improvements to the source region. In this context, this model adequately captures the essential physics in the helicon region to give reasonable estimates and assessment of such improvements. In the following subsection, this model will be used to assess the performance increase of suggested improvements to the source region.

4.3.3 Optimizing the Source Region

This subsection will now cover helicon source optimization suggestions and quantify the impact of these suggestions on the helicon performance. Three overall improvements to the helicon source region are proposed here: 1) increasing the helicon power 2) decreasing the source volume of the helicon antenna, and 3) reducing sheath losses by floating the dump plate. These improvements will be quantified at the helicon magnetic field value of $B_H = 0.07$ T, where the simulations peaks in electron density production. The philosophy of these improvements will be discussed and the improvements in the performance will be assessed with the 0D coupled model. Ionization cost in the helicon source will be reported as the primary figure of merit of the plasma source performance here.

Increasing Power

Increasing the power of the helicon plasma source is one way to attempt to improve the helicon plasma source performance. The installed power on MPEX is planned to be $P_{RF} = 200$ kW, while Proto-MPEX is currently operating with $P_{RF} = 100$ kW. Increasing helicon power has been shown to lead to mode jumps of the helicon plasma sources [116, 117] and has been explained by with a stability and power balance argument [42]. Moreover, light ion helicon plasma sources have observed that the RF power is typically a limiting factor in the ability of the helicon plasma source to operate in high-density modes at higher magnetic field strengths.

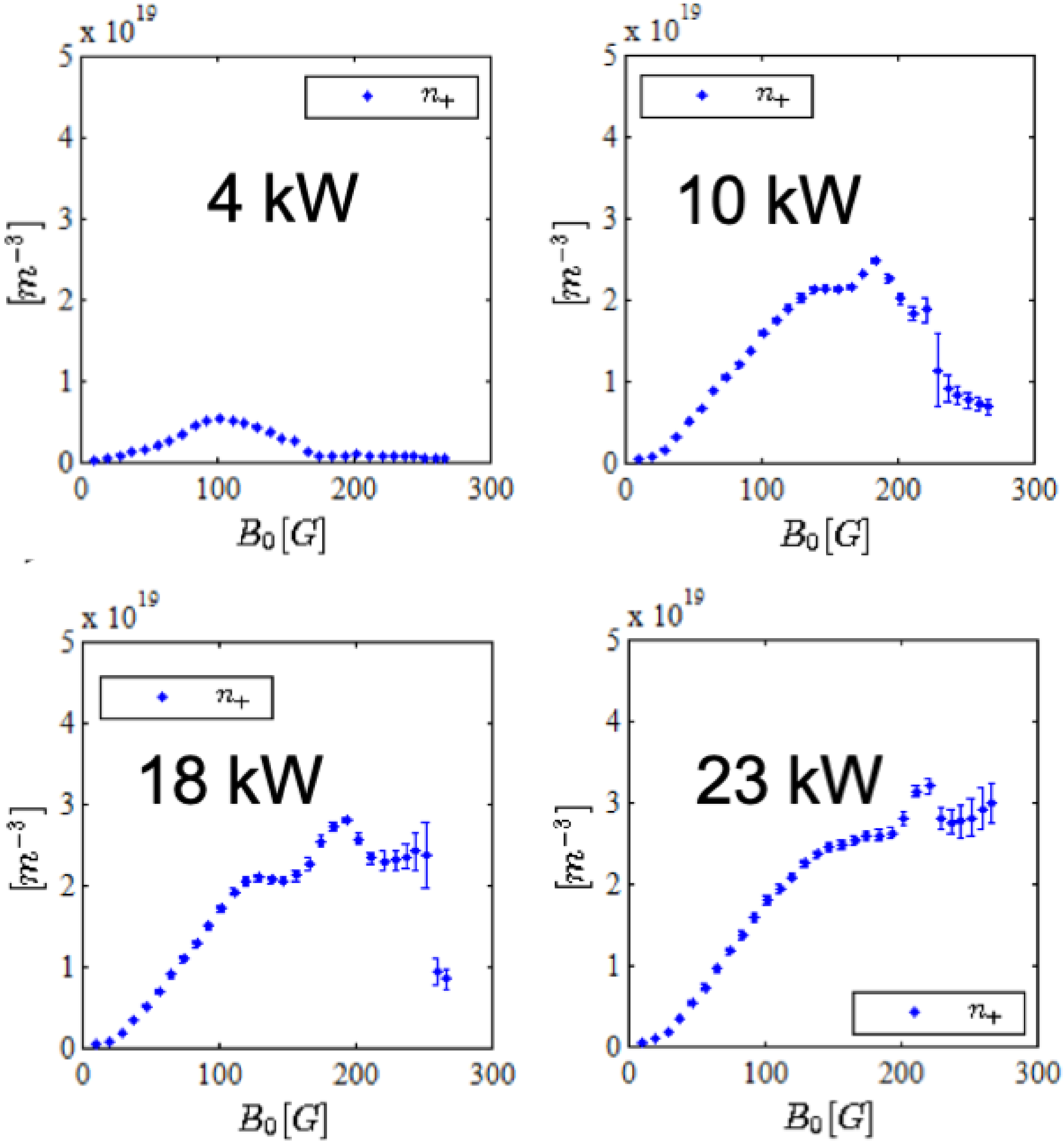

Figure 4.23: Electron density as a function of helicon magnetic field strength measured in MAGPIE helicon plasma source[4], for varying input RF power levels: $P_{RF} = 4$ kW (top left), $P_{RF} = 10$ kW (top right), $P_{RF} = 18$ kW (bottom left), $P_{RF} = 23$ kW (bottom right). The helicon plasma source on MAGPIE was operated with a driving frequency of $\omega = (2\pi)7$ MHz.

MAGPIE linear device [4] is an experiment similar to Proto-MPEX in that it is a linear plasma device which uses a helicon plasma source in a converging magnetic field configuration to produce high density

($n_e > 1 \times 10^{19}\ m^{-3}$) deuterium plasmas. The RF power dependence of the scaling of electron density with helicon magnetic field strength is shown in Fig. 4.23. From this figure, we see that increasing RF power allows MAGPIE to continue the trend of linearly increasing electron density with magnetic field strength. This is a commonly observed trend in helicon plasma sources and this trend gives experimental motivation that increasing the RF power on Proto-MPEX may enable operations at higher helicon magnetic field strengths. Therefore, it will be important to predict the behavior of the helicon plasma source at the higher planned power of $P_{RF} = 200$ kW. An important question to answer will be whether the helicon plasma source on MPEX will be able to achieve high-density plasma operation at magnetic field values of $B_H = 0.2$ T to achieve the plasma diameter of $d_p \approx 10$ cm planned for MPEX.

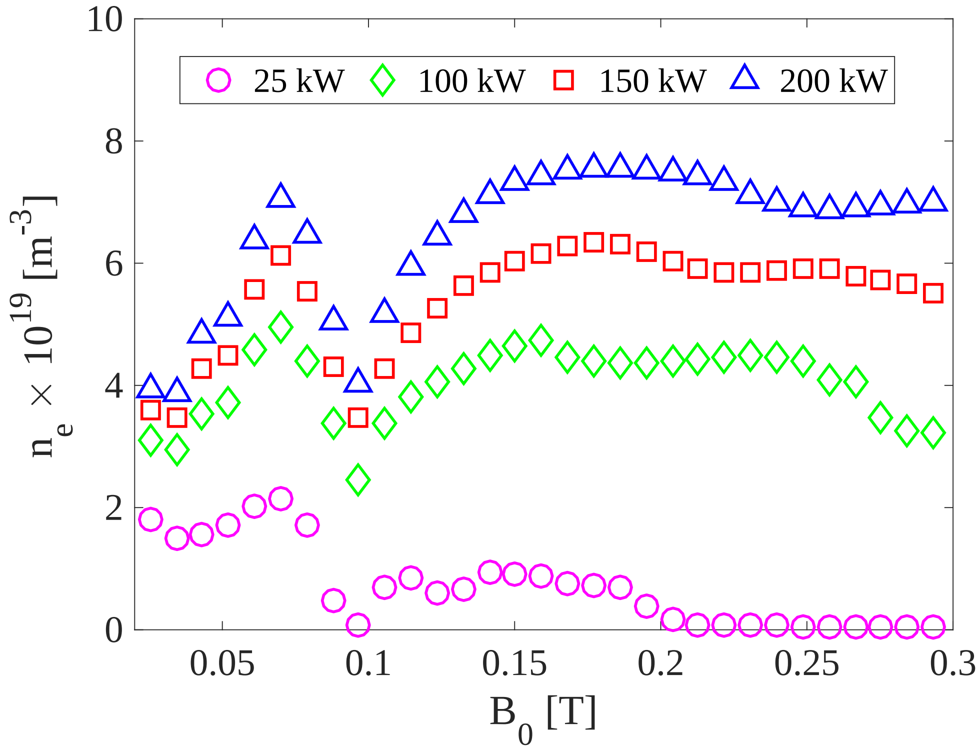

Figure 4.24: Electron density as a function of helicon magnetic field strength for several values of forward RF power

Figure 4.24 shows the predictions of electron density, from the coupled RF and 0D power-particle balance model, as a function of helicon magnetic field strength for varying levels of RF power. The magnetic field is scanned from $B_H = 0.02 - 0.3$ T to see if a steady-state power balance point of view allows for high-density helicon operation at magnetic field strengths of $B_H > 0.2$ T, which will be required for MPEX operation.

In the previous section, the hypothesis was presented for why electron density production deteriorated with increasing magnetic field strength when $B_H > 0.07$ T. This hypothesis was as follows, core power deposition in Proto-MPEX depends on exciting helicon normal modes which suppress mode conversion of the fast-wave to the slow-wave in the periphery of the plasma-column. The dispersion relation of helicon normal modes gives the proportionality $n_e \propto \frac{B_0 k_z}{\omega R_p}$, which shows a linear dependence of electron density to magnetic field strength. However, the production of electron density under the helicon antenna is also dependant on particle and power balance in the source volume, therefore if there isn't sufficient power to produce the electron density required to sustain the $n_e \propto \frac{B_0 k_z}{\omega R_p}$ proportionality, then the helicon plasma source falls off from regions where core power deposition is optimal. The edge power deposition is increased, and the power deposition at the periphery of the plasma column typically is subject to stronger losses to the walls and flux limiting surfaces. Thus the helicon falls away from efficiently producing plasma density when it is "power starved". The 0D power-particle balance coupled to the 2D RF model here should predict this power starvation. However, from Fig. 4.24 we see that the model is not predicting "power starvation", except for the case of the lowest value of RF forward power presented here, $P_{RF} = 25$ kW, there is a significant fall-off in electron density production efficiency at a magnetic field strength of $B_H = 0.18$ T. Instead, the model predicts a decrease in core coupling efficiency in the helicon magnetic field range $0.07 > B_H > 0.11$ T then a recovery in core power coupling and electron density production, which seems to stabilize and relatively flat steady-state electron density is observed as a function of magnetic field strength. Therefore, from the view of this steady state discharge, we do not believe that Proto-MPEX is in a "power-starved" regime and can be operated in magnetic fields higher than have currently been achieved. The planned increase in RF power to 200 kW will then further improve operation and enable higher electron densities to be produced at higher magnetic field values. Next, the ionization cost and electron density production at each value of magnetic field will be explored to understand at what power level is the helicon "power-starved". To explore this question the electron density and temperature along with the ionization cost (power divided by the integrate ion flux towards the target) will be tracked to asses this.

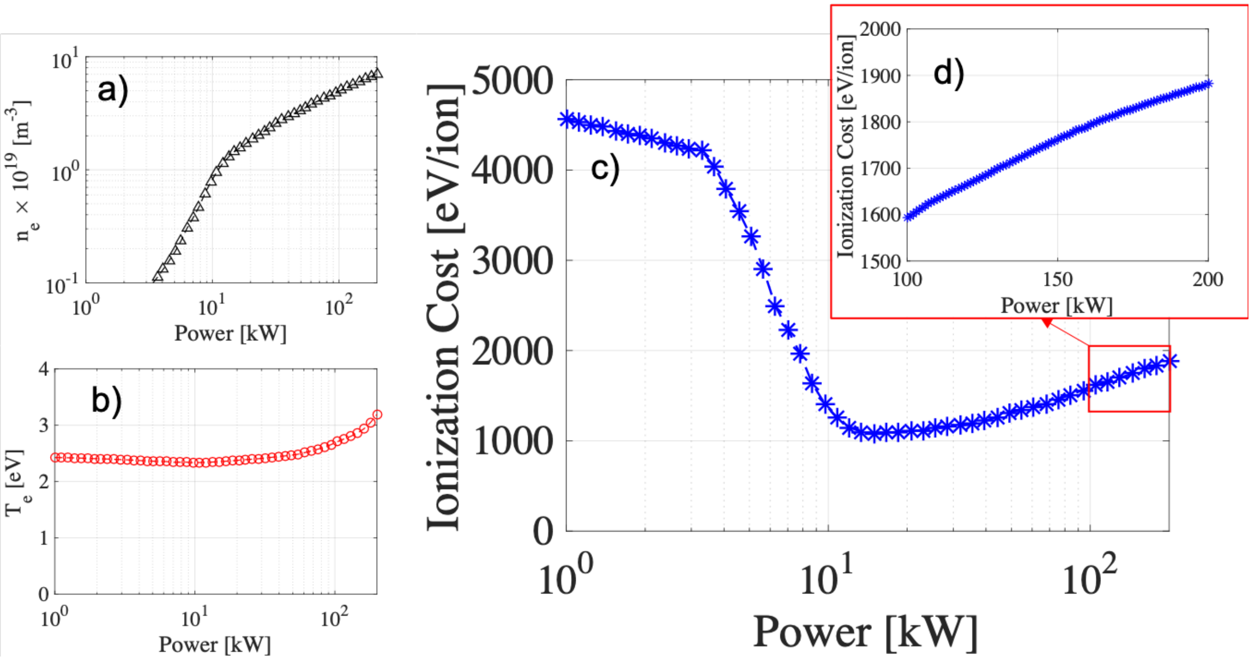

Figure 4.25: Effect of increasing RF power on the helicon plasma source's a) electron density, b) electron temperature, and c) ionization cost d) zoomed in plot of ionization cost. Helicon magnetic field strength is kept constant at $B_H = 0.07$ T.

Figure 4.25 shows that the increase in RF power will allow the helicon plasma source to produce higher electron density and operate with a higher electron temperature at the constant helicon magnetic field strength. However, at the magnetic field strength of $B_H = 0.07$ T the increase in RF power will also increase the ionization cost for power levels $P_{RF} > 20$ kW. For power levels between $P_{RF} < 20$ kW there is a sharp increase in electron density and decrease in ionization cost, with the minimum occurring around $P_{RF} \approx 11$ kW. Therefore, below $P_{RF} \approx 11$ kW the helicon source can be said to be "power-starved" because not enough power is available to access the modes of operation where increased power deposition occurs. From Fig. 4.20, it can be seen that no other modes are available for the helicon plasma source to access with increasing power, and the maximum in power deposition occurs at $n_e \approx 3 \times 10^{19}$ m^{-3} in this parameter space and therefore increasing the power past $P_{RF} > 20$ kW at $B_H \approx 0.07$ T will make density production more "expensive".

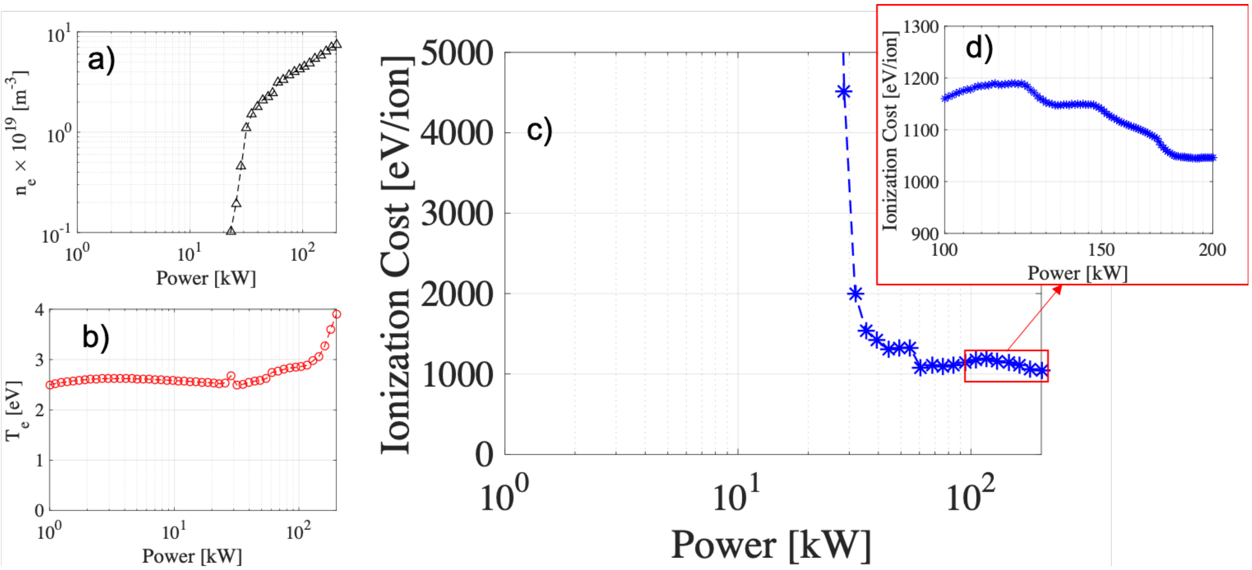

Figure 4.26: Effect of increasing RF power on the helicon plasma source's a) electron density, b) electron temperature, and c) ionization cost d) zoomed in plot of ionization cost. Helicon magnetic field strength is kept constant at $B_H = 0.20$ T.

Figure 4.26 also shows that at a magnetic field strength of $B_H = 0.20$ T the increase in RF power will allow the helicon plasma source to produce higher electron density and operate with a higher electron temperature at the constant helicon magnetic field strength. For $B_H = 0.20$ T this calculation indicates that a power of $P_{RF} > 30$ kW is required to access modes of operation where efficient core heating can be observed, which is a higher power than for the case of $B_H = 0.07$ T. At this magnetic field strength, the increase in RF power will also direct more flux towards the target plate at a lower ionization cost. From Figure 4.20, it can be seen that at this magnetic field strength the helicon source accesses more efficient electron density production modes at higher electron densities than for the case of the magnetic field strength of $B_H = 0.07$ T. Increasing the available power from $P_{RF} > 30$ kW still shows decreasing ionization cost as there are efficient modes of operation available $n_e \approx 6 - 8 \times 10^{19}\ m^{-3}$. Therefore, at this magnetic field strength, increasing the helicon power on Proto-MPEX will not only produce more electron density, but it will do so more efficiently. Since the ionization cost is being used here as the figure of merit for the helicon plasma source, this model predicts $\approx 12\%$ improvement in helicon performance when increasing the power from $P_{RF} = 100$ kW to $P_{RF} = 200$ kW for $B_H = 0.20$ T.

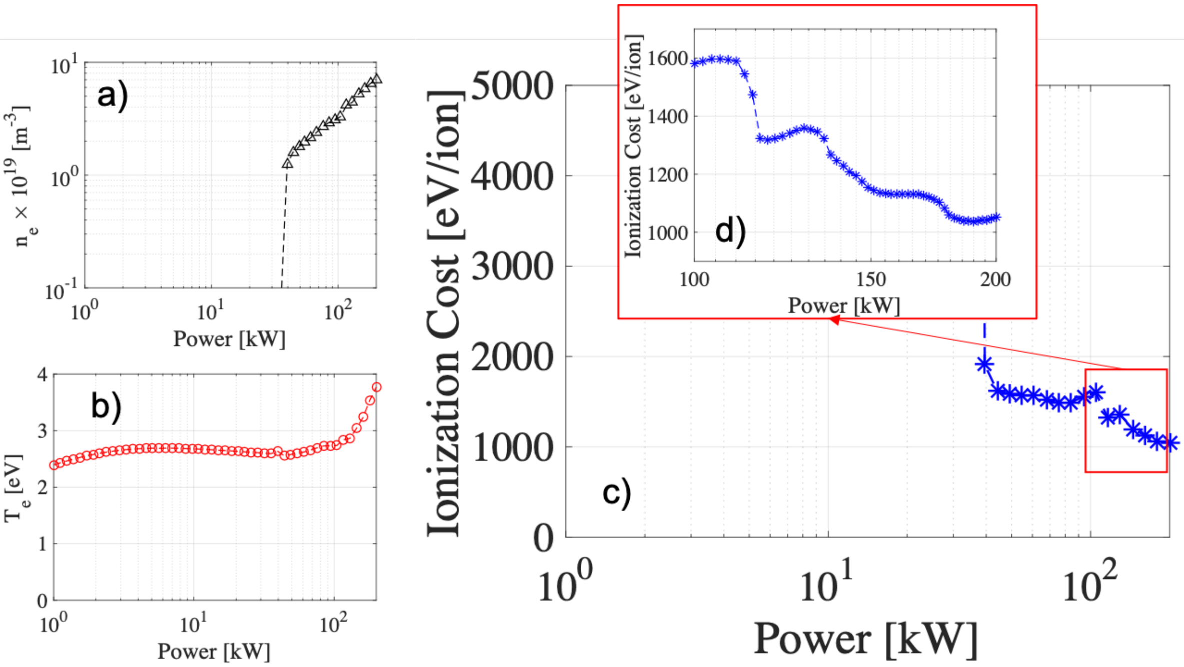

Figure 4.27: Effect of increasing RF power on the helicon plasma source's a) electron density, b) electron temperature, and c) ionization cost d) zoomed in plot of ionization cost. Helicon magnetic field strength is kept constant at $B_H = 0.30$ T.

Figure 4.27 also shows that at a magnetic field strength of $B_H = 0.30$ T the increase in RF power will allow the helicon plasma source to produce higher electron density and operate with a higher electron temperature at the constant helicon magnetic field strength. For $B_H = 0.30$ T this calculation indicates that a power of $P_{RF} > 40$ kW is required to access modes of operation where efficient core heating can be observed, which is a higher power than for the case of $B_H = 0.07$ T and $B_H = 0.20$ T, this observation is then consistent with the hypothesis that the Proto-MPEX helicon plasma sources can become "power-starved" and not access efficient operation when the power is too low at higher magnetic field strength, however this numerical model predicts this to occur at much lower power levels than are available. At this magnetic field strength, the increase in RF power will also direct more flux towards the target plate at a lower ionization cost. From Fig. 4.20, it can be seen that at this magnetic field strength the helicon source accesses more efficient electron density production modes at higher electron densities than for the case of the magnetic field strength of $B_H = 0.07$ T. Increasing the available power from $P_{RF} > 40$ kW still shows decreasing ionization cost as there are efficient modes of operation available $n_e \approx 4 - 7 \times 10^{19}\ m^{-3}$. Therefore, at this magnetic field strength, increasing the helicon power on Proto-MPEX will not only produce more electron density, but it will do so more efficiently. Since the ionization cost is being used here as the figure of merit for the helicon plasma source, this model predicts $\approx 36\%$ improvement in helicon performance when increasing the power from $P_{RF} = 100$ kW to $P_{RF} = 200$ kW for $B_H = 0.30$ T.

Smaller Source Volume

One of the most prevalent energy loss mechanisms in Proto-MPEX are the volumetric losses due to inelastic collisions with the neutral background. Several theoretical routes exist to reducing these losses, some of these routes are the following: 1) Increasing the electron temperature in the helicon source region will decrease the collisional energy loss per ionization event as shown in Fig. 4.5. 2) Decreasing the neutral gas pressure in this region. 3) Decrease the volume of the source region. Since the electron temperature is not an independent variable that can be experimentally tailored easily than option 1) will not be pursued. The helicon plasma source is estimated to be using $\approx 90\%$ of the neutral gas that is injected into the device [68], and most of the neutral gas content in the source region is estimated to be sustained by recombination of neutral gas at the dump-plate. Decreasing the neutral gas fueling rate of the device has shown to collapse the plasma into a low electron density mode and is thought to be because the source region lacks the neutral content to sustain electron density necessary for a helicon normal mode. Thus, decreasing the neutral density content in the source region is not easily controlled. However, decreasing the volume of the source can be easily accomplished by moving the dump plate from its current location ($z = 0.5$ m) closer to the source region.

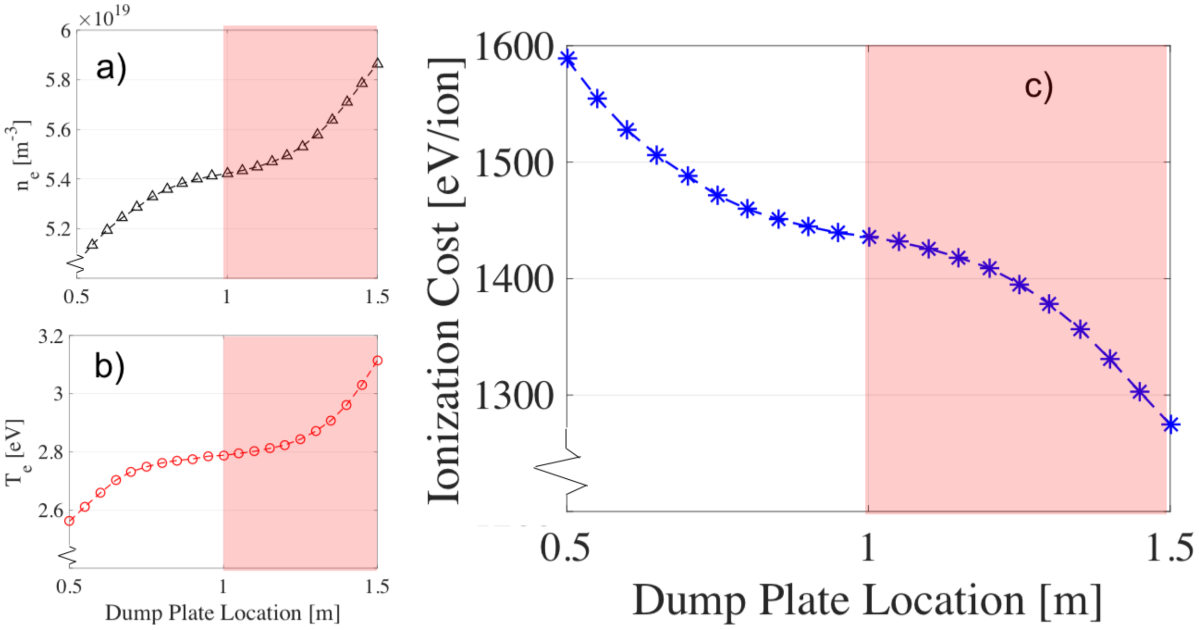

Figure 4.28: Effect of decreasing the volume of the source region, accomplished by moving the dump plate from it's current location, on the helicon plasma source's a) electron density, b) electron temperature, and c) ionization cost. Helicon magnetic field strength is kept constant at $B_H = 0.07$ T.

Figure 4.28 shows the effect of decreasing the helicon source volume by moving the dump-plate closer to the helicon antenna. The region shaded in red in this figure is the region where RF power deposition is predicted to still occur by the RF simulation. Moving the dump-plate into this region will change the RF characteristics of the source region, and thus a magnetic field reconfiguration is recommended before moving the dump-plate into this region. Figure 4.28 shows that decreasing the source volume by moving the dump plate 1 m inwards in the current magnetic field configuration is expected to improve the helicon performance by $\approx 21\%$ in terms of ionization cost. Both the electron density and temperature are increased due to moving the dump-plate inwards. The dump-plate was originally positioned far away from the helicon antenna with the intention of reducing the particle flux and impurity production from the dump-plate. Since reduced impurities in MPEX is an important aspect of the device, this aspect cannot be neglected. However, alternate methods of reducing impurity production can be implemented, such as neutral gas fueling axially from the dump-plate, and using dump-plate material with a high sputter threshold such as ceramics.

Floating the Dump Plate

Another significant loss term in the 0D model is the power and particle losses due to the presence of the plasma sheath at the boundary of the plasma and the dump-plate. The heat flux to a material wall due to the presence of plasma is given by Eq. 4.23. This heat flux to the material wall is also the heat flux leaving the plasma, and therefore this quantifies the loss of energy from the plasma through the sheath to the material wall.

$$q_{ss} = E_{ion} + E_{atomic} + E_{thermal} \tag{4.23}$$

$$E_{ion} = \Gamma_{se}\left(\frac{1}{2}kT_e + q(\phi_p - \phi_w)\right)(1 - R_E) \tag{4.24}$$

$$E_{atomic} = \Gamma_{se}\left(E_{iz} - W + \frac{1}{2}E_{diss}\right) \tag{4.25}$$

$$E_{thermal} = \Gamma_{se}\left(2kT_i(1 - R_E) + 2\sqrt{\frac{m_D}{(2\pi)m_e}}e^{\left(\frac{q(\phi_w - \phi_p)}{2T_e}\right)}\right) \tag{4.26}$$

The terms in Eq. 4.23 are as follows: E_{ion} is the kinetic energy of the ions accelerated through the plasma sheath. This depends on the flux of incoming ions (Γ_{se}) electron temperature (T_e), the electric potential of the wall (ϕ_w), the electric potential of the plasma (ϕ_p), and the energy reflection coefficient of the material R_E. E_{atomic} is the potential energy of incoming ion, this term depends on the flux of incoming ions (Γ_{se}), the ionization potential of the ion (E_{iz}), the work function of the material (W), and if the gas is a molecule, then the corresponding dissociation energy of the molecule (E_{diss}). $E_{thermal}$ is the convectively transmitted thermal energies of the electrons and ions, this term depends on the flux of incoming ions (Γ_{se}), the ion temperature (T_i), the electron temperature (T_e), the mass of the ions species (m_D), the electron mass (m_e), the electric potential of the wall ϕ_w, and the electric potential of the plasma (ϕ_p). Eq. 4.23 - 4.26, shows the dependence of heat flux to the material wall as a function of electrical bias on the target material. The relations show that as the bias is increasingly negative the thermal flux of electrons is completely repelled while the ion kinetic energy term begins to increase. When the bias increasingly tends towards the plasma potential, the thermal flux of electrons dominates the heat flux to the target, and this increases exponentially until the plasma potential is reached where the entire thermal flux of electrons can freely strike the target plate.

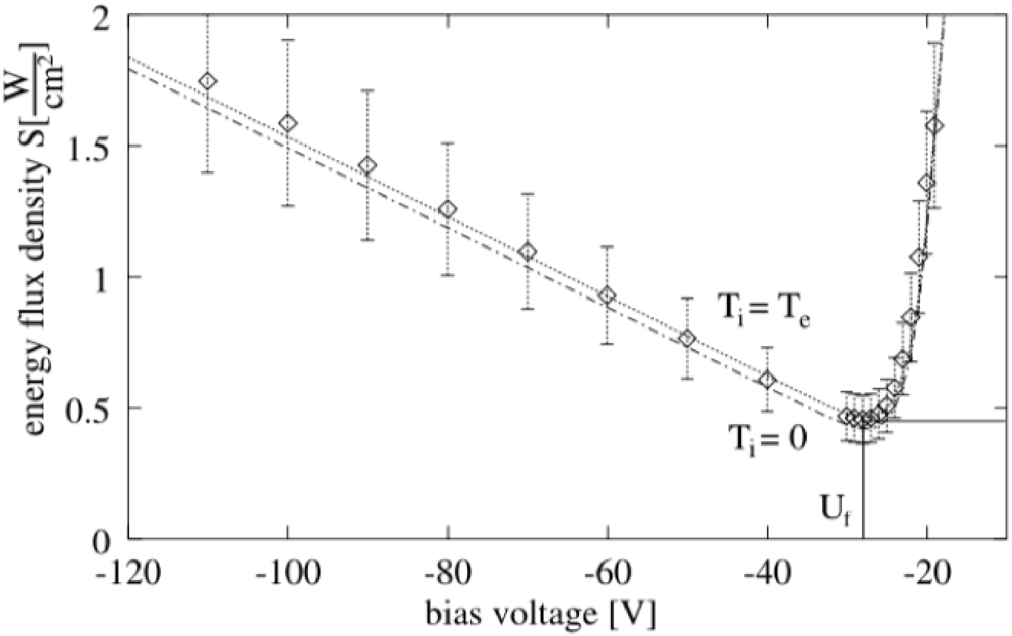

Figure 4.29: Measured energy flux density to a biased target in the presence of an Argon plasma as a function of bias voltage. Theoretical curves of heat flux assuming $\Gamma_{se} = 1.2 \times 10^{19}\ m^{-3}$ and $T_e = 1.8$ eV. Figure taken from Ref. [5].

Figure 4.29 shows the measured heat flux to a biased target in the presence of an Argon plasma as well as theoretical curves of heat flux to a material wall using Eq. 4.23, assuming $\Gamma_{se} = 1.2 \times 10^{19}\ m^{-3}$ and $T_e = 1.8$ eV. This figure shows that there is an electrical bias that reduces the heat flux to the material; the minimum heat flux is at the electrical bias where the term is given by Eq. 4.26 intersects with the term given by Eq. 4.24, this intersection occurs at the floating potential of the wall. Since the heat flux to the wall is minimized by keeping the target material at the floating potential, this means that the heat flux leaving the plasma is also minimized when the target material is biased to the floating potential. Therefore, this understanding could be used in Proto-MPEX to bias the dump-plate and therefore reduce heat flux losses through the sheath to the dump-plate. For the purposes of this model, the sheath heat transmission coefficient is scanned from the value of $\lambda_{se} = 5.5$ to $\lambda_{se} = 1.4$ to investigate the effect of reducing heat losses through the sheath.

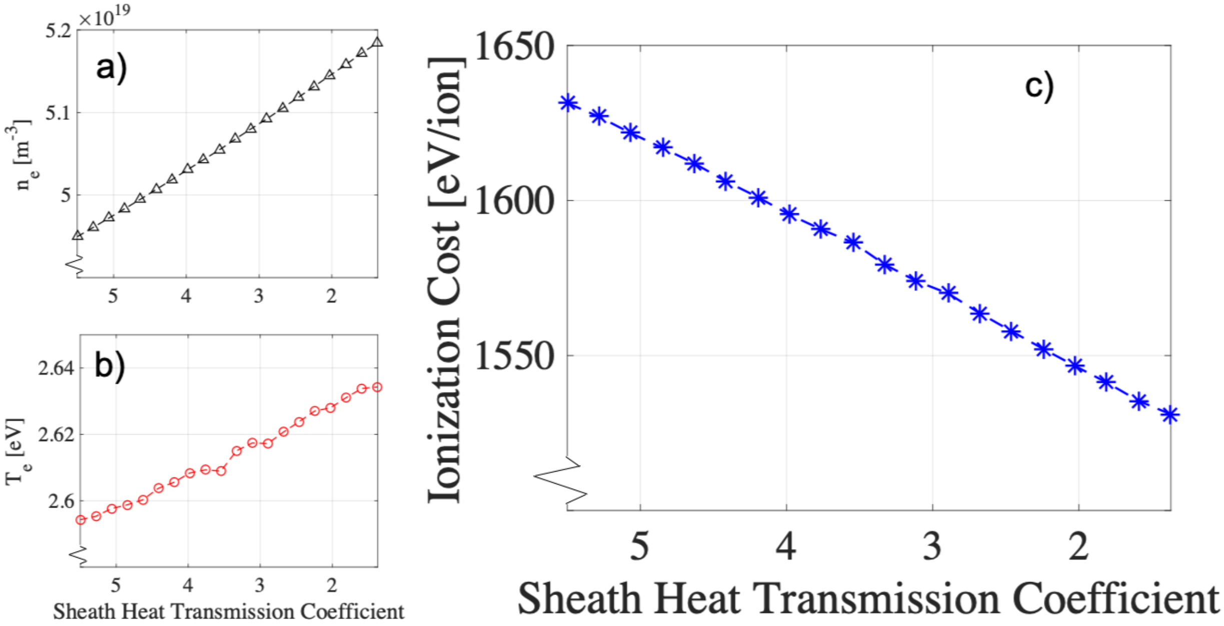

Figure 4.30: Effect of decreasing the sheath transmission coefficient of the dump-plate, accomplished by biasing the dump-plate to the floating potential, on the helicon plasma source's a) electron density, b) electron temperature, and c) ionization cost. Helicon magnetic field is kept constant at $B_H = 0.07$ T.

The dump-plate in Proto-MPEX is currently grounded and therefore not allowed to float electrically. If the plate was electrically isolated to enforce a floating potential exists on the plate this could lead to a reduction of sheath heat losses from the plasma. Figure 4.30 shows the effect of decreasing the sheath heat transmission coefficient, which we estimate to be the effect of changing the bias on the dump-plate and changing it to near the floating potential of the plasma. It's shown here if the heat flux to the dump-plate is reduced by allowing the dump-plate to float electrically and reach the floating potential of the plasma, small improvements can be expected from the helicon performance; improvement of ionization cost is estimated to be $\approx 6\%$. Both the electron density and temperature are increased slightly due to reducing the heat flux to the dump-plate by 75%, which was estimated here by reducing the sheath heat transmission coefficient from $\lambda_{se} = 5.5$ to $\lambda_{se} = 1.4$. The floating potential of the plasma is not experimentally known relative to the ground, and therefore the improvement estimated here is likely a best case scenario.

4.3.4 Discussion

Throughout this section of the thesis, a 0D volume averaged power-particle balance of the helicon source region is introduced and used with integrated core power deposition predicted from the RF simulations to estimate the steady-state helicon performance. First, the particle conservation equations for the neutral gas particles as well as electrons in the plasma are shown along with the energy conservation equations for the ions and electrons. These equations are then volume averaged to reduce them to a 0D set of rate equations for the neutral gas density, electron density, electron pressure, and ion pressure. These equations are integrated until a steady-state solution is reached and coupled to the integrated core power deposition contours predicted by the RF model. The predictions from this model are compared to experimentally measured parameters, namely the electron density dependence on helicon magnetic field strength. This model underpredicts the helicon parameters measured at the helicon source region. However, the electron density dependence on helicon magnetic field strength, in the regime of $0.04 <$ T $B_H < 0.11$ T, is well captured and shows a linear increase in electron density production up until $B_H \approx 0.07$ T and then a deterioration of electron density production. The model, however, predicts another region of increased electron density production in the regime $B_H > 0.11$ T, that is not observed experimentally. This is thought to be due to either the magnetic flux limiting at the chamber wall introducing increasing losses in the plasma column. This issue of the flux limiting at the chamber has since been fixed by power magnetic coil 3 with 600 A; however, experimental exploration of higher density operation has not been performed. This model was determined to adequately capture the physics in the helicon source region, so it is then used to quantify the expected improvement in the performance of the helicon source region from suggested optimization suggestions. These optimization suggestions include: 1) Increasing the RF power and operating at a higher magnetic field strength which increases the electron density and temperature in the helicon source and decreases the ionization cost of the source by $\approx 36\%$. 2) Reducing the volume of the helicon source region by moving the dump plate inwards, also is shown to increase electron temperature and density in the source region which leads to an improvement in ionization cost of $\approx 21\%$. 3) Electrically isolating the dump-plate to allow the plate to stay at the floating potential is estimated to improve ionization cost only slightly by $\approx 6\%$ in the best case scenario. If these improvements are taken together and the helicon source is operated at a magnetic field of $B_H = 0.20$ T then the model predicts an improvement in ionization efficiency (decrease in ionization cost) of $\approx 55\%$. These improvements will bring the ionization costs of the Proto-MPEX helicon source closer to that of VASIMR. These optimization suggestions of the helicon plasma source are planned to be explored in the 2019 experimental campaign but have not been so yet.

Chapter 5

Ion Heating by the Ion Cyclotron Antenna

5.1 RF Wave Propagation and Heating

5.1.1 Dispersion Analysis

Understanding the dispersive properties of the plasma column is critical to interpreting full-wave simulations. The dispersion relation can be formulated by solving a 0D Helmholtz equation using the dielectric tensor given by Eq. 3.107. Assuming knowledge of the parallel wave number, $k_{\|}$, the solutions to the dispersion relation are a bi-quadratic equation to which the approximations of the two roots are given by

$$k^2_{\perp_{FW}} = \frac{(k_0^2 R - k_{\|}^2)(k_0^2 L - k_{\|}^2)}{k_0^2 S - k_{\|}^2}, \tag{5.1}$$

and

$$k^2_{\perp_{SW}} = \frac{P}{S}(k_0^2 S - k_{\|}^2). \tag{5.2}$$

With Eqs. 5.1 and 5.2, we can now understand the perpendicular propagation characteristics of the waves that have a parallel wave number driven by the ICH antenna geometry. The perpendicular wave number of the wave solved for by Eqs. 5.1 and 5.2 is a complex quantity. The real part gives the perpendicular wave number while the imaginary part gives the inverse of the damping length. With the dispersion relation, the propagation characteristics of the slow and fast waves can be mapped out to help interpret results from the full-wave simulation. Both the IAW and KAW are found to propagate on the slow-wave branch of the dispersion relation, and therefore, only this branch is analyzed. Lower-hybrid oscillations were described to be efficient sources of electron heating at the Alfvén resonance in Ref. Timofeev2015, which analyzed the VASIMR beach heating scenario. These lower hybrid oscillations are described by the fast-wave branch of the dispersion relation. While typically the slow-wave branch of the dispersion relation contains larger $k_\perp$ than the fast-wave branch, near the Alfvén resonance the slow-wave branch experiences a decrease in

$k_\perp$ toward zero and the fast-wave branch's $k_\perp$ increases towards infinity. Therefore, the two branches of the dispersion relation reach a confluence near the Alfvén resonance, which could lead to efficient mode conversion between the two branches[67], and therefore strong electron heating at the Alfvén resonance.

The regions of propagation of the IAW and the KAW are discussed in Section 5.1.1. In Section 5.1.1 we discuss how electron temperature affects the wave propagation of the IAW and KAW. Next, a discussion of the energy access of the IAW to the core plasma is presented in Section 5.1.2 where we show that the IAW is restricted to the periphery of the plasma due to the small group velocity angle relative to the magnetic field.

Regions of Propagation

To help interpret the results from the full-wave simulation, we first solve the dispersion relation to understand the propagation characteristics of the plasma waves of interest. The relevant contours in the ICH region are the Alfvén resonance ($n_\parallel^2 = S$) and the ion cyclotron resonance ($\omega_{ci} = \omega$). The ion cyclotron resonance acts to strongly damp left-hand polarized waves and transfers the wave's energy to heat ions. The Alfvén resonance acts to cut off the IAW and KAW, therefore separating the regions of propagation of both waves. The IAW propagates on the low electron density side of the plasma column, the KAW propagates on the high electron density side at values of electron temperature that allow the electron thermal velocity to exceed the axial phase velocity of the wave. However, Proto-MPEX's ICH antenna operates in a regime where the thermal velocity is close to the parallel phase velocity of the wave and therefore both waves are expected to play a role in the heating.

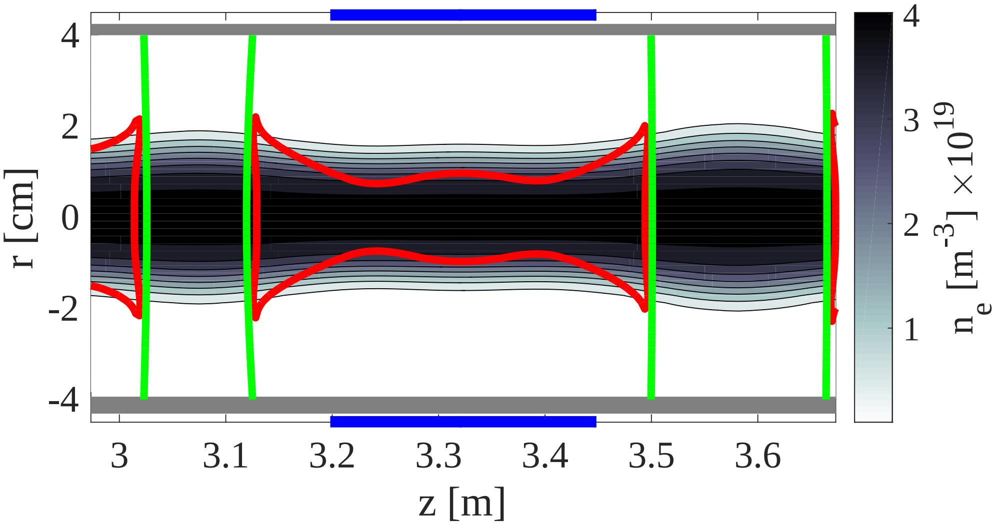

Figure 5.1: Schematic of the ICH region in Proto-MPEX. The electron density profile in the ICH region is shown. The green contours represent the magnetic field value at which the ion cyclotron resonance at 7.5 MHz driving frequency exists. The red contours are locations of the Alfvén resonance at $k_{\|} = 20\ \text{m}^{-1}$. The ICH antenna is represented by the solid blue line and is separated from the plasma by an alumina tube which is represented by the grey line.

Figure 5.1 shows a 2D schematic of the ICH region with the relevant contours drawn. The relevant contours that are depicted in Fig. 5.1 are the fundamental ion cyclotron resonance ($\omega = (2\pi)7.5$ MHz), depicted by the solid green lines, and the Alfvén resonance, which is depicted by the red contour lines. The contours of the Alfvén resonance have a dependence on the electron density, magnetic field strength, and parallel wave number. For the simulation of interest in this paper, the Alfvén resonance acts to restrict access of the IAW from the core plasma and confine the KAW to the core plasma.

Electron Temperature Effects

Electron temperature affects the propagation characteristics of both the IAW and KAW. However, in our regime, the KAW is affected more than the IAW by electron temperature. Figure 5.2 shows the calculation of the real part of $k_{\perp}$ as a function of electron density from Eq. 5.2. The electron density covers the range expected across the plasma column in the Proto-MPEX ICH region. The calculation is made for several values of T_e relevant to current and future experimental scenarios in Proto-MPEX.

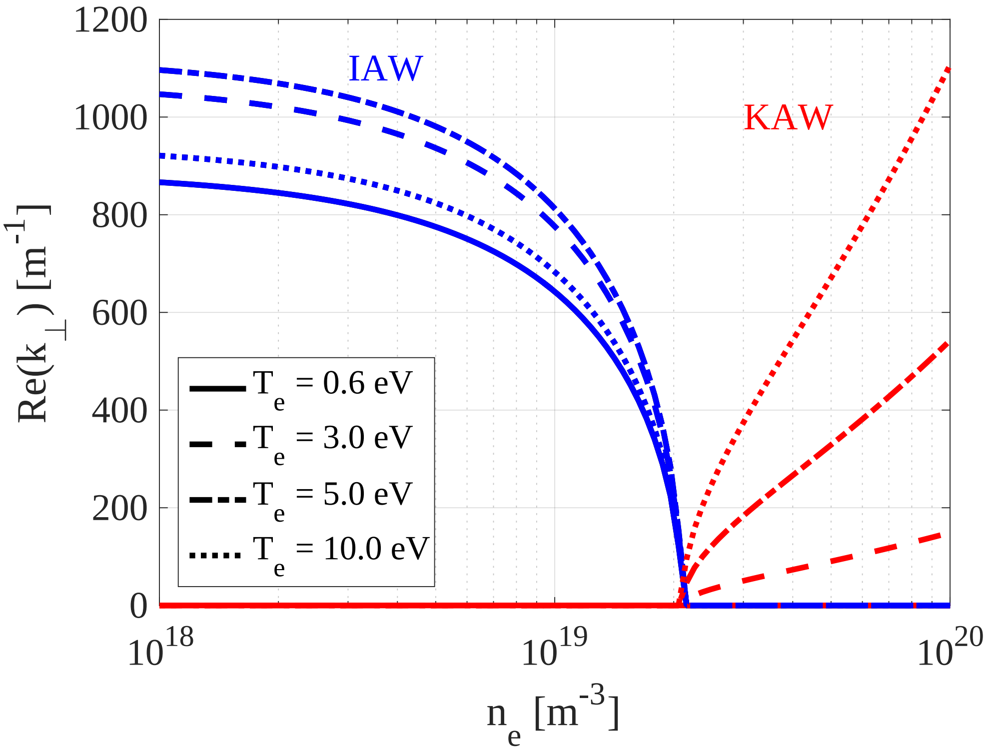

Figure 5.2: Dispersion calculations of Re($k_\perp$) as a function of electron density for several values of electron temperature. The inertial Alfvén wave (IAW) is depicted by the blue curves and it is calculated from the slow-wave branch of the dispersion relation when $S < n_\parallel^2$. The kinetic Afvén wave (KAW) is depicted by the red curves and it is calculated from the slow-wave branch of the dispersion relation when $S > n_\parallel^2$. The dispersion relation is solved assuming $k_\parallel = 20$ m^{-1}, $\omega = (2\pi)7.5$ MHz, $B_0 = 1.2$ T.

The dispersion calculation presented shows that the IAW is cut off from the core plasma at the Alfvén resonance, which occurs for electron density values of $n_e \approx 1 \times 10^{19}$ m^{-3} at a magnetic field strength of $B_0 = 1.2$ T. The plot shows that Proto-MPEX operates in a regime where the KAW begins to propagate. The IAW does not propagate when T_e is very large, such that $v_{th_e} \gg \omega/k_\parallel$. However, for the conditions of Proto-MPEX this regime of T_e is not accessible and therefore Proto-MPEX operates in a temperature regime where the physics of both the IAW and KAW are relevant. Therefore, a cold plasma model cannot be used to accurately model the ICH region, and the effect of electron temperature is necessary to describe the wave propagation in the ICH region. In Section 5.1.3 we investigate the effect of electron temperature on predicted core ion power absorption from the 3D numerical simulations.

5.1.2 IAW Group Velocity Restriction

The group velocity of an electromagnetic wave describes the direction in which the wave's energy propagates. In materials with complex dielectric properties, such as a plasma, the group velocity of the wave is not necessarily parallel to its phase velocity. To understand the propagation of the plasma wave's energy we utilize an expression for the angle between the phase velocity and the group velocity, α, which is written as

$$\tan\alpha = -\frac{1}{k}\frac{\partial k}{\partial\theta}, \tag{5.3}$$

and can be found in Ref. Swanson2003book. The dispersion relation for the IAW is given by Eq. 5.2. For simplicity we reduce the STIX tensor components in Eq. 5.2 to those of the cold plasma tensor. Full-wave simulations do not indicate significant temperature effect on the group velocity of the IAW, so for the purpose of this section this assumption will be sufficient. The angle between the phase velocity and the magnetic field is defined as $\tan\theta = k_\perp/k_\parallel$. Eq. 5.3 requires us to express the dispersion relation in terms of $k(\theta)$ as

$$k^2 = -\frac{Sk_0^2\omega_{pe}^2}{-\omega_{pe}^2\cos^2\theta + S\omega^2\sin^2\theta}. \tag{5.4}$$

The angle between the group velocity and the phase velocity is then

$$\begin{aligned}\alpha = \tan^{-1}\Bigg[&-\frac{1}{k}\frac{(S\omega^2+\omega_{pe}^2)\cos\theta\sin\theta}{Sk_0^2\omega_{pe}^2}\\ &\left(\frac{Sk_0\omega_{pe}^2}{\omega_{pe}^2\cos^2\theta - S\omega^2\sin^2\theta}\right)^{3/2}\Bigg].\end{aligned} \tag{5.5}$$

Therefore, the angle between the group velocity and the magnetic field is $\Psi = \alpha + \theta$.

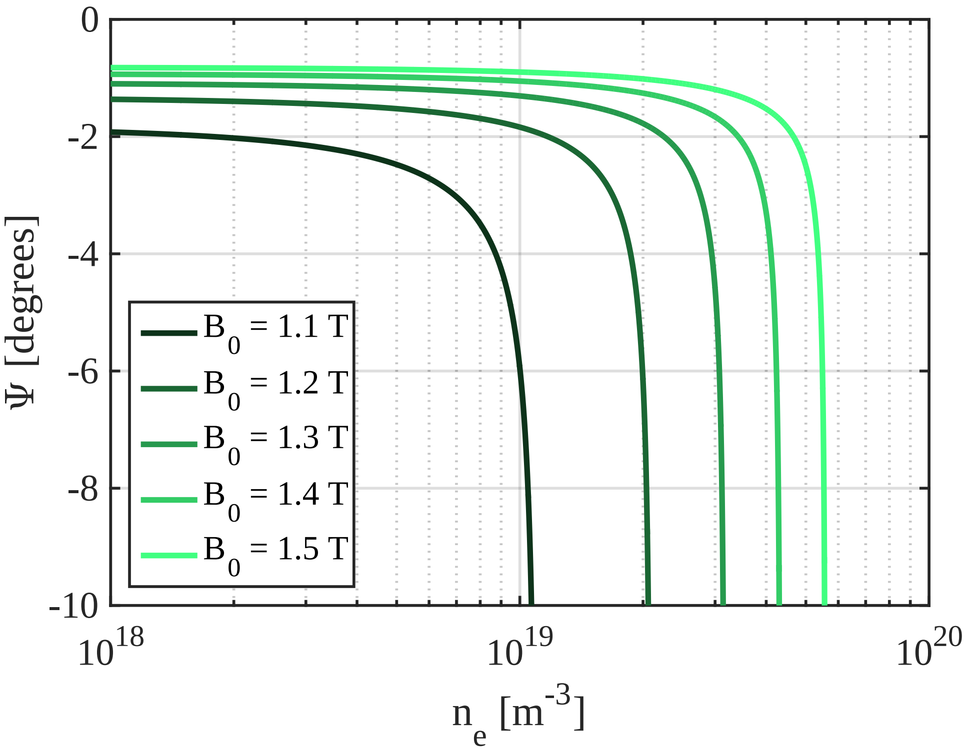

Figure 5.3: Calculations of the angle of the IAW group velocity from the magnetic field (Ψ), as a function of electron density for several values of magnetic field strength ($B_0 = 1.1$–1.5 T).

Figure 5.3 shows that before the IAW encounters the Alfvén resonance it propagates at a narrow group velocity angle with respect to the magnetic field. This acts to restrict the energy of this wave to the periphery of the plasma column and therefore prevents its energy from penetrating into the core plasma for Proto-MPEX's current geometry and operating frequency range. This is the primary reason that the IAW cannot couple power into the plasma core to heat ions there. The simulation results in the following section will show that the power deposition of the IAW is restricted to the periphery of the plasma, and power that is coupled to the core plasma is due to the excitation of the KAW.

5.1.3 Simulation Result

In this section, we show the results of the 3D full-wave simulation. First, we present a calculation for electron and ion power absorption and show contour plots of power deposition in the ICH heating region for each species. Next, we discuss the effect of increasing the electron temperature in the simulation from $T_e = 0.6$ eV to $T_e = 10$ eV. We show that by increasing the electron temperature the simulation predicts increased core ion heating. Contours of ion power deposition are presented at several values of electron temperature to show that plasma heating associated with the IAW is located in the periphery of the plasma and that core heating is due to the excitation of the KAW. Finally, the dependence of core ion heating on edge electron density is presented along with a discussion on the excitation mechanisms of the KAW.

Electron vs. Ion Heating

Past experiments on Proto-MPEX[69] and the Tara tandem mirror device[55] showed evidence of direct electron heating during ICH beach heating. The ICH antenna on Proto-MPEX is designed to directly heat the ions, therefore, it is useful to predict which species in the plasma are being heated by the rf to optimize the heating configuration for ion heating. The main diagnostics used to measure ion heating in the plasma are IR thermography [83] of the target plate and Ar II spectroscopy [69]. The IR thermography gives a 2D view of the power deposition on the target plate. However, this measurement cannot distinguish if the increased power to the target is due to increased ion energy in the bulk plasma or to increased electron temperatures. The Ar II spectroscopy directly measures the ion temperature. Since this is a line integrated measurement there is uncertainty in the radial location contributing to the ion temperature measurements. Therefore, calculations of the energy absorbed by the electrons vs. the ions can help explain the experimental measurements, as well as optimize the configuration for ion heating.

The power deposition mechanisms that are captured by the dielectric tensor used in the model are collisionless Landau damping, fundamental cyclotron resonance absorption, and collisional damping. For the case of collisional damping the collision frequency is calculated from Coulomb collisions for both electrons and ions, and electron-neutral collisions with deuterium molecules ($n_0 = 3.2 \times 10^{18}$ m^{-3}). The electron collision frequency in Proto-MPEX is shown to be very large ($\nu_{ei} > \omega$) [47], and therefore contributes significantly to the power absorption. Non-collisional electron heating (Landau damping) is also important in the ICH region because the ICH antenna operates such that $v_{p_\parallel} \approx v_{th_e}$. The Alfvén resonance is a location where strong electron heating is predicted to occur by both Landau and collisional damping[64, 65, 66, 67, 118]. The lower hybrid resonance layer in our geometry is located physically close to the ion cyclotron resonance at a lower magnetic field, enhanced electron heating can be expected near this layer. The ions are expected to be heated primarily by the resonant absorption of the wave at the fundamental ion cyclotron resonance. The power deposited to electrons and ions can be found by separately calculating the electron and ion currents from the expected conductivity due to each species. The conductivity due to each species is calculated from the Stix tensor, while only including the species of interest in the summation. Then using Ohm's law, the power absorbed by the electrons and ions independently is,

$$P_{e,i} = \mathbf{J}_{e,i} \cdot \mathbf{E}, \tag{5.6}$$

where

$$\begin{aligned}
\mathbf{J}_{e,i} &= \boldsymbol{\sigma}_{e,i} \cdot \mathbf{E}, && (5.7)\\
\boldsymbol{\sigma}_{e,i} &= i\omega\epsilon_0 \left(\mathsf{I} - \mathsf{K}_{e,i}\right). && (5.8)
\end{aligned}$$

$\mathbf{J}_{e,i}$ is the induced current and $\boldsymbol{\sigma}_{e,i}$ is the conductivity tensor associated with either electrons or ions. $\mathsf{K}_{e,i}$ is the plasma tensor given by Eq. 3.107 but retaining only the terms in the summations that represent the species of interest.

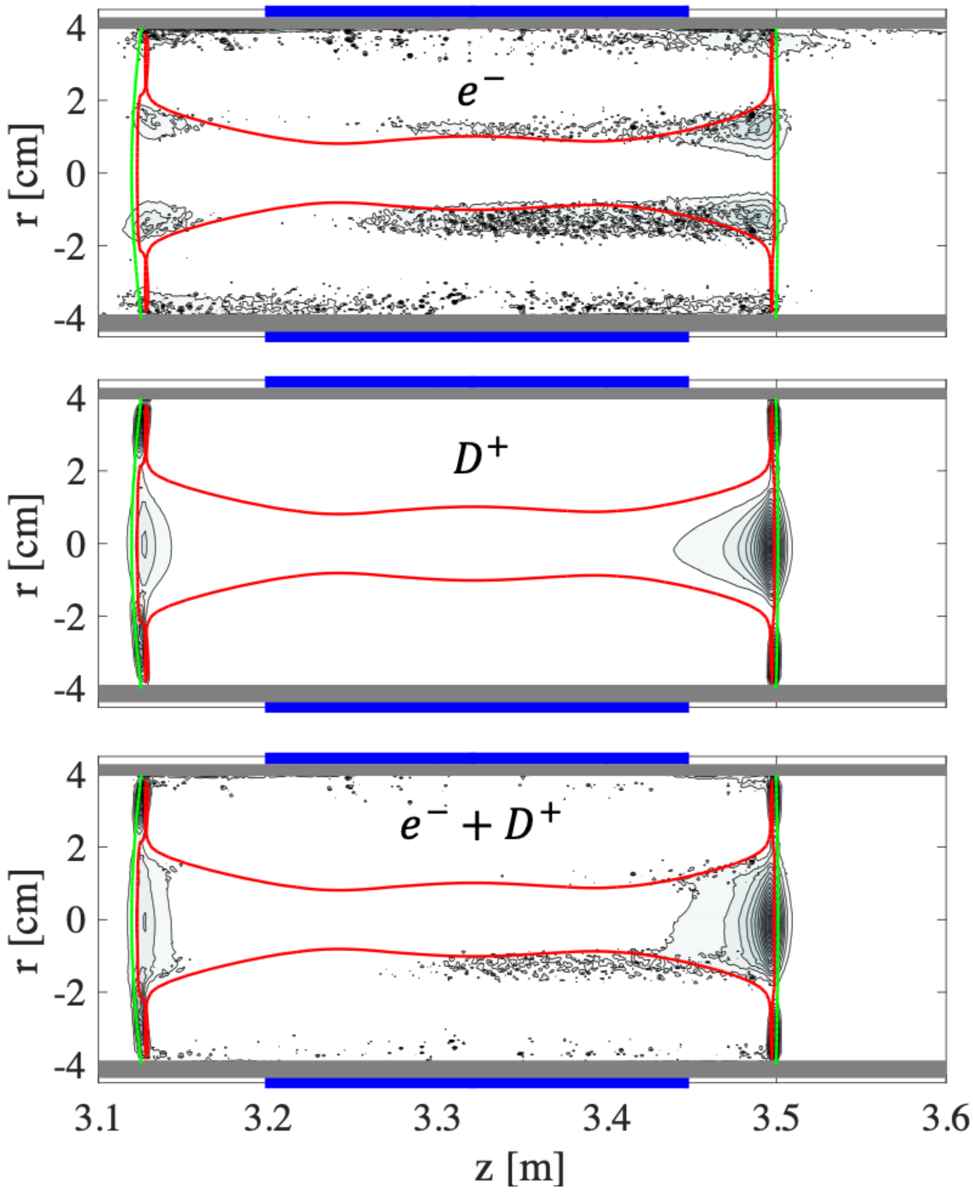

Figure 5.4: YZ plane contours of the normalized rf power absorption in the plasma by electrons only (top), ions only (middle), and by both ions and electrons (bottom). These calculations of the rf power absorption are from the 3D full-wave for an electron temperature of $T_e = 2.1$ eV. Contours of the Alfvén $k_\parallel^2 = (20\ \mathrm{m}^{-1})^2 = k_0^2 S$ are depicted by the red line, while contours of the fundamental ion cyclotron resonance $B_{IC} = \omega m_i/q$ are depicted by the green lines.

Figure 5.4 shows the contours from the calculation of the rf power absorption by the species present in the plasma. Interpreting these contours reveals the dominant power absorption mechanisms during ICH experiments. The ion power absorption is predominantly located at the fundamental cyclotron resonance location. The electron power absorption seems to occur in the periphery of the plasma column and at the Alfvén resonance and there is an enhancement of electron power deposition near the ion cyclotron resonance which we attribute to the presence of the lower hybrid resonance. Since electron absorption in Proto-MPEX is not negligible, there is an advantage to keeping the ion cyclotron resonance location in close proximity to the ICH antenna if efficient ion heating is desired. The proximity of the ion cyclotron resonance prevents the RF wave from being damped by the electrons before it reaches the resonance location, where it couples power to the ions. If electron heating is desired, moving the ion cyclotron resonance away from the plasma may be a viable route to heating electrons with low-frequency RF.

Electron Temperature Effect on Core Ion Heating

The effect of electron temperature on the ion heating efficiency in the core plasma, defined as $\chi < 0.6$, is important to understand to design an ICH system for MPEX. The IAW is not expected to contribute significantly to heating the plasma core due to the group velocity restriction explained in Section 5.1.2. Also, for the magnetic field and driving frequency used, the IAW is cut off from the core by the Alfvén resonance. Increasing the magnetic field at the ICH antenna can act to remove the Alfvén resonance from the plasma column. However, this does not increase the core power deposition from the IAW because of the proximity of the ion cyclotron resonance and the group velocity restriction on this wave. Therefore, observations of core ion heating are attributed to coupling to the KAW. Since the excitation of the KAW has an electron temperature dependence as shown in Fig. 5.2, the core ion heating efficiency of the ICH is also expected to have a dependence on electron temperature.

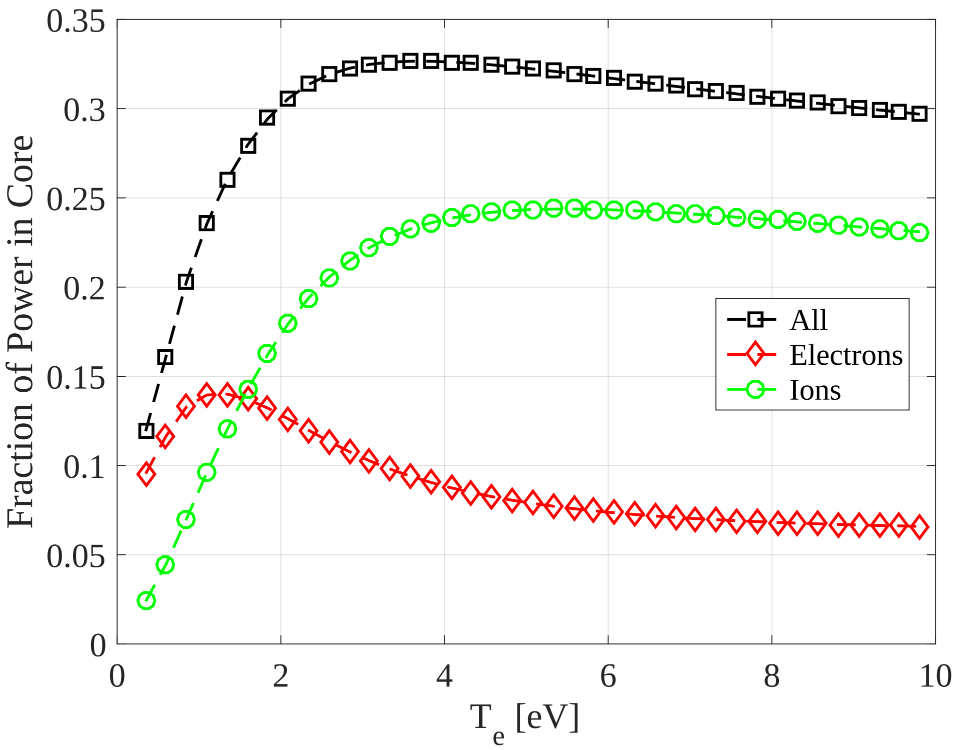

Figure 5.5: Integrated core power deposition for both ions and electrons (black squares), ions only (green circles), and electrons only (red diamonds) is normalized to the total power deposited in the simulation domain plotted as a function of electron temperature.

Figure 5.5 shows the integrated power absorbed in the core plasma and the division of this absorbed power by each species (electrons and ions) as a function of electron temperature. The core ion power deposition increases with electron temperature until $T_e \approx 5$ eV where it begins to slightly decline. The core electron power deposition is at its maximum at $T_e \approx 1$ eV. This is most likely due to a balance between excitation of the KAW in the core (which is responsible for heating electrons in the core near the Alfvén resonance) and a decreasing collision frequency. At electron temperatures of $T_e > 2$ eV, rf absorption by the ions dominates the absorption by the electrons, and for electron temperature $T_e > 4$ eV we calculate $\approx 80\%$ of the power delivered to the core is attributed to ion heating.

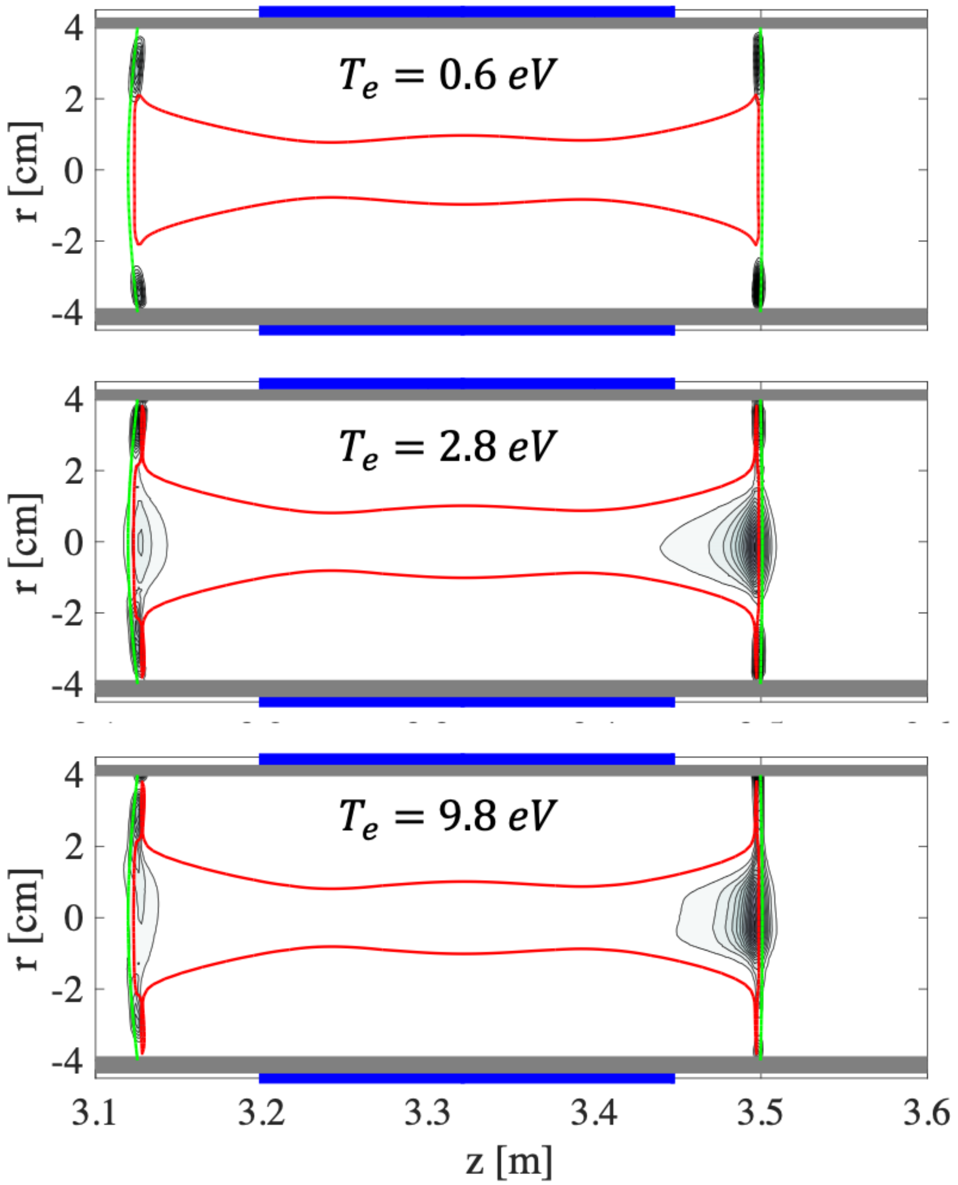

Figure 5.6: YZ plane contours of the normalized rf power absorbed by the ions (P_i) shown for increasing values of electron temperature $T_e = 0.6$ eV (top), $T_e = 2.1$ eV (middle), and $T_e = 9.8$ eV (bottom). Contours of the Alfvén $k_\parallel^2 = (20\ m^{-1})^2 = k_0^2 S$ are depicted by the red line, while contours of the fundamental ion cyclotron resonance $B_{IC} = \omega m_i / q$ are depicted by the green lines.

Figure 5.6 shows where the ion power is deposited in the simulation domain as the electron temperature varies from a cold plasma ($T_e = 0.6$ eV) to a plasma with higher electron temperature ($T_e > 2$ eV). The Alfvén resonance is depicted by the red contour line and, as was explained in Section 5.1.1, this boundary acts to separate the region where the IAW can propagate from the region where the KAW propagates. The green contours are the location of the fundamental cyclotron resonance, and we see that the ion power absorption takes place near the resonance. For the case of colder plasmas, we see that the ion power absorption is only present in the periphery of the plasma column in the region where the IAW propagates. As T_e is increased above 2 eV, power absorption in the core plasma begins to increase. This power absorption region is separated from the absorption in the periphery by the Alfvén resonance, which provides further evidence that the power absorption in the periphery of the plasma is attributed to the IAW and the power absorption in the core plasma is attributed to the KAW.

Dependence on Edge Electron Density

Figure 5.7 shows the fraction of power in the core plasma coupled to electrons, ions, and both species as a function of edge electron density ($n_{e_{edge}}$). This figure shows a significant increase in core power deposition when the edge electron density is increased up until $n_{e_{edge}} \approx 2{\times}10^{18}$ m^{-3}, then a slight decrease in coupling is observed. Values of edge electron density above $n_e > 10^{18}$ m^{-3} begin to affect the propagation characteristics of the KAW in the core plasma and are unlikely to be experimentally relevant. However, the numerical effect of the higher edge electron density on core power deposition is enlightening for understanding the coupling of rf power to the KAW. Below $n_{e_{edge}} < 1 \times 10^{17}$ m^{-3} the amount of core power deposition becomes less than 5%, while $n_{e_{edge}} = 1 \times 10^{18}$ m^{-3} shows $\approx$ 30% of the total power being coupled to the core. The edge electron density profile in Proto-MPEX is not well known, but it seems an important consideration for coupling ICH power into the core plasma.

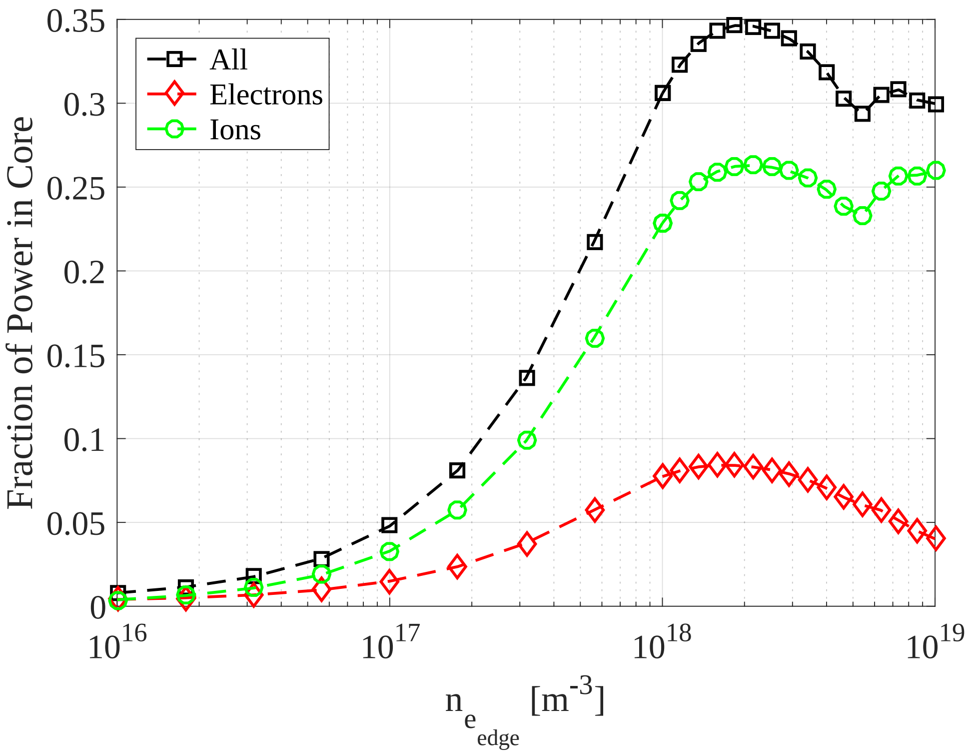

Figure 5.7: Integrated core power deposition for both ions and electrons (black squares), ions only (green circles), and electrons only (red diamonds) is normalized to the total power deposited in the simulation domain plotted as a function of electron density in the edge ($n_{e_{edge}}$). Electron temperature is set to $T_e = 5$ eV.

The excitation mechanisms of the KAW are important to understand in order to optimize the ICH antenna for core ion heating. The candidate excitation mechanisms for the KAW are either from evanescent near fields under the antenna or transition of the IAW to the KAW. When considering the transition of the IAW as the excitation mechanism of the KAW the energy access of the IAW becomes an important consideration. The group velocity of the IAW is almost parallel to the magnetic field for the field strength directly under the antenna. Therefore, the most likely location for the transition to occur would be near the ion cyclotron resonance. This is because the group velocity of the IAW becomes increasingly perpendicular to the magnetic field as the wave approaches the Alfvén resonance, and the Alfvén resonance is moving to lower values of electron density as the wave approaches the ion cyclotron resonance, this trend is shown in Fig. 5.3. When considering evanescent excitation of the KAW, the size of the evanescent gap, the region of plasma density where $n_{\parallel}^2 \geq S$), would determine the efficiency of coupling RF power into the KAW. Changing the inner diameter of the ceramic tube effectively changes the evanescent gap size in the simulation domain. Reducing the evanescent gap by 2 cm increased power coupling by $\approx 5\%$. The increase in coupling was linear and not very effective. If the KAW was excited through evanescent fields directly under the antenna, an exponential increase in power coupling would be expected.

The dependence on edge electron density shown in Fig. 5.7 supports the idea that the excitation mechanism of the KAW is via a transition that occurs near the ion cyclotron resonance. The idea is that at higher values of electron densities, up until the Alfvén resonance layer, the group velocity of the IAW becomes increasingly perpendicular. Exploring this mechanism further, and confirming the physics of the dependence on edge electron density is outside of the scope of this paper and will be left for future work.

5.1.4 Experimental Observations of RF Heating

In this subsection, we describe measurements of target heat flux and line of sight measurements of ion temperature at the Spool 9.5 to infer where RF heating of the ICH is taking place. We first present evidence of periphery dominated heating by the ICH during the 2016 experimental campaign. With the preliminary understanding of the wave propagation, a cold plasma model was then used to suggest a scenario that moves the ion cyclotron resonance away from the antenna to allow the inertial Alfvén wave to access the core plasma. This suggestion however required a major reconfiguration of the magnetic coil geometry. Instead, an experiment was devised to test this theory. This led to the experimental suggestion of lowering the driving frequency from 8.5 MHz to 7.5 MHz and performing magnetic field scans to move the ion cyclotron resonance away from the ICH antenna incrementally. However, these experiments led to a surprising observation of strong core heating. This led to analyzing the kinetic Alfvén wave and realizing that this wave allows energy to access the Proto-MPEX core plasma. Evidence of strong core heating was observed from IR measurements of the target heat flux as well as Ar II Doppler Broadening measurements at different radial lines of sight.

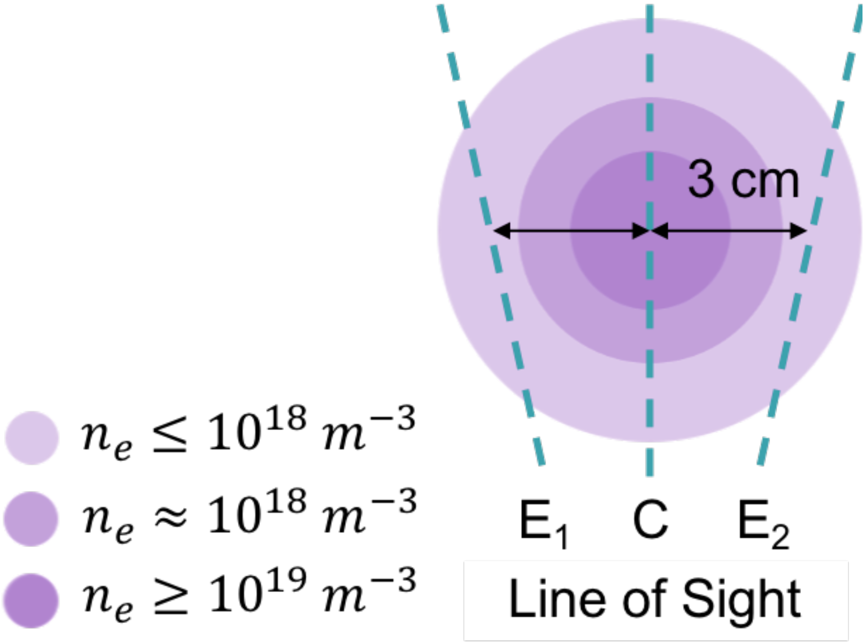

Figure 5.8: Cartoon schematic of lines of sight through the Proto-MPEX plasma column at Spool 9.5.

Figure 5.8 shows a schematic of the line of sight of the Ar II Doppler Broadening measurements reported in this work. E1 and E2 are complementary chord measurements of the edge of the plasma column at passing through a radial chord about 3 cm into the plasma. The Central line of sight labeled C passes through the geometric center of the device.

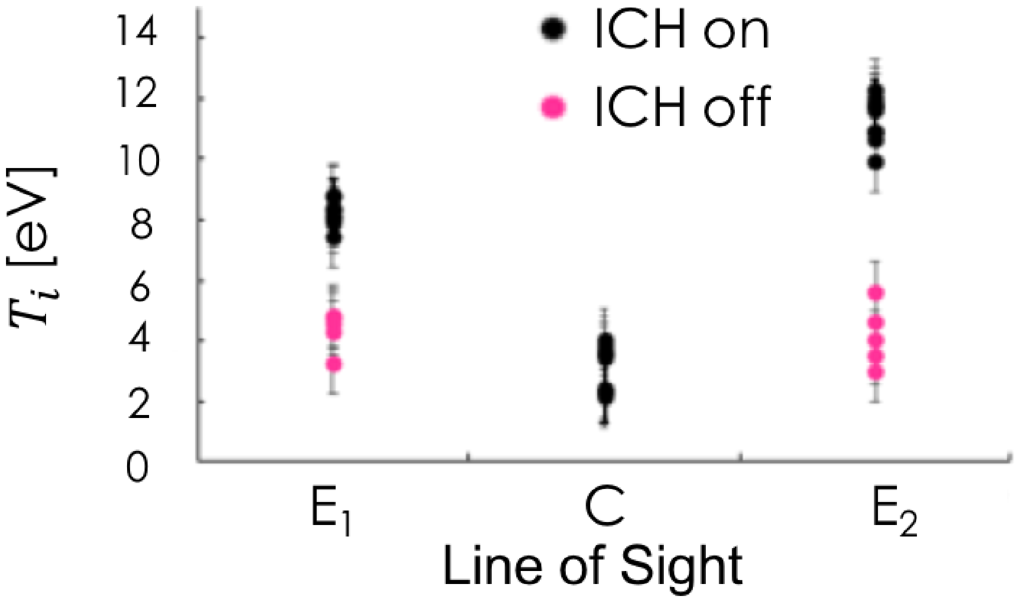

Figure 5.9: Ar II Doppler Broadening Spectroscopy measurements at Spool 9.5 during the 2016 experimental campaign. Experiments were run with magnetic field current of 6000 A producing a magnetic field under the ICH antenna of $B_0 = 1.4$ T, the driving frequency of the antenna was set to $\omega = 2\pi(8.5\ MHz)$, and the applied power was $P_ICH = 16$ kW. Helicon only conditions are depicted by the pink dots, while conditions with the ICH power turned on are depicted by the black dots. The central line of sight has helicon only data points covered by ICH on data points which indicates that no discernible heating along that line of sight was observed.

Figure 5.9 shows the measured ion temperature from the Ar II Doppler Broadening Spectroscopy along the lines of sight shown in Fig. 5.8. This figure shows that only the E1 and E2 lines of sight showed significant heating when the RF power was turned on. The central line of sight has helicon only data points covered by ICH on data points which indicates that no discernible heating along that line of sight was observed. These observations along with IR thermography that only indicated an increase in heat flux in the periphery of the plasma column were indications that the RF heating only acted to heat the periphery of the plasma column and no significant heating of core plasma was observed. These measurements have been published in Ref. Beers2018. This initial experimental campaign motivated the creation of the full-wave model described above to find an experimental scenario which optimized heating of ions in the core plasma. The initial cold wave model was implemented using a cold plasma tensor which only simulates the propagation of the inertial Alfvén wave and cannot simulate the kinetic Alfvén wave. This simulation approach precluded a scenario in the current magnetic field geometry that allowed for reasonable core heating efficiency. The reasons for this was that in scenarios of magnetic field strength under the antenna near the ion cyclotron frequency, the presence of the Alfven resonance in the plasma column cut-off the inertial Alfvén wave from accessing the core plasma. However, for scenarios where the magnetic field strength was raised the shallow group velocity of the inertial Alfvén wave coupled with the proximity of the ion cyclotron resonance location to the ICH antenna, in the current magnetic coil geometry, did not allow wave energy access into the core plasma. Instead of a scenario where the magnetic field coils were reconfigured in the ICH location to move the ion cyclotron resonance far away from the ICH antenna was suggested experimentally. However, since re-configuring the magnetic coils would require a shutdown of the device for an extended period, experiments were instead proposed to move the ion cyclotron resonance only slightly from the antenna to observe if the heating moves radially inwards. During this experimental campaign, significant core heating was observed on both Ar II Doppler Broadening of the central line of sight and increased heat flux in the core plasma measured by the IR camera.

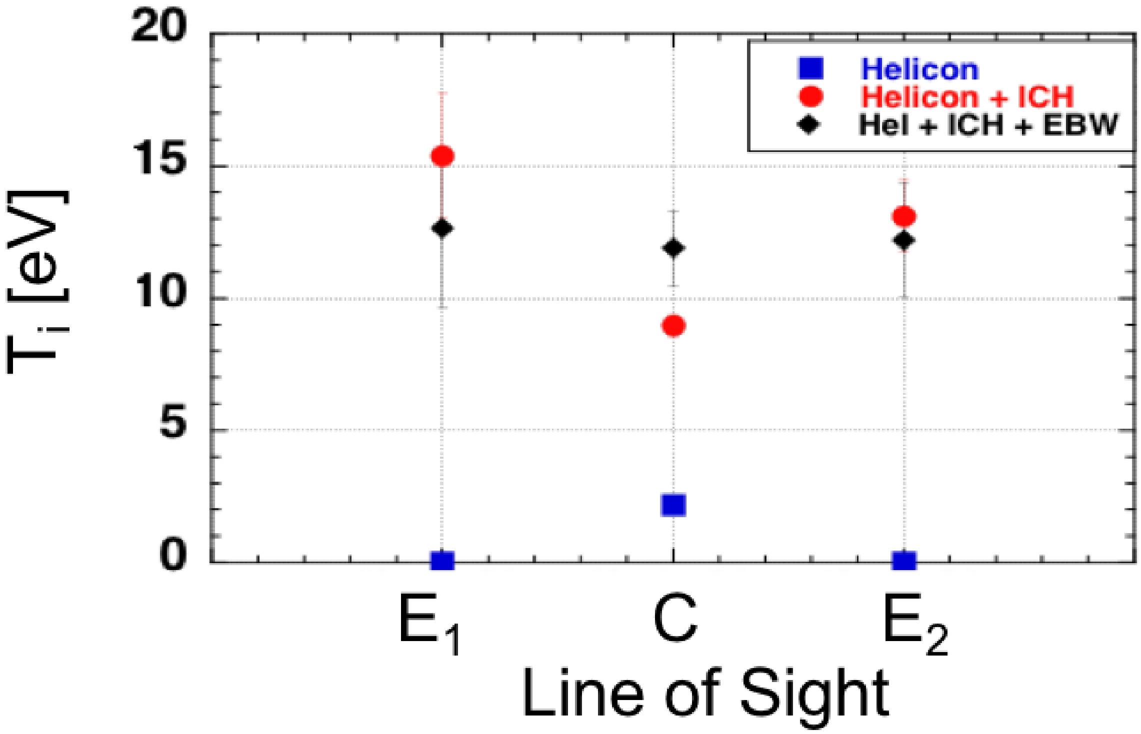

Figure 5.10: Ar II Doppler Broadening Spectroscopy measurements at Spool 9.5 during the 2017 experimental campaign. Experiments were run with magnetic field current of 5800 A producing a magnetic field under the ICH antenna of $B_0 = 1.2$ T, the driving frequency of the antenna was set to $\omega = 2\pi(7.5\ MHz)$, and the applied power was $P_ICH \approx 20$ kW. Helicon only shots are denoted with blue squares, Helicon and ICH pulses are denoted with red circles, and helicon with both EBW and ICH is denoted as black diamonds.

Figure 5.10 shows the measured ion temperature for 3 RF heating scenarios. These heating scenarios are helicon only, helicon with ICH, and helicon with both ICH and ECH. We can see that for that where the experiments run with the conditions in Fig. 5.9 did not show any significant increase of ion temperature in the central line of sight during application of ICH power, the experimental case depicted in Fig. 5.10 show significant increase in ion temperature in the central line of sight when ICH power is applied. Although the ion temperature profile is hollow, the central line of sight is expected to be dominated by the core measurement since the Ar II emission intensity is expected to follow the electron density profile and we have measured the electron density profile to be centrally peaked in Proto-MPEX. When ECH is applied the central line of sight seems to increase in ion temperature while the edge ion temperature decreases. Application of the ECH in these conditions is not expected to significantly increase the electron temperature in the ICH region, as most of the power deposition from the ECH (as inferred by IR thermography) is deposited at the periphery of the plasma, and therefore is expected to modify the edge electron temperature and electron density. Most likely, the applied EBW acts to increase the electron density in the edge plasma and, as predicted numerically and shown in Fig. 5.7, the core heating efficiency of the ICH increases.

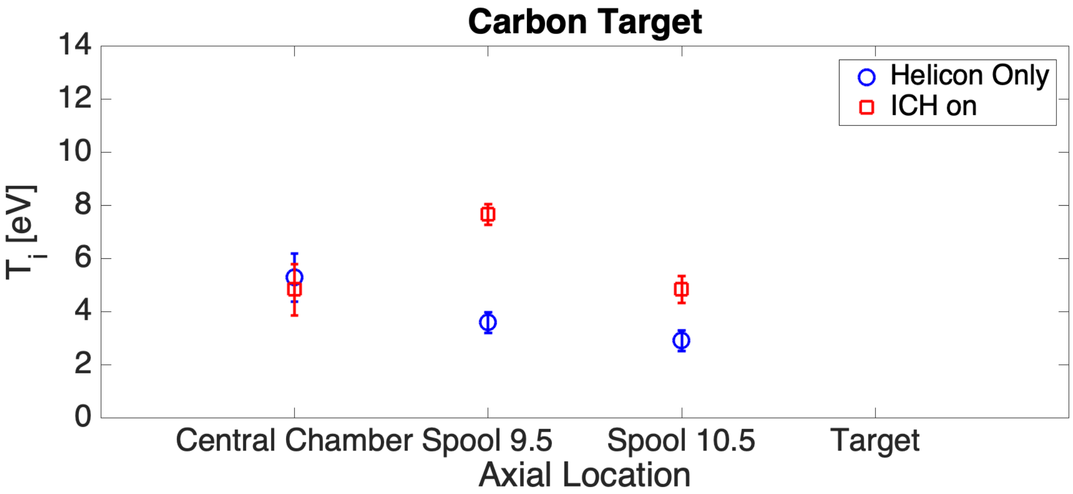

Figure 5.11: Ar II Doppler Broadening Spectroscopy measurements in the central chord along the axis of Proto-MPEX during the 2017 experimental campaign. Experiments were run with magnetic field current of 5800 A producing a magnetic field under the ICH antenna of $B_0 = 1.2$ T, the driving frequency of the antenna was set to $\omega = 2\pi(7.5\ MHz)$, and the applied power was $P_ICH \approx 20$ kW. helicon only data is represented by the blue circles and helicon with applied ICH data is represented with the red diamonds.

Figure 5.11 shows Ar II Doppler Broadening measurements for the central line of sight in different axial locations along with the device. The ICH antenna is located between the Central Chamber and Spool 9.5. From this plot, we see that there is a significant increase in the ion temperature when ICH is applied at the 9.5 measurement location and it decreases the ion temperature decreases as we move away from that measurement location. This indicates that the axial location where the ions are heated is located at Spool 9.5. Spool 9.5 is the first location of the ion cyclotron resonance downstream of the ICH antenna. Since this heating scheme is expected to be a single pass heating, this is the location where the RF power deposition is expected to occur most significantly. From Fig. 5.11 we see that there is no significant ion temperature increase in the central chamber. Since the ion heat transport is expected to be dominated by convection, and the plasma flow is directed towards the target, we do not expect much ion heat to transport back to the central chamber location. The ion temperature is significantly decreased at Spool 10.5 and at the target the ion temperature was too low to measure. This is believed to be caused by charge exchange with neutrals, the density of which is expected to be much higher closer to the target. The next section will describe the effect of neutral gas build up and not having enough pumping between the ICH and the target to remove the neutrals born from plasma recombination at the target. The measurements presented in Fig. 5.10 and 5.11 show that there is core heating and it is peaked where the wave encounters the first ion cyclotron resonance location. This shows a good demonstration that the ICH antenna is heating ions via the fundamental ion cyclotron resonance.

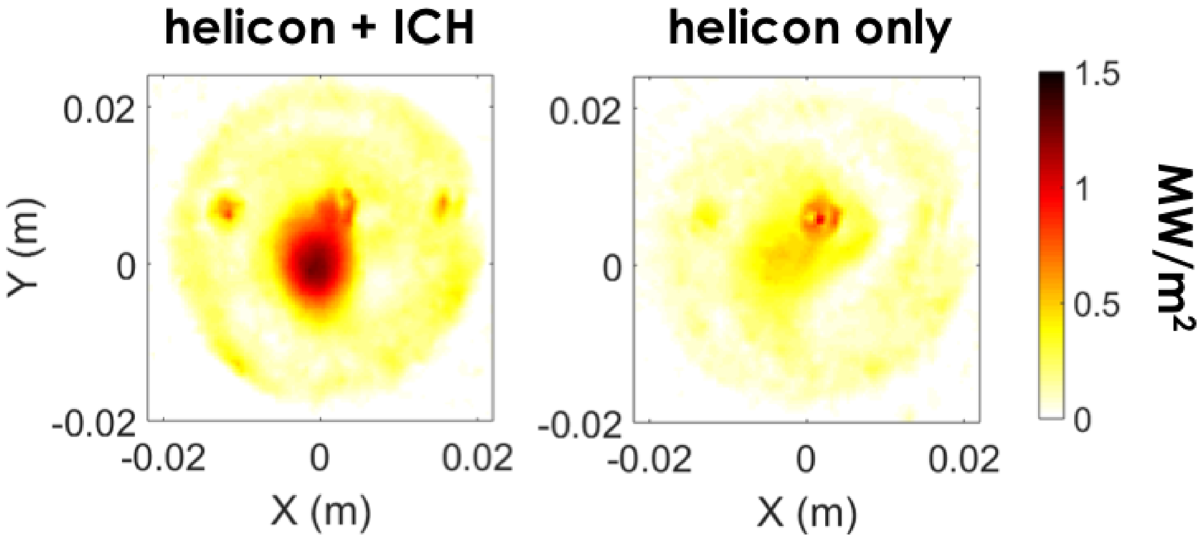

Figure 5.12: Images of target heat flux measured by IR thermography of the heat flux delivered to the target during application of "helicon only" RF power (right) and with the addition of ICH power (left).

Since the spectroscopy measurements are line integrated at these locations the 2D heat flux measurement made by the IR camera is then used to infer the radial distribution of ion heat. Figure 5.12 shows measurements made by the IR camera of the heat flux to the target plate with and without ICH applied power. From this figure, one can see that heat flux increases in the plasma core when RF power is applied. This measurement doesn't discriminate between ion and electron heat but does a good job at showing the 2D distribution of heat, it is a complimentary measurement to the Ar II Doppler Broadening, and with these combined measurements we infer that core heating of ions is taking place during the operation of the ICH antenna.

5.1.5 Measurements of the Kinetic Alfvén Wave

In this subsection, the results of an experiment to measure the RF magnetic fields of the Kinetic Alfvén wave will be reported and discussed. The measurements were made in the old magnetic field configuration. To be able to measure the kinetic Alfvén wave in Proto-MPEX in this configuration the driving frequency of the

ICH antenna had to be dropped to 6.5 MHz and the magnetic field coils had to be operated at the highest current attainable to remove the ion cyclotron resonance from the measurement location. Operating the ICH antenna at 6.5 MHz proved to be a challenging task for the RF transmitter and limited data was able to be taken during the campaign. However, the radial scan B-dot probe measurements ended up successfully measuring a propagating Kinetic Alvén Wave in the ICH region which compared well with simulations of the wave fields from COMSOL.

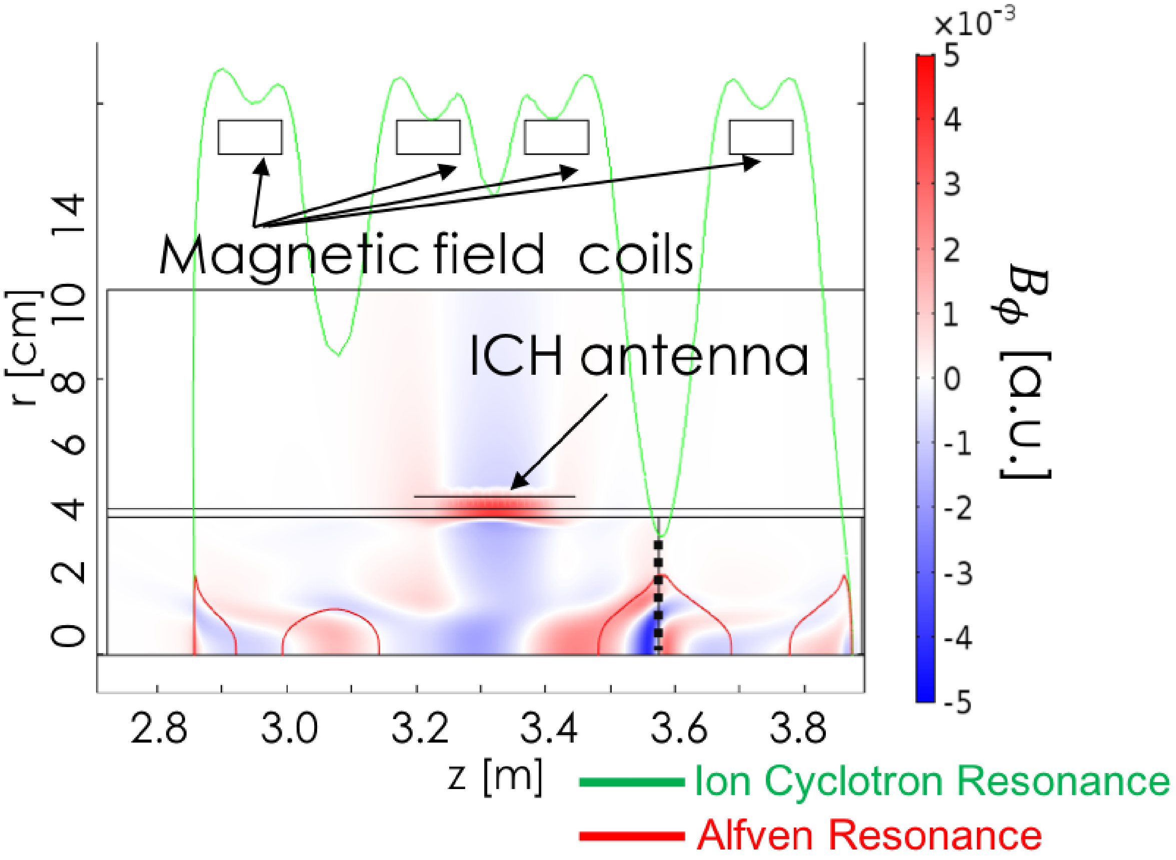

Figure 5.13: Contours of the $\hat{\phi}$ component of the RF magnetic field from COMSOL simulation of the experimental conditions during B-dot probe experiments to measure the Kinetic Alfvén Wave. The simulation was run with 6800 A in the magnetic coil currents, a peak electron density of $n_e = 4 \times 10^{19}\ m^{-3}$, electron and ion temperature of $T_e = T_i = 5$ eV. The green contours in the plot are contours of the ion cyclotron resonance, the red contours are contours of the Alfvén resonance at $k_{\|} = 20\ m^{-1}$. The measurement was taken at an axial location $z = 3.58$ m depicted by the dashed solid black line.

Figure 5.13 shows contours of the azimuthal component of the RF magnetic field calculated by the COMSOL simulation. The contours of the ion cyclotron resonance and the Alfvén resonance are shown in the figure. The measurement location is denoted by the dashed solid black line. It is apparent that the ion cyclotron resonance at these conditions is just barely moved away from the location where the probe accessibility was available. At conditions where the ion cyclotron resonance is not moved away then only the evanescent fields exist in this region. The Alfvén resonance in Fig. 5.13 is depicted by the red contours for a parallel wave-number of $k_{\|} = 20\ m^{-1}$. We see that in the measurement region where we had probe access we expect the Kinetic Alfvén Wave to propagate.

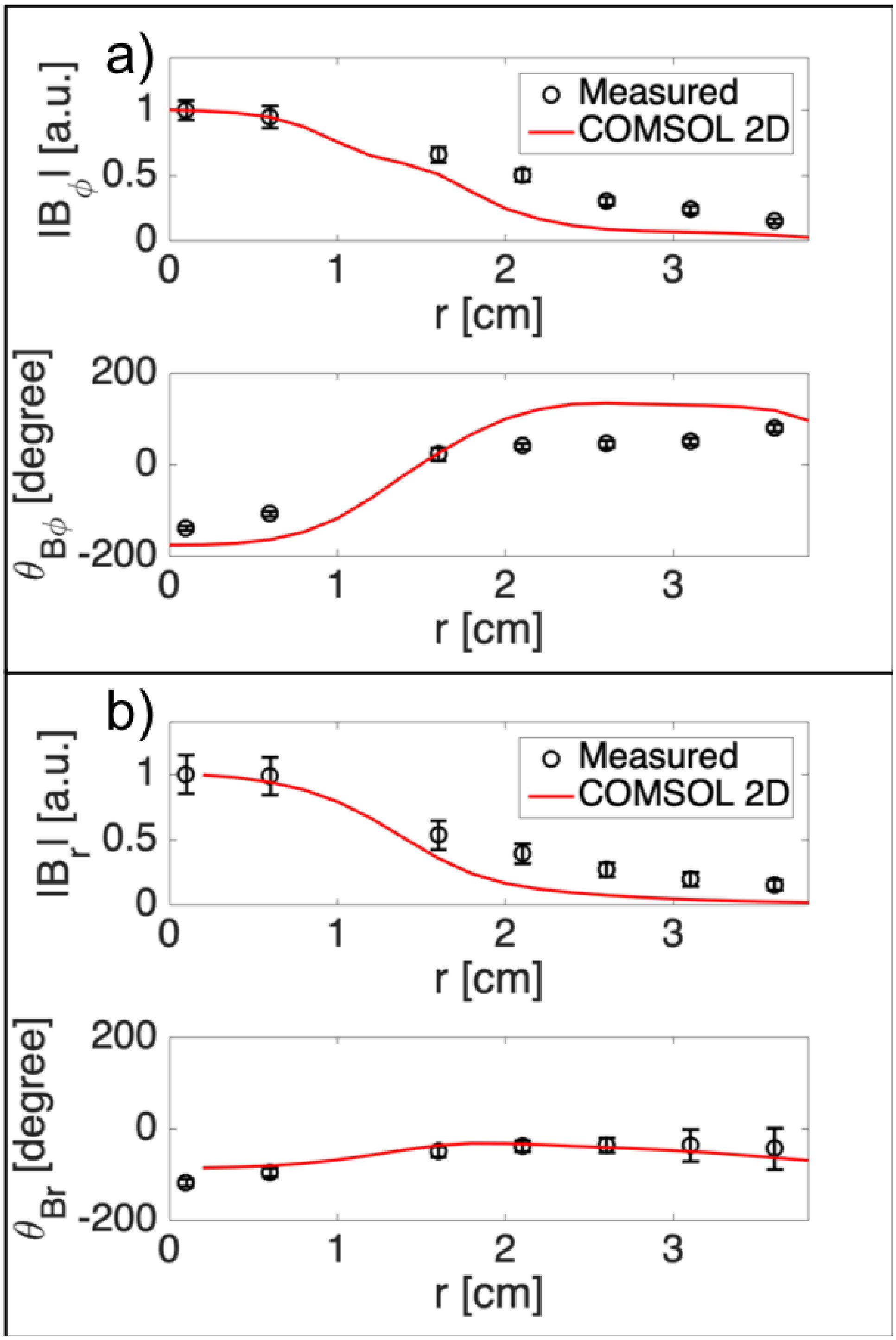

Figure 5.14: a) Measurements of the amplitude (top) and phase (bottom) of the radial ($\hat{r}$) component of the RF magnetic field produced by the ICH antenna in Proto-MPEX. b) Measurements of the amplitude (top) and phase (bottom) of the azimuthal (ϕr) component of the RF magnetic field produced by the ICH antenna in Proto-MPEX. The black circles represent the experimental measurements, the solid red line represents the comparison to the COMSOL simulation result shown in Fig. 5.13.

Figure 5.14 shows the comparison of the simulation shown in Fig. 5.13 with experimentally measured RF magnetic field profiles from Proto-MPEX. We see that the amplitude of both the radial and azimuthal components of the RF magnetic field peak on-axis. This is an indication that there is penetration of wave energy into the core of Proto-MPEX. The phase variation of the azimuthal magnetic field is flat at a radius of $r > 1.5$ cm and then decreases sharply at a radius of $r < 1.5$ cm. From Fig. 5.13 we can see that the Alfvén resonance exists in close proximity to this radial location, the Alfvén resonance causes a sharp change in the dielectric properties of the plasma, and therefore the wave undergoes a change in propagation characteristic. A similar but less pronounced phase variation is observed on the radial component of the RF magnetic field. The comparison of the experimental measurements to the COMSOL simulation is quite good, and the main features of the B-dot probe measurements are captured by the simulation. These features being the central peaking of the wave-fields and the radial phase variation. Several unknowns and uncertainties exist in the Proto-MPEX measurement region, those uncertainties being the value of the peak electron density is not measured in this region and is only measured at the target and at Spool 6.5. The peak electron density used in these simulations ($n_e = 4 \times 10^{19}\ m^{-3}$) are a typical electron density value expected in this region. The current Double Langmuir Probe's used in the device was not designed to measure electron densities lower than $n_e < 1 \rightarrow, es10^{18}\ m^{-3}$ and therefore accurate measurements of the edge electron density profile is something that is not well diagnosed in Proto-MPEX. A flat electron density profile is assumed to exist at the edge of the device all the way out to the ceramic window. With this said these unknowns do slightly alter the RF magnetic fields predicted by COMSOL, by reducing the gradient of the phase decrease or changing the width of the amplitude of the fields, however, the main features that were being looked for in this comparison are retained quite well.

5.1.6 Discussion

The propagation characteristics of the waves in the ICH region in Proto-MPEX have been investigated numerically with dispersion analysis and a 3D full-wave model. This full-wave model made use of a simplified dielectric tensor derived by assuming a linear response of a plasma with a Maxwellian energy distribution function of both the ions and the electrons. The addition of the kinetic effects into the plasma tensor was shown to predict core ion heating. Analysis of the dispersion properties in the ICH region shows that both the IAW and the KAW can propagate in the Proto-MPEX plasma. However, the IAW cannot couple power into the plasma core due to the narrow-angle of the group velocity and the Alfvén resonance restricting its access to the core. This consideration is important for the efficiency of the beach heating on Proto-MPEX since the wave is launched at the periphery of the plasma and cannot access the core if the ion cyclotron resonance is located in close proximity to the antenna as is the case in the current experimental configuration. However, the excitation of the KAW is possible in the temperature regime of Proto-MPEX and opens an avenue for efficient heating of core ions.

The simulation results show that when the edge electron density is sufficiently high ($n_e > 1 \times 10^{17}$ m^{-3}), and the electron temperature is increased to where the KAW is expected to propagate ($T_e > 2$ eV), the core power deposition increases significantly (5%–30% of the total power). These numerical results demonstrate that kinetic effects are required to capture the physics of the ICH system on Proto-MPEX. This result is unexpected at such low values of electron temperature where cold plasma physics is typically sufficient to capture wave-propagation.

Since both electrons and ions are expected to absorb RF energy in Proto-MPEX a question of interest is the split between heating electrons and ions in the core. To answer this question, contours of power absorbed by the ions vs. the power absorbed by the electrons are presented to show the locations where this heating is occurring. The ion heating primarily occurs at the ion cyclotron resonance, whereas the electron heating occurs either at the periphery of the plasma column or at the Alfvén resonance. The most significant contribution to core electron heating occurs from the interaction of the plasma wave with the Alfvén resonance. This can be attributed to either Landau damping at this resonance[118] or mode conversion to lower hybrid oscillations[66]. Then, integrated core power from the full-wave calculations shows that above $T_e > 4$ eV the ions absorb ($\approx 80\%$) of the power coupled to the core or (20% of the total power). Therefore, this work numerically demonstrates a theoretical route to efficient core ion heating on Proto-MPEX.

Experimental observations of core ion heating have been shown here as inferred from both heat flux and ion temperature measurements. The ion temperature measurements showed an increase in the ion temperature in the central line of sight at Spool 9.5 and a slightly lower increase in ion temperature at Spool 10.5 when ICH power was applied to the plasma. The ion temperature peaked at Spool 9.5 indicated that the ion heat source is located closest to that location, this is indeed the location of the ion cyclotron resonance downstream of the antenna where the RF power is expected to be absorbed by the fundamental cyclotron resonance. This is further evidence that the ICH antenna is acting to resonantly heat the ions in the plasma. Heat flux measurements at the target indicate a significant increase in heat flux delivered to the target during application of ICH power. The combined observations from the ion temperature and heat flux measurements show strong evidence of core ion heating. The ion temperature at Spool 10.5 significantly decreases from that at Spool 9.5, at the target the increase in ion temperature was not observed, this is believed to be due to a large population of neutrals that charge exchanges the ion power and therefore this heat is lost. The next section which will cover the role of neutral gas dynamics in ion power delivery to the target will cover the expected loss of ion power due to charge exchange.

Since the simulation results numerically predicted the propagation of the Kinetic Alfv'en wave and showed significant core heating due to the propagation of this wave, it was important to validate this hypothesis with experimental measurements. In order to measure the kinetic Alfvén wave in Proto-MPEX, the driving frequency of the ICH antenna had to be dropped to 6.5 MHz and the magnetic field coils had to be operated at the highest current attainable to remove the ion cyclotron resonance from the measurement location. The experimental campaign to do this was plagued with issues arising from operating the FRT-86 transmitter at the low frequency where the tuning of the transmitter was finally successful, but the data set able to be measured was quite limited. Despite experimental setbacks, a radial scan with the B-dot probe measurements ended up successfully measuring a propagating Kinetic Alvén Wave in the ICH region which compared well with simulations of the wave fields from COMSOL.

5.2 Effect of Neutral Gas

A critical part of the successful ion heating on Proto-MPEX is the requirement of high electron density ($> 3\times10^{19}\ m^{-3}$) produced by the helicon plasma source along with low neutral gas content ($\gg 0.1$ Pa) in the electron and ion heating sections. Experimental evidence[22] along with theoretical calculations of electron damping coefficients show that the electron-neutral collision frequency must be kept low ($\nu/\omega < 10^{-4}$) for core electron heating to take place. Ion heating also requires low neutral gas content ($P < 0.05$ Pa) to limit charge exchange interactions that would prevent efficient delivery of ion heat to the target plate.

Previous research on light-ion helicon sources in the 5-20 kW [119, 3, 120, 34, 107] range has shown that stable, collisional light-ion plasmas with electron densities $> 1 \times 10^{19}\ m^{-3}$ require neutral gas pressures in the range of 0.7 to 2 Pa at the helicon antenna region. Therefore, to maintain high neutral gas pressures at the plasma source (> 0.7 Pa) and low pressures in the heating sections ($\gg 0.1$ Pa), differential pumping systems are required. Moreover, Proto-MPEX has recently demonstrated the production of high-density ($n_e 5 \times 10^{19}\ m^{-3}$) deuterium helicon plasmas[43]; however, the neutral gas pressure in the heating sections was too high (≈ 0.2 Pa) and hence unsuitable for the requirements of the electron and ion heating schemes ($\gg 0.1$ Pa). Therefore, to proceed and demonstrate electron and ion heating in Proto-MPEX, the need for improved neutral gas management became clear. High-density deuterium helicon discharges ($> 3 \times 10^{19}$ m^{-3}) were produced while simultaneously producing the low neutral gas pressures ($\gg 0.1$ Pa) in the heating sections required by the heating schemes with the use of conduction limiting elements, and optimizing gas puffing and timing with respect to the helicon RF pulse. These experimental techniques proved to produce the required neutral gas pressures in the electron heating section of the device. However, as will be described in this section the part of the device between the ICH antenna and the target plate does not have sufficient pumping and neutral gas management and therefore significant charge exchange losses of ion power exist in this region. The source of neutral gas in this section of the device is from plasma recombination at the target. It will be shown here that the pumping in this section is not sufficient enough to remove the neutrals produced in this manner. Thus leading to a build-up of neutral gas content in the section between the ICH antenna and the target. This section will show that the build of neutral gas in this section leads to a deterioration of ICH performance over time.

5.2.1 Power Balance Considerations

For effective transport of ion heat to the target, charge exchange interactions of ions with neutrals must be minimized. To estimate the required neutral gas pressure in Proto-MPEX for effective Ion Cyclotron Resonance Heating (ICRH) a power loss calculation has been performed for conditions relevant to Proto-MPEX. The following assumptions were used in this calculation: The charge exchange reaction rate $<\sigma_{CX} v_i>$ between deuterium atomic ions and D_2 molecules is obtained from the Atomic Data and Analysis Structure (ADAS) Database. We assume that the volumetric power lost p_{CX} scales as a function of ion temperature T_i, electron density n_e and neutral gas density n_0 as:

$$p_{CX} = \frac{5}{2} k T_i n_e n_0 < \sigma_{CX} v_i > \tag{5.9}$$

We calculate the total power lost in a plasma column one meter long since that is the distance between the ICRH antenna and the target plate. The electron density is assumed to have a radial profile described by the following expression:

$$n_e(r) = n_{e_{core}} \left(1 - \left(\frac{r}{R_p}\right)^4\right)^2 \tag{5.10}$$

Where $R_p = 1.8$ cm is taken to be the plasma radius, $n_{e_{core}} = 4 \times 10^{19}\ m^{-3}$ is the core electron density value based on experimental data (Figure 8), and r is the radial coordinate. The volumetric power loss p_{CX} is integrated over the radius assuming a plasma column one meter long to obtain the total power loss in Watts.

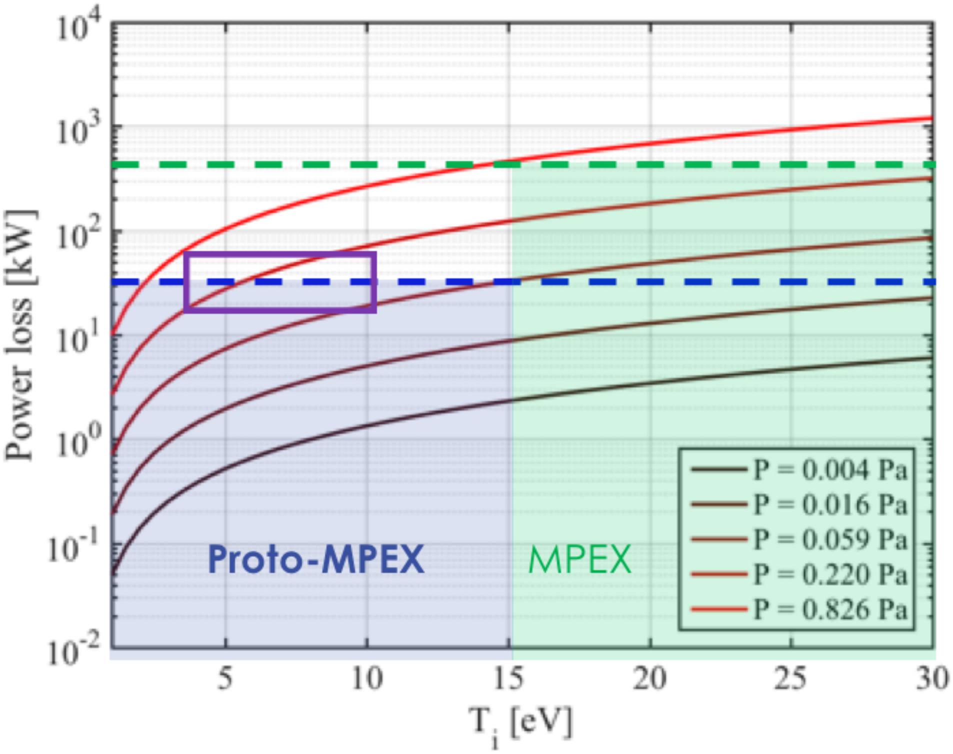

Figure 5.15: Calculation of the power loss due to charge exchange interactions as a function of ion temperature T_i for various D neutral gas density values reported as pressure values at room temperature. The calculation is based on a plasma column 1 meter long with peak electron density of 4×10^{19} m^{-3}. The Proto-MPEX operating power is denoted by the dashed blue line and the operational domain is highlighted in blue, while the MPEX operating power is denoted by the dashed green line and the operational domain is highlighted in green.

Figure 5.15, presents the results of the power loss calculations due to charge exchange between deuterium ions and D atomic neutrals. The ion temperatures of interest to both Proto-MPEX and MPEX are between 10 and 20 eV. The ICH power envisioned for MPEX is 400 kW; therefore, to keep the charge exchange losses to a reasonable level ($<$ 30% of the ICRH power) with 20 eV ions, the neutral gas pressure in the ion Heating section must be kept below 0.05 Pa, for neutral gas pressure above 0.22 Pa we see that significant charge exchange power losses will take place in MPEX and the 20 eV ion temperature cannot be sustained. For the conditions of the Proto-MPEX experiments reported here a purple box encompasses the operational domain. We see that we are operating in a domain where very little ion power is expected to reach the target.

5.2.2 Neutral Gas Management in Proto-MPEX

In this section, we present measurements from deuterium plasmas in Proto-MPEX which provide evidence that improvements in neutral gas management produced conditions suitable for performing electron heating experiments; namely, high electron density ($> 3 \times 10^{19}\ m^{-3}$) simultaneously with low neutral gas pressure ($\gg 0.1$ Pa) in the electron heating section. However, the focus of the experimental improvements was to reduce the neutral gas content in the electron heating section, the section between the ICH antenna and the target showed an increase in neutral gas pressure. The neutral gas content in this region is likely sourced from plasma recombination at the target plate. The neutral gas content in the region between the ICH antenna and the target makes delivery of ion heat to the target difficult. In this subsection, we will report baratron measurements throughout different axial locations in the device to infer the neutral gas content in those sections of the device. Although this is not a direct measurement of neutral gas content and it doesn't reveal any information about the radial distribution of neutrals in the plasma, it is the only measurement available in the device to infer neutral gas content in a region and is therefore used here for this purpose.

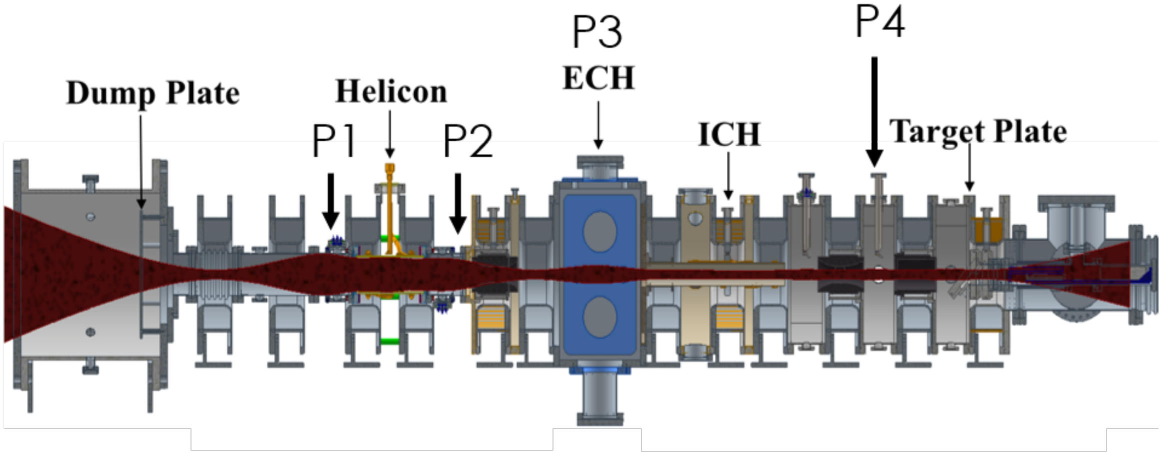

Figure 5.16: Simplified schematic of Proto-MPEX showing the location of the axial locations of the baratrons in Proto-MPEX, which measurements are reported in this section.

Figure 5.16 shows a simplified schematic of Proto-MPEX showing the axial location of the baratrons which the measurements from are discussed in this section. The baratrons located at P1 and P2 are considered to be in the helicon source section of the device with P1 being upstream of the helicon antenna and P2 being downstream of the helicon antenna. A "skimmer" exists between P2 and P3 which allows for a sustained differential pressure between the two regions that are in relatively close proximity to each other. The skimmer is a conductance limiting obstruction that prevents neutral gas from diffusing from the helicon section to the rest of the device. The skimmer consists of a metal plate with a hole that is sized for the plasma diameter. The philosophy of this is simply to only allow a path for the neutrals from the helicon section to enter the electron heating section of the device by traversing through the plasma column. The neutrals have a small mean free path for ionization in the plasma in the helicon section, and therefore are likely to be ionized rather than leaving the plasma column as a neutral on the downstream side of the skimmer. The gas puffing was experimentally optimized. So that the timing and amount of gas puffed were to maximize electron density produced in the helicon region, while reducing neutral gas content in the electron heating region (P3). A more detailed explanation of the experimental techniques to achieve the differential pumping can be found in the publication by Caneses[68].

The time evolution of the gas pressure at various locations along the device (P1 to P4) is shown in Fig. 5.18 for cases with and without plasma. For this data set, D_2 gas is injected behind the helicon antenna approximately 100 ms before the RF pulse. During this time, P1 and P2 indicate that the pressure rises to about 1 Pa at the source at the time gas breakdown occurs and plasma is produced. Once the high-density plasma is established, the neutral pressure in the helicon source region is strongly reduced within 100 ms of the initiation of the RF pulse. This reduction in neutral gas is likely caused by strong consumption of neutral gas through electron-impact ionization, this mechanism is commonly referred to as ion pumping[121].

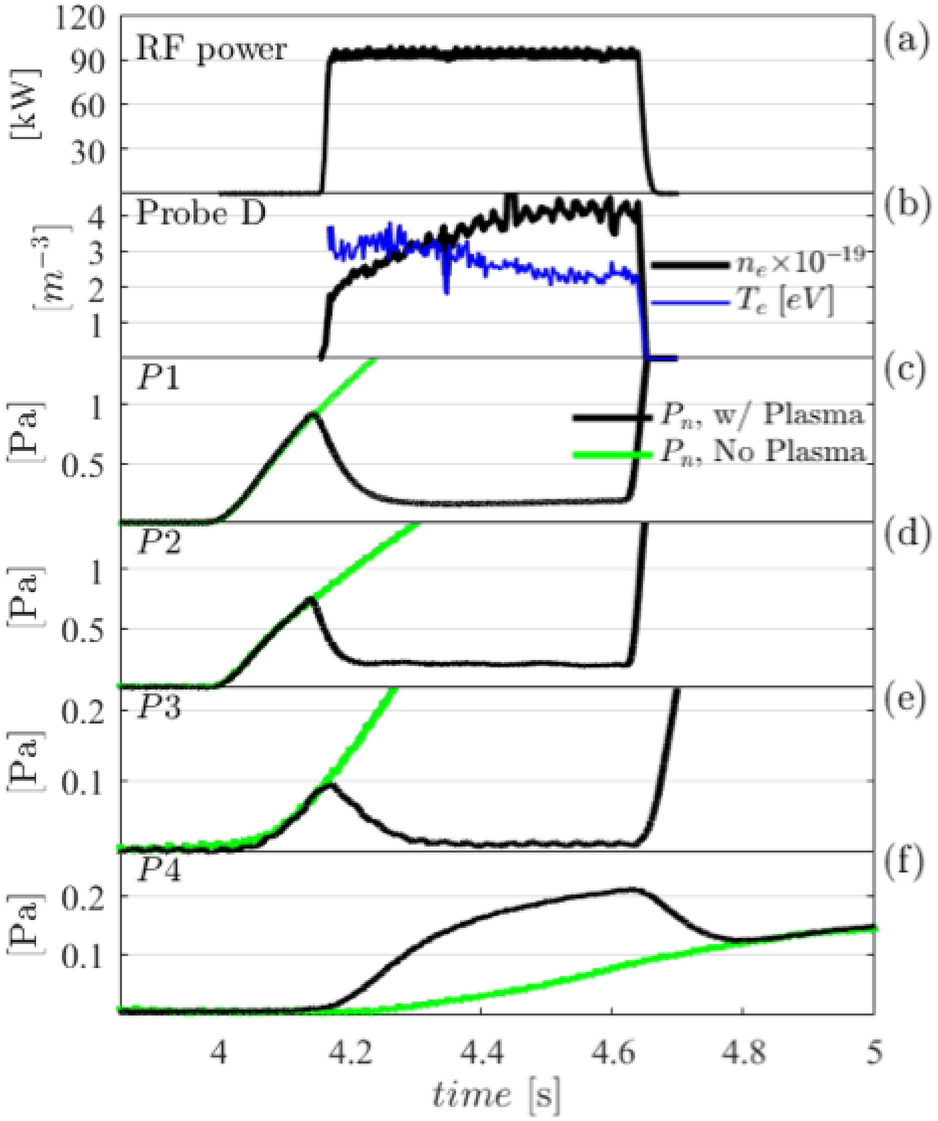

Figure 5.17: (a) RF power trace, (b) plasma density and electron temperature in the Target section, (c)(f) neutral gas pressure at P1 to P4. Deuterium gas is pulsed injected behind the helicon antenna at a flow rate of 0.7 SLM.

The most important point to note from Fig. 5.18 is that the plasma density at the target region reaches values up to 4×10^{19} m^{-3} while the pressure in the electron heating section (P3) is reduced to less than 0.01 Pa. Moreover, we observe that only in the target region does the neutral gas pressure increase in the presence of the plasma (see P4). This effect is believed to be caused by the production of neutral gas through surface recombination of the plasma which flows towards the target plate. This production of neutral gas in this region becomes troublesome for delivering ion heat to the target plate. After the RF power is turned off, the neutral pressure in the target region falls temporarily and then increases again. This peculiar effect is clearly seen in Fig. 5.18 for a 0.5 second discharges. Moreover, as the discharge evolves in time, a pressure difference is created between the electron heating section at ≈ 0.01 Pa and both the helicon source and target section at ≈ 0.2 Pa. This pressure difference is supported by the conductance-limiting elements that separate these regions. The conductance-limiting element that separates the helicon region from the electron heating region is a stainless steel plate with a hole sized to the diameter of the plasma. The conductance-limiting element that separates the target region from the electron heating region is a quartz sleeve that is placed between the ICH antenna and the plasma.

After the end of the RF pulse, the neutral pressure in the target region (P4) drops temporarily and then increases again until the end of the gas pulse. This can be seen in Fig. 5.18. The target region pressure variation at the end of the RF pulse can be understood in terms of plasma-surface recombination on the target plate and pumping rates as follows: Upon injection of the neutral gas in the source region without a plasma, it takes a finite amount of time for the gas to diffuse and reach the target region. In this case, the neutral pressure in the target region increases linearly as shown by the green traces in Fig. 5.18. Upon application of RF power, the formation of a high-density plasma plugs the conductance-limiting elements and prevents direct diffusion of gas from the source to the target regions. At this point, particles are transported from the source to the target via the plasma itself. Provided the ionization fraction of the plasma is high, surface-recombination of plasma at the target plate is the main driver of neutral gas production in the target region (black trace in Fig. 5.18). Upon termination of the RF power, neutral gas production via plasma-surface recombination at the target plate ceases and neutral pressure begins to decrease in the target region due to the pumping action of the turbo-pump and ballast tank. Without the plugging effect of the plasma on the skimmers, neutral gas from the source region can freely diffuse into the target region. Once enough time has elapsed, diffusion of neutral gas from the source region begins to fill the target region and the neutral gas pressure increases. This effect then increases the neutral content in the region between the ICH antenna and the target and leads to deterioration of ICH performance that will be described in the following subsection.

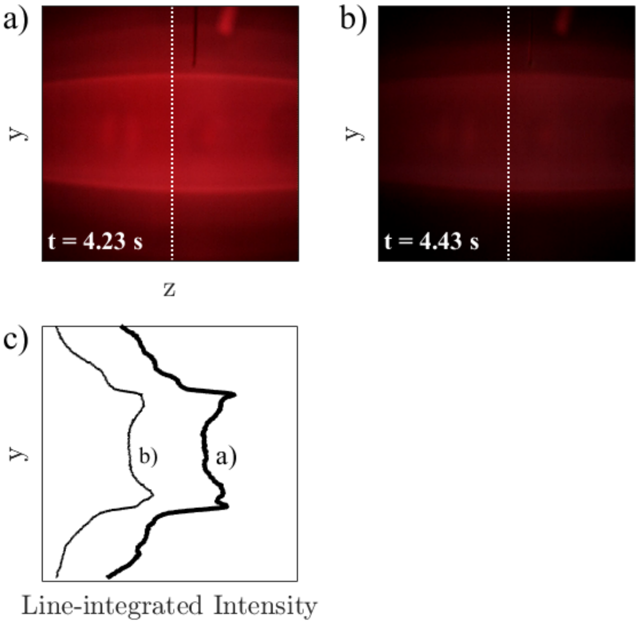

Figure 5.18: Line-integrated D_α emission in the electron heating region (a) near the start and (b) end of the RF pulse. (c) Line-integrated D_α emission across the radius shown as a white dotted line in Figures 5a and 5b.

The above discussion focused on the axial variation of neutral gas density throughout Proto-MPEX, however since the baratrons are located at the periphery of the device the measurements do not reveal anything about the radial distribution of neutral gas in the device. The high electron density core in Proto-MPEX is expected to support a hollow neutral gas profile. Evidence of this can be inferred from measurements of D_α light with a fast frame camera in the device. Figure 5.18 shows a measurement made by a fast-frame camera with an installed D_α filter. This measurement shows that the line integrated D_α light emission is hollow in Proto-MPEX, which means that the actual light emission profile is more hollow. This measurement is dependant on the electron and neutral density as well as the electron temperature. The electron density in Proto-MPEX is centrally peaked, while the electron temperature is relatively flat and both of these parameters increase the D_α emissions. Therefore, if the neutral gas density were to be flat, then a centrally peaked light emission profile would be expected. However, since the light emission profile is instead hollow, one can expect the neutral gas density to be peaked in the periphery and the core plasma to be nearly fully ionized.

5.2.3 ICH Performance Observation

The previous section described the wave propagation physics of how RF wave energy can access the core plasma in Proto-MPEX via the excitation of the kinetic Alfvén wave. Experimental evidence of core ion heating was shown by reporting measurements of increased ion temperature and target heat flux during the ICH pulse. However, as we will discuss in this subsection there is an observed transient cooling of the target parameters as well as the ion temperature. Since MPEX is supposed to operate as a steady state device, a heating scenario where the increased heat flux and ion temperature is not sustained in a steady state is not favorable. As described in the previous subsections charge exchange of energetic ions with neutral gas is expected to be a large power loss mechanism for the ions, and there is evidence that Proto-MPEX is operating in a regime that cannot sustain ion heating in the presence of the neutrals expected in the region between the ICH and target. The cooling of the target parameters and the ion temperature is on the time scale of the neutral gas dynamics in the device.

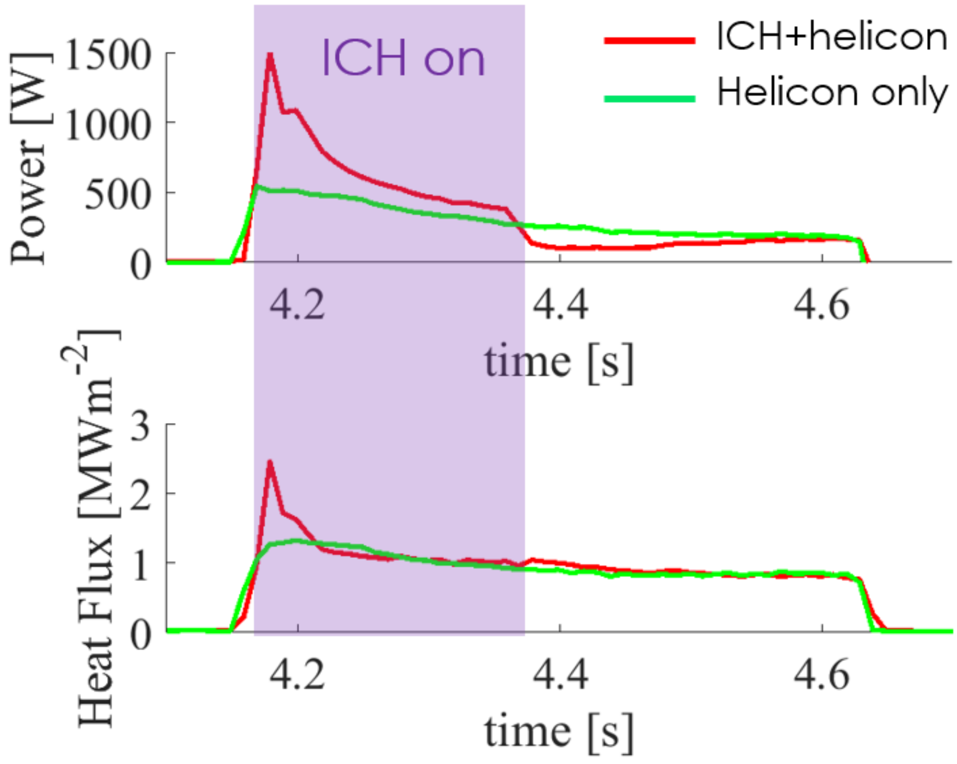

Figure 5.19: Integrated power delivered to the target (top) and maximum heat flux measured on the target (bottom) during a typical pulse using a carbon target. The experimental conditions for the pulse were: magnetic coil currents set to 5800 A, an antenna driving frequency $f = 7.5$ MHz, and an ICH power of $P_{ICH} \approx 25$ kW. The timing of the ICH pulse is shaded in purple and the start of the pulse was 10 ms after the start of the helicon pulse.

Figure 5.19 shows the integrated power on target as well as the peak heat flux on the target as a function of time for a typical ICH pulse during the 2017 experimental campaign. This figure shows that there is an immediate increase in both the peak heat flux and the power on target compared to the helicon only pulse. However, a transient deterioration of the effect of the ICH on the target parameters occurs, and the peak heat flux returns to helicon only levels in about 30 ms into the pulse duration, while the power on target is diminished as well and returns to values close to the helicon only before the end of the pulse. The power on target falls sharply, even bellow helicon only levels, when the ICH power is turned off. The behavior of the target heat flux is indicative of plasma cooling mechanisms that have a characteristic time on the order of several ms to several hundred ms. The cooling is thought to be due to the neutral gas density build up in the region between the target and the ICH antenna. The neutral gas is born from plasma recombination at the target plate and this neutral content is not pumped out of the target region effectively as can be seen in P4 of Fig. 5.18. The cooling of the target parameters occurs much faster than the cooling of the ion temperature at Spool 9.5 and Spool 10.5, as shown in Fig. 5.20. This is because the source of neutrals is located at the target plate and therefore the neutrals are expected to have an axial profile that decays away from the target. The ICH antenna has a ceramic sleeve around it that acts as a conductance limiting element, and thus neutrals born at the target from plasma recombination are confined to the region between the target plate and the ICH antenna.

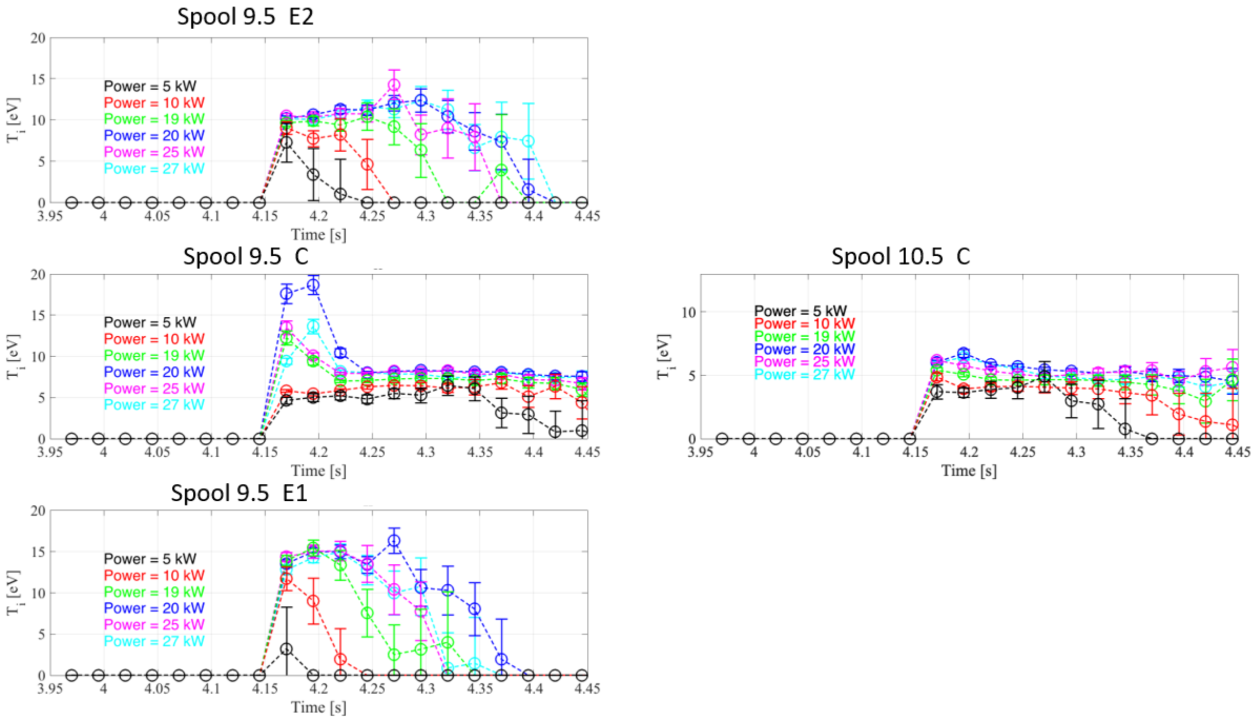

Figure 5.20: Ion temperature measurements at Spool 9.5 (left column) and Spool 10.5 (right column) during an ICH pulse that lasted 300 ms start at $t = 4.15$ s and ending at $t = 4.45$ s. The measurements at Spool 9.5 had 3 lines of sight measured corresponding to Fig. 5.8, with line of sight E2 (top right), C (center right), and E1 (bottom right). The measurement at Spool 10.5 was only taken for the central line of sight. The experimental conditions for the pulse were: magnetic coil currents set to 5800 A, and an antenna driving frequency $f = 7.5$ MHz. Measurements for several power levels ranging from $P_{ICH} = 5 - 27$ kW where obtained and reported here with the color scheme labeled in the plot.

Figure 5.20 shows the ion temperature measurements in time during an ICH pulse in Proto-MPEX for axial locations at Spool 9.5 and Spool 10.5 and the 3 lines of sight available to the measurement at Spool 9.5. The integration time of the spectrometer for these measurements is 25 ms. This measurement was made for several ICH power levels between 5 to 27 kW. The ion temperature decreases in time and this "cooling" is more pronounced at the periphery of the plasma at Spool 9.5. As discussed in the subsection above the neutral gas density profile is expected to be hollow and therefore charge exchange losses in the periphery of the plasma column occur much faster than in the core plasma. The ion temperature "cooling" occurs faster at the Spool 10.5 central line of sight than at the same line of sight at Spool 9.5. These observations are consistent with the explanation that the ion temperature is reduced by charge exchange with neutral gas content that comes off the target after plasma recombination occurs there, as the neutral gas is sourced from the target plate and reaches Spool 10.5 location much faster than Spool 9.5 location.

The ion temperature cooling occurs much faster at lower power levels. From Fig. 5.20, one can see that at the lower power levels the ion temperatures measured at E1 and E2 cool and reduce to 0 much faster at lower power levels. As the ICH power is increased, the increased ion temperatures can be sustained for much longer when the ICH power is higher. The central line of sight at Spool 9.5 and Spool 10.5 exhibit a cooling behavior that is most apparent at the lowest power levels reported here ($P_{ICH} = 5 - 10$ kW). When the power is raised however, the ion temperature is sustained for a longer time. This behavior suggests that the increased ICH power leads to a "pump-out" of the neutrals from the plasma column. Two mechanisms are proposed here for the "pump-out" behavior observed. One of these mechanisms is such that the electron heating caused by the ICH antenna increases the ionization rate coefficient of the plasma column, thus increasing the "ion-pumping" of the plasma column. Another potential mechanism for the ICH to lead to a decrease in neutral content in the plasma is simply through heating the neutrals via charge exchange, the higher pressure of hotter neutrals leads to more efficient pumping of them. Also, higher energy neutrals have a much longer mean free path and therefore can leave the plasma without any interactions.

5.2.4 Discussion

In this section, we have discussed the effect of neutral gas pressure on transporting ion heat from the ICH heating region to the target. Charge exchange is the largest power loss channel for the ions in the Proto-MPEX plasma. An estimate of the power loss due to charge exchange is first presented to give a conservative estimate of the pressure regime that Proto-MPEX and MPEX are to be operated at if ion power is to be delivered from the ICH antenna region to the target plate. We next present a section describing the neutral gas management in Proto-MPEX. Although a lot of effort and experimental optimization went into reducing the neutral gas content in the electron heating region, the region between the ICH antenna and the target has been largely ignored. This region shows an increase in pressure at the baratron located at P4, which is the region between the ICH antenna and the target. The source of this neutral gas is believed to be from plasma recombination at the target, and we can see that the pumping at the target is insufficient to remove this source of neutral gas from the region, which ultimately leads to a build-up of neutral gas at the section between the ICH antenna and the target. This neutral gas acts to charge exchange with the energetic ions and this is the largest power sink for the ions in Proto-MPEX. The final subsection covers the experimental observations of ICH performance. In this subsection, we observe a transient decrease in ICH performance in both the target parameters of power on target and peak heat flux, as well as bulk plasma ion temperature measurements. The bulk plasma ion temperature measurements show a transient cooling of the ions that is consistent with this cooling being due to neutral gas sourced from the target moving towards the ICH antenna region. This transient cooling of bulk ion temperature seems to be mitigated by increasing the ICH power. This is hypothesized to be due to the increasing ICH power removing neutral gas content from the plasma column. The removal of neutral gas from the region is proposed to be either through increasing the ionization efficiency of the plasma column by heating the electrons or from heating the neutral gas content in the plasma, therefore increasing the removal rate of neutral particles and making the neutrals more transparent to the plasma by increasing their mean free path. The next section will describe another mechanism in which charge exchange losses with thermal neutrals in the plasma is mitigated, this led to a dramatic improvement in transient plasma performance on Proto-MPEX which enabled optimization studies.

5.3 Sheath Heating

In this section, we describe experimental observations of the change in ICH performance when the target material was changed from a carbon (reported in the previous section) to stainless steel (SS) target. The changes in ICH performance include a steady state elevated heat flux and power on target observed with the stainless steel target. Higher ion temperatures were observed with the stainless steel target over the carbon target. The axial location of peak ion temperature measured changed from Spool 9.5 with the carbon target to Spool 10.5 with the stainless steel target. This indicates that another dominant heat source for the ions exists closer to the target. The proposed mechanism to explain these observations is that the reflection coefficient of the deuterium ions on the stainless steel target is much larger than that of deuterium ions on a carbon target. The reflection coefficients dictate the probability that a sheath accelerated ion can be reflected from a material surface retaining a fraction of the energy that it impacted the material surface with. Therefore, this reflection of sheath accelerated ions from the material surface can produce a flux of energetic neutrals entering the plasma column. These energetic neutrals then charge exchange with the plasma ions and act as a heat source. It is this additional source of heat that is hypothesized to be responsible for mitigating the effect of the energy loss by charge exchange with thermal neutrals and therefore lead to the observations of improved ICH performance with the stainless steel target. First, the experimental observations of the difference in ICH performance with the stainless steel vs the carbon targets are presented. Next, a simple theoretical picture of sheath heating is presented along with expressions for determining the additional heat source due to the flux of energetic neutrals. Then a calculation of a simple power balance balancing charge exchange losses with energy gain from energetic neutrals is done for the reflection coefficients of stainless steel and carbon target. Finally, a discussion of the section is presented.

5.3.1 Experimental Observations

This subsection reports on experiments in which the target material was changed from carbon (C) to stainless steel (SS). Heat flux and power on target for the case of both the SS and C target are reported here. The IR target measurements show a Steady State increase in target heat flux for the duration of the ICH pulse for the case of the SS target rather than the transient cooling observed on the C target. Also, Ar II Doppler Broadening measurements are present to show the changing target material to the SS target results in higher T_i, both with and without ICH. This increased ion temperature is maintained at locations close to the target. The location of the peak axial heat flux location moves from Spool 9.5 with the carbon target to Spool 10.5 with the SS target, which indicates that a dominant heat flux exists closer to the target.

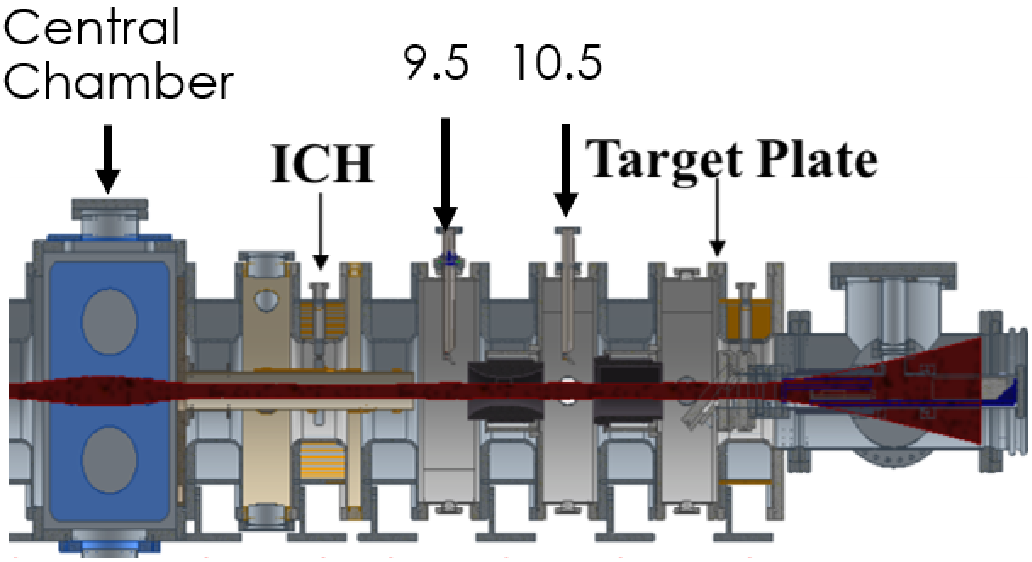

Figure 5.21: Schematic of Proto-MPEX showing locations relevant to the measurements discussed in the section here.

Figure 5.21 shows a schematic of Proto-MPEX with locations in the device labeled that are pertinent to the discussion in this section. The central chamber is the measurement location upstream of the ICH antenna and typically has a low magnetic field strength there. No significant ion heating is expected there. The location of the ICH antenna is shown and labeled in this schematic, then downstream locations of the ICH are then Spool 9.5 and Spool 10.5, as well as the location of the target plate, is labeled. Spool 9.5 is the location where most of the RF heating is expected to take place.

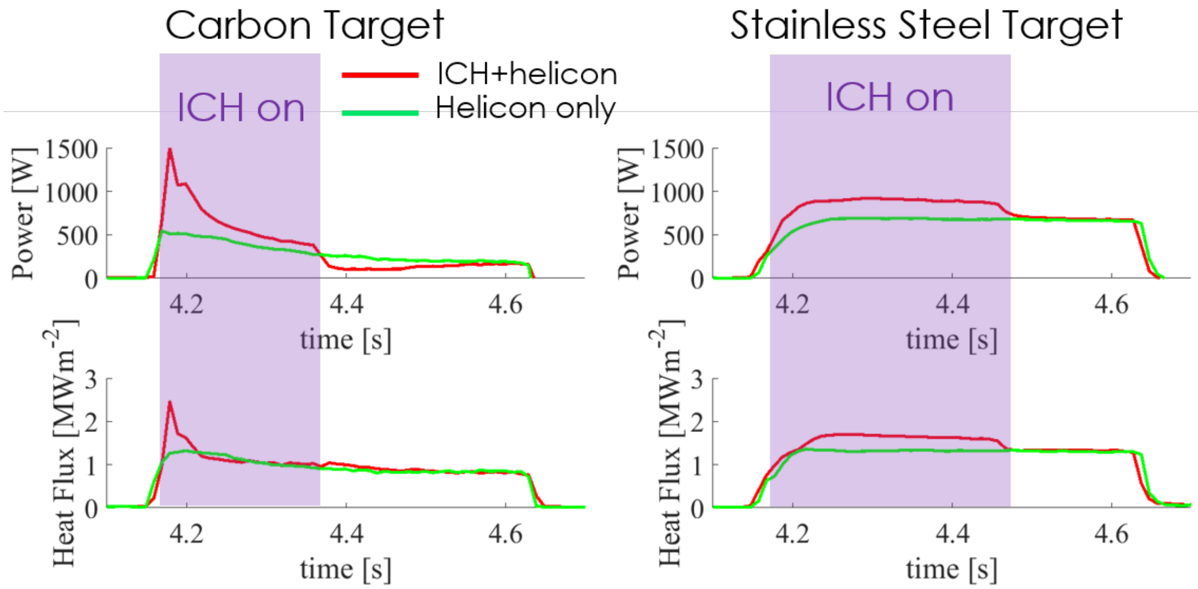

Figure 5.22: IR camera measurements of Power to target (top row) and Maximum Heat Flux in the Core Plasma (bottom row) for the case with a carbon target (left column) and a stainless steel Target (right column). The green line shows the case of a helicon only pulse while the red line shows measurements from a helicon and ICH pulse. The ICH pulse timing for these conditions is highlighted in purple. The experimental conditions for this series of shots are for the carbon target PS2 current is set to 5800 A, the driving frequency is 7.5 MHz, and the ICH power is $P_{ICH} \approx 25$ kW. For the SS target, thePS2 current is set to 5800 A, the driving frequency is 6.5 MHz, and the ICH power is $P_{ICH} = 25$ kW.

Figure 5.22 shows the heat flux to the target plate for both a carbon and SS target plate. While the carbon target typically experiences an increased heat flux to the target for only the initial transient that lasts less than 100 ms, and then the heat flux returns to the helicon only value. Although the peak of the increased heat flux of the SS target is lower than that for the carbon target, the SS target is able to reach steady state increased heat flux and power to target for experimental conditions that are similar to the case of the C Target. In the previous section, we explained the transient behavior of the carbon target due to the release and build up of neutral gas from plasma recombination at the target plate. This effect is seemingly mitigated for the case of a SS target. The sections below will aim to explain this behavior in terms of the higher reflection coefficients of SS over the carbon target, the reflection coefficient introduces an energetic flux of neutral particles into the plasma column which acts to then charge exchange with the ions and mitigate the losses from Charge Exchange with the thermal neutrals in the plasma. Ar II Doppler Broadening measurements are presented below to give further evidence of this is mechanism.

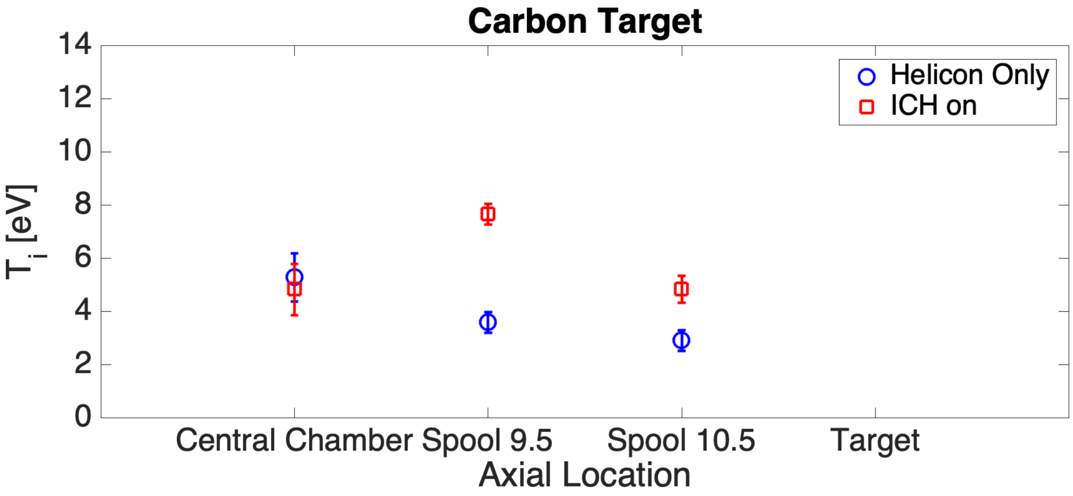

Figure 5.23: Ion temperature as a function of axial position measured by Ar II Doppler line broadening for chord passing through the center of the plasma column, with and without ICH for a carbon target.

Figure 5.23 shows the measurements of ion temperature along the axis of Proto-MPEX for the case of a carbon target. These measurements show that at Spool 9.5 the ion temperature with applied ICH power peaks and increases by ≈ 4 eV when ICH power is applied to the plasma column. At the central chamber no significant increase above helicon only levels is observed, since the ICH antenna is expected to heat the downstream resonance location and the ion heat transport is dominated by convection which is directed towards the target, no significant heating is expected to be observed at the Central Chamber. Spool 10.5 still shows ion heating of ≈ 2 eV after the application of ICH power, however, the ion temperature measured there, with the ICH on, is $T_i \approx 5$ eV which is much lower than the 7 eV observed at Spool 9.5. The measurement at the target was not able to resolve an ion temperature for either the helicon only or the applied ICH case which indicates that ion temperature at this location is fairly low. This observation of the axial profile of the ion temperature reveals that the dominant heat source for the ions is located closer to Spool 9.5, and there is a source of ion cooling when approaching the target plate. This is explained in the section above, the heating near Spool 9.5 is because the first downstream ion cyclotron resonance is located there, and the majority of the RF wave energy is expected to be absorbed there. The cooling further downstream is due to the neutral gas content born from the target plate.

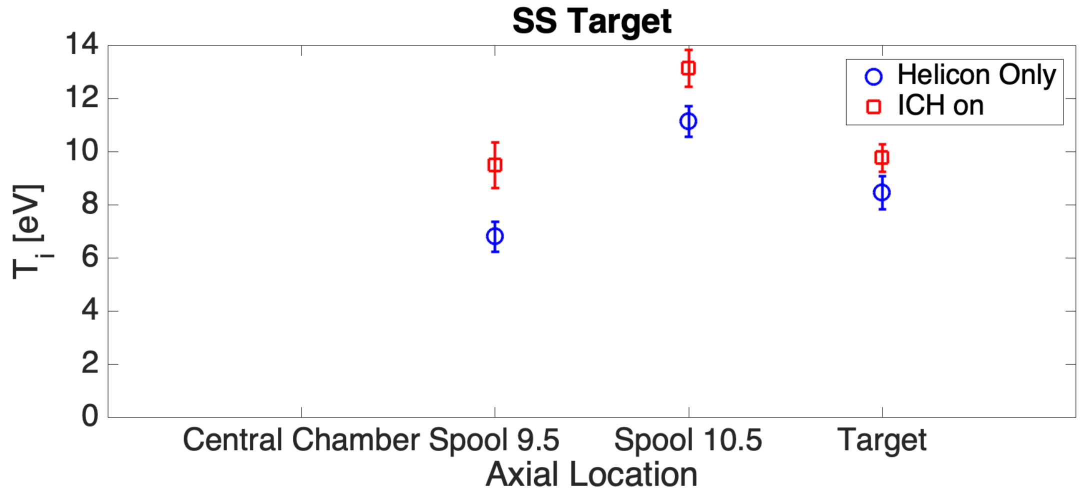

Figure 5.24: Ion temperature as a function of axial position measured by Ar II Doppler line broadening for chord passing through the center of the plasma column, with and without ICH for a stainless steel target.

Figure 5.24 shows results of time-averaged spectroscopic measurements of Ti at different axial locations with and without ICH, for both C and SS targets, for measurement chords that pass through the device axis. The measured ion temperature for the case of the SS target is much higher than for the case of the carbon target for either helicon only or ICH and helicon pulses. This suggests there is an additional heating mechanism present with the stainless steel target apart from the RF heating due to ICH. There is an increase of about $2 - 3$ eV of ion temperature when ICH heating is applied at Spools 9.5 and 10.5 for the case of the stainless steel target and at the target an increase of $1 - 2$ eV. No measurements were taken in the Central Chamber for the case of the stainless steel target. The axial peaking of the ion temperature in Fig. 5.24 is indicative of the axial location of the dominant heat source in the plasma. A notable feature of the stainless steel target ion temperature measurements is that the ion temperature peaks at Spool 10.5 rather than at Spool 9.5. Since the RF heating is expected to take place at Spool 9.5, this is where the ion temperature is expected to peak if this was the dominant heating mechanism. This data instead indicates that a dominant heating mechanism exists closer to the target. Since the additional heating mechanisms is attributed to the charge exchange of neutrals reflected from the target it is important to discuss the mean free path of these particles in the Proto-MPEX plasma column. In Fig. 5.26 show that the mean free path of the energetic neutrals reflected from the target is on the order of $\approx$ 10 cm, while the mean free path of the thermal neutrals near the target is on the order of several mm's. This suggests that sheath heating of the bulk ions may dominate as a heating mechanism for the ions in the plasma when a target material with high enough reflection coefficient is present.

5.3.2 Simple Theoretical Picture

In this subsection we will present a simple theoretical picture of the ”sheath-heating” physics we will then use to explain experimental observations in the following subsection. First, ionization and charge exchange cross-sections are presented, as well as charge exchange means free path calculations of an atomic deuterium neutral particle in order to set the stage for the physical arguments of the sheath heating we will be presenting in this section. We then present a simple cartoon schematic of the sheath heating model and derive a 0D power balance expression for this phenomena. Finally, I show calculations of sheath heating as a function of electron temperature and neutral gas pressure for a carbon target and a stainless steel target.

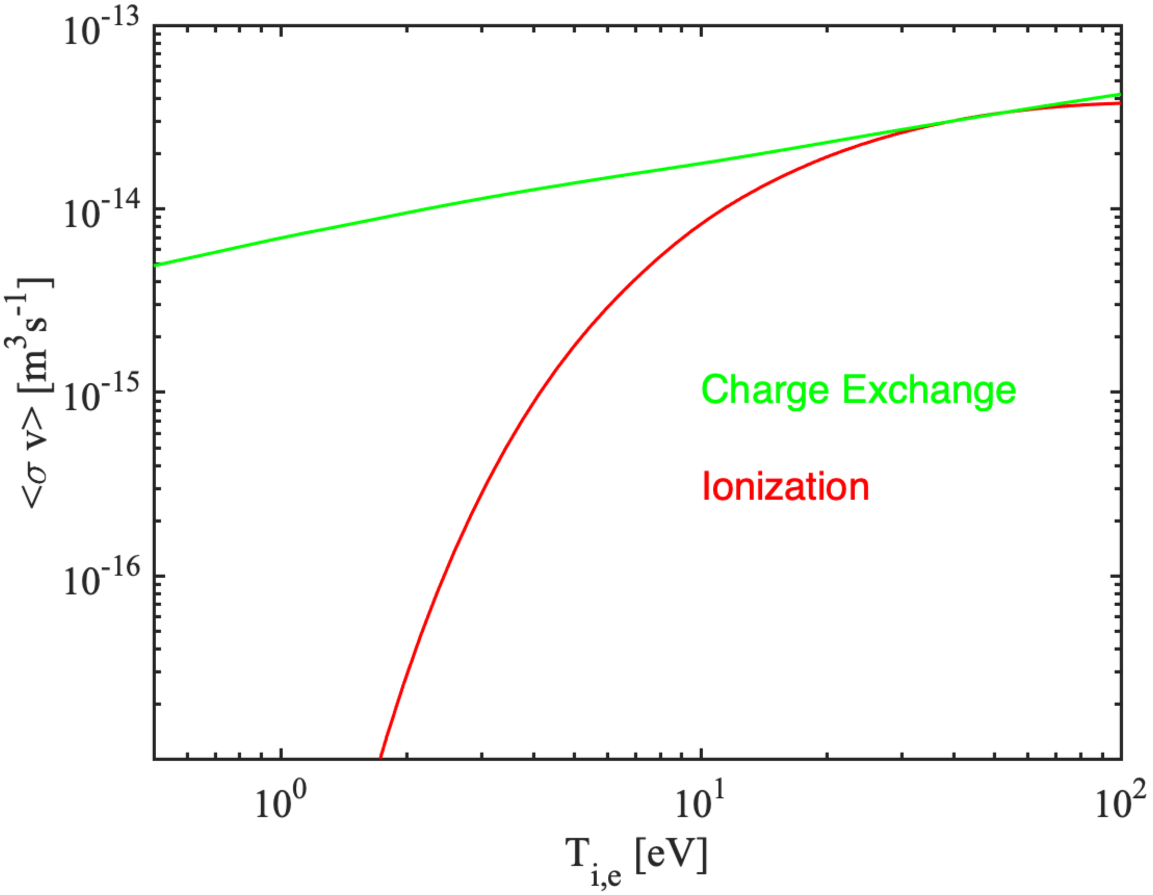

Figure 5.25: Effective reaction rates for ionization and charge exchange for atomic hydrogen as a function of electron temperature (ionization reaction rate) and ion temperature (charge exchange reaction rate).

Figure 5.25 shows the effective reaction rates of ionization and charge exchange, as a function of electron (ionization) and ion (charge exchange) temperature. The effective reaction rates for these processes are taken from ADAS. The reaction rate for charge exchange is at least an order of magnitude greater than the ionization reaction rate for $T_e < 4$ eV. Since this is the electron temperature regime for the Proto-MPEX target plasma in most ICH experiments, I expect charge exchange to dominate over ionization in the plasma column. The physical picture I now present for the ”sheath” heating of bulk ions will operate under the assumption that charge exchange is the governing processes for the ion energy balance in Proto-MPEX relevant plasma conditions.

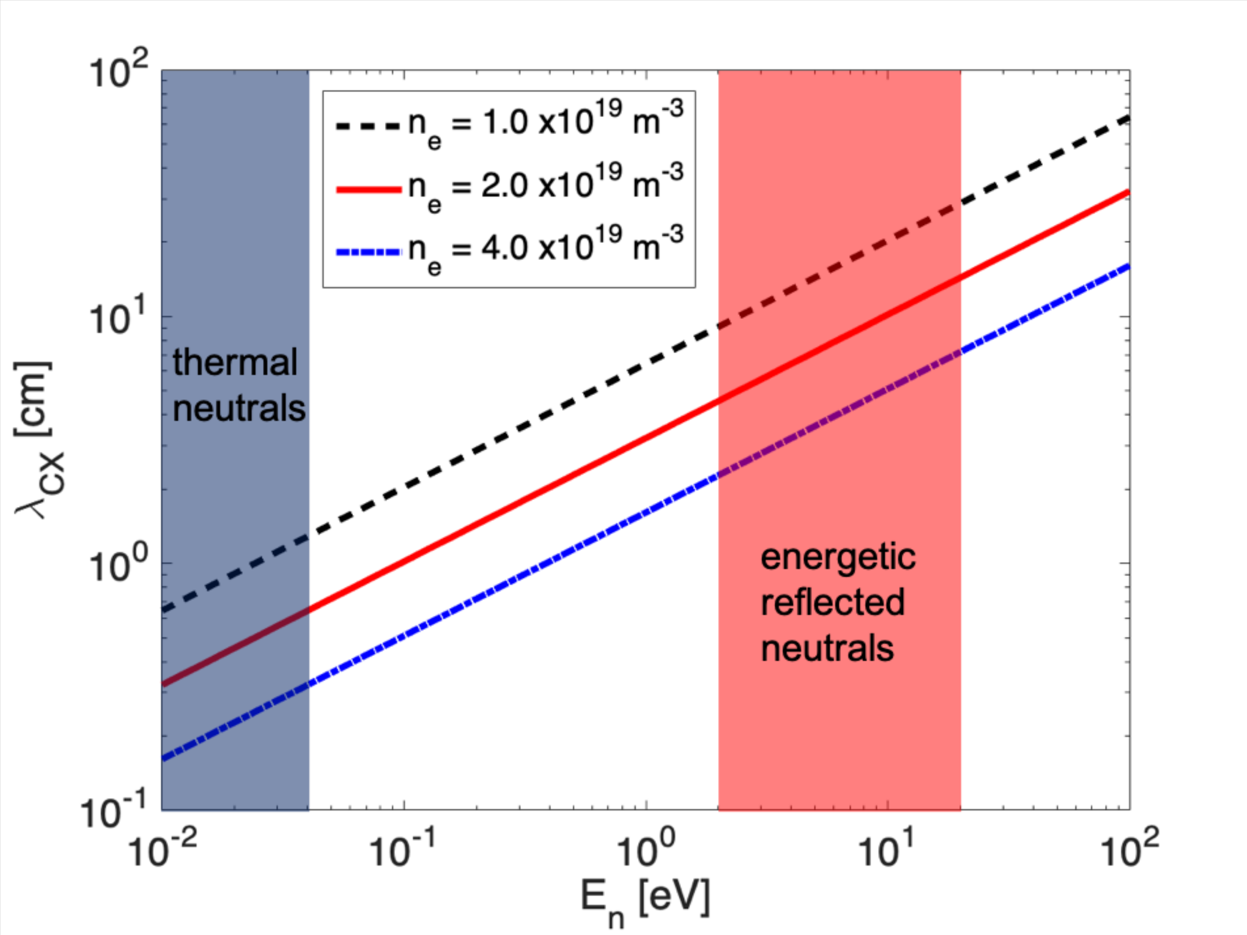

Figure 5.26: Mean free path of neutral atoms as a function of neutral particle energy, calculated for several values of electron density ($n_e = 1 \times 10^{19}$, 2×10^{19}, 4×10^{19} m^{-3})

Figure 5.26 shows calculations of the charge exchange mean free path of a neutral particle as a function of energy. The calculation is shown for several values of electron density ($n_e = 1 \times 10^{19}$, 2×10^{19}, 4×10^{19} m^{-3}). Figure 5.26 shows that the population of thermal neutrals ($T_0 < 500°$ K) have a charge-exchange mean-free path of $\lambda_{CX} < 1$ cm for most of the plasma core ($n_e > 1 \times 10^{19}\ m^{-3}$). HoIver, the energetic neutrals born from either charge exchange with an ion in the bulk plasma or reflection of an ion from the target material are shaded in red and have a charge exchange mean free path of several cm's if not 10's of cm's in the bulk plasma.

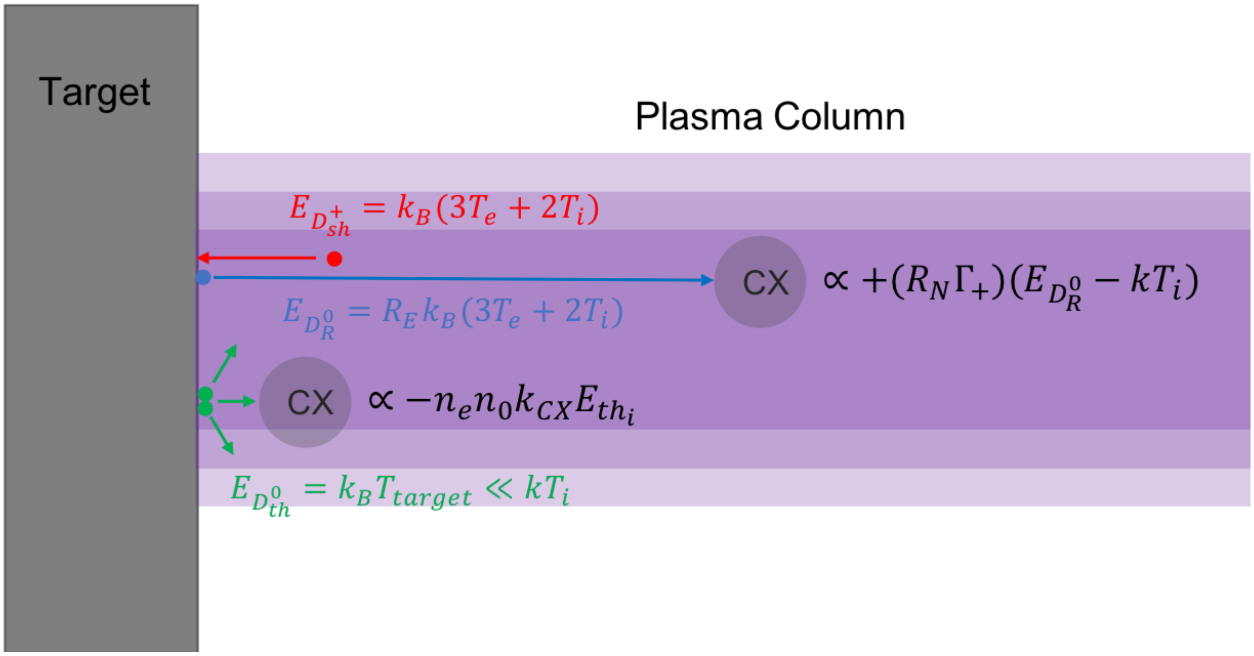

Figure 5.27: Simple cartoon of the physics of the sheath heating model.

The physical picture that we have when explaining sheath heating is depicted by Fig. 5.27. In this physical picture, we depictions that are accelerated by the plasma sheath are then neutralized at the material surface and can undergo a physical reflection, where they reflect from the material surface retaining a fraction of the energy gained from acceleration through the sheath. These energetic neutrals now have a mean free path of several cms in the Proto-MPEX plasma column. However, these reflected neutrals are assumed to have a velocity distribution that is narrow and perpendicular to the target or parallel with the plasma column. This picture assumes the reflection is a geometric one and with the knowledge that the ion velocity distribution function at the sheath is narrow and nearly perpendicular to the material surface. Therefore, the flux of energetic neutrals born in this way can charge exchange fully with the bulk plasma and contributed significantly to the bulk plasma's power balance. Ions in the bulk plasma that are charge exchanged are assumed to be lost from the plasma where they likely thermalize at the chamber wall. We assume this because their mean free path is also on the order of several cm's however these ions tend to have an isotropic velocity distribution, and therefore are likely to leave the plasma column before experiencing another collisional interaction. Another population of neutrals also comes off the target, plate and that is the neutrals that are desorped from the target plate. These likely come back as molecular Deuterium and therefore act as an energy sink for both the electrons and ions in the bulk plasma.

A 0D model can be written quantifying the sheath heating on observable quantities in the bulk plasma. We begin by writing the continuity equation for ion pressure:

$$\frac{3}{2}\frac{\partial p_i}{\partial t} + \nabla \cdot \left(q_i + \frac{5}{2}p_i v_i\right) = Q_i. \tag{5.11}$$

In Eqn. 5.11 the time derivative of the ion pressure, defined as a function of electron density and ion temperature as $p_i = n_e k_B T_i$, is defined by the divergence of the conductive heat flux due to ions (q_i) and the convective heat flux that depends on the the fluid velocity of the ions (v_i) as well as any volumetric sources or sinks (Q_i). Since the goal here is to quantify the "sheath" heating effect on bulk ion temperatures we simplify the model assuming radial losses are negligible and axial convective and conductive fluxes into the cylinder are at equilibrium with the sheath losses and therefore cancel each other out. The only source of heat into the plasma volume is then flux of energetic neutrals reflected from the target, which is balance by volumetric charge exchange with thermal neutrals and collisional thermalization with electrons. We now perform a volume integration on Eqn. 5.11 and expand the terms to receive:

$$\frac{3}{2}\frac{\partial p_i}{\partial t} = 3\frac{m_e}{M_+} n_e \nu_{ei} k_B (T_e + T_i) + \frac{5}{2}\frac{S_{im}}{V_p} R_N \Gamma_{se}(R_E(2kT_i + 3kT_e) - kT_i) - n_e n_0 k_{CX} E_{th_i} \tag{5.12}$$

The first term in Eq. 5.11 is the energy exchange between electrons and ions due to Coulomb collisions, where ν_{ei} is the electron-ion Coulomb collision frequency, m_e is the electron mass, M_+ is the ion mass of Deuterium, T_e and T_i is the electron and the ion temperature respectively. The middle term in Eqn. 5.11 is the energy gained by the ions through charge exchange with energetic neutrals coming off the target. The entire population of these reflected neutrals is assumed to interact with the plasma with the physical justification for this stated above. R_N is the particle reflection coefficient (this dictates the fraction of the flux of ions reflected from the material surface as energetic neutrals) that is tabulated as a function of incoming ion energy in the following report Eckstein2002, R_E is the energy reflection coefficient (which dictates the fraction of energy retained by the reflected neutral from the accelerated ion), which is tabulated in the same report. The energy of the incoming ions is estimated by $E_{im} = k_B(3T_e + 2T_i)$[99]. S_{im} is the surface area of the plasma cylinder and V_p is the volume of the plasma. The last term in Eq. [1] gives the volumetric charge exchange given by plasma with electron density n_e and neutral gas density (assumed to be atomic deuterium at room temperature) which is scanned and reported as a pressure in Pa assuming room temperature to relate this to the baratron pressures measured in Proto-MPEX. However, this calculation of neutral gas density in the core plasma is more than likely an overestimate of the neutral gas density in the plasma, as Proto-MPEX shows strong evidence of having a hollow neutral gas density profile and a nearly fully ionized core plasma [68].

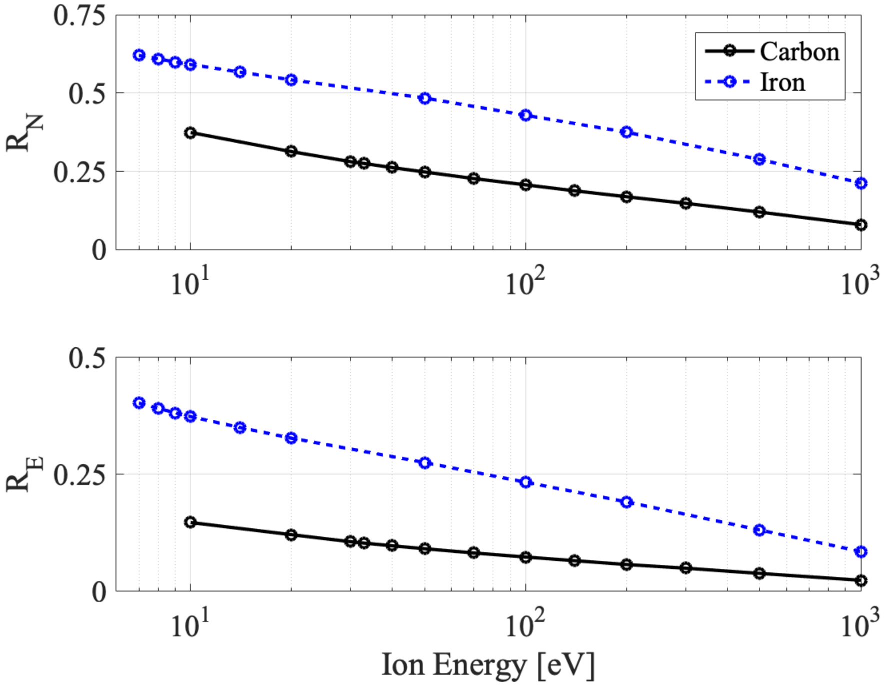

Figure 5.28: Particle reflection coefficient (top) and energy reflection coefficient (bottom) as a function of ion impact energy for carbon and iron.

The higher reflection coefficients are shown in Fig. 5.28, which plots the tabulated coefficients from Eckstein2002 for both carbon and iron. Therefore, a SS target is expected to have a greater heat flux of energetic neutrals reflected from the target which balances the energy losses from the charge exchange with the thermal neutrals.

A simplified model attempting to quantify the additional heating due to the ”sheath heating” is described in the subsection above. Here, we present the results of this model. First, the particle and energy reflection coefficient for carbon and iron (since iron is the major constituent of SS it will be used as an analog SS) is presented in Fig. 5.28. This figure shows that both the particle and energy reflection coefficient is higher for iron than for carbon for all values of ion impact energy of interest to Proto-MPEX. For an ion impact energy

$E_{im} = 6$ eV, the product of the particle and energy reflection coefficient of carbon is ≈ 0.05 and ≈ 0.22 for SS, which increases the energy flux of neutrals entering the plasma up to $\approx 4.4\times$ for a SS target over a C target.

To now quantify the effect of "sheath heating" Eqn. 5.12 is integrated over a cylindrical plasma with a radius of $R = 2$ cm and a length of $L = 10$ cm. The electron density in the plasma volume is assumed to be constant at $n_e = 2 \times 10^{19}\ m^{-3}$, and the ion flux to the target plate is assumed to be constant at $\Gamma_+ = 5 \times 10^{23}\ m^{-2}s^{-1}$. The integration starts at an initial condition of $T_i = 0.3$ and integrated for 1 ms which is where the solution is at steady state and the final values of ion temperature are taken to be the steady-state solution. This calculation assumes a constant electron temperature (T_e) and neutral gas density (n_0) that is scanned over Proto-MPEX relevant parameter space and reported in Fig. 5.29. The neutral gas density is reported as a neutral gas pressure calculated at room temperature for straightforward comparison to the baratron pressures reported in previous sections.

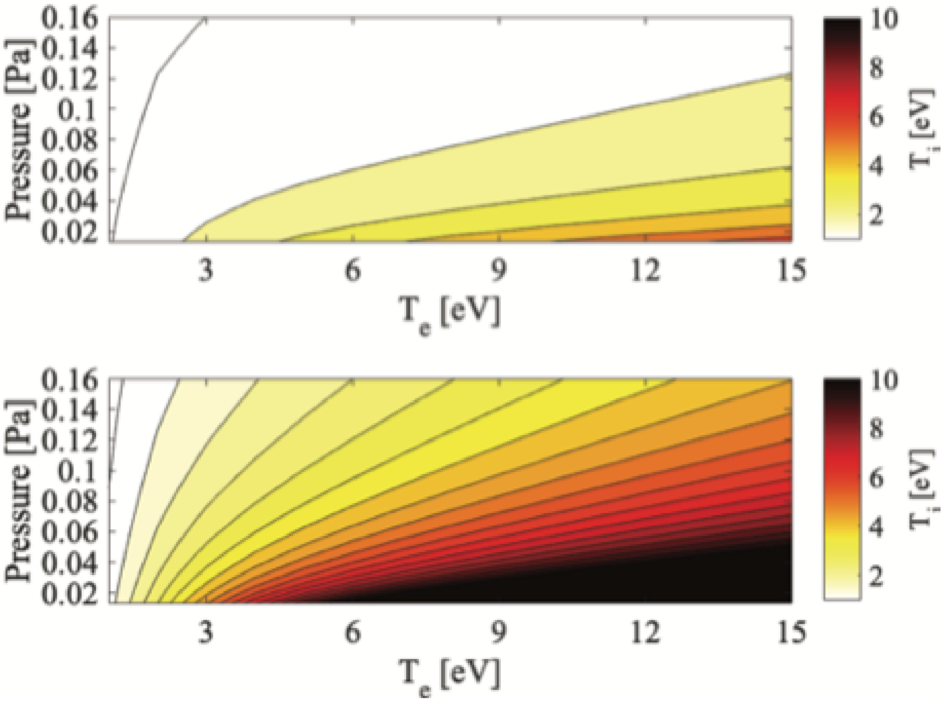

Figure 5.29: Ti as a function of Te and neutral pressure for sheath accelerated ions reflecting off a target made of carbon (top) and iron (bottom), determined from Eqn. 5.12

Figure 5.29 shows contours of ion temperature calculated as a function of electron temperature and neutral gas pressure with particle and energy reflection coefficients used for carbon and an iron target. This figure shows that significantly higher ion temperatures can be expected for all the points in this parameter space for the case of a target material with iron being a major constituent (SS) rather than for a pure carbon target. This is because the higher particle and energy reflection coefficients of the target material contribute to significantly increasing the flux of energetic neutrals that charge exchange in the plasma volume and add energy to the ion fluid. This additional energy gain can significantly offset the charge exchange losses due to the thermal neutrals born from recycling at the target. This build-up of the neutral population is believed to be the reason for the transient behavior of ion temperature and target heat flux for the case of the carbon target, where the case of the SS target observes a steady state increase of heat flux and ion temperature sustained throughout the ICH pulse.

5.3.3 Discussion

This section described the physics of sheath heating, which in summary is the heating of the bulk plasma via charge exchange of energetic neutrals. The energetic neutrals enter the plasma by the reflection of ions, that are accelerated through the plasma sheath, by the target material. A simplified model of the effect of sheath heating on the power balance of the ion fluid is then formulated and presented here. The section then goes on to describe the observations from measurements of ion temperature by Ar II Doppler broadening spectroscopy for experiments with a carbon target and a stainless steel target. The bulk plasma with the stainless steel target shows significantly higher ion temperatures throughout the plasma column, especially near the target region, when compared the case of the carbon target. Heat flux measurements of the target plate also show that for the case of the stainless steel target the heat flux increase is sustained throughout the entire ICH pulse duration, whereas in the case of the carbon target the increased heat flux is transiently observed for only several 10's of ms after the beginning of the ICH pulse. This is attributed to the build-up of thermal neutrals from the recycling of particles at the target as discussed in the previous section. This population of thermal neutrals acts to charge exchange with the energetic ions and ion power is lost in this way. To combat this effect neutral gas pumping should be increased in the target region as discussed in the previous section. However, for the case of the stainless steel target this power loss channel seems to be balanced and mitigated by the charge exchange of energetic "sheath" accelerated neutrals, as evidenced by the higher ion temperatures as well as the sustained heat fluxes to the target. This effect is quantified and the calculation is presented in this section which shows that the reflection coefficient of iron can increase the flux of energetic neutrals entering the plasma column over that of a carbon target, thus balancing the charge exchange losses from the thermal neutral population. This effect can be increased to further benefit Proto-MPEX ion temperatures, by using a material with even higher reflection coefficients such as tungsten.

5.4 Optimization and Extrapolation to MPEX

The previous sections highlighted, how RF heating in Proto-MPEX is expected to work, the role of neutral gas in the transport of ion heat to the target, and the effect of target material on the observations of heat flux to the target as well as bulk plasma ion temperature measurements. Now that a steady state, well behaved ICH discharge was obtained an experimental optimization study of the ICH was done by scanning the current in the magnetic field coils in the ICH region. This scan showed that there is a magnetic field regime which is preferable for core heating by the ICH antenna. These experimental results were then compared with RF simulations of the ICH heating region. The modeling agreed well with the experimental observations. The modeling results are then investigated to explain why the region of favorable heating exists. Finally, experimental power scans were performed and target parameter extrapolations to MPEX conditions are favorable and show that ICH and helicon alone could satisfy MPEX heat flux requirements with the planned 400 kW of ICH heating power.

5.4.1 Experiments Scanning Magnetic Field

In this subsection, experimental results from an optimization of the magnetic field in the ICH region are presented. These results show that there is an optimum magnetic field strength range that application of ICH power will efficiently heat the core plasma as shown by the heat flux to the target. However, Ar II Doppler Broadening measurements show that near the target the ion temperature only shows a similar trend to the target heat flux in the periphery of the plasma and not in the core plasma. These experiments were from the 2018 experimental campaign after the magnetic field on Proto-MPEX was reconfigured for electron heating experiments. For this experimental campaign the driving frequency of the ICH antenna was reduced to $\omega = 2\pi(6.5MHz)$, the magnetic field strength of the fundamental ion cyclotron resonance at this driving frequency is $B_{ICH} = 0.85$ T. The ICH antenna was reconfigured to an external ICH antenna that was now a 30 cm long antenna rather than the 25 cm antenna used during the previous experimental campaigns, this antenna shifts the $k_{\|}$ spectrum of the antenna to smaller values.

Target measurements

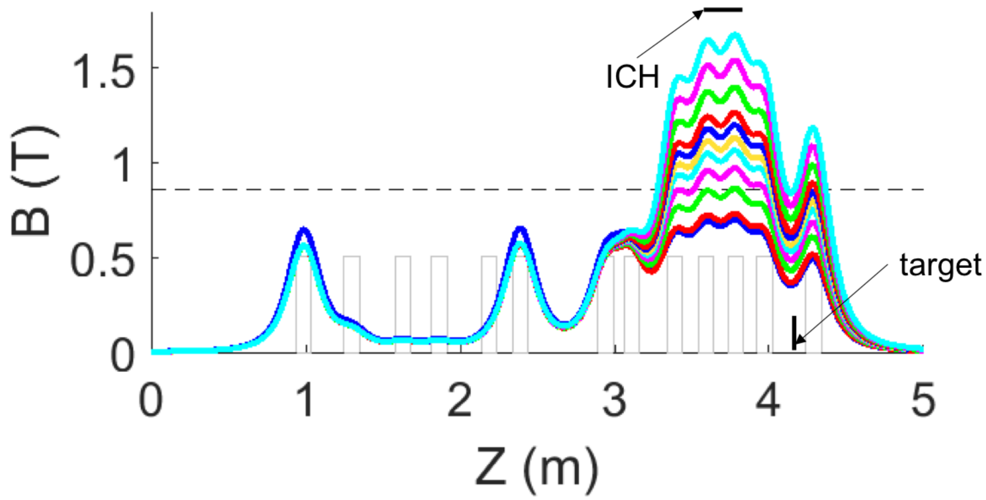

Figure 5.30: Magnetic field profile in Proto-MPEX during the magnetic field optimization experiments. The figure shows the effect of increasing the magnetic field current in PS2 which controls magnets 9 through 13. The ICH antenna and target plate locations are depicted labeled. The magnetic field strength of the ion cyclotron resonance at $f = 6.5MHz$ is shown by the dashed black line.

The axial magnetic field profile for varying values of PS2 current Proto-MPEX is shown in Fig. 5.30. As the current in the magnetic coils is increased the field evolves as shown in this figure. The lowest current setting for PS2 in this figure is $PS2 \approx 2800$ A and the highest current setting is $PS2 = 6040$ A. At a value of $PS2 > 3800$ A the magnetic field strength under the antenna begins to become greater than the B_{ICH}. The ICH antenna is labeled in this image and is depicted by the solid black line, and is located at Spool 9.5 in this configuration. The target plate here is located at Spool 12.5 and is also labeled in Fig. 5.30. For these experiments, the ICH antenna was powered with $P_{ICH} = 23 - 30$ kW. The data below will be presented as the Heat Flux values measured by the IR camera, however, when comparing with simulations the IR target measurements will be normalized to the applied ICH power to remove variations caused by differences in applied power.

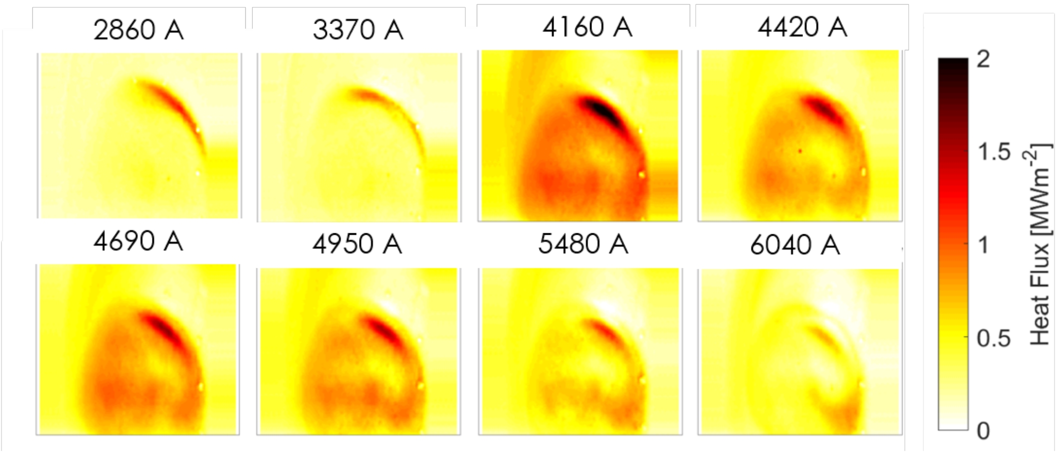

Figure 5.31: Array of 2D images of the measured heat flux on target during application of ICH power for several values of PS2 current.

An array of the heat flux contours on the target plate is shown for several values of PS2 current in Fig. 5.31. In this figure, it is observed that at lower values of magnetic field strength, where the ion cyclotron resonance is not present in the plasma column, no significant heating is observed in the core plasma on the target when ICH power is applied. When the coil current is raised above $PS2 > 3800$ A significant heating of the entire plasma column occurs. This heating is optimum for a range of magnetic coil current of about 1000 A, and then begins to deteriorate in efficiency as the magnetic coil current is raised above $PS2 > 5000$ A. At this higher magnetic field the increased heat flux begins to fade away from the core plasma and then is only present in the periphery of the plasma column.

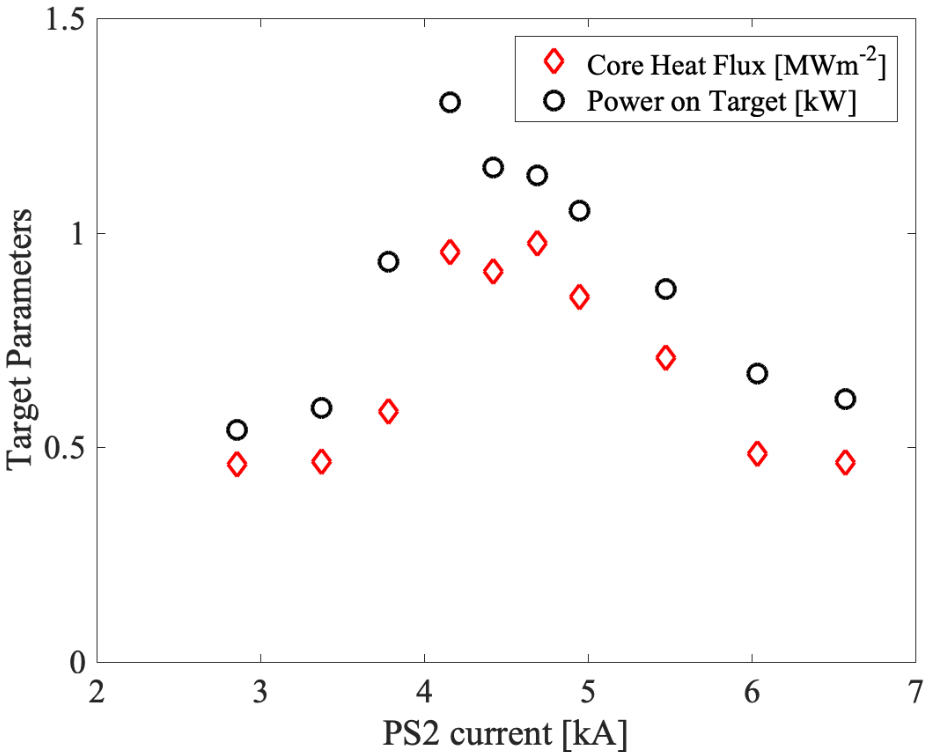

Figure 5.32: Target parameters measured by the IR camera as a function of PS2 current. ”Power to the target” is the heat flux integrated over the entire view of the target plate and is shown with black circles in units of kW. The ”Peak Heat Flux” is simply the maximum heat flux anywhere on the target plate, and is shown with blue squares and given in units of MWm^{-2}. The ”Core Heat Flux” is the maximum value of heat flux inside of a 1.8 cm radius centered in the plasma column and is given in units of MWm^{-2}.

Figure 5.32 shows the target parameter values from the same set of experiments as taken in Fig. 5.31. This figure shows integrated heat flux as power on target, a peak heat flux (maximum heat flux value on target), and a peak core heat flux (maximum heat flux inside 1.8 cm radius of the plasma column). For this series of data the ICH power was kept within the range of $P_{ICH} = 23 - 30$ kW; however, due to a need to re-configure the matching network for the ICH antenna at each new magnetic field value, keeping the exact forward power equivalent was not practical. Therefore, some of the variations observed in this figure are due to the variation in power applied. However, the general trend observed in Fig. 5.32 does show an optimum magnetic field range for ICH operation. For magnetic coil current values lower than $PS2 < 3800$ A, we see there is no significant core heat flux and power on target is not increased over helicon only levels. Since at this value of PS2 the magnetic field everywhere in Proto-MPEX is below the ion cyclotron resonance and the ion cyclotron resonance is not present in the plasma column (see Fig. 5.30), therefore the ”beach heating" technique is not expected to work in such magnetic field configurations. This alone is an excellent demonstration that the ion heating we are proposing is, in fact, a resonant ion heating scheme. What is interesting, however, is that the optimum magnetic current coil range of ICH operation is about 1000 A and the heating efficiency begins to deteriorate significantly for $PS2 > 5000$ A. The physics of this is more interesting and will be explored further below with the full wave simulation.

Ar II Doppler Broadening Measurements

The ion temperature measurements discussed in this section were taken with a setup shown in Fig. 2.19 on Spool 12.5.

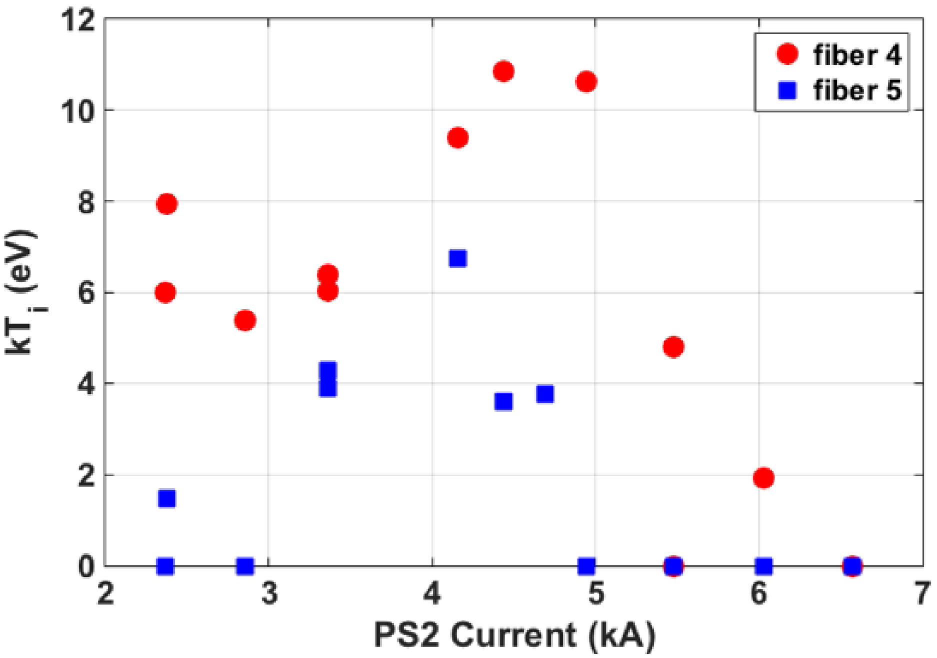

Figure 5.33: Ion temperature measured as a function of PS2 current on fiber 4 (red circles) and fiber 5 (blue squares).

Figure 5.33 shows the ion temperature measured by fiber 4 and fiber 5 which correspond to measurements of the periphery. The periphery measurements, especially on fiber 4, show a similar trend as the heat flux measurements, where ion temperature increases with PS2 current around 3500 A and begins to decrease past 5000 A. Fiber 5, which is the outer most fiber, begins to decrease in ion temperature much earlier, however from inspecting the fast frame camera images this is due to flux compression. The plasma's radius becomes smaller with increasing magnetic field strength, therefore, in the location of fiber 5's measurement the electron density falls to such a value that a relevant signal is no longer measurable and $T_i = 0$ eV is reported in this figure.

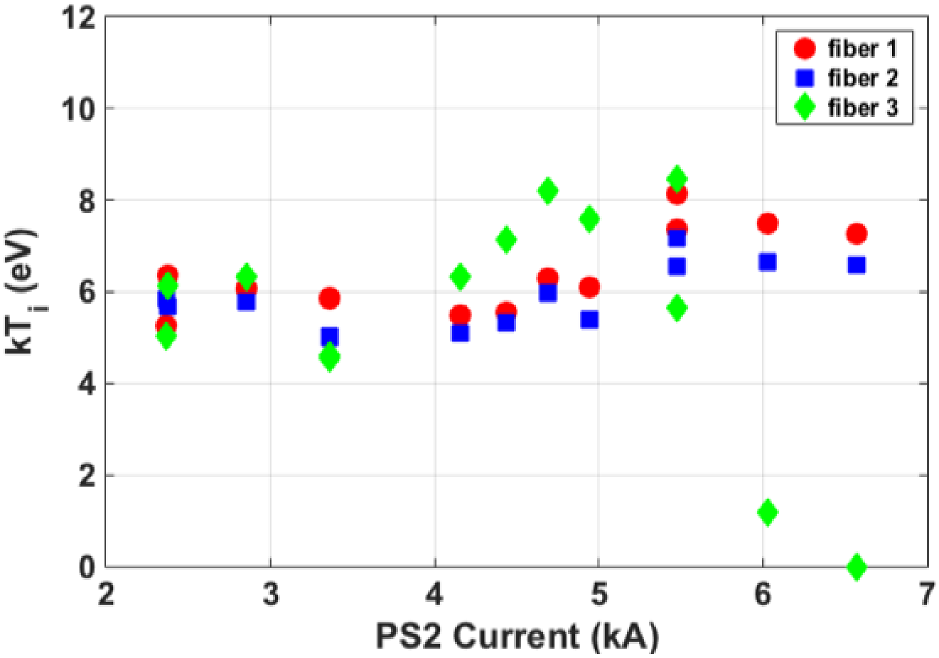

Figure 5.34: Ion temperature measured as a function of PS2 current on fiber 1 (red circles), fiber 2 (blue squares), and fiber 3 (green diamonds).

Figure 5.34 shows the ion temperature measured by fiber 1, fiber 2, and fiber 3 which correspond to measurements of the innermost region of the plasma. The outer most fiber in this set of measurements (fiber 3), shows a similar trend as the heat flux measurements and the ion temperature measurements on fiber 4, that is that ion temperature increases with PS2 current around 4000 A and begins to decrease past 5000 A. The innermost fibers do not show a similar trend, instead they remain relatively constant within 2 eV and seem to measure higher ion temperatures at the higher magnetic fields, $PS2 > 5000$ A. This trend does not seem to be in agreement with the measurements of heat flux on target. Several explanations resolve the discrepancy of the IR measurement with the ion temperature measurement. It is important at this stage to point out the ion temperature that is measured by the Ar II Doppler Broadening measurement is only the component that is parallel to the line of sight, which is perpendicular to the axis of the device. Something to note as well is that the RF heating of the ions occurs at a magnetic field strength that is higher than that at which the target is located and therefore some of the perpendicular (to the magnetic field direction) component of the ion energy distribution function (IEDF) is expected to be converted into the parallel component of the IEDF. On axis the background magnetic field direction is parallel to the axis of the device, however, at larger radii, the background magnetic field has a radial direction (because the magnetic field at the target is diverging). Therefore, the measurements at the outer radius of the plasma column can detect part of the parallel component of the IEDF, whereas fiber 1 and fiber 2 do not measure the parallel component of the IEDF since they are viewing a location closer to the axis of the device. The increase of ion temperature with PS2 can then be due to the perpendicular component of the magnetic field to be conserved better at higher PS2 current since as PS2 current is raised the magnetic field at the target is closer to the magnetic field of the ion cyclotron resonance. Another potential discrepancy between the IR heat flux measurement in the core plasma and the Ar II Doppler Broadening measurement is that the heat flux on the target could be due to increased electron temperature in the core and not increased ion; temperature, however, RF simulations of the ICH antenna predicts heating of core ions more efficiently than core electrons. Finally, since the target region is dominated by interactions of the ions with neutrals, such as charge exchange with thermal and energetic neutrals coming off the target plate, these mechanisms may be dominant in the core plasma and therefore complicate the interpretation of this measurement.

5.4.2 Comparison of Simulations to Experiment

In this subsection, we aim to validate the COMSOL model of the ICH antenna with experimental measurements. This is done such that the COMSOL models can then be used to investigate the physics where optimum ICH heating was observed and design the model can faithfully be used to design ICH heating on MPEX. We have previously compared B-dot probe measurements of an experiment where the Kinetic Alfvén wave was expected to propagate with COMSOL simulations of the wave-fields. However, since the goal of designing an ICH antenna heating system on MPEX is to efficiently heat core ions, the approach taken here is to compare the integrated core power from the COMSOL simulation with measurements of peak heat flux in the core on the target plate during application of ICH power. The heat flux on the target is then used as an analog for efficient heating by the ICH antenna.

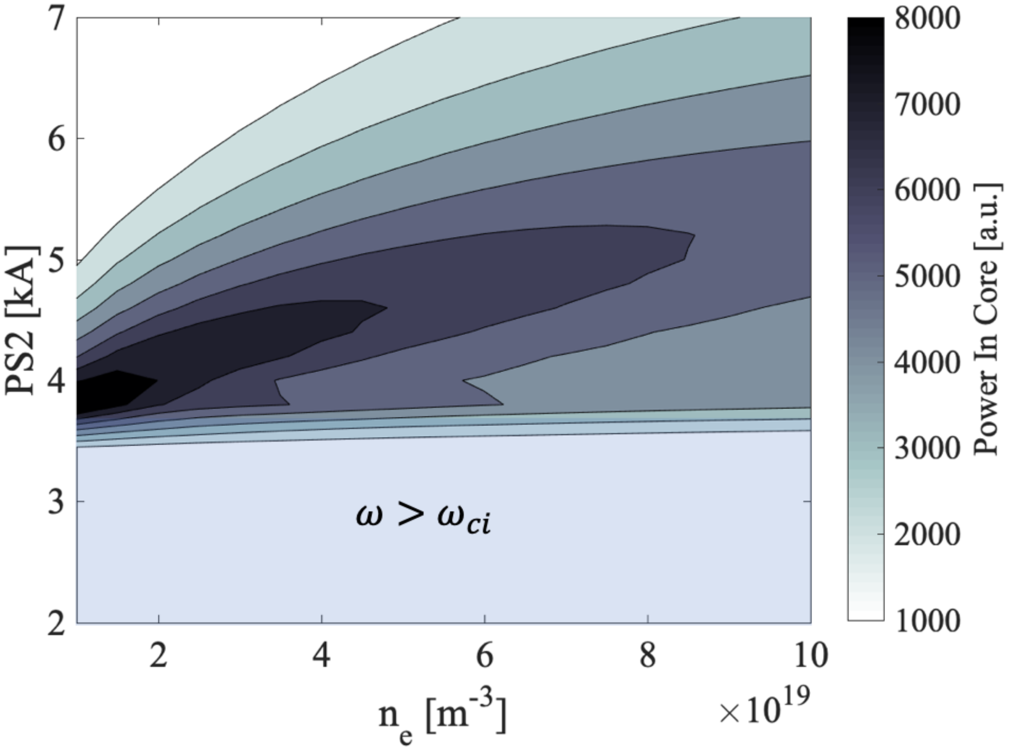

Figure 5.35: Integrated core power deposition contours as a function of magnetic field coil current (PS2) and peak electron density from the 2D COMSOL simulation for $m = -1$ azimuthal mode.

Since there is an uncertainty in the electron density in the ICH region, especially during the application of ICH power, the peak electron density is scanned in the COMSOL model along with the magnetic field coil current in the coils that PS2 is connected to. The integrated core power deposition is tracked across this parameter space and the results are shown in Fig. 5.35. In this figure, we see that there is a region of optimum core power deposition in the parameter space of core electron density and magnetic coil current in PS2. The lower bound of the magnetic coil current we see the below $PS2 < 3800$ A no significant core heating is predicted by the simulation. This is because at this value of magnetic coil current the magnetic field strength profile in Proto-MPEX is such that everywhere in the device the ion cyclotron frequency is absent ($\omega > \omega_{ci}$), and therefore no resonant heating of the ions can occur, also the Alfvén wave does not propagate in this regime. After the magnetic coil current in the simulation is raised ($PS2 > 3800$ A) such that the magnetic field is such that ($\omega < \omega_{ci}$), we see that contours of core heating now appear. These contours seem to follow a dispersion relationship pattern in the space where these contours are shown in Fig. 5.35. This is believed to be bounded by the presence of the Alfvén resonance in the parameters directly under the ICH antenna, more about this will be discussed in the following subsection.

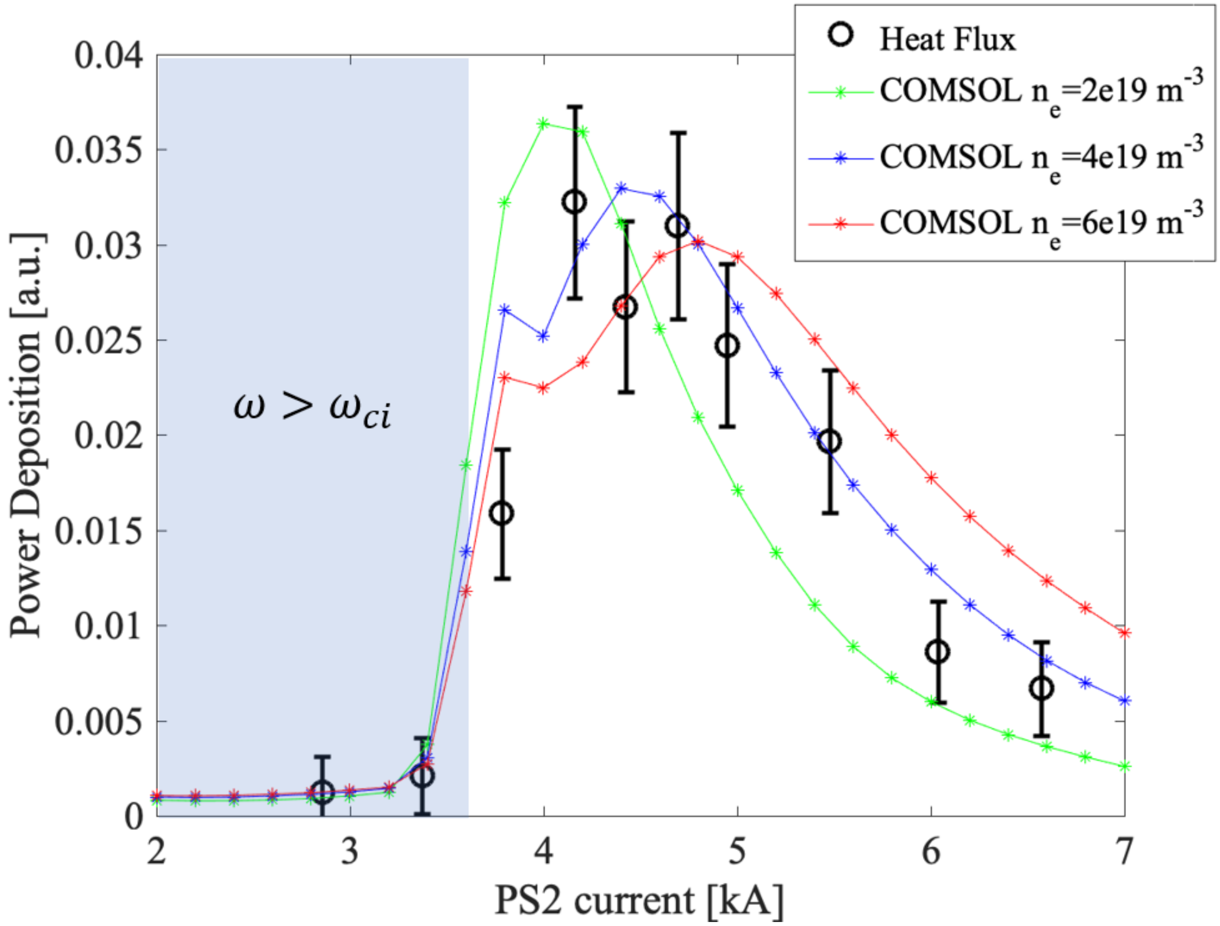

Figure 5.36: Experimentally measured power to the target plate, normalized to forward ICH power as a function of the magnetic field coil current (PS2) compared to normalized numerical predictions of core power deposition from the COMSOL simulation for the $m = +1$ azimuthal mode.

Figure 5.36 shows measurements of power on target normalized to the ICH forward power. The baseline (lowest valued measurements) here was also adjusted to match the simulation results baseline, this corresponds to subtracting out the helicon only contribution in the data. Numerical predictions of core power deposition from the COMSOL simulation are plotted in Fig. 5.36 for comparison to experimental data. These numerical simulations are normalized (divided by a constant 2.2×10^5) such that the amplitude is close to the normalized heat flux measurements so that a qualitative comparison can be made to the experimental data. From this data we see that the simulations capture the magnetic field strength at which there is a sharp increase in heating efficiency ($PS2 > 3800$ A), then when the magnetic field is increased the efficiency falls off. The peak of the core heating efficiency varies in the simulation data depending on the peak electron density. Since there is not a measurement made near the ICH antenna this is not a parameter that is experimentally constrained. The peak electron density in the core is expected to vary with PS2 strength due to several effects such as flux compression and flux of plasma decreasing due to increasing PS2 currents during helicon only experiments. Therefore, the electron density in the ICH region is bounded between $n_e = 2 - 6 \times 10^{19}$ m^{-3}. This range of electron density captures the decreasing efficiency of the ICH with PS2 current quite well. Now that we have gained confidence in the numerical simulations to predict optimum magnetic field geometry, a systemic parametric study is carried out in the following subsection that will characterize

5.4.3 Numerical Optimization of the ICH region

The focus of this subsection will be to numerically scan the optimization parameter space of the ICH antenna to better understand how to optimize the ICH antenna and magnetic field geometry for ion heating. The parameters that will be scanned in this study will include the following 1) antenna length 2) driving frequency 3) distance to ion cyclotron resonance. However, before the investigation of these parameter spaces, the physics that bounds the region of efficient power deposition when operating in $\omega_{ci} > \omega$ will be discussed.

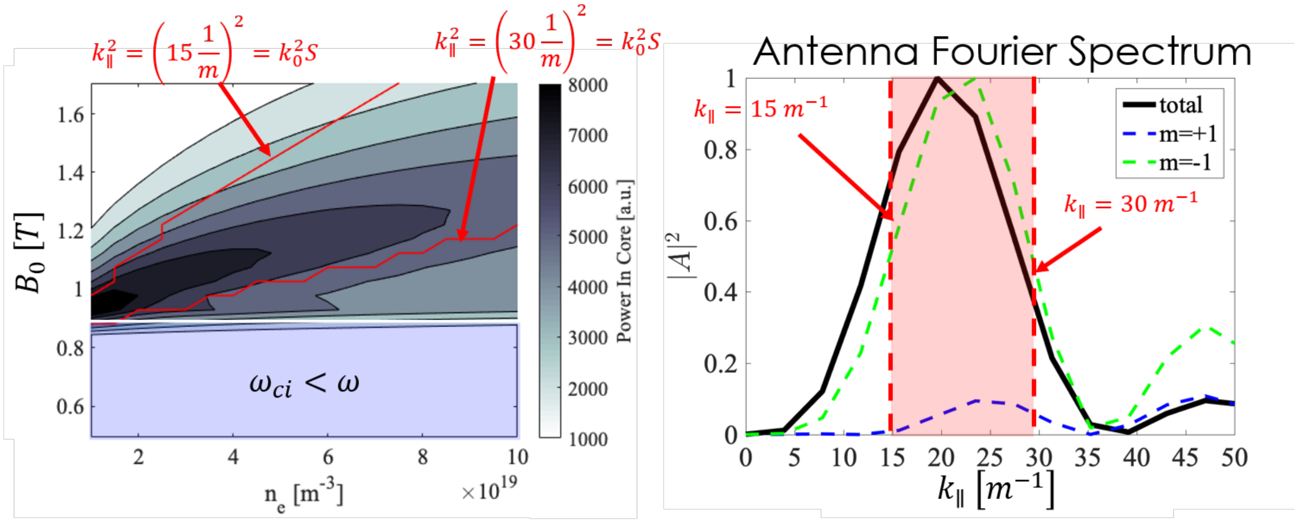

Figure 5.37: Integrated core power deposition contours as a function of average magnetic field strength under the ICH antenna and peak electron density from the 2D COMSOL simulation for $m = -1$ azimuthal mode (left). The Alfvén resonance contours for the values of $k_{||}$ that bound the full-width half-max of the fundamental antenna spectrum are shown. Antenna Fourier spectrum of the $m \pm 1$ modes as well as the summation of both modes (right). The full-width half-max of the main spectral feature is highlighted in red.

The hypothesis proposed here is that the region of efficient core power deposition observed in Fig. 5.37

is bounded by where the plasma column underneath the antenna contains the Alfvén resonance in the main spectral feature of the ICH antenna. This is believed to be key for efficient excitation of the Kinetic Alfvén wave and therefore efficient heating of the core plasma. The 2D models ICH antenna vacuum spectrum of both $m = \pm 1$ azimuthal modes and the summation of both modes is shown in Fig. 5.37. Since the power deposition contours are from the $m = -1$ azimuthal mode, which has been shown in the previous section to predict experimental optimization quite well, the $k_{\|}$ spectrum of the $m = -1$ azimuthal mode are only considered here. The values of $k_{\|}$ that define the FWHM of the main spectral feature of the antenna are used to then plot contours of the Alfvén resonance on the power deposition contours in Fig. 5.37. These contours bound the region of increased power deposition well with the exception of the higher magnetic field and electron density region that seem to curve away from the contour of the Alfvén resonance at $k_{\|} = 15$ m^{-1}.

Antenna Length

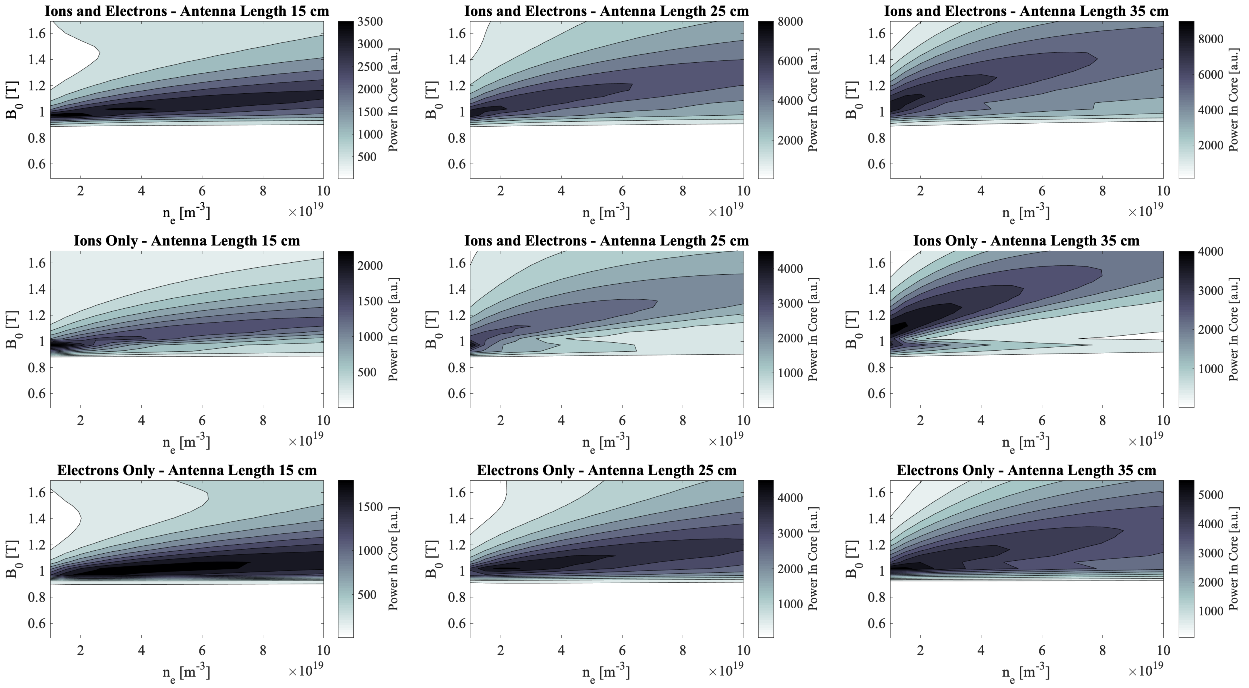

Figure 5.38: Contours of integrated core power deposition to ions and electrons (top row), ions only (middle row), and electrons only (bottom row) as a function of magnetic field strength under the antenna and peak electron density in the core plasma. These contours are plotted for conditions of driving frequency of $f = 7$ MHz and it is in the experimental magnetic field configuration. The antenna length is varied in this array of figures and the figures correspond to an antenna length of 15 cm (left column), 25 cm (middle column), and 35 cm (right column).

Figure 5.38 is an array of contours of power deposition in the core plasma to the different species for several different antenna lengths. The main features in this array of plots are that as the antenna length is increased the contours representing the peak power deposition of the antenna begins to shift to higher magnetic field values for constant electron density values. This is because the longer that the antenna is the $k_{\|}$ spectrum of the antenna shifts to lower values. This pushes the Alfvén resonance location at constant electron density values to higher values of magnetic field strength. Therefore, the antenna length is an important parameter to consider when designing the magnetic field configuration under MPEX.

The shortest antenna length presented in Fig. 5.38 shows that the smallest amount of core power deposition occurs for the 15 cm antenna, while the 25 cm antenna shows significantly more core power deposition that the 15 cm antenna. The 35 cm shows the most core power deposition of the antenna lengths, however, it is a modest increase over the 25 cm antenna. The quantitative value of power deposition is not predicted accurately from the 2D axisymmetric simulations. The reasons for this is that only the $m = -1$ azimuthal mode is taken into account, and a small value of electrical conductivity is added to the air region around the antenna which acts to cause artificial loading on the antenna and therefore the power deposition in the plasma layer is not accurately captured. However, qualitative comparisons between the magnitudes of power deposition can still be made and it seems that the shortest antenna is a poor choice to couple power into the plasma core.

Driving Frequency

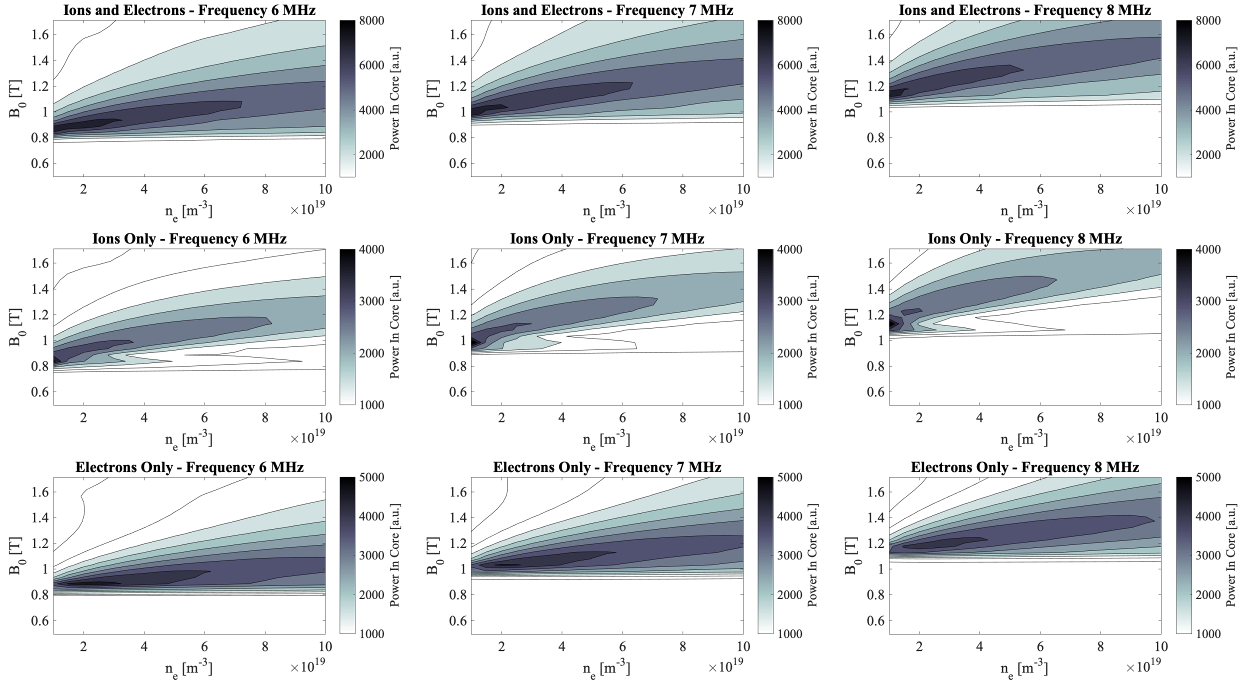

Figure 5.39: Contours of integrated core power deposition to ions and electrons (top row), ions only (middle row), and electrons only (bottom row) as a function of magnetic field strength under the antenna and peak electron density in the core plasma. These contours are plotted in the experimental magnetic field configuration, for an antenna with a length 25 cm. The driving frequency was varied in this array of figures and the driving frequency corresponds to $f = 6$ MHz (left column), $f = 7$ MHz (middle column), and $f = 8$ MHz (right column).

Figure 5.40 is an array of contours of power deposition in the core plasma to the different species for several different driving frequencies. From this figure, the main feature induced by increasing the driving frequency of the antenna is that the contours of high power deposition are shifted to higher magnetic field strengths. However, changing the driving frequency does not show more efficient core power coupling in general and this knob can simply be used to tailor the antenna to the magnetic field configuration.

Distance to Ion Cyclotron Resonance

An important aspect of ICH antenna performance is to understand the effect of increasing the distance of the antenna to the ion cyclotron resonance. Initially, when only the IAW was considered and the cold plasma model was used to simulate the ICH region, increasing the distance from the ICH antenna to the ion cyclotron resonance was recommended to allow the IAW to access the core plasma. However, with the understanding that the KAW can propagate in the Proto-MPEX plasma column and is responsible for heating the core plasma this original recommendation no longer holds the same logical merit and the effect of moving the ion cyclotron resonance far away from the antenna is relatively unexplored, which is what is aimed to be accomplished here. To explore moving the ion cyclotron resonance away from the ICH antenna, 3 separate magnetic field configurations are simulated by adding magnetic field coils with the same spacing as the spacing between coils 9 through 12 and applying PS2 current to these additional coils.

Figure 5.40 shows the magnetic field configurations used to explore the distance between the ion cyclotron resonance and the ICH antenna. The ”standard” configuration is the magnetic field configuration that corresponds to the 2018 experimental campaign magnetic coil configuration. When $PS2 > 4000$ A in this configuration the ion cyclotron resonance is between $1 - 20$ cm away from the ICH antenna. The ”long” configuration is made by adding an additional magnetic field coil between coils 11 and 12 that are spaced ≈ 19 cm away from coil 11, the spacing between coil 11 and coil 12, ≈ 32 cm, is kept between the newly added coil and the last coil in the simulation. The ”longer” configuration is then made by adding yet another coil in the same fashion between the last coil and the coils by the ICH antenna.

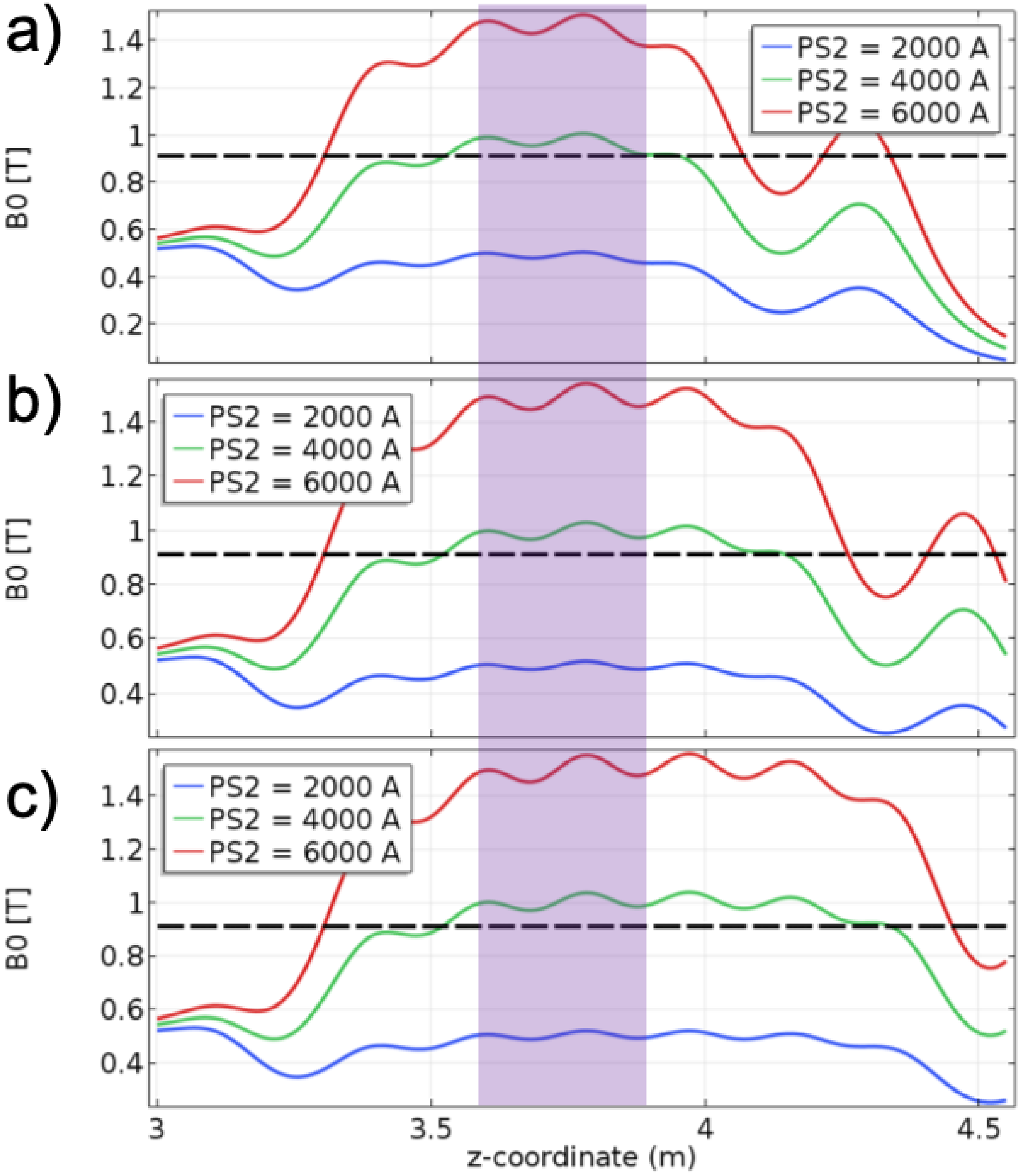

Figure 5.40: On axis magnetic field profile in ICH region for the magnetic configurations used in this section to study the effect of increasing the distance from the antenna to the ion cyclotron resonance is shown here a) "standard", b) "long", and c) "longer". The magnetic field profile is shown for 3 increasing PS2 currents in each configuration. The black dashed line represents the magnetic field strength of the ion cyclotron resonance at $f = 7$ MHz, the shaded purple region represents the location of the ICH antenna.

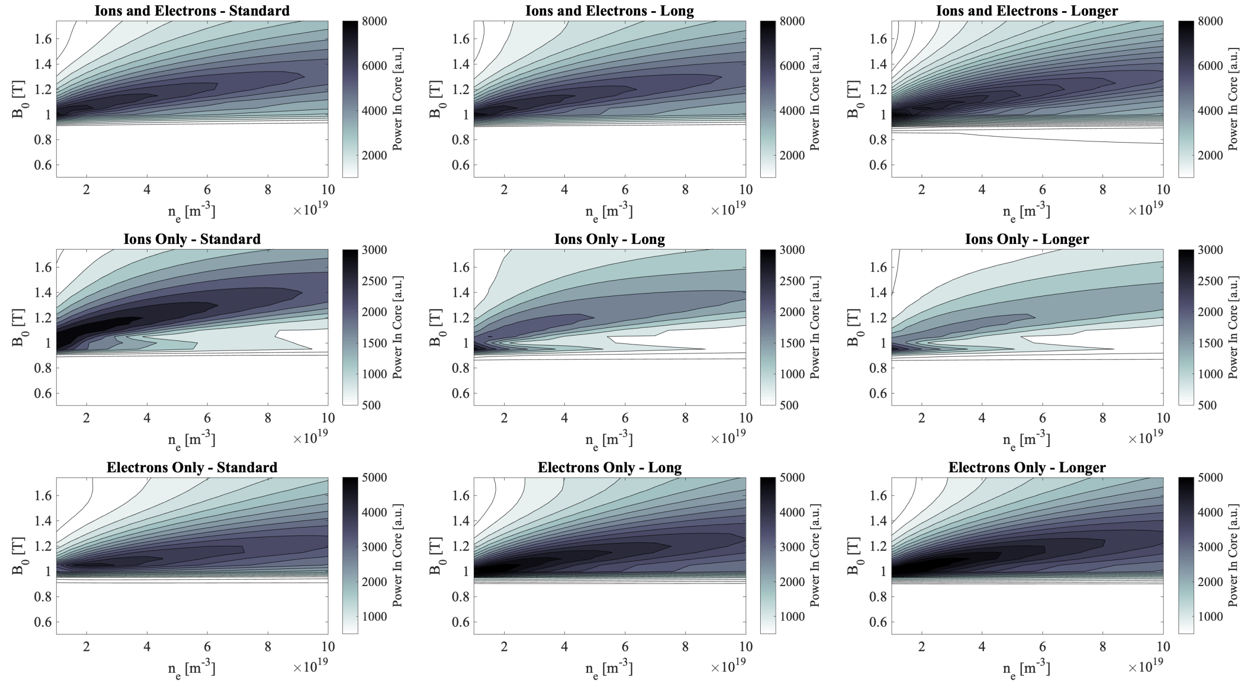
Ions and Electrons - Standard
Ions and Electrons - Long
Ions and Electrons - Longer
Ions Only - Standard
Ions Only - Long
Ions Only - Longer
Electrons Only - Standard
Electrons Only - Long
Electrons Only - Longer

Figure 5.41: Contours of integrated core power deposition to ions and electrons (top row), ions only (middle row), and electrons only (bottom row) as a function of magnetic field strength under the antenna and peak electron density in the core plasma. These contours are for an antenna with a length 25 cm and a driving frequency of $f = 7$ MHz. The magnetic field configuration was varied to move the distance of the antenna to the ion cyclotron resonance from the antenna, the magnetic field configurations in this figure are as follows: standard configuration (left column), long configuration (middle column), and longer configuration (right column).

Figure 5.41 is an array of contours of power deposition in the core plasma to the different species for several different magnetic field configurations. From this figure, the main effect of moving the ion cyclotron resonance further away from the antenna is that more RF power is absorbed by the electrons vs the ions in the plasma volume. This is because the kinetic Alfvén wave is excited under the ICH antenna and deposits energy to the electrons along the Alfvén resonance contours as it propagates towards the ion cyclotron resonance, this damping is not as strong as ion cyclotron damping and therefore the damping takes place over a longer distance. However, when the kinetic Alfvén wave encounters the ion cyclotron resonance it damps very strongly and the energy is absorbed by the ions at the ion cyclotron resonance. Therefore, as the ion cyclotron resonance is moved away from the ICH antenna the wave will deposit energy to the electrons and have less energy to heat the ions with, therefore if the ion cyclotron resonance is located in close proximity to the ICH antenna ions will be heated more efficiently than when the ion cyclotron resonance is moved away from the antenna.

5.4.4 Power Scans and Extrapolation to MPEX

This subsection shows heat flux, and power on target measurements as a function of ICH power and extrapolates the results to ICH power relevant to MPEX. This extrapolation shows that helicon and ICH power alone (without the additional heat from EBW/ECH) can achieve parallel heat fluxes on MPEX of $q = 10$ MWm^{-2} with 200 kW of helicon power and 400 kW of ICH power. Ion temperature measurements as a function of ICH power are also presented across several viewing chords, measurements at different axial locations with the central viewing chord all show a linear increase of ion temperature with ICH power. However the 5 viewing chords closest to the target, which correspond to Fig. 2.19, only show increasing ion temperature with ICH power in the periphery of the plasma column (fiber 1 and fiber 2), and not in fibers 3 through 5 which view the core plasma. These experiments were carried out in the magnetic configuration shown in Fig. 5.30 with $PS2 = 4250$ A, which we see is an optimum magnetic field configuration. The driving frequency of the antenna was $f = 6.5$ MHz.

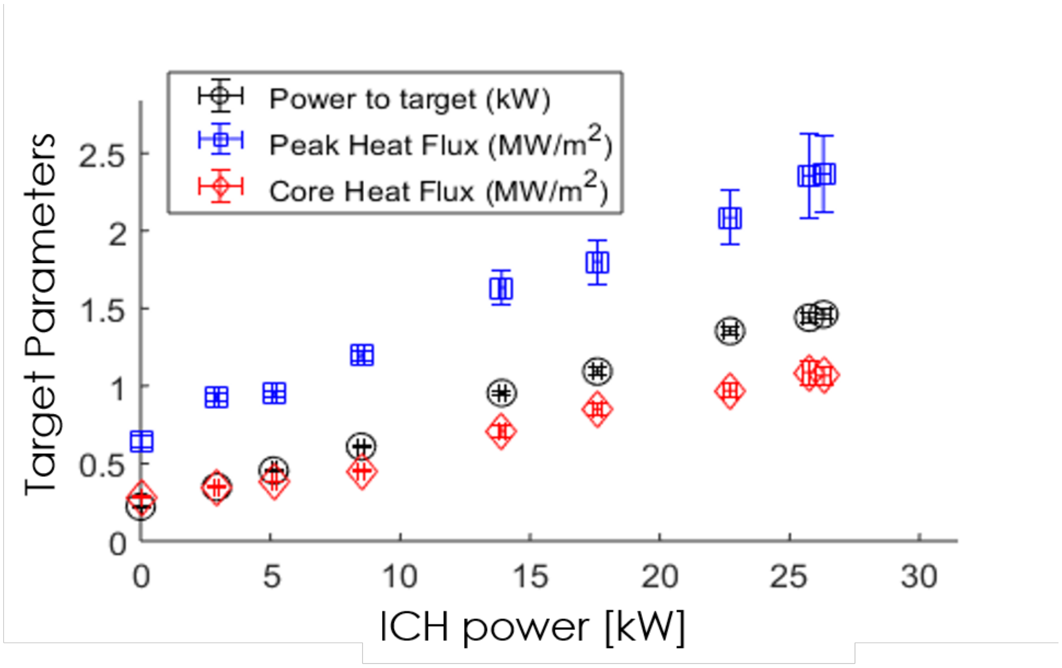

Figure 5.42: Measurements from the IR camera of integrated power to target (black circles), eak heat flux (blue squares), and peak heat flux in the core plasma (red diamonds) as a function of ICH power.

Measurements of heat flux and power on target are shown in Fig. 5.42 as a function of ICH power. Power on target, peak heat flux, and core heat flux all are linearly increasing with applied ICH power.

Extrapolating the core heat flux measured here to the planned 400 kW of ICH power shows that we can expect the core heat flux to be $> 10\ MWm^{-}2$ with only 100 kW of helicon power and 400 kW of ICH power, and not including additional heat flux due to ECH heating.

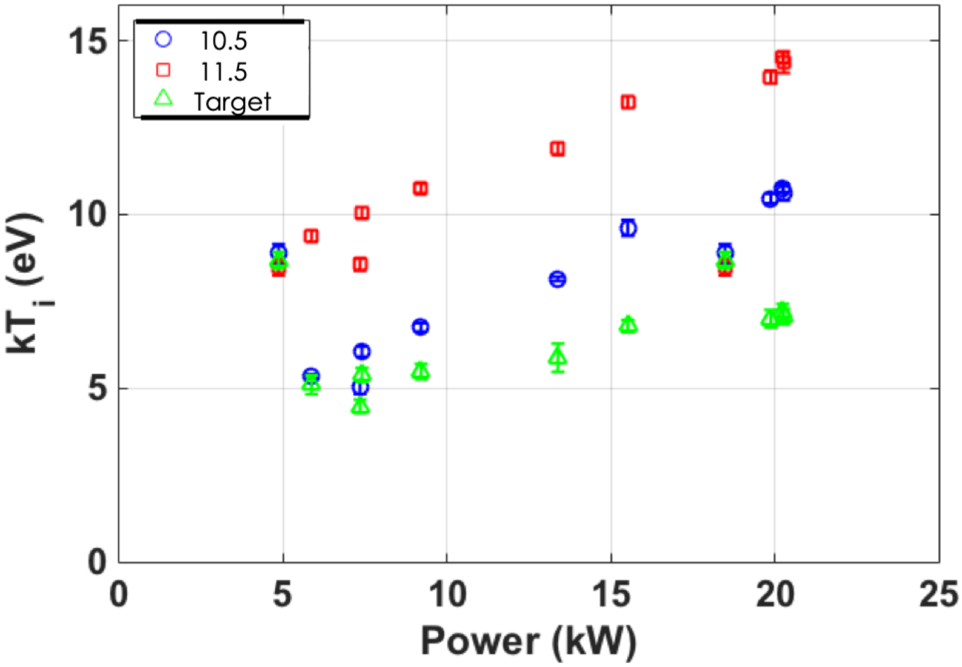

Figure 5.43: Ion temperature measured as a function of ICH power in the central viewing chord at Spool 10.5, Spool 11.5, and at the target.

MPEX also requires an ion temperature produced by the ICH of up to $T_i = 20eV$ at the target, the ion temperature measured at the target on Proto-MPEX so far has been between $T_i = 5 - 10$ eV. It is therefore important to understand how ion temperature is expected to scale with increasing ICH power. Figure 5.43 shows the ion temperature measured in the central viewing chord at several axial locations in the device. This parameter does not make sense to extrapolate to MPEX in the same fashion as target heat flux because it will largely depend on several factors including, the size of the plasma column, the electron density profile, and the neutral gas density in the plasma column. Since many of these factors will change from Proto-MPEX to MPEX the best that can be done is an estimate from a power balance.

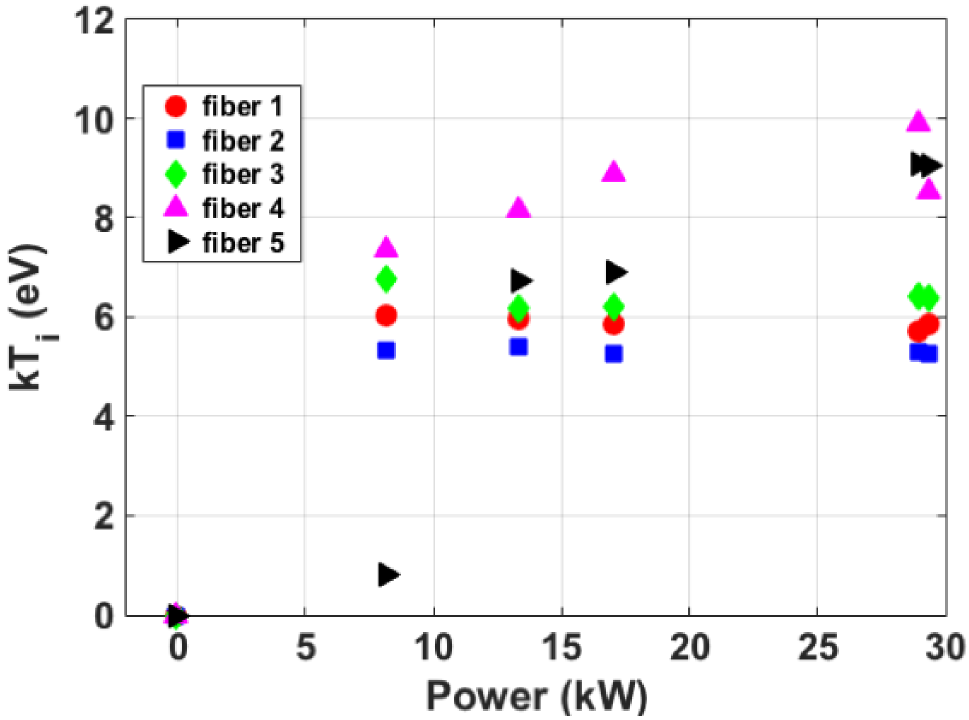

Figure 5.44: Ion temperature measured as a function of ICH power at the 5 viewing chords near the target shown by Fig. 2.19.

Figure 5.44 shows ion temperature measurements as a function of ICH power near the target in the view chords corresponding to Fig. 2.19. These measurements show a linear scaling of ion temperature with ICH power only for fiber 4 and fiber 5, which are the fibers measuring the periphery of the plasma column. However, the innermost fibers do not show a linear trend of ion temperature with ICH power. This discrepancy could be due to the reasons stated in the discussion above for the ion temperature measurements at the target as a function of PS2 current. Again resolving the discrepancy between the target measurements and Ar II measurements at the target requires more exploration and will be left for future work.

5.4.5 Discussion

This section covered the optimization of the ICH antenna. First, experimental measurements of target heat flux and Ar II ion temperature measurements from scanning PS2 current were presented. The target heat flux measurements showed that an optimum range of PS2 current for the ICH antenna as between 4000 A $< PS2 <$ 5000 A, as this range of PS2 current, measured the highest power on target and core heat flux. The ion temperature measurements were taken very close to the target plate, and the measurements taken in the periphery of the plasma followed the trend of the IR camera measurements. However, the centermost lines of sight do not show the same trend as the heat flux measurements. This is thought to be either due to the strong interactions with neutrals near the target, or an artifact of the measurement only sampling the perpendicular IED.

A comparison of the experimentally measured heat flux is then made to a 2D axisymmetric simulation of the ICH antenna. The simulation results of integrated core power deposition quantitatively agree with the IR measurements and shows a region of optimized power deposition between 4000 A $< PS2 <$ 5000 A. This model is then used to numerically explore the optimization space of 1) antenna length 2) driving frequency and 3) distance to the ion cyclotron resonance. This numerical exploration then allows us to understand how each of these experimental design knobs affects efficient core ion heating in the parameter space of magnetic field strength and electron density. The length of the ICH antenna allows control of the $k_{\|}$ spectrum of the antenna. From this numerical study, it is observed that the slope of the region of efficient core heating is controlled by the $k_{\|}$ spectrum of the antenna. As explained previously to efficiently heat the core plasma the magnetic field strength, driving frequency, and electron density under the antenna must allow the Alfvén resonance to exist in the core plasma column. The driving frequency of the antenna simply shifts the efficient region of core power deposition around the magnetic field space, however, it does not affect the slope of efficient core power deposition in the ICH region. The driving frequency also does not seem to affect the efficiency of core power deposition either. The driving frequency of the ICH antenna is a useful knob for controlling the magnetic field strength at which the antenna is to be operated. Finally, the distance to the ion cyclotron resonance is scanned by inspecting the cases of 3 different magnetic field configurations, the ”standard”, ”long”, and ”longer” magnetic field configurations are inspected and it is observed that as the ion cyclotron resonance is moved physically far from the ICH antenna, that more of the RF energy is absorbed by the electrons over the ions. If ion energy absorption is to be maximized then the ion cyclotron resonance should be located as close a possible to the ICH antenna.

Finally, an extrapolation of heat flux by the ICH to planned powers on MPEX is done in this section. First, an ICH power scan is done and shows a linear trend in both powers on target and maximum core heat flux. Extrapolating these measurements to the 400 kW of ICH power planned to be installed on MPEX. The results show that ICH and helicon alone can reach the heat flux goal on MPEX of heat flux greater than 10 MWm^{-2}, without the addition of ECH heating. This is a great result that shows the viability of the ICH antenna to heat the plasma to achieve one of MPEX's target parameters. A question remains about the MPEX goal of achieving ion temperatures at the target of $T_i = 20$ eV. Ion temperature measurements are shown as a function of ICH power applied and they show that ion temperature increases linearly with applied power at the central view locations at spool 10.5, spool 11.5, and at the target. However, the ion temperature measurements taken with the view chords closer to the target do not show this linear trend of increasing with power in the innermost view chords. This trend seems to be in disagreement with the measurements of heat flux at the IR target and is most likely due to an artifact of the ion temperature measurement only sampling the perpendicular IED.

Chapter 6

Conclusions and Future Work

6.1 Summary and Conclusions

This section serves to reiterate and summarize the work presented throughout this thesis. The conclusions arrived at, and the relevance of this work is also presented. The work relevant to the helicon plasma source is presented first. The novelty of this source is that it is the highest power helicon source in operation to our knowledge. The helicon work here also shows that core heating by the fast wave is responsible for the efficient density production and the linear scaling with magnetic field strength. Next, ion cyclotron heating work will be discussed. This work is significant because it proved the viability of heating ions via the beach heating technique in the high electron density present in Proto-MPEX. To the knowledge of the Proto-MPEX team, heating ions in the core plasma for conditions where the electron density is greater than the Alfvén resonance has not been reported; on the contrary, authors have published numerical papers excluding the possibility of core ion heating in high electron density conditions [122]. This is especially true for an antenna scheme such as Proto-MPEX which requires coupling power from the periphery through a low-density region to the high-density core plasma. This thesis presents numerical calculations along with experimental evidence showing that this has been accomplished on Proto-MPEX.

6.1.1 Helicon Plasma Source

MPEX requires a plasma diameter of $d_p \approx 10$ cm, and the size of the plasma column will be dictated by the flux limiting surface in the device. The flux limiting surface in Proto-MPEX occurs at helicon window because this region operates at the lowest magnetic field strength in the device. Thus, the strength of the magnetic field under the helicon dictates the diameter of the plasma column at the target; for the current geometry of the helicon window, the helicon source must operate at magnetic field strengths of $B_H \approx 0.2$ T to accomplish the plasma diameter needed for MPEX. High-density plasmas have not been achieved on Proto-MPEX at $B_H = 0.2$ T. A metric for the performance of the plasma source, used to compare to other plasma source is the ionization cost, which is estimated to be $E_{IZ} \approx 1000 \ \frac{eV}{ion}$ on Proto-MPEX for it's best performing plasma. VASIMR has shown that they have achieved an ionization cost of $E_{IZ} \approx 200 - 300 \ \frac{eV}{ion}$, which shows that Proto-MPEX can improve its performance by a factor of $\times 3 - \times 4$.

The helicon plasma sources have shown to operate more efficiently with increasing magnetic field strength. Proto-MPEX has shown to operate in the "helicon-mode" up to a magnetic field strength of $B_H \leq 0.07$ T, then the device stagnates and falls off in electron density production at higher magnetic field strengths. The experimental observations show that when the helicon operates in "helicon-mode" a transition of power coupling from edge to the core is simultaneously accompanied by the formation of a fast-wave radial eigenmode. These observations are hypothesized to be due to the plasma column entering the anti-resonance regime where the fast-wave doesn't transfer power to the slow-wave in the periphery of the plasma, which allows for more energy available for core power deposition. Therefore, it is shown that helicon sources have the potential to be used as plasma sources for applications requiring high electron density ($n_e > 4 \times 10^{19}$ m^{-3}) in light gases when they operate in a mode which allows significant core power deposition. Next, a 2D axisymmetric model was used to gather numerical evidence to reassert that the power coupling is due to the fast-wave allowing cavity like RF magnetic field structures under the helicon antenna. This understanding of the operation regime of the helicon source is different than in other sources, whereas other others have asserted that power deposition in helicon sources is dominated by the slow-wave in the periphery of the plasma column.

Next, a 0D volume averaged power-particle balance of the helicon source region is introduced and used with integrated core power deposition predicted from the RF simulations to estimate the steady-state helicon performance. This model underpredicts the helicon parameters measured at the helicon source region. However, the electron density dependence on helicon magnetic field strength, in the regime of $0.04 <$ T $B_H < 0.11$ T, is well captured and shows a linear increase in electron density production up until $B_H \approx 0.07$ T and then a deterioration of electron density production. This model shows evidence that the high-density mode operations where electron density increases linearly as a function of magnetic field strength are associated with increased core power deposition, that can be predicted numerically. This model predicts another region of increased electron density production in the regime $B_H > 0.11$ T, that is not observed experimentally; however, experimental exploration of higher density operation has not been performed at these higher magnetic field strengths. This model was determined to adequately capture the physics in the helicon source region, so it is then used to quantify the expected improvement in the performance of the helicon source region from suggested optimization suggestions. These optimization suggestions include: 1) Increasing the RF power and operating at a higher magnetic field strength which increases the electron density and temperature in the helicon source and decreases the ionization cost of the source by $\approx 36\%$.

2) Reducing the volume of the helicon source region by moving the dump plate inwards, also is shown to increase electron temperature and density in the source region which leads to an improvement in ionization cost of $\approx 21\%$. 3) Electrically isolating the dump-plate to allow the plate to stay at the floating potential is estimated to improve ionization cost only slightly by $\approx 6\%$ in the best case scenario. If these improvements are used together then the model predicts an decrease in ionization cost of $\approx 55\%$.

6.1.2 Ion Cyclotron Heating

Proto-MPEX is the first device to our knowledge to demonstrate high power ICH beach heating at values of n_e greater than the Alfvén resonance value, where only the kinetic Alfvén wave can propagate. Nevertheless, considerable experimental data has been obtained together with numerical simulations have produced evidence to show the feasibility of ICH system for MPEX. First, the propagation characteristics of the waves in the ICH region in Proto-MPEX have been investigated numerically with dispersion analysis and a 3D full-wave model. This full-wave model made use of a simplified Maxwellian dielectric tensor. The addition of the thermal effects into the plasma tensor was shown to be critical to predicting core ion heating. Analysis of the dispersion properties in the ICH region shows that both the IAW and the KAW can propagate in the Proto-MPEX plasma. However, it is the excitation of the KAW that opens an avenue for efficient heating of core ions in Proto-MPEX. In addition to the numerical simulations of the KAW, a radial scan with the B-dot probe measurements successfully measured a propagating Kinetic Alvén Wave in the ICH region which compared well with simulations of the wave fields from COMSOL.

The simulation results show that when the edge electron density is sufficiently high ($n_e > 1 \times 10^{17}$ m^{-3}), and the electron temperature is increased to where the KAW is expected to propagate ($T_e > 2$ eV), the core power deposition increases significantly (5%–30% of the total power). These numerical results demonstrate that thermal effects are required to capture the physics of the ICH system on Proto-MPEX. This result is unexpected at such low values of electron temperature where cold plasma physics is typically sufficient to capture wave-propagation. The numerical simulations also predict the split between heating electrons and ions in the core. Contours of power absorbed by the ions vs. the power absorbed by the electrons are presented to show the locations where this heating is occurring. The ion heating primarily occurs at the ion cyclotron resonance, whereas the electron heating occurs either at the periphery of the plasma column or at the Alfvén resonance, which is a significant contribution to core electron heating due to either Landau or collisional damping of the fast-wave. Integrated core power from the full-wave calculations shows that above $T_e > 4$ eV the ions absorb ($\approx 80\%$) of the power coupled to the core or (20% of the total power). Therefore, this numerically demonstrated a theoretical route to efficient core ion heating on Proto-MPEX.

Experimental evidence of core ion heating has been shown as well from both heat flux and ion temperature measurements. The ion temperature measurements showed an increase in the ion temperature in the central line of sight at Spool 9.5 and at Spool 10.5 when ICH power was applied to the plasma. The ion temperature peaked at Spool 9.5 indicated that the ion heat source is located closest to that location, this is the location of the ion cyclotron resonance downstream of the antenna where the RF power is expected to be absorbed by the fundamental cyclotron resonance. Heat flux measurements at the target indicate a significant increase in heat flux delivered to the target during application of ICH power. The combined observations from the ion temperature and heat flux measurements show strong evidence of core ion heating.

The effect of neutral gas pressure on transporting ion heat from the ICH heating region to the target is then explored. Charge exchange is the largest power loss channel for the ions in the Proto-MPEX plasma. An estimate of the power loss due to charge exchange is first presented to give a conservative estimate of the pressure regime that Proto-MPEX and MPEX are to be operated at if ion power is to be delivered from the ICH antenna region to the target plate. The region between the ICH antenna and the target shows an increase in pressure at the baratron located in this region. The source of this neutral gas is from plasma recombination at the target, and which the pumping at the target is insufficient to remove this source of neutral gas from the region. This ultimately leads to a build-up of neutral gas, which acts to charge exchange with the energetic ions and this is the largest power sink for the ions in Proto-MPEX. Then transient "cooling" behavior of the plasma is shown. This "cooling" includes a transient decrease in ICH performance in both heat flux to the target as well as ion temperature. The ion temperature measurements show a transient cooling of the ions that is consistent with this cooling being due to neutral gas sourced from the target moving towards the ICH antenna region and is mitigated by increasing the ICH power.

When target material was changed from carbon to stainless steel significantly higher ion temperatures throughout the plasma column as well as steady-state heat flux to the target was observed. These improvements to plasma performance were attributed to "sheath" heating, which in summary is the heating of the bulk plasma via charge exchange of energetic neutrals. The energetic neutrals enter the plasma by the reflection of ions, that are accelerated through the plasma sheath. The increase in reflection coefficient of the stainless steel vs the target allowed these energetic neutrals to mitigate the energy losses from charge exchange with thermal neutrals. This effect is quantified and the calculation is presented in this section which shows that the reflection coefficient of iron can increase the flux of energetic neutrals entering the plasma column over that of a carbon target, thus balancing the charge exchange losses from the thermal neutral population.

Next, the optimization of the magnetic field under the ICH antenna was shown. Experimental measurements of target heat flux and Ar II ion temperature measurements from scanning PS2 current were presented. The target heat flux measurements showed that an optimum range of PS2 current for the ICH antenna as between 4000 A $< PS2 <$ 5000 A, as this range of PS2 current, measured the highest power on target and core heat flux. The ion temperature measurements were taken very close to the target plate, and the measurements taken in the periphery of the plasma followed the trend of the IR camera measurements but the centermost lines of sight do not. This is thought to be either due to the strong interactions with neutrals near the target, or an artifact of the measurement only sampling the perpendicular IED. Then the experimentally measured heat flux to the target is compared to a 2D axisymmetric simulation results of the ICH antenna. The simulation results of integrated core power deposition quantitatively agree with the IR measurements and shows a region of optimized power deposition between 4000 A $< PS2 <$ 5000 A. This model is then used to numerically explore the optimization space of 1) antenna length 2) driving frequency and 3) distance to the ion cyclotron resonance. The results of this showed that if ion absorption is to be maximized then the ion cyclotron resonance should be located as close a possible to the ICH antenna, and the antenna length should be between 25-35 cm long. The driving frequency of the antenna can then be chosen such that the ICH heating is compatible with the magnetic field required for electron heating.

Finally, an extrapolation of heat flux by the ICH to planned powers on MPEX is presented. Ion temperature measurements are shown as a function of ICH power applied and they show that ion temperature increases linearly with applied power at the central view locations at spool 10.5, spool 11.5, and at the target. However, the ion temperature measurements taken with the view chords closer to the target do not show this linear trend of increasing with power in the innermost view chords. This is due to the strong neutral interactions near the target, and with increases in electron temperature and ICH power, ion temperature will likely be sustained there. ICH power scan shows a linear trend in both power on target and maximum core heat flux. Extrapolating these measurements to the 400 kW of ICH power planned to be installed on MPEX show that ICH and helicon alone can reach the heat flux goal on MPEX of heat flux greater than 10 MWm^{-2}. This shows the viability of the ICH antenna to heat the plasma to achieve the MPEX's target heat flux goal.

6.2 Future Work

The previous sections outlined the wave propagation theory for the ICH region and showed avenues for core ion heating in Proto-MPEX conditions. Core heating by the ICH was demonstrated by measurements of the ion temperature as well as an increase of target heat flux as measured by the IR camera. Extrapolation of heat flux to the IR target to MPEX parameters show that MPEX could meet its goal of heat fluxes greater than 10 MWm^{-2} with the addition of ICH to a helicon only plasma. The ion temperature also showed linear scaling, therefore it is controllable, with the ICH antenna for most regions of the device. These were very successful demonstrations of the viability of ICH heating for MPEX. However, certain questions do remain for the ICH antenna operation. One of the more critical observations when operating the ICH antenna was a reduction in electron density when operating the ICH antenna. Since MPEX requires high electron density values at the target, the electron density drop that occurs during application of ICH power is an issue that must be overcome for a viable ion heating source. Increasing the ionization efficiency of the helicon antenna is another option for working around the electron density drop caused by the ICH antenna. The second issue with ICH is the power handling capability of the ICH antenna and the coaxial lines. Viable options for increasing the power handling capability are discussed here.

6.2.1 Exploring High Field Plasma Source Operation

As discussed in Chapter 4, operating the helicon plasma source in an efficient "helicon-mode" above helicon magnetic field strengths $B_H > 0.1$ T have been predicted numerically but not achieved experimentally. Operating at B_H above this threshold is critical for the MPEX plasma source because B_H controls the plasma diameter at the target. A larger plasma diameter is required so that divertor relevant plasma material interactions can be realized on MPEX. In this thesis, several optimizations to the plasma source region are suggested being 1) increasing RF power, 2) reducing the volume of the source, and 3) floating the dump plate to reduce sheath losses. These optimizations are now currently being explored on Proto-MPEX to realize operation of the plasma source above helicon magnetic field strengths $B_H > 0.1$ T.

6.2.2 Electron Density Drop and Electron Heating

During ICH antenna operation the electron density has been observed to decrease from helicon only values on measurements made with Double Langmuir Probes and Thompson Scattering. This behavior is problematic for ICH operation in MPEX, because of the requirement to produce electron densities in the range of $n_e = 5 - 10 \times 10^{19}\ m^{-3}$ at the target. Electron density has been observed to drop by a factor of 1.5 to 3 dropping to values of $n_e = 1 - 4 \times 10^{19}\ m^{-3}$ during application of ICH power to the plasma.

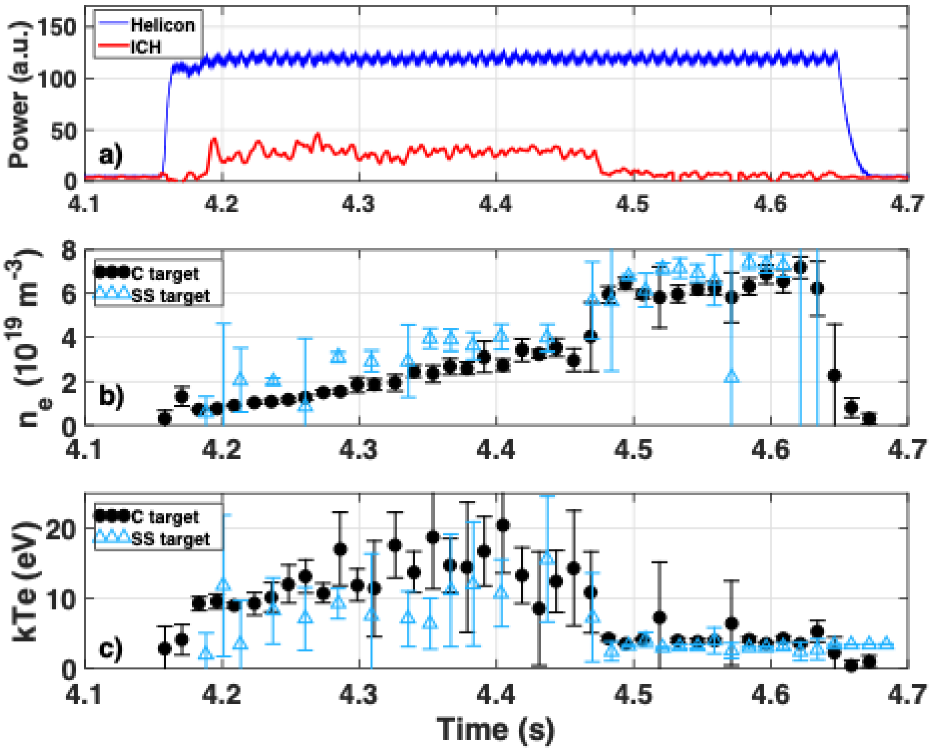

Figure 6.1: a) Helicon and ICH power traces showing relative pulse timings. (b) Electron density (n_e) and c) electron temperature (T_e) measured with a DLP at the target ($r = 0$) vs time for typical shot.

Figure 6.1 shows a typical timing of the helicon RF pulse with respect to the ICH pulse. This figure shows the temporal behavior of the electron density and temperature measured at the target for both a stainless steel and carbon target. In this figure we see that during the ICH power pulse the electron density reaches values of $n_e < 4 \times 10^{19}$ m^{-3} for the carbon target and jump back up to values of $n_e > 6 \times 10^{19}$ m^{-3} when the ICH power is turned off. The stainless steel target exhibits very similar behavior and therefore the density drop is not dependant on the target material. In this figure, we also see that the electron temperature is increased during the application of ICH power up to values of $T_e > 10$ eV and decreases back down to values of $T_e = 2 - 4$ eV after the ICH pulse. The increase of the electron temperature is much higher as measured by the DLP compared to Thompson scattering measurements from the 2016 experimental campaign shown in Fig. 6.2.

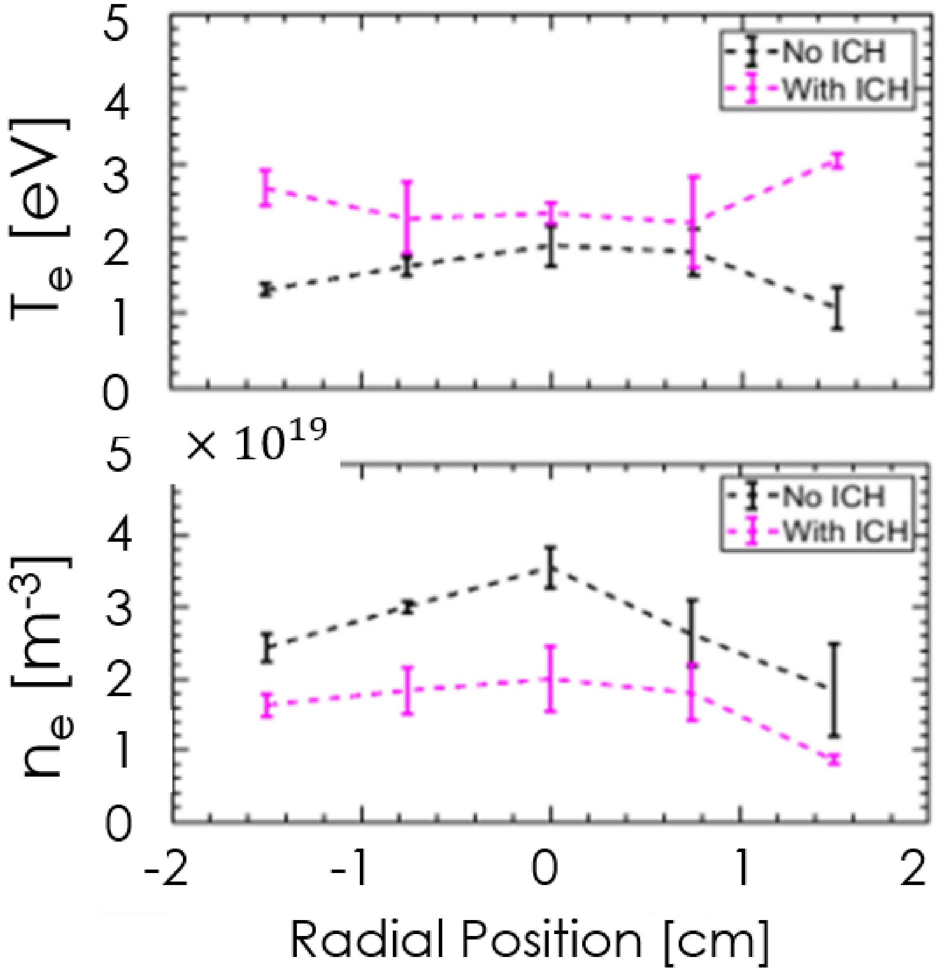

Figure 6.2: Thompson scattering measurements of the electron density drop during ICH operation during the 2016 experimental campaign.

Figure 6.2 shows Thompson scattering measurements of the electron density drop during the 2016 experimental campaign[69]. These measurements are shown to validate the DLP measurements shown in Fig. 6.1. In these experiments the helicon only electron density was peaked at values of $n_e \approx 4 \times 10^{19}\ m^{-3}$ and fell to values of $n_e \approx 2 \times 10^{19}\ m^{-3}$ during ICH operation. The electron temperature in these measurements also show an increase in electron temperature during ICH experiments, however, this increase is much more modest than the DLP measurements indicate. These measurements show that the electron temperature is increased by $T_e = 0.5 - 1.5$ eV from helicon only values. Since the electron and ion temperatures are both increased during the operation of ICH heating, the reason for the drop in electron density may be attributed simply to a drop in electron density due to an increase in the plasma flow. If the plasma flow were to increase during ICH operation than flux conservation would demand that the electron density drops.

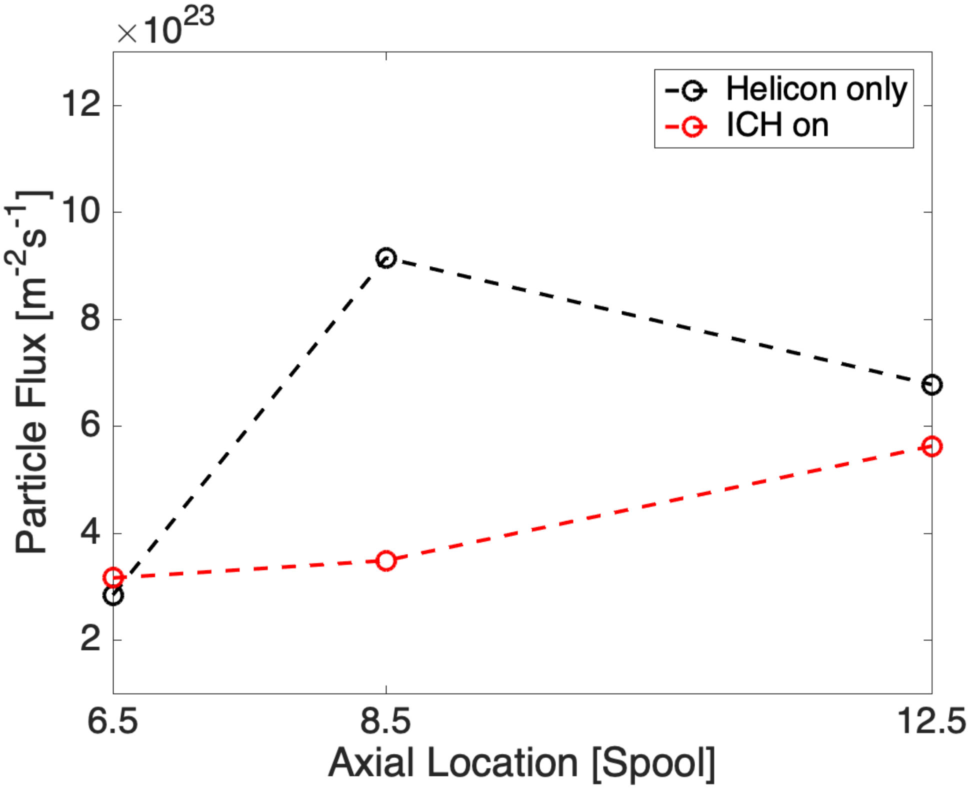

Figure 6.3: Particle flux at $r = 0$ calculated from measurements of flow made by Mach Probes, electron density and temperature measured by the DLP probes, and ion temperature measured by Ar II Doppler Broadening.

To understand if the plasma flow increases during ICH operations Mach probe measurements were taken at several axial locations along the device to understand the flow along with the device with and without ICH power. Mach probes measure the Mach number which is the plasma flow normalized to the ion sound speed, to convert this measurement to plasma flow, the ion sound speed must be calculated from the electron and ion temperatures according to $C_{si} = \sqrt{\frac{5}{3}\frac{kT_e+kT_i}{m_i}}$. The Mach probes are used with DLP measurements of electron temperature and density as well as ion temperature measurements from the Ar II spectroscopy to calculate the plasma flux towards the target before and after ICH as $\Gamma_+ = n_e M C_{si}$, where M is the Mach number measured by the probes. From this calculation, we see that the particle flux decreases when ICH is applied both at Spool 8.5 and Spool 12.5, but not at Spool 6.5. The variation of flux along the axis is due to the different magnetic field strengths at those axial locations causing flux compression to increase and decrease flux. From this estimate, we see that there is a drop of electron density that is accompanied by a drop in plasma flux and therefore the electron density drop is not due to simply increasing the plasma flow.

An exploration of plasma transport during ICH heating should be done to understand the drop in electron density during ICH heating. This exploration is left for future work on the ICH antenna.

6.2.3 Self-Consistent Modeling

The calculations done here cannot predict the mechanisms responsible for the transition into the "helicon-mode", the neutral gas profile near the target during ICH heating, or the mechanism for the electron density drop during ICH. Coupling these RF models to neutral gas and plasma transport simulations are required to shed light on the transition into these phenomena. Efforts are now underway to develop a self-consistent simulation for MPEX that couple the RF simulations to SOLPS [123] calculations of Proto-MPEX. These coupled RF heating, plasma transport, and neutral gas transport simulations will then allow answering these remaining research questions. These efforts are left for others for future work.

6.2.4 Excitation Mechanism of the KAW

The energy access channel by which the KAW is excited is still an open question. The mechanisms in question then are 1) evanescent energy under the antenna accessing the core plasma and exciting the KAW, or 2) a transition of the IAW into the KAW that occurs near the ion cyclotron resonance. The dependence on edge electron density shown in Fig. 5.7 supports the idea that the excitation mechanism of the KAW is via a transition that occurs near the ion cyclotron resonance, because at higher values of electron densities, up until the Alfvén resonance layer, the group velocity of the IAW becomes increasingly perpendicular. Exploring how energy from the periphery of the plasma access the core to excite the KAW is then an open question and will be left for future work.

6.2.5 Power Handling Limits

The planned power on MPEX for the ICH antenna is to be 400 kW, whereas currently the ICH antenna was operated up to $P_{ICH} = 35$ kW. This increase in power up to more than an order of magnitude now brings into question the power handling capabilities of the ICH antenna and its components. The engineering factors that limit power handling are the electric field between the antenna current straps and the vacuum window, the voltage in the coaxial transmission line between the outer and inner conductor, and the voltage and current across the matching capacitors. The electric field between the antenna and the current straps is dependant on the RF power coupled to the antenna and the loading of the antenna, which is determined by the plasma conditions such as magnetic field strength under the antenna, antenna type, the distance of the antenna from the plasma column, and the dielectric material between the antenna and the plasma. The limitations of the maximum electric field between the antenna and the dielectric are to avoid breakdown and arcing in this region. The voltage in the coaxial transmission line is dependant on the RF power launched and the loading of the antenna. The power handling limit here is set such to prevent the electric field between the inner and outer conductor from arcing. The matching network limits are dependant on the launched RF power, the loading of the plasma, and the design of the matching network and its components.

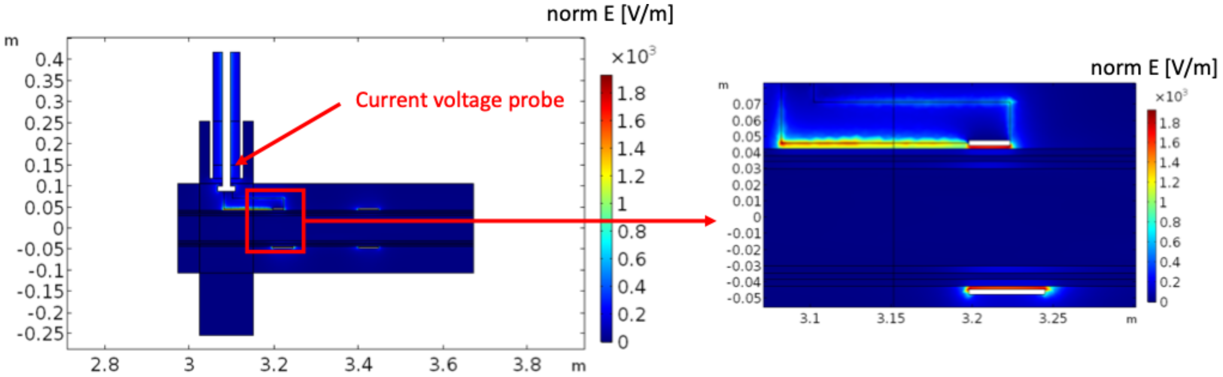

Figure 6.4: 3D COMSOL simulations of the peak electric field in the region between the ICH antenna and the dielectric window. The dielectric window is assumed to have the dielectric properties of quartz in this example simulation.

Figure 6.4 shows a 3D simulation of the ICH antenna and the peak electric field produced here. The simulation predicts plasma loading by tracking the S_{11} in the coaxial launch port and calculating the antenna loading in the presence of the plasma as follows: $Z_{load} = Z_0 \left(\frac{1+S_{11}}{1-S_{11}}\right)$. The simulation also tracks voltage and current on the coaxial feed in the location shown. The voltage on the coaxial cable is tracked by integrating the radial electric field on a line between the inner and outer conductor in the coaxial feed. The current in the cable is tracked by using Ampere's law and integrating the tangential magnetic field on a circle enclosing the inner conductor. This 3D model can now be used to predict plasma loading and do the engineering calculations required for designing an antenna system to handle 400 kW of ICH power. Some ideas to explore for power handling are to use multiple ICH antennas staggered, and fill the region between the ICH antenna and the ICH window with insulting gases such as SF_6. The engineering design work for designing a 400 kW ICH system will be left for future work, however, a model capable of numerically predicting the necessary features of the ICH antenna has been made here.

References

[1] E. Bering, M. Brukardt, J. Squire, T. Glover, V. Jacobson, and G. McCaskill, "Recent improvements in ionization costs and ion cyclotron heating efficiency in the VASMIR engine," in *44th AIAA Aerospace Sciences Meeting and Exhibit*, p. 766, 2006.

[2] C. M. Samuell and C. S. Corr, "Low-pressure hydrogen plasmas explored using a global model," *Plasma Sources Science and Technology*, vol. 25, no. 1, p. 015014, 2015.

[3] Y. Mori, H. Nakashima, F. W. Baity, R. H. Goulding, M. D. Carter, and D. O. Sparks, "High density hydrogen helicon plasma in a non-uniform magnetic field," *Plasma Sources Science and Technology*, vol. 13, no. 3, p. 424, 2004.

[4] J. F. Caneses and B. Blackwell, "RF compensation of double Langmuir probes: modelling and experiment," *Plasma Sources Science and Technology*, vol. 24, no. 3, 2015.

[5] B. Koch, W. Bohmeyer, G. Fussmann, P. Kornejew, and H.-D. Reiner, "Energy flux measurements in a steady-state discharge at PSI-2," *Journal of Nuclear Materials*, vol. 290, pp. 653–657, 2001.

[6] F. F. Chen, *An indispensable truth: how fusion power can save the planet.* Springer Science & Business Media, 2011.

[7] F. F. Chen, *Introduction to Plasma Physics and Controlled Fusion*, vol. 1. Springer, 1984.

[8] J. Wesson and D. J. Campbell, *Tokamaks*, vol. 149. Oxford University Press, 2011.

[9] J. P. Freidberg, *Plasma physics and fusion energy.* Cambridge University Press, 2008.

[10] H. J. N. van Eck, *The linear plasma generator Magnum-PSI.* PhD thesis, Technical University Eindhoven, Eindhoven, Netherlands, 2013.

[11] D. Goebel, G. Campbell, and R. Conn, "Plasma surface interaction experimental facility (PISCES) for materials and edge physics studies," *Journal of Nuclear Materials*, vol. 121, pp. 277–282, 1984.

[12] National Academy of Sciences, "14 Grand Challenges for Engineering in the 21st Century: Provide Energy from Fusion," 2019.

[13] "Priorities, Gaps and Opportunities: Towards A Long-Range Strategic Plan For Magnetic Fusion Energy," Tech. Rep. October, Fusion Energy Sciences Advisory Committee, 2007.

[14] R. Hazeltine and H. Neilson, "Research needs for magnetic fusion energy sciences," in *Report of Research Needs Workshop*, 2009.

[15] R. Maingi, S. Zinkle, H. Guo, B. LaBombard, J. Allain, R. Doerner, C. Kessel, D. Youchison, A. Hubbard, and A. Leonard, "Report on Science Challenges and Research Opportunities in Plasma Materials Interactions. 2015, from the US DoE Fusion Energy Sciences Workshop on Plasma Materials Interactions, May 4-7, 2015."

[16] J. Rapp, T. Biewer, T. Bigelow, J. Caneses, J. Caughman, S. Diem, R. Goulding, R. Isler, A. Lumsdaine, C. Beers, *et al.*, "Developing the science and technology for the material plasma exposure experiment," *Nuclear Fusion*, vol. 57, no. 11, p. 116001, 2017.

[17] J. B. Caughman, R. H. Goulding, T. M. Biewer, T. S. Bigelow, I. H. Campbell, J. Caneses, S. J. Diem, A. Fadnek, D. T. Fehling, R. C. Isler, *et al.*, "Plasma source development for fusion-relevant material testing," *Journal of Vacuum Science & Technology A: Vacuum, Surfaces, and Films*, vol. 35, no. 3, p. 03E114, 2017.

[18] J. Rapp, T. Biewer, J. Canik, J. Caughman, R. Goulding, D. Hillis, J. Lore, and L. Owen, "The development of plasma-material interaction facilities for the future of fusion technology," *Fusion Science and Technology*, vol. 64, no. 2, pp. 237–244, 2013.

[19] M. Greenwald, R. Callis, D. Gates, W. Dorland, J. Harris, R. Linford, M. Mauel, K. McCarthy, D. Meade, F. Najmabadi, *et al.*, "Priorities, gaps and opportunities: Towards a long-range strategic plan for magnetic fusion energy," *US Department of Energy Fusion Energy Sciences Advisory Committee Report No. DOE/SC-0102*, 2007.

[20] S. J. Zinkle, J. Blanchard, R. W. Callis, C. E. Kessel, R. J. Kurtz, P. J. Lee, K. McCarthy, N. Morley, F. Najmabadi, R. Nygren, *et al.*, "Fusion materials science and technology research opportunities now and during the iter era," *Fusion Engineering and Design*, vol. 89, no. 7-8, pp. 1579–1585, 2014.

[21] J. Scholten, P. Z. van Emmichoven, H. van Eck, P. Smeets, G. De Temmerman, S. Brons, M. van den Berg, H. van der Meiden, M. van de Pol, M. Graswinckel, *et al.*, "Operational status of the magnum-psi linear plasma device," *Fusion Engineering and Design*, vol. 88, no. 9-10, pp. 1785–1788, 2013.

[22] T. M. Biewer, T. S. Bigelow, J. Caneses, S. J. Diem, D. L. Green, N. Kafle, J. Rapp, and P.-M. Team, "Observations of electron heating during 28 ghz microwave power application in Proto-MPEX," *Physics of Plasmas*, vol. 25, no. 2, p. 024501, 2018.

[23] S. Diem, D. Green, R. Harvey, and Y. V. Petrov, "An electron Bernstein wave heating scheme for the Proto-MPEX linear device," *Physics of Plasmas*, vol. 25, no. 7, p. 072124, 2018.

[24] C. Lau, J. Caneses, T. S. Bigelow, T. M. Biewer, J. B. Caughman, R. H. Goulding, P. A. Piotrowicz, J. Rapp, H. B. Ray, and M. Showers, "Evidence of electron heating at different radial locations on Proto-MPEX," *Physics of Plasmas*, vol. 26, no. 3, p. 032503, 2019.

[25] T. Biewer, C. Lau, T. Bigelow, J. Caneses, J. Caughman, R. Goulding, N. Kafle, M. Kaufman, J. Rapp, and P.-M. Team, "Utilization of OXB mode conversion of 28 GHz microwaves to heat core electrons in the upgraded Proto-MPEX," *Physics of Plasmas*, vol. 26, no. 5, p. 053508, 2019.

[26] P. Piotrowicz, R. Goulding, J. Caneses, D. Green, J. Caughman, C. Lau, J. Rapp, and D. Ruzic, "Computational investigation of ion cyclotron heating on Proto-MPEX," *Physics of Plasmas*, vol. 26, no. 3, p. 033511, 2019.

[27] R. W. Boswell, "Plasma production using a standing helicon wave," *Physics Letters A*, vol. 33, no. 7, pp. 457–458, 1970.

[28] R. W. Boswell, "Very efficient plasma generation by whistler waves near the lower hybrid frequency," *Plasma Physics and Controlled Fusion*, vol. 26, no. 10, pp. 1147–1162, 1984.

[29] F. F. Chen and D. Arnush, "Generalized theory of helicon waves. I. Normal modes," *Physics of Plasmas*, vol. 4, no. 9, pp. 3411–3421, 1997.

[30] D. Hayden, D. Juliano, M. Neumann, M. Allain, and D. N. Ruzic, "Helicon plasma source for ionized physical vapor deposition," *Surface and Coatings Technology*, vol. 120, pp. 401–404, 1999.

[31] A. V. Arefiev and B. N. Breizman, "Theoretical components of the VASIMR plasma propulsion concept," *Physics of Plasmas*, vol. 11, no. 5, pp. 2942–2949, 2004.

[32] J. P. Squire, F. R. Chang-Diaz, V. T. Jacobson, T. W. Glover, F. W. Baity, M. D. Carter, R. H. Goulding, R. D. Bengtson, and E. A. Bering III, "Investigation of a light gas helicon plasma source for the VASIMR space propulsion system," vol. 694, no. 1, pp. 423–426, 2003.

[33] J. Rapp, T. Biewer, T. Bigelow, J. Caughman, R. Duckworth, D. Giuliano, R. Goulding, D. Hillis, R. Howard, R. Ellis, *et al.*, "The Material Plasma Exposure eXperiment MPEX: Pre-design, development and testing of source concept," in *2015 IEEE 26th Symposium on Fusion Engineering (SOFE)*, pp. 1–8, IEEE, 2015.

[34] J. F. Caneses and B. D. Blackwell, "Collisional damping of helicon waves in a high density hydrogen linear plasma device," *Plasma Sources Science and Technology*, vol. 25, no. 5, p. 055027, 2016.

[35] J. Rapp, L. W. Owen, X. Bonnin, J. F. Caneses, J. M. Canik, C. Corr, and J. D. Lore, "Transport simulations of linear plasma generators with the B2.5-Eirene and EMC3-Eirene codes," *Journal of Nuclear Materials*, vol. 463, pp. 510–514, 2015.

[36] P. Fiflis, D. Andrucyzk, a. L. Roquemore, M. McGuire, D. Curreli, and D. N. Ruzic, "Lithium pellet production (LiPP): A device for the production of small spheres of lithium," *Review of Scientific Instruments*, vol. 84, no. 6, pp. 2013–2016, 2013.

[37] K. P. Shamrai and V. B. Taranov, "Volume and surface RF power absorption in a helicon plasma source," *Plasma Sources Science and Technology*, vol. 5, no. 3, p. 474, 1996.

[38] D. Arnush, "The role of Trivelpiece–Gould waves in antenna coupling to helicon waves," *Physics of plasmas*, vol. 7, no. 7, pp. 3042–3050, 2000.

[39] D. Blackwell, T. Madziwa, D. Arnush, and F. Chen, "Evidence for Trivelpiece-Gould modes in a helicon discharge," *Physical Review Letters*, vol. 88, no. 14, p. 145002, 2002.

[40] F. F. Chen and D. Curreli, "Central peaking of magnetized gas discharges," *Physics of Plasmas*, vol. 20, no. 5, p. 057102, 2013.

[41] D. Curreli and F. F. Chen, "Equilibrium theory of cylindrical discharges with special application to helicons," *Physics of Plasmas*, vol. 18, no. 11, p. 113501, 2011.

[42] K. P. Shamrai, "Stable modes and abrupt density jumps in a helicon plasma source," *Plasma Sources Science and Technology*, vol. 7, no. 4, p. 499, 1998.

[43] R. H. Goulding, J. B. O. Caughman, J. Rapp, T. M. Biewer, T. S. Bigelow, I. H. Campbell, J. F. Caneses, D. Donovan, N. Kafle, E. H. Martin, H. B. Ray, G. C. Shaw, and M. A. Showers, "Progress in the development of a high power helicon plasma source for the materials plasma exposure experiment," *Fusion Science and Technology*, vol. 72, no. 4, pp. 588–594, 2017.

[44] Y. Sakawa, T. Takino, and T. Shoji, "Contribution of slow waves on production of high-density plasmas by m=0 helicon waves," *Physics of Plasmas*, vol. 6, no. 12, p. 4759, 1999.

[45] M. Light, F. F. Chen, and P. L. Colestock, "Low frequency electrostatic instability in a helicon plasma," *Physics of Plasmas*, vol. 8, no. 10, pp. 4675–4689, 2001.

[46] M. Yoshitaka, N. Hideki, F. W. Baity Jr, R. H. Goulding, M. D. Carter, and D. O. Sparks, "Focusing magnetic field contribution for helicon plasma on Mini-RFTF," *Thin solid films*, vol. 506, pp. 583–587, 2006.

[47] P. A. Piotrowicz, J. F. Caneses, D. L. Green, R. H. Goulding, C. Lau, J. B. Caughman, J. Rapp, and D. N. Ruzic, "Helicon normal modes in Proto-MPEX," *Plasma Sources Science and Technology*, vol. 27, no. 5, p. 055016, 2018.

[48] P. A. Piotrowicz, J. F. Caneses, M. A. Showers, D. L. Green, R. H. Goulding, J. B. Caughman, T. M. Biewer, J. Rapp, and D. N. Ruzic, "Direct measurement of the transition from edge to core power coupling in a light-ion helicon source," *Physics of Plasmas*, vol. 25, no. 5, p. 052101, 2018.

[49] J. Rapp, T. M. Biewer, T. S. Bigelow, J. Caughman, R. C. Duckworth, R. J. Ellis, D. R. Giuliano, R. H. Goulding, D. Hillis, R. Howard, *et al.*, "The development of the material plasma exposure experiment," *IEEE Transactions on Plasma Science*, vol. 44, no. 12, pp. 3456–3464, 2016.

[50] P. Stangeby, "The Chodura sheath for angles of a few degrees between the magnetic field and the surface of divertor targets and limiters," *Nuclear Fusion*, vol. 52, no. 8, p. 083012, 2012.

[51] J. Lehane and F. Paoloni, "Hydromagnetic wave propagation in inhomogeneous magnetic fields," *Plasma Physics*, vol. 12, no. 11, p. 823, 1970.

[52] Y. Yasaka, R. Majeski, J. Browning, N. Hershkowitz, and D. Roberts, "ICRF heating with mode control provided by a rotating field antenna," *Nuclear Fusion*, vol. 28, no. 10, p. 1765, 1988.

[53] T. H. Stix and R. W. Palladino, "Observation of ion cyclotron waves," *The Physics of Fluids*, vol. 3, no. 4, pp. 641–647, 1960.

[54] D. Roberts and N. Hershkowitz, "Enhanced slow-wave beach heating of mirror plasmas with two-ion species," *Physics of Fluids B: Plasma Physics*, vol. 4, no. 6, pp. 1475–1485, 1992.

[55] S. N. Golovato, K. Brau, J. Casey, J. Coleman, M. J. Gerver, W. Guss, G. Hallock, S. Horne, J. Irby, R. Kumazawa, J. Kesner, B. Lane, J. Machuzak, T. Moran, R. Myer, R. S. Post, E. Sevillano, D. K. Smith, J. D. Sullivan, R. Torti, L. Wang, Y. Yasaka, X. Z. Yao, and J. Zielinski, "Plasma production and heating in a tandem mirror central cell by radio-frequency waves in the ion cyclotron frequency range," *Physics of Fluids*, vol. 31, no. 12, pp. 3744–3753, 1988.

[56] E. A. Bering, F. R. Díaz, J. P. Squire, T. W. Glover, M. D. Carter, G. E. McCaskill, B. W. Longmier, M. S. Brukardt, W. J. Chancery, and V. T. Jacobson, "Observations of single-pass ion cyclotron heating in a trans-sonic flowing plasma," *Physics of Plasmas*, vol. 17, no. 4, 2010.

[57] R. H. Goulding, P. A. Piotrowicz, C. J. Beers, T. Biewer, J. F. Caneses, J. B. Caughman, N. Kafle, E. G. Lindquist, H. B. Ray, J. Rapp, and M. A. Showers, "Results of ion cyclotron heating experiments on Proto-MPEX utilizing a movable stainless steel target," *Fusion Science and Technology*, in press.

[58] R. H. Goulding and P. A. Piotrowicz, "Ion Cyclotron Heating on Proto-MPEX," in progress.

[59] W. Gekelman, S. Vincena, and D. Leneman, "Experimental observations of shear Alfvén waves generated by narrow current channels," *Plasma Physics and Controlled Fusion*, vol. 39, no. 5A, p. A101, 1997.

[60] C. Kletzing, S. Bounds, J. Martin-Hiner, W. Gekelman, and C. Mitchell, "Measurements of the shear Alfvén wave dispersion for finite perpendicular wave number," *Physical review letters*, vol. 90, no. 3, p. 035004, 2003.

[61] W. Gekelman, S. Vincena, B. Van Compernolle, G. Morales, J. Maggs, P. Pribyl, and T. Carter, "The many faces of shear Alfvén waves," *Physics of Plasmas*, vol. 18, no. 5, p. 055501, 2011.

[62] S. Vincena, W. Gekelman, and J. Maggs, "Shear Alfvén waves in a magnetic beach and the roles of electron and ion damping," *Physics of Plasmas*, vol. 8, no. 9, pp. 3884–3896, 2001.

[63] B. McVey, "ICRF antenna coupling theory for a cylindrically stratified plasma," 1984.

[64] L. Chen and A. Hasegawa, "Plasma heating by spatial resonance of Alfvén wave," *The Physics of Fluids*, vol. 17, no. 7, pp. 1399–1403, 1974.

[65] A. Hasegawa and L. Chen, "Theory of plasma heating by nonlinear excitation of lower hybrid resonance," *The Physics of Fluids*, vol. 18, no. 10, pp. 1321–1326, 1975.

[66] A. Timofeev, "On the influence of Alfvén resonance on ion cyclotron resonance heating," *Plasma Physics Reports*, vol. 40, no. 1, pp. 1–13, 2014.

[67] A. V. Timofeev, “On RF heating of inhomogeneous collisional plasma under ion-cyclotron resonance conditions,” *Plasma Physics Reports*, vol. 41, no. 11, pp. 873–881, 2015.

[68] J. F. Caneses, P. A. Piotrowicz, T. M. Biewer, J. B. O. Caughman, R. H. Goulding, N. Kafle, and J. Rapp, “Differential pumping requirements for the light-ion helicon source and heating systems of Proto-MPEX,” *Physics of Plasmas*, vol. 083518, 2018.

[69] C. J. Beers, R. H. Goulding, R. C. Isler, E. H. Martin, T. M. Biewer, J. F. Caneses, J. B. O. Caughman, N. Kafle, and J. Rapp, “Helicon plasma ion temperature measurements and observed ion cyclotron heating in proto-MPEX,” *Physics of Plasmas*, vol. 25, pp. 1–9, 2018.

[70] S. Hiroe, R. Colchin, G. Haste, F. Baity, D. Bates, L. Berry, T. Bigelow, R. Burris, J. Cobble, W. Davis, *et al.*, “Summary of ELMO Bumpy Torus (EBT-S) experiments from 1982 to 1984,” *Nuclear fusion*, vol. 28, no. 12, p. 2249, 1988.

[71] A. Ando, M. Inutake, M. Hatanaka, K. Hattori, H. Tobari, and T. Yagai, “Alfvén wave excitation and single-pass ion cyclotron heating in a fast-flowing plasma,” *Physics of Plasmas*, vol. 13, no. 5, pp. 1–7, 2006.

[72] M. Light, I. D. Sudit, F. F. Chen, and D. Arnush, “Axial propagation of helicon waves,” *Physics of Plasmas*, vol. 2, no. 11, pp. 4094–4103, 1995.

[73] D. Brunner, B. LaBombard, R. Ochoukov, and D. Whyte, “Scanning retarding field analyzer for plasma profile measurements in the boundary of the Alcator C-Mod tokamak,” *Review of Scientific Instruments*, vol. 84, no. 3, 2013.

[74] V. I. Demidov, S. V. Ratynskaia, and K. Rypdal, “Electric probes for plasmas: The link between theory and instrument,” *Review of Scientific Instruments*, vol. 73, no. 10, p. 3409, 2002.

[75] D. Brunner, B. LaBombard, R. M. Churchill, J. Hughes, B. Lipschultz, R. Ochoukov, T. D. Rognlien, C. Theiler, J. Walk, M. V. Umansky, and D. Whyte, “An assessment of ion temperature measurements in the boundary of the Alcator C-Mod tokamak and implications for ion fluid heat flux limiters,” *Plasma Physics and Controlled Fusion*, vol. 55, no. 9, p. 095010, 2013.

[76] D’Errico, John. Efficient nonlinear regression fitting using fminspleas. (https://www.mathworks.com). MATLAB Central File Exchange. Retrieved May 5th 2019.

[77] E. H. Martin, *Electric Field Measurements of the Capacitively Coupled Magnetized RF Sheath Utilizing Passive Optical Emission Spectroscopy.* PhD thesis, North Carolina State University, 2014.

[78] R. C. Isler, R. W. Wood, C. C. Klepper, N. H. Brooks, M. E. Fenstermacher, and A. W. Leonard, “Spectroscopic characterization of the DIII-D divertor,” *Physics of Plasmas*, vol. 355, 1997.

[79] MATLAB 2015b, The MathWorks, Natick, MA, USA, 2015.

[80] R. E. Bell and R. E. Bell, “Inversion technique to obtain an emissivity profile from tangential line-integrated hard x-ray measurements,” *Review of Scientific Instruments*, vol. 558, no. 66, 1995.

[81] R. E. Bell, “An inversion technique to obtain full poloidal velocity profiles in a tokamak plasma,” *Review of Scientific Instruments*, vol. 68, no. May 1996, pp. 1273–1280, 1997.

[82] Killer, Carsten. Abel Inversion using abelinversion. (https://www.mathworks.com). MATLAB Central File Exchange. Retrieved May 5th 2019.

[83] M. Showers, T. M. Biewer, J. B. O. Caughman, D. C. Donovan, R. H. Goulding, and J. Rapp, “Heat flux estimates of power balance on Proto-MPEX with IR imaging,” *Review of Scientific Instruments*, vol. 87, no. 11, p. 11D412, 2016.

[84] Criminisi, Antonio. Computing the plane to plane homography using homographysolve. MATLAB Central File Exchange. Retrieved May 5th 2019.

[85] COMSOL Multiphysics v. 5.4. www.comsol.com. COMSOL AB, Stockholm, Sweden.

[86] A. Stampa and H. Wulf, "The behaviour of electrostatic double probes in plasmas with high-amplitude RF fields," *Journal of Physics D: Applied Physics*, vol. 11, no. 7, p. 1119, 1978.

[87] D. G. Swanson, *Plasma waves.* CRC Press, 2003.

[88] M. Brambilla, *Kinetic theory of plasma waves: homogeneous plasmas*, vol. 96. Oxford University Press, 1998.

[89] E. Jaeger, L. Berry, and D. Batchelor, "Full-wave calculation of sheared poloidal flow driven by high-harmonic ion Bernstein waves in tokamak plasmas," *Physics of Plasmas*, vol. 7, no. 8, pp. 3319–3329, 2000.

[90] MATLAB Symbolic Toolbox 2015b, The MathWorks, Natick, MA, USA, 2015.

[91] R. Fitzpatrick, *Plasma physics: an introduction.* CRC Press, 2014.

[92] M. A. Lieberman, A. J. Lichtenberg, *et al.*, *Principles of plasma discharges and materials processing*, vol. 2. Wiley Online Library, 2005.

[93] S. Pancheshnyi, S. Biagi, M. Bordage, G. Hagelaar, W. Morgan, A. Phelps, and L. Pitchford, "The LXCat project: Electron scattering cross sections and swarm parameters for low temperature plasma modeling," *Chemical Physics*, vol. 398, pp. 148–153, 2012.

[94] H. Summers, "The ADAS user manual, version 2.6 (2004)," *URL http://www. adas. ac. uk.*

[95] F. W. Baity, G. C. Barber, M. D. Carter, R. H. Goulding, D. O. Sparks, F. R. Chang-Daz, G. E. McCaskill, and J. P. Squire, "Design of RF systems for the RTD mission VASIMR," vol. 417, no. 1999, pp. 417–420, 1999.

[96] B. N. Breizman and A. V. Arefiev, "Single-pass ion cyclotron resonance absorption," *Physics of Plasmas*, vol. 8, no. 3, pp. 907–915, 2001.

[97] R. Comfort, "The magnetic mirror force in plasma fluid models," *Modeling magnetospheric plasma*, vol. 44, pp. 51–53, 1988.

[98] D. Bohm and E. P. Gross, "Theory of plasma oscillations. b. excitation and damping of oscillations," *Physical Review*, vol. 75, no. 12, p. 1864, 1949.

[99] P. C. Stangeby, *The plasma boundary of magnetic fusion devices.* CRC Press, 2000.

[100] S. I. Braginskii, "Transport processes in a plasma," *Reviews of Plasma Physics*, vol. 1, p. 205, 1965.

[101] Y. Mouzouris and J. E. Scharer, "Modeling of profile effects for inductive helicon plasma sources," *IEEE transactions on plasma science*, vol. 24, no. 1, pp. 152–160, 1996.

[102] D. Arnush and F. F. Chen, "Generalized theory of helicon waves. II. Excitation and absorption," *Physics of Plasmas*, vol. 5, no. 5, p. 1239, 1998.

[103] S. Cho, "Eigenmode dispersion relations in radially inhomogeneous helicon plasmas," *Physics of Plasmas*, vol. 16, no. 6, p. 063504, 2009.

[104] A. Ando, M. Inutake, M. Hatanaka, K. Hattori, H. Tobari, and T. Yagai, "Alfven wave excitation and single-pass ion cyclotron heating in a fast-flowing plasma," *Physics of plasmas*, vol. 13, no. 5, p. 057103, 2006.

[105] Y. Zhang, W. Heidbrink, S. Zhou, H. Boehmer, R. McWilliams, T. Carter, S. Vincena, and M. Lilley, "Doppler-shifted cyclotron resonance of fast ions with circularly polarized shear alfvén waves," *Physics of Plasmas*, vol. 16, no. 5, p. 055706, 2009.

[106] E. A. Bering, F. R. Chang-Díaz, J. P. Squire, M. Brukardt, T. W. Glover, R. D. Bengtson, V. T. Jacobson, G. E. McCaskill, and L. Cassady, "Electromagnetic ion cyclotron resonance heating in the VASIMR," *Advances in Space Research*, vol. 42, no. 1, pp. 192–205, 2008.

[107] J. Caneses, B. Blackwell, and P. Piotrowicz, "Helicon antenna radiation patterns in a high-density hydrogen linear plasma device," *Physics of Plasmas*, vol. 24, no. 11, p. 113513, 2017.

[108] A. W. Molvik, A. R. Ellingboe, and T. D. Rognlien, "Hot-electron production and wave structure in a helicon plasma source," *Physical Review Letters*, vol. 79, no. 2, pp. 233–236, 1997.

[109] B. Breizman and A. Arefiev, "Radially localized helicon modes in nonuniform plasma," *Phys. Rev. Lett.*, vol. 84, no. 17, pp. 3863–3866, 2000.

[110] J. L. Kline, E. E. Scime, R. F. Boivin, A. M. Keesee, X. Sun, and V. S. Mikhailenko, "RF absorption and ion heating in helicon sources," *Physical Review Letters*, vol. 88, no. 19, p. 195002, 2002.

[111] K. Niemi and M. Krämer, "Helicon mode formation and radio frequency power deposition in a helicon-produced plasma," *Physics of Plasmas*, vol. 15, no. 7, pp. 073503–1–073503–11, 2008.

[112] M. D. Carter, F. W. Baity, G. C. Barber, R. H. Goulding, Y. Mori, D. O. Sparks, K. F. White, E. F. Jaeger, F. R. Chang-Díaz, and J. P. Squire, "Comparing experiments with modeling for light ion helicon plasma sources," *Physics of Plasmas*, vol. 9, no. 12, pp. 5097–5110, 2002.

[113] A. I. Akhiezer, V. S. Mikhailenko, and K. N. Stepanov, " Ion-sound parametric turbulence and anomalous electron heating with application to helicon plasma sources," *Physics Letters A*, vol. 245, pp. 117–122, 1998.

[114] F. F. Chen, "Physics of helicon discharges," *Physics of Plasmas*, vol. 3, pp. 1783–1793, 1996.

[115] W. Eckstein, "Calculated sputtering, reflection and range values," 2002.

[116] A. J. Perry, "The application of the helicon source to plasma processing," *Journal of Vacuum Science & Technology B: Microelectronics and Nanometer Structures*, vol. 9, no. 2, p. 310, 1991.

[117] T. Shoji, Y. Sakawa, S. Nakazawa, K. Kadota, and T. Sato, "Plasma production by helicon waves," *Plasma Sources Science and Technology*, vol. 5, pp. 5–10, 1993.

[118] T. H. Stix, *Waves in plasmas.* Springer Science & Business Media, 1992.

[119] Y. Sakawa, M. Ohshima, Y. Ohta, and T. Shoji, "Production of high-density hydrogen plasmas by helicon waves in a simple torus," *Physics of Plasmas*, vol. 11, no. 1, pp. 311–319, 2004.

[120] B. D. Blackwell, J. F. Caneses, C. M. Samuell, J. Wach, J. Howard, and C. Corr, "Design and characterization of the Magnetized Plasma Interaction Experiment (MAGPIE): a new source for plasma–material interaction studies," *Plasma Sources Science and Technology*, vol. 21, no. 5, p. 055033, 2012.

[121] A. Fruchtman, "Neutral gas depletion in low temperature plasma," *Journal of Physics D: Applied Physics*, vol. 50, no. 47, p. 473002, 2017.

[122] R. Ikezoe, Y. Kubota, M. Ichimura, M. Hirata, S. Sumida, S. Jang, K. Izumi, A. Tanaka, R. Sekine, and H. Kayano, "A full wave simulation on the density dependence of a slow wave excitation in the GAMMA 10/PDX central cell with TASK/WF3D," *Plasma and Fusion Research*, vol. 14, pp. 2402003–2402003, 2019.

[123] L. W. Owen, J. Rapp, J. Canik, and J. D. Lore, "Transport modeling of convection dominated helicon discharges in Proto-MPEX with the B2.5-Eirene code," *Physics of Plasmas*, vol. 24, no. 11, 2017.